On-line simulation of inverter-induction motor drives for rapid transit

Huang, F.

Award date:
1991

Awarding institution:
University of Bath

ON-LINE SIMULATION OF INVERTER - INDUCTION MOTOR DRIVES FOR RAPID TRANSIT

Submitted by F. Huang, B.Sc.

for the degree of

Doctor of Philosophy

of the University of Bath

1991

ProQuest LLC
789 East Eisenhower Parkway
P.O. Box 1346
Ann Arbor, MI 48106-1346

Summary

An on-line simulator for voltage source inverter squirrel cage induction motor drives for rapid-transit is presented. The simulator has been used for a typical metro system duty cycle. The simulation results have been validated by comparison with measurements from a laboratory based simulator.

The system model uses a 7-dimensional, time-varying non-linear model, implemented on a multi-processor computer using multi-task operating system software. The simulator is capable of modelling various pulse width modulation systems, together with transient effects arising from "gear changes" and pulse dropping.

A small scale laboratory-based traction drive system was constructed. This system consists of a 68000 single-board computer, a 3-phase GTO thyristor inverter, and a squirrel cage induction motor-DC generator system. The purpose of the laboratory drive was to validate the simulator.

Acknowledgements

The author is indebted to his academic supervisor, Dr. R.J. Hill, for his guidance throughout this work. He would like to thank Professor J.F. Eastham, Head of the School of Electronic and Electrical Engineering for provision of facilities.

Financial support from the Chinese Government and British Council is gratefully acknowledged.

Thanks also go to Mr. A.R. Daniels for offering computer facilities and to Dr. B.J. Cardwell from Brush Electrical Machines Ltd. for supplying technical information.

Finally, the author would like to give a special thanks to those who have given invaluable consultancy and technical help, in particular, Dr. M.J. Balchin, Mr. D. Carpenter, and Mr. R. Hill-Cottingham.

Contents

List of principal symbols

ψ	Air-gap flux linkage
f	Stator supply frequency
	or modulation frequency
f_{sl}	Slip frequency
f_r	Rotor electrical speed frequency $(=f-f_{sl})$
ω	Stator angular frequency
ω_b	Base or rated angular frequency
ω_s	Synchronous speed
ω_{sl}	Slip speed
ω_r	Rotor speed $(=\omega_s-\omega_{sl})$
ω_w	Train wheel speed
V_m	Magnetising voltage
V_s	Stator supply voltage
V_{sp}	Peak value of V_s
V_{an}	Motor phase to neutral voltage
V_{ao}	Inverter phase to center tap voltage
V_{no}	Motor neutral to center tap voltage
V_{dc}	DC link voltage
I_{in}	System input current
I_{dc}	DC link current
I_a	Stator current
I_r	Rotor current
I_m	Magnetising current
T_e	Motor torque
T_{em}	Maximum motor torque
T_l	Load torque

T_w Tractive torque referred to wheel axle

T_m Maximum transmittable torque

P_e Motor output power

R_s Stator resistance

R_r Rotor resistance

L_{sl} Stator leakage inductance

L_{rl} Rotor leakage inductance

L_m Magnetising inductance

p Number of poles

s Slip

J Inertia

α Train accelerating rate

G Motor/wheel speed ratio

f_h h^{th} harmonic frequency

f_c Carrier frequency

M_r Modulation ratio

M_d Modulation depth

V_c Carrier amplitude

q_i i^{th} switching angle for sinusoidal PWM

α_i i^{th} switching angle for optimised PWM

Chapter 1 : Introduction

1.1 AC traction drives

Railway electrification schemes have been implemented for over 100 years. During this long period of time, DC traction drive systems have been most commonly used. AC drives, however, have not been extensively applied to railway traction systems until the end of the 1970s [1,2].

The rapid development of microprocessor controlled power electronic devices has made AC drives more attractive in the last two decades. In 1970, Brown Boveri started to test the first diesel electric locomotive with inverter fed squirrel cage traction motors [3]. Since then, AC drives have been introduced into railway traction systems in most European countries, Japan, and North America.

Basically, AC drives in railway traction systems can be classified into two types, which are current source inverter fed synchronous motor drives and voltage source inverter fed asynchronous motor drives. For the former, much research and development has been done in France [4-7]. The latter have been adopted in many countries, particularly Japan [9-18] and Germany [19-28] but also

elsewhere [29-39]. Today, AC drives with voltage source inverter fed induction motors are standard.

Asynchronous drives have the following advantages compared with DC drives:

a) There are no commutators, brushes, slip rings or rotor windings in squirrel cage induction motor (SCIM) drives, so the volume / weight density is high, the maximum operating temperature, voltage and speed can also be high, and the motor has very low maintenance costs.

b) Since the regeneration ability of the induction motor is inherent, there are no contactors required to change over from motoring to braking, as is the case with DC motors.

c) The absence of contactors and other moving parts implies that little sparking and interference can occur.

In general, the advantage of DC motors with their simple electrical operating characters is balanced by the mechanical superiority of SCIMs. Modern techniques have given SCIM drives equivalent electrical operating characters to those of DC motors, with sacrifices in high cost and complexity.

The differences between synchronous and asynchronous drives can be stated in terms of the power converter and the machine. Due to natural commutation in synchronous drives, the inverter circuits are simpler than those for asynchronous drives. However, with no slip rings or commutators and a mechanically robust winding, the superiority of asynchronous motors is obvious. References [40-44] give more detail of both types of drives.

Asynchronous drives have been applied both for mainline electric locomotives and electric multiple units (EMU) for rapid transit railways. In both cases, the drive systems have one or more variable voltage variable frequency (VVVF) voltage source invertor (VSI) and a number of squirrel cage induction motors (SCIMs). For metro systems, the traction supply voltage may be 600V, 750V, 1500V DC. For mainlines, the DC voltage is either 1500V or 3000V DC, or is converted from a single phase supply normally at 11, 15, 20, and 25 kV.

1.2 On-line simulation of VSI-SCIM drives

The superiority of asynchronous drives over other drives has been generally accepted. To effectively design VSI-SCIM drives, much work has already been done in modelling and simulating such drive systems.

Computer simulation plays a key role in designing and optimising AC traction drive systems and obviates the necessity for the construction of expensive prototypes. Using a simulator, the system design engineers can optimise the system parameters according to certain predetermined criteria; and the system operators can choose the right control strategy to achieve the best system performances.

In general, the modelling of SCIMs for computer simulation can be carried out either in the frequency domain or in the time domain. Being a simple and fast technique, the frequency domain model can predict the system steady state behaviour. This model, however, is not suitable for transient behaviour[45,46]. Time domain simulation is a much more sophisticated technique that can perform both system steady state and transient analysis, and must be used when the system transient behaviour is important [47-54].

Due to the time-varying and non-linear characteristics of the system model in time domain, the simulation must be carried out with the assumption that within the simulation period the motor speed is constant. This linearises the system model. In the method, the system transient behaviour can only be viewed at each individual speed point [54]. To simulate a specific operating point, the motor speed must be pre-

calculated and then applied to the simulation as a constant. It has been shown [50] that due to the unknown initial conditions at each simulation point, a large portion of the program run time is taken up by settling the end result - only the last few cycles are of interest.

The time domain linearised system model is not suitable for determining a continuous system transient response following a designed train duty-cycle. To carry out this task, the motor speed must be treated as a variable by introducing another mechanically-related (torque-speed) nonlinear state equation. The simulator may then be controlled according to a practical train operating duty-cycle implemented in the form of PWM firing angles. This is most conveniently done by on-line simulation. The complexity of the model calculations must, however, be compromised with the flexibility of the simulation.

The multi-processor based parallel computer used in this work was designed by Dale [55] and modified by Berry [56]. It enables the on-line simulation to be carried out with relative ease. Apart from requiring a different model structure, the on-line simulator implemented by parallel computer differs from a conventional simulator in that it has a multi-task operating system (TRIPOS). In this operating system more

than one task can be handled at the same time. The programming language is BCPL. Moreover, it has an on-line graphic display unit, enabling the user to retain full control over the operating simulation. In contrast, conventional simulations are usually implemented using general-purpose languages and run on mainframe computers.

1.3 Scope of the thesis

The objective of this work is to simulate a DC-fed VSI-SCIM drive system for rapid transit railways in a on-line mode using a parallel computer. The first task is to define and model a practical DC-fed VSI-SCIM drive system, with a typical train operating urban duty-cycle; this is followed by implementation using different PWM schemes; the simulator has then been used to investigate transient behaviour. To verify the simulator, a laboratory based small scale drive system was designed and constructed, and the simulation results were compared with measurements from the experimental drive.

Chapter 2 contains a general description of DC-fed VSI-SCIM drive systems. This also includes information about the train resistance, maximum transmittable torque, and the traction drive duty-cycle. In chapter 3, various PWM schemes and different techniques such as over-modulation, gear changing, and pulse dropping are

summarised. The DC-fed VSI-SCIM drive system modelling is presented in chapter 4. The computer implementation of the system model and the system input is given in chapter 5. The design and implementation of the laboratory based drive system are presented in chapter 6. In chapter 7, the simulated and experimental results for a laboratory based system are compared. The simulation results for a practical traction drive following a designed urban duty-cycle are presented in chapter 8. Finally, some conclusions are drawn and future work is proposed in chapter 9.

Chapter 2 : VSI-SCIM traction drives

2.1 Introduction

A squirrel cage induction motor is mechanically superior to both DC and synchronous motors due to its robustness and maintenance-free features. The microprocessor controlled VVVF-VSI can provide a near sinusoidal three-phase supply. The combination of these two subsystems makes such a system extremely attractive to railway traction drive manufacturers.

In this chapter, the basic characteristics of an induction motor and its variable-speed operation are outlined first. Then, the operation of a voltage source inverter is described. This is followed by the consideration of practical train resistance and the maximum transmittable torque. The tractive torque should be selected such that it is large enough to drive the train at the designed acceleration rate and sufficient small such that it does not produce slipping or sliding between wheels and rails. Bearing in mind the above considerations, a practical traction drive duty-cycle is described.

2.2 Induction motor characteristics

In a cage induction motor, the stator windings are supplied with balanced three-phase sinusoidal voltages which establish a spatially distributed sinusoidal air-gap flux (ψ). This flux rotates at the synchronous speed (ω_s) relative to the stator windings. The rotating flux induces a counter-emf in the stator called the air-gap or magnetising voltage (V_m). It also induces rotor voltage and current. The interaction between the rotor current and the air-gap flux then produces the motor electromagnetic torque.

If the supply frequency is f and its angular frequency is ω, then the synchronous speed is

$$\omega_s = 2/p(2\pi f) = 2/p*\omega \qquad (2.1)$$

where p is the number of poles. With respect to the synchronous speed, The rotor speed (ω_r) exhibits a slip speed (ω_{sl})

$$\omega_{sl} = \omega_s - \omega_r \qquad (2.2)$$

Often, the slip speed is expressed in a per unit form

$$s = \frac{\omega_s - \omega_r}{\omega_s} \qquad (2.3)$$

From Faraday's law, the induced rotor voltages are at a slip frequency,

$$f_{sl} = \omega_{sl}/(2\pi)*p/2 = f - f_r \qquad (2.4)$$

where f_r is rotor electrical speed frequency.

In analysing an induction motor operation, a per-phase equivalent circuit is normally used as shown in Figure 2.1. Except at low frequency, the magnetizing inductance can be transferred to the input terminals. The magnetising voltage is given by

$$V_m = k_1 f\psi \approx V_s \qquad (2.5)$$

where V_s is stator supply voltage and k_1 is a constant. If f_{sl} is low such that $R_r >> 2\pi f_{sl}L_{lr}$, it can be shown that the rotor current is

$$I_r = K_2\psi f_{sl} \qquad (2.6)$$

where k_2 is a constant. The motor electromagnetic torque is

$$T_e = K_3\psi^2 f_{sl} \qquad (2.7)$$

where k_3 is a constant. The variation of torque with slip or motor speed for a constant supply voltage and frequency is shown in Figure 2.2. As shown in the figure, three regions are defined by plugging, motoring, and regenerating.

In the plugging region ($1.0 < s < 2.0$), the rotor direction is reverse that of the air-gap flux. This condition may arise if the stator supply phase sequence is reversed when the rotor is moving, or because of an overhauling type of load which drives the rotor in the opposite direction. The energy due to a plugging brake is dissipated in the machine, which may cause excessive machine heating. Therefore, this region is not used for traction.

In the regeneration region ($s < 0$), the rotor moves at super synchronous speed in the same direction as the air-gap flux so the slip becomes negative, creating negative or regeneration torque. The negative slip, corresponding to a power factor > 90°, generates energy and sends it back to the source. In AC traction drives, the negative slip (regenerating) operation can be realized by reducing the stator frequency to a value lower than the rotor speed to obtain a regenerative braking effect.

2.3 Variable-speed operation

The variable-speed operation of a cage induction motor can be achieved by varying either the supply voltage and/or the supply frequency.

By varying the stator voltage and keeping the frequency constant, the torque-speed curves becomes as shown in Figure 2.3. As can be seen in the figure, with increase of stator voltage the maximum torque(T_{em}) is raised. This is because the flux is proportional to stator voltage. Moreover, the slip corresponding to maximum torque under different stator voltages is the same. If the rated stator voltage is kept constant, and the frequency is increased beyond the rated value, the air-gap flux decreases, and so also does the maximum torque. The resultant torque-speed curves are shown in Figure 2.4.

Normally three drive regions are required for traction drive operation to fully utilise the capabilities of the motor. They are the constant torque, constant power and high-speed regions. These three drive regions can be implemented from varying the voltage and frequency in different ways. The total performance of the induction motor under the three regions is shown in Figure 2.5.

Constant torque performance is achieved by increasing the voltage and frequency simultaneously, so as to keep the flux constant. During this period, the slip frequency is kept constant. The constant flux and slip frequency keep the rotor current and the stator current constant. This can be understood from eqns. 2.6 and 2.7.

At low supply frequencies, the motor reactance decreases and the voltage drop is mainly due to the stator resistance. To compensate for this, the supply voltage has to be increased.

Following the constant torque operation period, the motor torque is made proportional to $1/f$. It is clear from eqn. 2.7 that if the rated supply voltage is kept constant, to achieve this the slip ($s = f_{sl}/f$) must also be constant. Due to the constant slip, the rotor speed must be proportional to the synchronous speed [$\omega_r = (1-s)\ \omega_s$]. Hence the motor electromechanical power $P_e = T_e\omega_r$ must be constant. In addition, the constant slip also maintains the rotor current constant. This can be seen from eqn. 2.6.

In the high-speed region, the motor torque is proportional to $1/f^2$. Again, from eqn. 2.7, this requires the slip frequency to be kept constant at the pullout value. Under this condition, the rotor current, from eqn. 2.6, is proportional to $1/f$.

2.4 Voltage source inverters

To perform the full traction duty-cycle driving operation, a VVVF AC supply source is required. Various switching devices can be used to construct a VVVF AC supply source. The most widely used power switching

devices are bipolar transistors, MOSFETs, thyristors, and gate turn-off thyristors (GTOs). Table 2.1 presents the major features of the above devices. As can been seen from the Table, GTO thyristors have the most favourable features for the purpose of traction drives. Indeed, GTOs dominate today's AC traction drives [57-59].

The most commonly used inverter is the voltage source inverter which consists of three half-bridge switching units. Each unit, corresponding to one phase, has two switching devices. The DC voltage across the inverter is obtained from either a DC supply (in transit trains) or the output of an AC-DC converter (in locomotives) through a low pass input filter.

In industrial applications, the LC low pass filter is used to smooth the DC link voltage. For traction drives, since the supply circuit is also used as signalling system circuit, this filter is specially designed to prevent harmonic currents being injected back to the supply [60-62].

A simplified inverter circuit diagram is shown in Figure 2.6. The center-tap of the DC supply is only for convenience of analysis. Under square-wave operation, the upper and lower GTOs in each phase are switched on and off alternatively for 180 degree intervals. The three phases are shifted by 120 degrees. Figure 2.7 (a-

c) shows the inverter phase voltage (referred to the center-tapped point) and the line voltage. For a wye-connected load with isolated neutral the load phase voltages are

$$\begin{aligned} V_{an} &= V_{ao} + V_{no} \\ V_{bn} &= V_{bo} + V_{no} \\ V_{cn} &= V_{co} + V_{no} \end{aligned} \qquad (2.8)$$

Since for a balanced load, $V_{an} + V_{bn} + V_{cn} = 0$, adding equations (2.8)

$$V_{no} = 1/3(V_{ao}+V_{bo}+V_{co}) \qquad (2.9)$$

Substituting equation (2.5) in (2.4) yields

$$V_{an} = 2/3*V_{ao} - 1/3(V_{bo}+V_{co}) \qquad (2.10)$$

Figure 2.7 (d) shows the resultant load phase voltage. It can be shown that the phase voltage of the load does not contain any triplen harmonics. The central to neutral voltage contains all triplen harmonics.

The square wave of the inverter output voltage is determined only by the switching pattern and not by the load. The load currents are, however, mostly affected by the load and will lag the voltage if the load is inductive. The anti-parallel connected diodes shown in

Figure 2.6 provide a feedback path for the lagged current.

Power conversion through the inverter is shown in Figure 2.7 (d). The load is assumed to be an induction motor with a sinusoidal load current. During the interval ωt_1, the phase voltage is positive and the current is negative, i.e., reactive current is flowing to the source through the feedback diode D_1. In interval ωt_2, the GTO, Q_1, is carrying active load current. The next half-cycle has similar operation. Note that in the interval ωt_2, DC power is inverted into AC power, and in the interval ωt_1, AC power is converted back to DC power. It is clear that when the interval ωt_2 is larger than the interval ωt_1, the power factor $\varnothing < 90°$, and the motor slip is in the range, $0 < s < 1$, i.e. the machine is in the motoring mode; when $\omega t_1 > \omega t_2$, $\varnothing > 90°$, and the motor slip $s < 0$, i.e. the machine is in regenerating mode.

The above description assumes the inverter operates under square-wave modulation. In practice, for constant torque operation square-wave modulation is unsuitable. Instead, pulse width modulation (PWM) is used. The idea of PWM is based on cutting the square waves into a series of pulses. Various PWM schemes are outlined in detail in the next chapter.

2.5 Train resistance

The principle of vehicle movement is based on action and reaction between tractive force and vehicle resistance. The total resistance to motion of a moving train is composed of a number of components such as tractive resistance, gradient and curve resistance, and accelerating resistance. The tractive resistance consists of rotating, rolling, and the air resistance.

The following explains how in practice, train resistance may be calculated. The data used was supplied by Brush Electrical Machines Ltd., and gradient and curve resistances are not included.

For multiple-unit stock with a flat end profile, the resistance is given by

$$R = WR_m + NR_w + R_o \qquad (2.11)$$

where R is total train resistance (N), W is gross weight of train (tonnes), R_m is the specific mechanical and track resistance (N/tonnes), N is the number of vehicles in the train, R_w is the specific wind resistance (N/car), and R_o is head and wake resistance (N/train). Typical values for R_m, R_w, and R_o are given in Appendix A. If W is 110 tonnes and N is 3 cars, then WR_m, NR_w, and R_o are as shown in Figure 2.8 (a-c).

If $y_1 = f(x_1)$, $y_2 = f(x_2)$,... $y_n = f(x_n)$ represent n points of R_m; where x represents the speed. Applying the polynomial interpolation method [63], the value of R_m at any intermediate point is given by:

$$R_m(x) = \frac{(x-x_2)(x-x_3)\ldots(x-x_n)}{(x_1-x_2)(x_1-x_3)\ldots(x_1-x_n)} * y_1 + \frac{(x-x_1)(x-x_3)\ldots(x-x_n)}{(x_2-x_1)(x_2-x_3)\ldots(x_2-x_n)} * y_2 + \ldots\ldots\ldots + \frac{(x-x_1)(x-x_2)\ldots(x-x_{n-1})}{(x_n-x_1)(x_n-x_2)\ldots(x_n-x_{n-1})} * y_n \qquad (2.12)$$

Having applied this method to R_w and R_o, the total resistance at any instant speed can be found as the sum of the three variables. Figure 2.8 (d) presents the resultant interpolated resistance. To obtain this curve a look-up table of 120 points was made with a speed resolution of 1 km/h. Throughout this work, this look-up table was used as the value of the train resistance.

Alternatively, the total resistance can be expressed in a general form for any given train weight W and number of cars N. From Figure 2.8 (d), it is clear that at very low speed (0-5 km/h), the total resistance decreases linearly. It then increases nonlinearly. After approximating the three resistances as a second order function, R_m, R_w, and R_o may be expressed as

$$R_m = 10.556 + 0.104941*x + 3.667*10^{-4}*x^2$$

$$R_w = 27.4545 + 1.95943*x + 0.0423334*x^2$$

$$R_o = 617.167 - 6.97169*x + 0.307667*x^2 \qquad (2.13)$$

where x varies from 5 to 120 km/h. Thus the total resistance is in the form

$$R(x) = \begin{cases} ((11.09-66)/5*x + 66)W; \cdots\cdots\cdots\cdots\ 0 < x \leq 5 \\ (3.667*10^{-4}*W + 0.0423336*N + 0.307667)x^2 \\ +(0.104941*W + 1.95943*N - 6.97169)x \\ +(10.556*W + 27.4545*N + 617.167); \cdots\ 5 < x < 120 \end{cases} \qquad (2.14)$$

Figure 2.8 (e) shows the generalized resistance with W as 110 tonnes and N as 3 cars.

2.6 Maximum transmittable torque

To drive a vehicle , the applied force must exceed the resistance force. The difference between applied and resistance force determines the acceleration rate. For railway traction drive applications, the torque which is generated by the motors and can be transmitted from the wheels to the rails is limited by a value called the maximum transmittable torque, which can be expressed as [64]

$$T_m = AW_t/(100-KA)r9.8/G \qquad (2.15)$$

where A is the adhesion level, W_t is the axle load (N), K is the weight transfer coefficient, r is the wheel radius (m) and G is the motor/wheel speed ratio.

Figure 2.9 (a,b) shows a typical variation of adhesion with train speed under dry and wet rail conditions, which has been obtained from a number of tests under different conditions [65].

From the data supplied by Brush Electrical Machines Ltd., the weight transfer coefficient K has been set at 15% and the maximum adhesion level as 26%. In addition, wheel radius r is set at 0.41 m, and the motor/wheel speed ratio G as 60/13.

From the above data, the maximum transmittable torque under dry and wet rail conditions has been calculated and is shown in Figure 2.10 (a,b). Under normal operation, the tractive torque produced by the motor is limited to this value, otherwise the wheel and rail will tend to slip or slide.

2.7 Traction drive duty-cycle

In general, electric rail-cars require a large torque at low speeds to attain a high rate of acceleration. At high speeds, however, they require a smaller torque sufficient to maintain a given speed. To satisfy these torque requirements and to optimise the capability of the inverters and motors, the three drive regions described in section 2.3 are normally adopted (Figure

2.11). The change-over point between the first two regions is normally made at the rated or base frequency (ω_b), and the second change is made at around the middle point between base frequency and maximum frequency [66].

After accelerating through these three regions, the train speed is normally kept constant for a certain period, called the coasting period. The length of this period is determined by the distance between stations. The operating characteristics in the braking mode are similar to those for motoring. The maximum rating of the traction drive is exploited during braking.

A train operation duty-cycle can be described by the curve of speed with the corresponding time. To implement the duty-cycle in a traction drive, the supply frequency - time variation must be determined. The motor speed is given by $\omega_r = G\omega_w$, where ω_w is the wheel speed. For a given motor slip angular frequency ω_{sl}, the synchronous angular frequency is the sum of the slip angular frequency and the rotor angular frequency ω_r. The supply angular frequency is given by $\omega = p/2*\omega_s$, where p is the number of poles.

To find the relationship between train speed and required time in the duty-cycle, the tractive torque and the resistance torque must be determined. If T_e and T_w

are the torques referred to the motor shaft and the wheel shaft respectively, then

$$T_w = \omega_r/\omega_w * T_e = GT_e \qquad (2.16)$$

This equation has been derived according to $P = T_w\omega_w = T_e\omega_r$, where P is the power. The train resistance torque (T_l) can be obtained by multiplying the train resistance by the wheel radius. The total train resistance must be divided by the number of motored axles.

Once the total torque is determined, the accelerating rate of the train (α) at variable train speed is given as

$$\alpha = (T_w - T_l)/J \qquad (2.17)$$

where T_w and T_l are both functions of train speed and J is the inertia under a specific train load. If the train speed is treated as a constant in a small time interval Δt, During the i^{th} interval, since $\alpha(i) = [\omega_w(i)-\omega_w(i-1)]/\Delta t$

$$\omega_w(i) = \alpha(i)\Delta t + \omega_w(i-1) \qquad (2.18)$$

with $\omega_w(0) = 0$.

Using eqn. 2.17 and 2.18 together with T_e and T_l derived in section 2.3 and 2.5, the relationship between train

speed and time can be described by a speed-time curve. Using this information a benchmark traction drive duty-cycle, with a maximum speed of 120 km/h, has been calculated (Figure 2.12).

The above calculation is affected by the time step duration (Δt). It was found that Δt = 1 ms gave sufficient accuracy.

2.8 A practical traction drive system

VSI-SCIM drives have been extensively introduced in Japan. An example of such a system runs from a suburban city into the underground railway through the central part of Tokyo [18]. The power circuit for this system and its main features are shown in Figure 2.13 and Table 2.2. The train is formed of 8 cars, comprising 6 motored and 2 trailer cars. Each inverter drives 8 motors in parallel, and each motored car is driven by 4 motors. The control capacity of the inverter is 1350 kW (1745 kVA). High power GTO thyristors rated at 3 kA turn-off current and 4.5 kV withstand voltage are used. The GTO characteristics are shown in Table 2.3. A three-stage switching pattern has been adopted , consisting of asynchronous PWM, followed by synchronous PWM and square-wave operation.

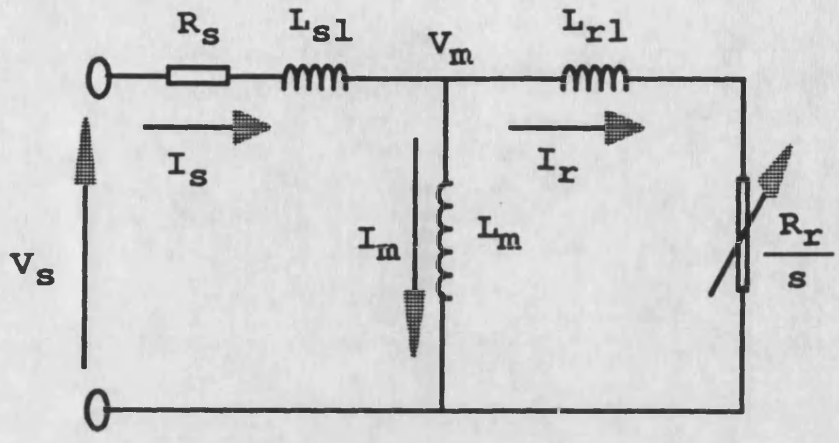

Figure 2.1 Per phase equivalent circuit

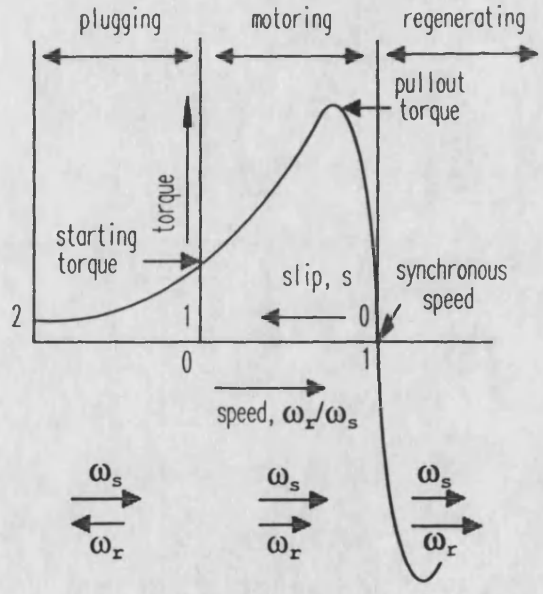

Figure 2.2 Torque-speed curve at constant voltage and frequency

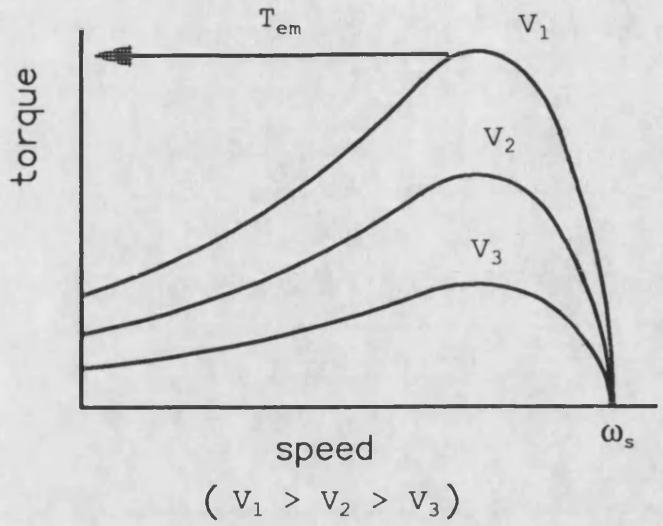

Figure 2.3 Torque-speed curves with variable stator voltage

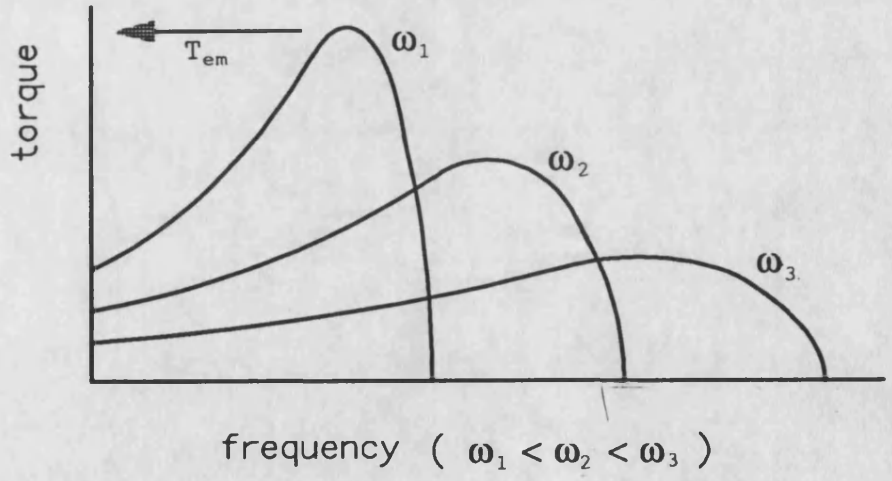

Figure 2.4 Torque-speed curves with variable frequency

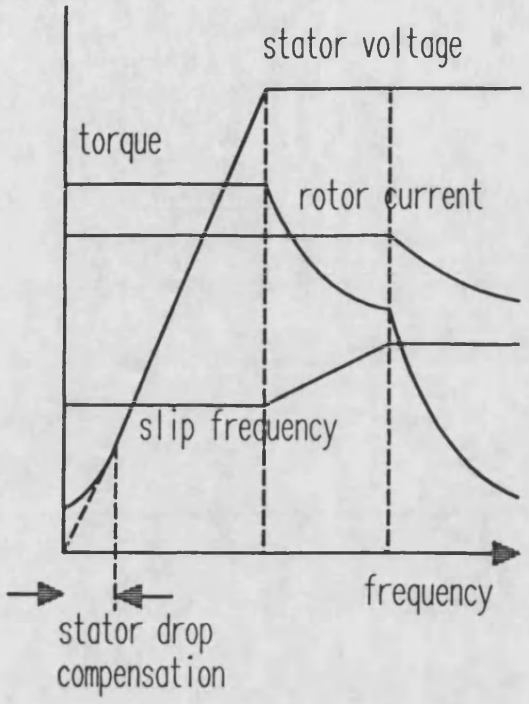

Figure 2.5 Characteristics of induction motor operating in three drive regions

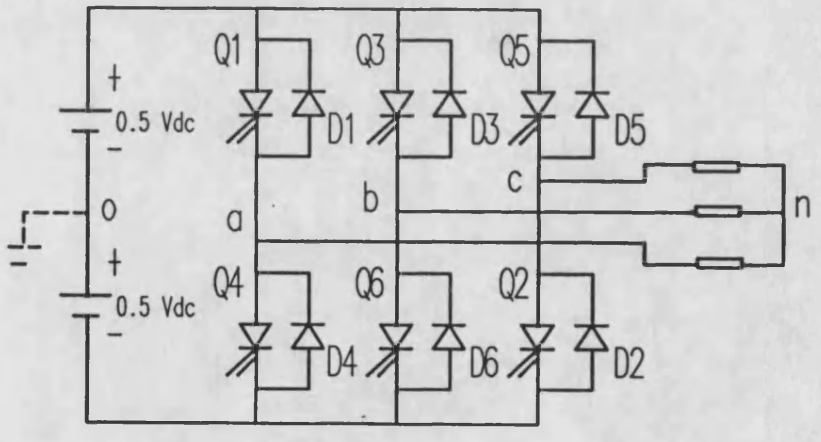

Figure 2.6 Three-phase bridge inverter

Table 2.1 Main features of switching devices

Item	Thyristor	GTO	Bipolar transistor	MOSFEF
Break down voltage (V)	4000	4500	1000	1000
current density (A/cm^2)	100	100	40	10
Surge current capability	Good	Good	Bad	Bad
Switching frequency (kHz)	5	3	20	2000
Gate drive power	Low	Medium	High	low
Self turn-off ability	No	Yes	Yes	Yes
Operating junction temperature limit (°C)	125	125	150	200

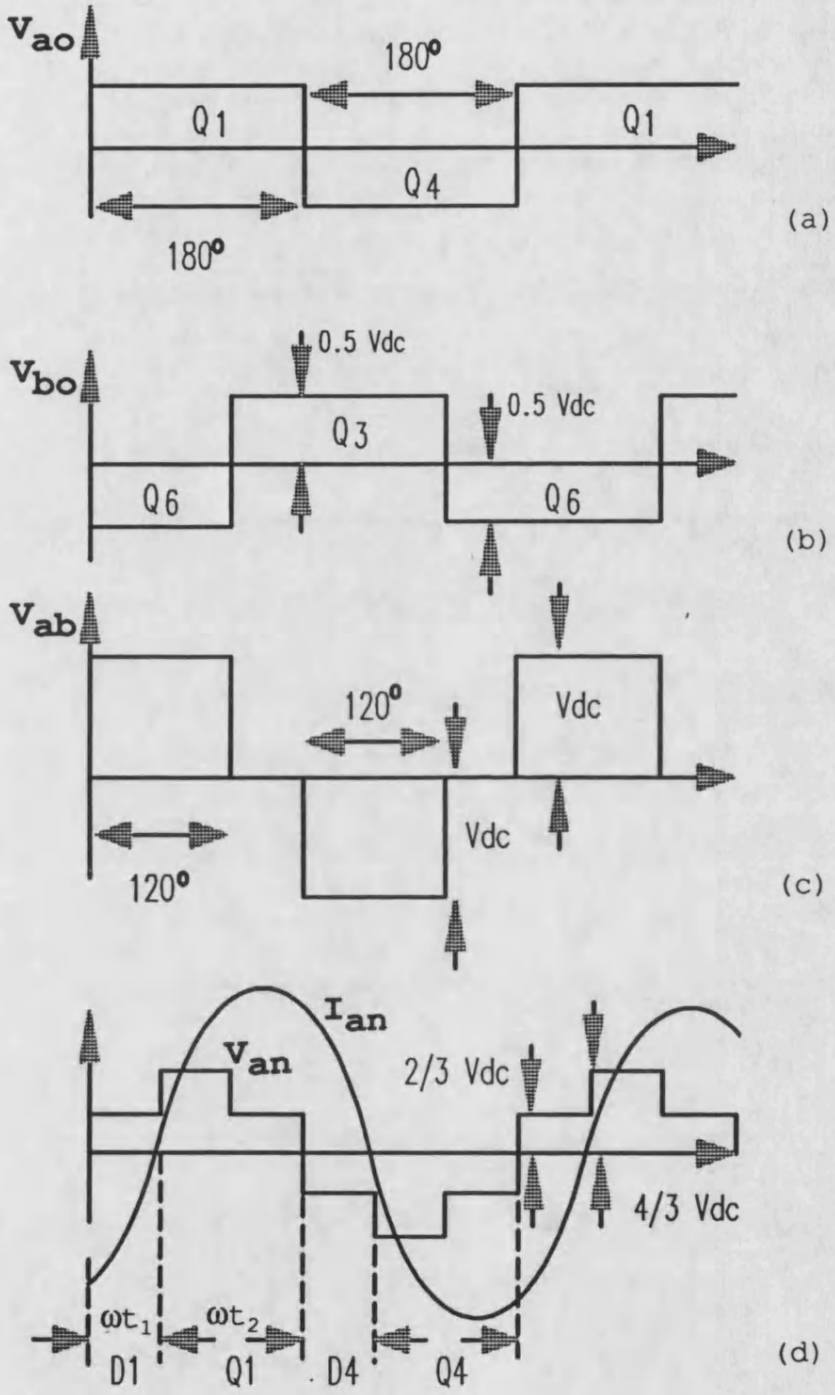

Figure 2.7 Voltage waveforms in bridge inverter

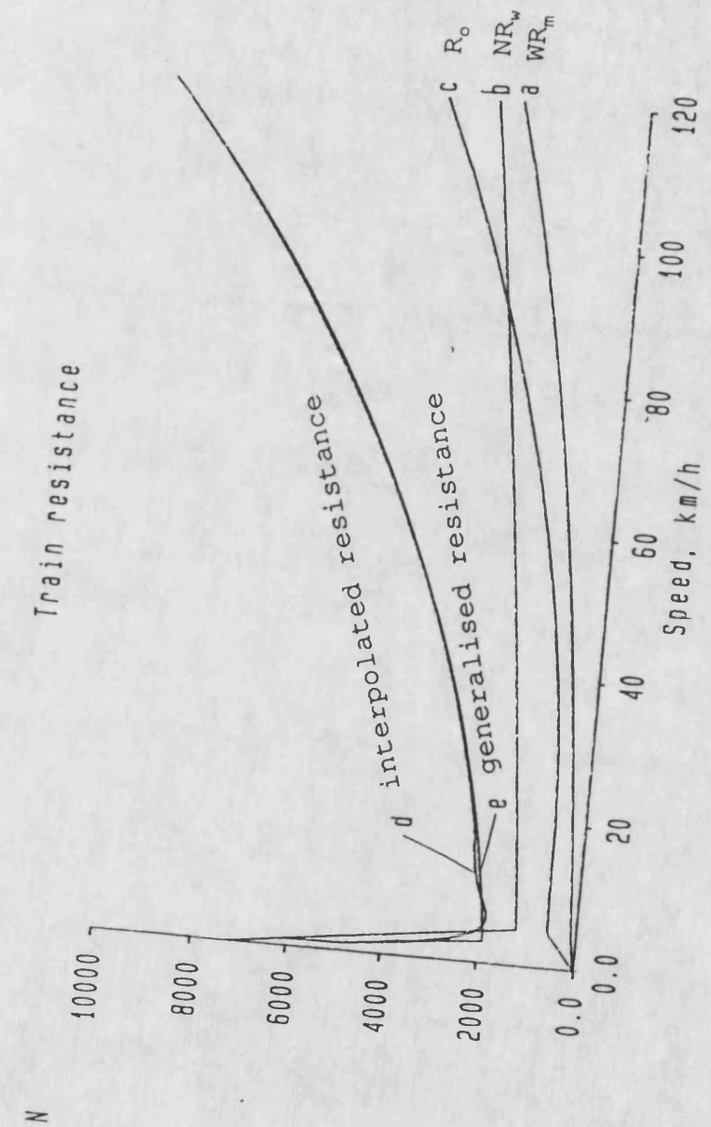

Figure 2.8 Train resistance

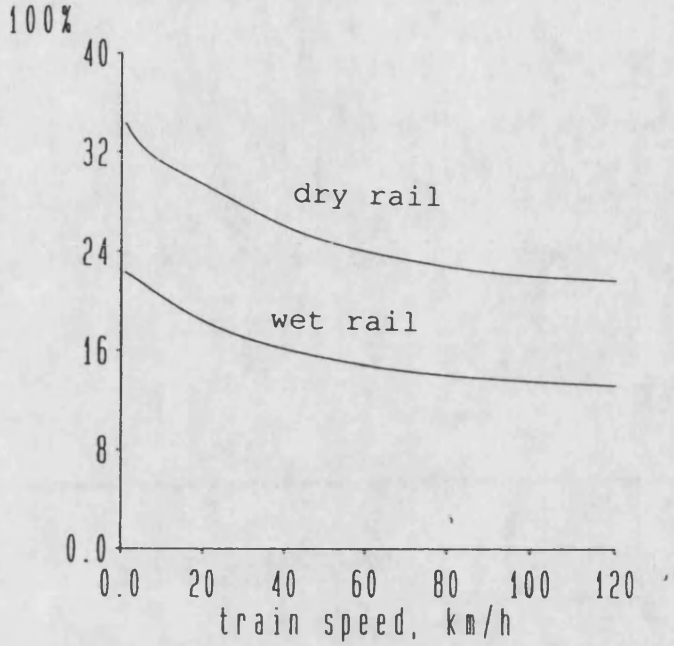

Figure 2.9 Adhesion coefficient

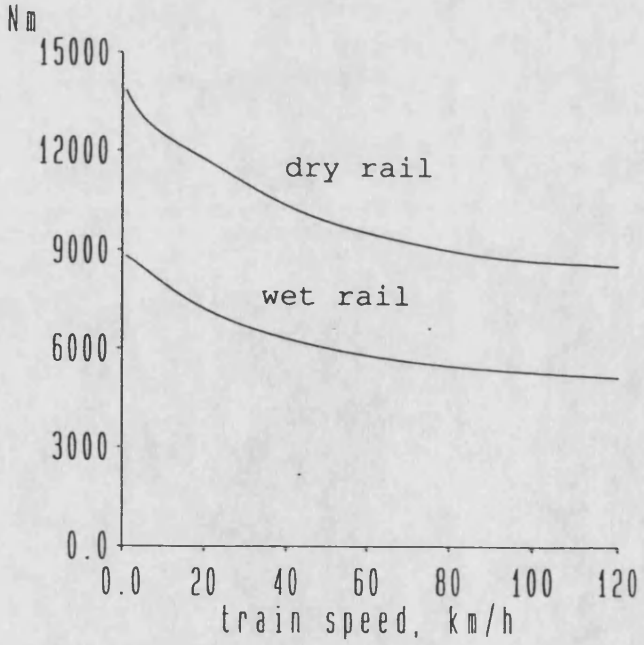

Figure 2.10 Maximum transmittable torque

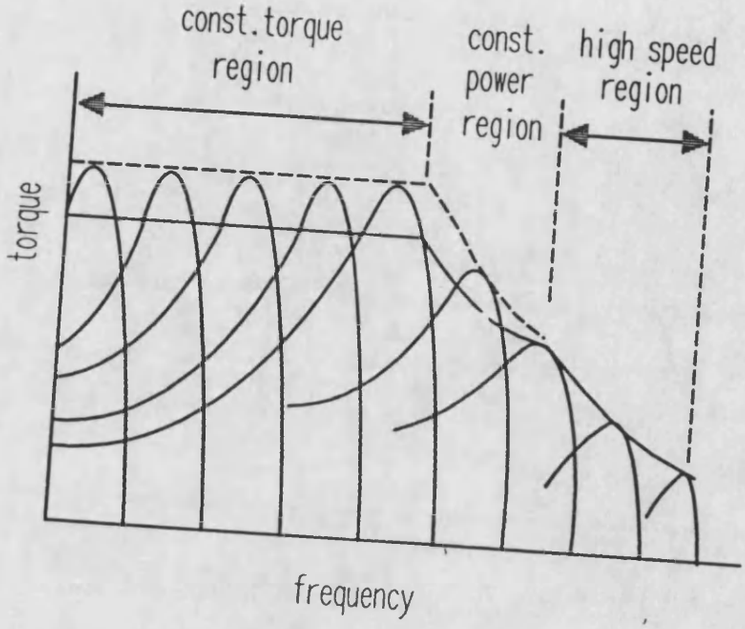

Figure 2.11 Torque-speed curves in three drive regions

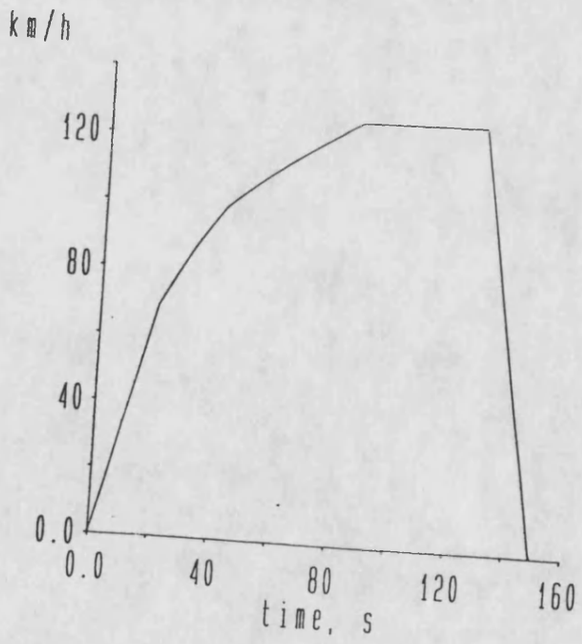

Figure 2.12 Practical train duty-cycle

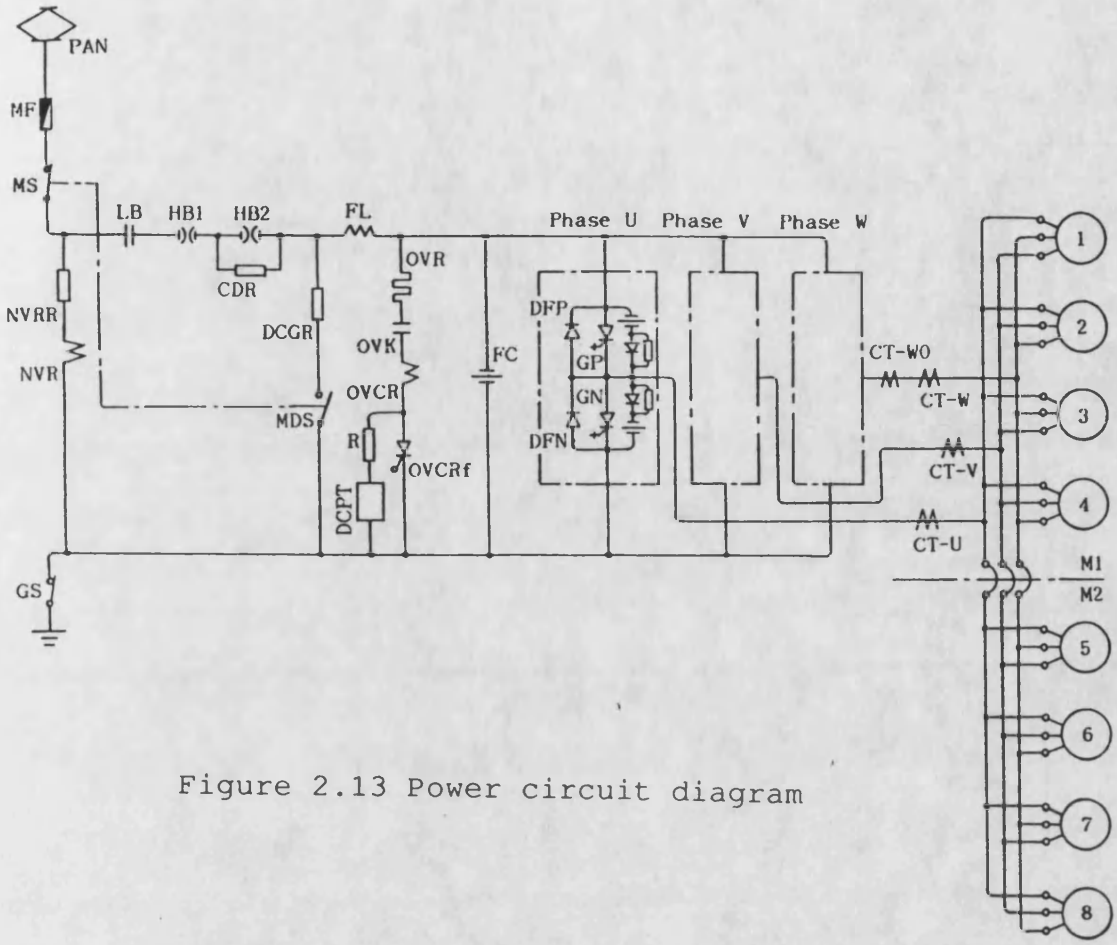

Figure 2.13 Power circuit diagram

Train Formation	Tc2 - M2 - M1 - M2 - M1 - M2 - M1 - Tc1
Tare Weight	Tc1, Tc2 ···· 25.7 t M1, M2 ···· 32.7 t
Rail Gauge	1067 mm
Wheel Diameter	860 mm
Catenary Voltage	1500V DC
Maximum Service Speed	120km/h
Acceleration	3.5 km/h/s
Deceleration	Normal Use 3.5 km/h/s(On ground) 4.0 km/h/s(Underground)
Traction Motor	3 phase Cage Rotor type Induction Motor 130kW, 1100V, 92A, 47.5Hz, 1382rpm
Drive Equipment	Parallel Cardan Flexible Plate Coupling System Herical Gear Reduction Gear Ratio 85/14=6.07
Inverter	GTO-VVVF · Heat-pipe Natural Cooling System Current Limit Value 2300A (Inverter Output Current) Voltage Limit Value 2000V (Filter Capacitor Voltage) Mass: 1060kg
Filter Equipment	Filter Capacitor: 5000μF (Contained in Inverter Unit) Filter Reactor : 9 mH 505 A (Natural Cooling) 1080kg

Table 2.2 Main particulars

Table 2.3 Characteristics of GTO thyristor

ELECTRICAL CHARACTERISTICS

CHARACTERISTIC	SYMBOL	TEST CONDITION	TYP.	MAX.	UNIT
Peak On-State Voltage	V_{TM}	I_{TM} =3000A , T_j =125℃	-	3.4	V
Gate Trigger Voltage	V_{GT}	V_D =24V , T_C =25℃ R_L =0.1Ω	-	1.2	V
Gate Trigger Current	I_{GT}		-	3.0	A
Delay Time	t_d	V_D =1/2 Rated dI/dt=300A/μS I_{TM} =3000A T_C =25℃ I_G =40A , t_r =1μS	-	3.0	μS
Turn-On Time	t_{gt}		-	10	μS
Holding Current	I_H	T_C =25℃ , R_L =0.1Ω	-	65	A
Strage Time	t_s	I_T =3000A V_D =1/2 Rated V_{DM} =2/3 Rated C_S =6μF , R_S =5Ω diRG/dt =50A/μS T_C =120℃	25	27	μS
Gate Turn-Off Time	t_{gq}		-	30	μS
Tail Time	t_{tail}		V_D=900V	115	μS
Gate Turn-Off Current	I_{RG}		700	800	A
Thermal Resistance	$R_{th(j-f)}$	DC	-	.016	℃/W

MAXIMUM RATING

Repetitive Peak Off-State Voltage : V_{DRM} =4500V
R.M.S On-State Current : $I_{T(RMS)}$ =800A
Peak Turn-Off Current : I_{TGQH} =3000A
Critical Rate of Rise of On-State Current : di/dt =400A/μS
Critical Rate of Rise of Off-State Voltage : dv/dt =500V/μS

Chapter 3 : Pulse width modulation schemes

3.1 Introduction

In section 2.4, the square-wave operation of a voltage source inverter was discussed, where the upper and lower switching devices in each phase are switched on and off alternately for 180° intervals. Under square-wave operation, the inverter control logic is fairly simple and the switching losses are low. This operation is not suitable to operate at low voltage and frequency, because the harmonic currents become excessive and cause machine heating and torque pulsation problems.

Ideally, the output voltage of a voltage source inverter should always be sinusoidal. This is not possible in practice, but can be approached by the use of pulse width modulation. The harmonic content of the PWM voltage waveform can be reduced by increasing the number of pulses. However, the number of pulses per cycle must be controlled below a certain limit, which is mainly determined by the switching time and the switching losses of the components in the inverter circuit. Thus this is a trade-off between the reduction of harmonics and the switching losses of the components.

There are many PWM schemes. The first distinction is identified as asynchronous or synchronous. Synchronous

PWM schemes include natural sampling, regular sampling, harmonic elimination and harmonic minimisation schemes.

The first two schemes above may be implemented by comparing a modulating waveform (sine wave) with a carrier waveform (triangular wave) to produce a PWM pole switching waveform. These two schemes are also called sinusoidal PWM schemes. The pole switching angles for the latter two schemes are calculated by mathematical equations considered later.

3.2 Fundamentals of sinusoidal PWM

In general, a PWM waveform can be either a 2-level or a 3-level waveform as shown in Figure 3.1 (a,b). The pole switching waveforms are referred to the D.C. link centre-tap. The 3-level waveform is generated by a full-bridge inverter and the 2-level waveform is the output of a half-bridge inverter. The differences between the two schemes are that the voltage jump of the 2-level waveform is twice as big as that of the 3-level waveform, and that the 3-level scheme has the advantage of effectively doubling the switching frequency. This results in cancellation of the output harmonic components at switching frequency together with the sidebands [67].

To fully define a sinusoidal PWM waveform, two variables are required. These are the modulation ratio and modulation depth. The modulation ratio (M_r) is defined as the ratio of carrier frequency (f_c) to modulating frequency (f). The modulation depth (M_d) is defined as the ratio of carrier amplitude (V_c) to modulating signal amplitude (V_{sp}). When the value of modulation ratio is an integer, the corresponding waveform is called synchronous PWM. Otherwise, it is called asynchronous PWM. If the modulation depth is less than one, the PWM operation is in the linear range, i.e., the amplitude of the fundamental component varies linearly with M_d and is independent of M_r (provided $M_r > 9$) [67]. This is given by

$$V_{sp} = M_d V_{dc}/2 \qquad (3.1)$$

Beyond this range, the operation is called over-modulation.

Theoretically, the harmonics in the inverter output voltage appear as sidebands, centred around the switching frequency and its multiples, in the form [68]

$$f_h = (jM_r \pm k)f \qquad (3.2)$$

where j and k are integers. the harmonic order h corresponds to the k^{th} sideband of the j times the modulation ratio M_r

$$h = jM_r \pm k \qquad (3.3)$$

where the fundamental frequency corresponds to h = 1. For odd values of j, harmonics exist only for even values of k, and for even values of j, harmonics exist only for odd values of k. The above holds true for all values of M_d in the range 0 to 1.

For three-phase PWM applications, the modulation ratio M_r should be an odd integer and a multiple of 3. Choosing M_r as an odd integer results in odd symmetry of the pole switching waveform [f(-t) = -f(t)] as well as half-wave symmetry [f(t) = -f(t+T/2)]. Therefore, only odd harmonics are present and the even harmonics disappear from the waveform. Choosing M_r as a multiple of 3 cancels out the most dominant harmonics in the line voltage, since if $V_{ao3} = \sin(3\omega t)$ and $V_{bo3} = \sin[3(\omega t-120)]$, then $V_{ab3} = 0$.

3.3 Natural sampling schemes

With natural sampling PWM schemes, the pulse widths are 'naturally' defined by the instantaneous intersections of the carrier and modulating functions. A

comparison process is necessary to determine the intersection points and it is for this reason that natural sampling is conveniently implemented by analogue techniques. A natural sampled PWM waveform could be either single-edge sampled as shown in Figure 3.2 (a) or double-edge sampled as in Figure 3.2 (b). With the increase of complexity, the harmonic content of a double-edge sampled PWM waveform is better than that of a single-edge sampled PWM.

It can be shown that the down- and up-slope switching points for a double-edge sampled PWM are given by

$$\text{D:} \quad M_d \sin(\theta_{2i-1}) + 2M_r/\pi * \theta_{2i-1} = 2(2i-1)$$

$$\text{U:} \quad M_d \sin(\theta_{2i}) - 2M_r/\pi * \theta_{2i} = 4i \qquad (3.4)$$

where θ_n is the angle at the n^{th} switching point, and i = 1,2,3 ··· M_r-1. It is clear that the above equation is transcendental and so the value of θ can only be obtained by a numerical method.

With M_r = 15, M_d = 0.9, Figure 3.3 shows double-edge sampled waveforms, the pole switching waveform, and the harmonic content of the pole switching waveform. As predicted, the first odd carrier harmonic component appears at h = 15, with the upper and lower sidebands separated by twice the modulating frequency. The first even carrier harmonic component (at h = 30) is almost

zero. It has sidebands separated by the modulating frequency with odd multiples.

The switching angles for single-edge sampled PWM can be expressed in a similar way. Figure 3.4 shows a single-edge sampled PWM, with $M_r = 15$, $M_d = 0.9$. Again as predicted, both odd and even harmonics are present, with a large number of sidebands separated by multiples of the modulating frequency.

3.4 Regular sampling schemes

In regular sampling, the sampling instances, as defined by the carrier frequency, are uniformly spaced and independent of the modulation function. This scheme is also a uniform sampling scheme. Since the amplitude of the modulating signal is held constant after each sampling, the subsequent intersection point between the carrier and the constant can be expressed analytically. Comparing with the transcendental properties which natural sampling schemes have, regular sampling schemes have the inherent compatibility to digital implementations.

Figure 3.5 shows two forms of regular sampling: i.e., regular symmetric and regular asymmetric sampling. In the case of symmetric sampling, each edge of the sampled pulse is modulated by the same amount. This results in a

sampled pulse which is symmetrical about the sample point as shown by the solid line. In asymmetric sampling, each pulse edge is modulated by a different amount as shown by the broken line. The number of sampling points in asymmetric sampling is twice that in symmetric sampling. The extra sampling points give more information about the modulating waveform. This also increases the complexity of implementation.

Usually, sampling points are made at odd numbers of quarter carrier cycle ($\pi/2M_r$), i.e., at carrier waveform peak points. Hence the switching points for asymmetric sampled PWM waveform are given by

$$\begin{aligned} &D: \quad \theta_i = M_r/\pi[i - (M_d/2)\sin((i-1/2)\pi/M_r)]; && i = \text{odd} \\ &U: \quad \theta_i = M_r/\pi[(M_d/2)\sin((i-1/2)\pi/M_r) - i]; && i = \text{even} \end{aligned} \qquad (3.5)$$

For symmetric sampled PWM, the down-slope switching points are the same as the above, with the up-slope switching points symmetrical to the down-slope points about the sampling points.

Figure 3.6 shows a regular asymmetric sampled PWM waveform and its harmonic spectrum. The symmetric PWM waveform and its harmonic spectrum is given in Figure 3.7. In both cases, the modulation ratio is $M_r = 15$, and the modulation depth is $M_d = 0.9$. As can be seen, the

harmonics of regular sampled PWM are similar to the corresponding natural sampling case, but slightly deteriorated because of the sample-hold process.

3.5 Gear changing technique

Changes in modulation ratio, often referred to as "gear changing", are determined by permitted values for both the harmonic content of the waveform and the maximum switching frequency. As stated in section 3.1, the maximum switching frequency is determined by the inverter switching losses. The acceptable harmonic content determines the minimum switching frequency. It has also been shown that the value of the modulation ratio should be an odd triplen integer. The practical maximum switching frequency for traction drive application is 500 - 700 Hz [69]. During the constant torque period in a rail traction drive, the modulation ratio must be adjusted in steps to keep the maximum switching frequency below this limit. Figure 3.8 shows a typical pattern of modulation ratio variations.

In any individual application, the design of a specific gear changing pattern is determined by its own duty-cycle requirement. As discussed in section 2.7, three drive regions are required for traction drive applications. The constant torque region is performed

using a PWM waveform. The constant power and high speed regions are performed by quasi-square waveforms.

Under constant torque operation, since the acceleration rate of the machine is nearly constant, therefore the supply frequency is required to increase linearly with time. For example, if 20 seconds is required in the duty-cycle to accelerate the speed of the machine from zero to base speed (assumed at 50 Hz), and if the supply frequency is linearly increased by 1 Hz/s, then the time for each step is only 0.4 s. It is clear that if an integer number of cycles for each supply frequency is required, the minimum supply frequency is 2.5 Hz. For synchronous PWM operation, an integer number of cycles is essential.

To start the motor smoothly from a very low supply frequency, an asynchronous PWM scheme is introduced. Usually, the transition from asynchronous to synchronous PWM is made at 2 Hz [70]. Asynchronous PWM involves the inverter GTOs being chopped at a certain frequency, regardless of the supply frequency. With asynchronous PWM control it is also possible to vary the supply frequency in small steps, typically with a step of about 0.1 Hz. One disadvantage in using asynchronous PWM is that sub-harmonics appear in the inverter output waveform which will affect the machine performance [71].

For traction application, however, these sub-harmonics are not a severe problem [70].

With synchronous PWM operation, when one gear ratio is switched over to another, the corresponding voltage tends to vary. This is because the GTOs are not ideal switching devices. There is always a delay time or dead-zone. The losses of the inverter output voltage varies with the number of pulses per cycle. Variations of the inverter output voltage due to gear changes can be corrected by modifying the modulation depth M_d.

3.6 Over-modulation and pulse dropping

In the linear range of PWM operation, the maximum value of fundamental peak voltage at the inverter output is $V_{sp} = V_{dc}/2$, when $M_d = 1$, whereas the maximum value under quasi-square waveform is $V_{sp} = 4/\pi * V_{dc}/2$. In order to transfer from PWM to square-wave operation smoothly, M_d must be increased greater than 1. This is called over-modulation. With over-modulating operation, the amplitude of the fundamental frequency component does not vary linearly with the modulation depth. Instead, it varies within the range $V_{dc}/2 \leq V_{sp} \leq 4/\pi * V_{dc}/2$ depending on the values of M_r. Figure 3.9 shows the normalized fundamental peak voltage as a function of the modulation depth M_d for a given modulation ratio $M_r = 15$.

With increase in the modulation depth, some of the pulses must be merged. Ideally the pulses to be dropped should be infinitely small and the dropping of these small pulses should not cause any variation in the amplitude of the inverter output voltage. However, this is impossible in practice, since all switching devices have a specific switching time, this time determining the minimum pulse width. The associated voltage jump caused by pulse dropping is undesirable for most applications. In particular, a voltage jump at 10% of the full voltage will be introduced during a transition from a three-pulse to an one-pulse mode [70].

One way to overcome this problem is to use a modified PWM scheme [70]. The idea of the modified PWM scheme is that the position of the pulse to be dropped should be as near as possible to the zero crossings of the fundamental of the pole switching waveform. This is illustrated in Figure 3.10. By using this scheme, the voltage change due to the transition from three-pulse to one-pulse mode is very small and the system performance is very smooth [70].

3.7 Optimised PWM schemes

The idea of using optimised PWM schemes is to minimise certain system performance criteria, such as the elimination of certain harmonic voltages, or

minimisation of current distortion. In contrast to natural and regular sampled PWM generation, which use practical circuit implementation based on well defined modulation processes, optimised PWM has no identifiable modulation process. The optimised PWM is generated by first defining a general PWM waveform in terms of a set of switching angles and then determining these switching angles using numerical methods.

A generalised PWM switching waveform, with quarter- and half-wave symmetry, can be defined as shown in Figure 3.11, where there are m switching angles per quarter cycle, and with unit amplitude. This waveform can be expressed in a Fourier Series form. Using half- and quarter-wave symmetry properties, it can be simplified as [72]

$$V_n = \frac{4}{n\pi}\left[1 + 2\sum_{i=1}^{m}(-1)^i \cos n\alpha_i\right] \qquad (3.6)$$

where α_i are the angles to be determined and n is an odd integer. For n = 1, V_1 corresponds to the fundamental component of the waveform.

3.8 Harmonic elimination scheme

By giving a required value to V_1 in eqn. (3.6) and equating the other m-1 equations to zero, any m-1 harmonics can be eliminated. The resultant equations are nonlinear and transcendental in nature. A typical

technique for solving these equations is by use of the Newton-Raphson method. The iteration equation is given by

$$\begin{bmatrix}\alpha_1\\ \alpha_2\\ \vdots\\ \alpha_m\end{bmatrix}_{p+1} = \begin{bmatrix}\alpha_1\\ \alpha_2\\ \vdots\\ \alpha_m\end{bmatrix}_{p} - \frac{8}{\pi} \begin{bmatrix}+\sin(\alpha_1), -\sin(\alpha_2), \ldots, \pm\sin(\alpha_m)\\ +\sin(5\alpha_1), -\sin(5\alpha_2), \ldots, \pm\sin(5\alpha_m)\\ \vdots \quad \vdots \quad \vdots \quad \vdots\\ +\sin(n\alpha_1), -\sin(n\alpha_2), \ldots, \pm\sin(n\alpha_m)\end{bmatrix}^{-1} * \begin{bmatrix}V_1\\ V_2\\ \vdots\\ V_m\end{bmatrix}$$

(3.7)

The harmonic numbers to be eliminated are normally in the form of 6n±1. This is because the generalized waveform contains only odd harmonics. Moreover, as stated before, the triplen harmonics cannot exist in the line voltage for three-phase drives.

Sample calculations for harmonic elimination for 3, 5 and 7 angles per quarter cycle have been performed. Figure 3.12 presents the switching angles as a function of the amplitude of the fundamental component. Figure 3.12-a shows three angles per quarter cycle, i.e. harmonic No. 5 and 7 are eliminated, b shows five angles per quarter cycle, where harmonic No. 5, 7, 11, and 13 are eliminated, and c shows seven angles.

In practical implementations, the above equations would usually be calculated on a mainframe computer, and the results stored in a microprocessor in the form of look-up table for generating the necessary PWM waveform

in real time. For most applications, a very large computer memory would be necessary. One way to avoid this problem is to adopt a algorithm which generates a near optimal PWM waveform [73]. From Figure 3.12, it is clear that for most of the range, the curves may be approximated by straight lines, with some modifications at the extremities.

3.9 Harmonic minimisation scheme

In contrast to the harmonic elimination scheme, harmonic minimisation scheme is implemented by optimizing the PWM switching patterns according to certain performance criteria. These criteria could be connected with any parameters concerned with the system operation, such as current harmonics, operating losses, torque and speed ripples.

One of the widely accepted system criteria is the total current harmonic distortion (THD). For an induction motor operating under normal condition, the equivalent circuit for harmonic components can be approximated by an equivalent inductance which represents the sum of the stator and reflected rotor inductances [74-76]. The harmonic currents can be determined by the corresponding voltages (eqn. (3.6)) divided by the equivalent impedance. The i^{th} harmonic current is given by

$$I_i(\alpha) = V_i(\alpha) / (i\omega L) \qquad (3.8)$$

where i = 6n±1, n is an integer, and L is the equivalent inductance. To minimise THD of current, the function

$$L(\alpha) = \sum_{i=6n\pm1} W_i I_i(\alpha)^2 \qquad (3.9)$$

where W_i is a weighting factor, must be minimised subject to the constraint

$$V_1 = \frac{4}{\pi} [1 + 2\sum_{i=1}^{m} (-1)^i \cos\alpha_i] \qquad (3.10)$$

where V_1 is the required value at a specific supply frequency. In general, weighting factor W_i is chosen according to the application. One of the most effective methods to calculate the above equations is Powell's method based on the steepest descent idea. Sample calculations for minimisation of THD of current have been performed using the parallel computer. Figure 3.13 shows 2, 3, and 4 switching angles per quarter cycle as a function of the amplitude of the fundamental component.

As discussed in section 3.8, the main problem concerned with optimized PWM switching strategies is that the angles have to be calculated using a mainframe computer and then stored in a microprocessor as a look-

up table. To overcome this drawback, some sub-optimal switching strategies have been developed. Using modified modulating signal [77] and fictitious frequency ratio techniques [78], these strategies closely approximate optimised PWM performance.

3.10 Effects of current harmonics

As described in the previous sections, the harmonic content of the line voltage is in the form of $6n\pm1$ (n is an integer). Consequently, the motor current will contain the same number of harmonic components.

The effects of current harmonics on the machine itself can cause overheating problem. Moreover, motor torque pulsations and ripples on the DC link current are also affected by these harmonic currents.

The composition of the DC link current from the three phase currents is illustrated in Figure 3.14, where only the fundamental component is considered. For harmonics, the composition method is the same. The total DC link current is the sum of the compositions from both fundamental and harmonics. A general method for calculating the DC link current is described in [79]. It has been shown that the harmonic number of the DC link current is always a multiple of 6. It is suspected by the author that the largest DC link current harmonic

component exists nearby where the largest motor current harmonic component exists.

In traction application, the harmonics in the DC link current can be injected into the traction supply network which may also be used as the signalling circuit. Hence interference to the signalling system may be generated if the same frequency are used. To reduce the possibility of interference the line current harmonics must be reduced below an acceptable level by adjusting the PWM scheme and a input filter must be added.

It has been shown that the motor torque is produced by interaction between the rotor current and the air-gap flux rotating at the synchronous speed. In addition to the fundamental component in the rotor current which produces the "fundamental" torque, harmonics of 6n-1 (for negative phase sequence) and 6n+1 (for positive phase sequence) always produce torque pulsations at a multiple of six of the fundamental. Again, the largest torque pulsation is produced by the largest pair of rotor current harmonic components.

Torque pulsations at low frequency can affect the mechanical performance of the drive system. These torque pulsations can be reduced by reducing the harmonics of the motor current.

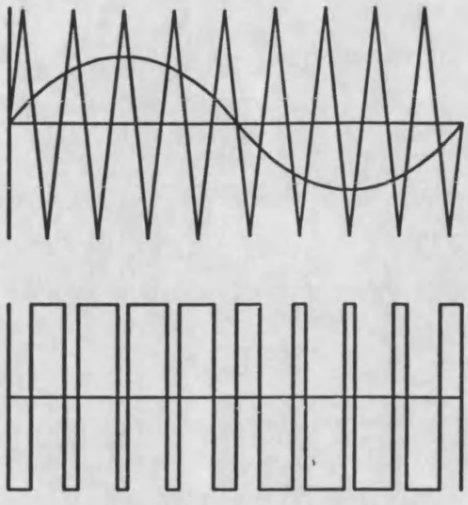

(a) Two level

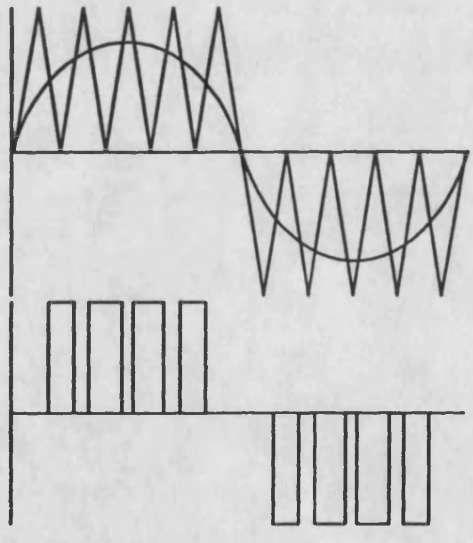

(b) Three level

Figure 3.1 PWM waveform

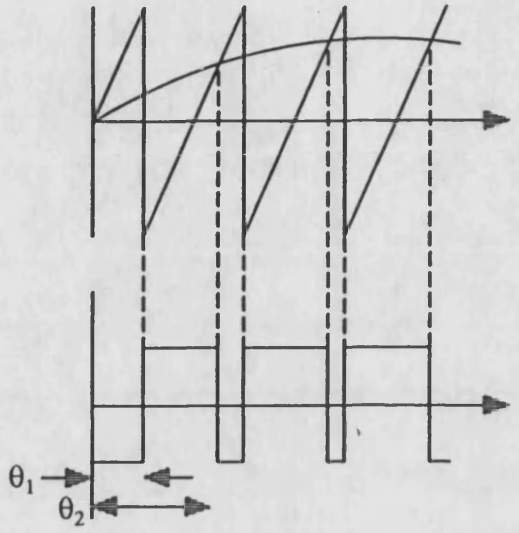

(a) single edge

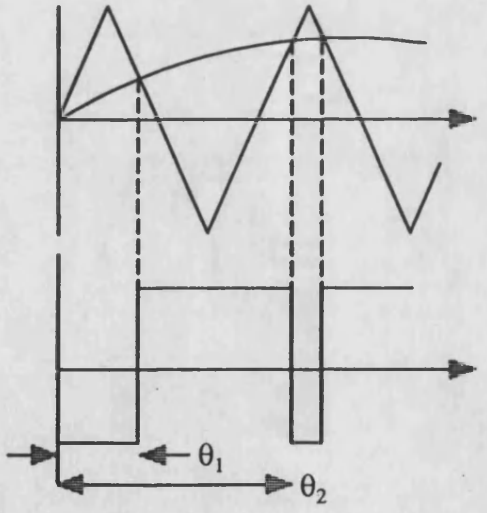

(b) double edge

Figure 3.2 Natural sampling process

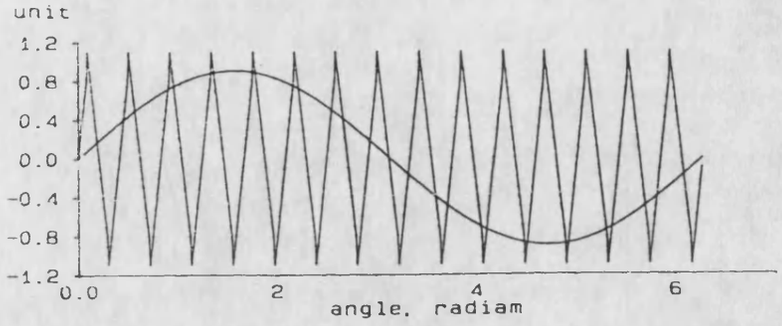

(a) sampling process

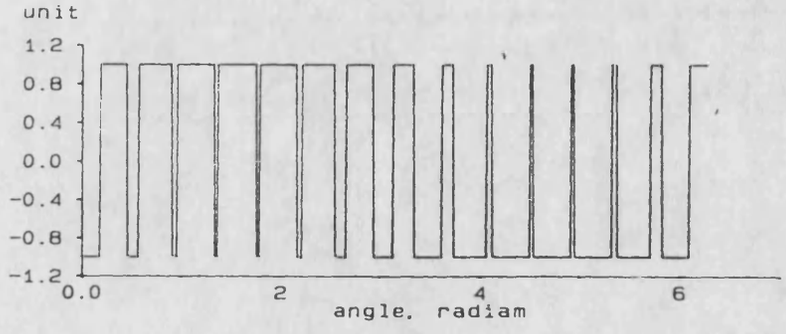

(b) pole switching waveform

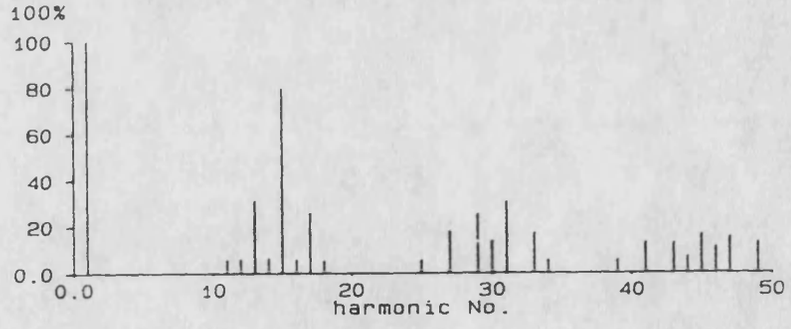

(c) harmonic spectrum

Figure 3.3 Natural sampled double edge PWM waveform and harmonic spectrum

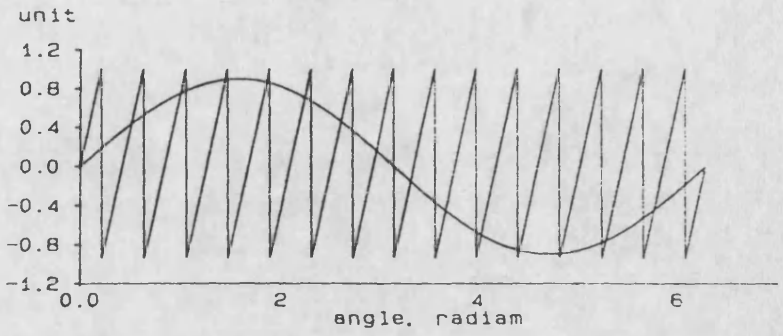

(a) sampling process

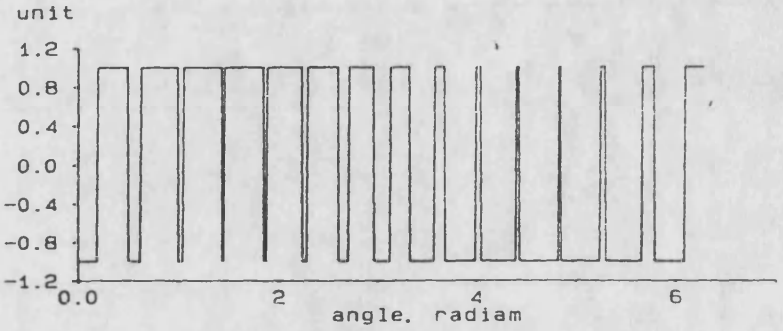

(b) pole switching waveform

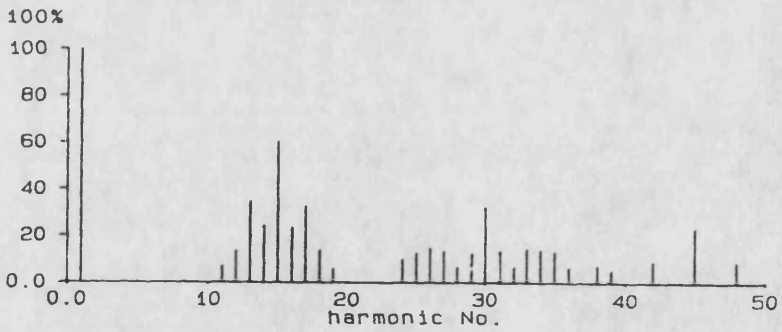

(c) harmonic spectrum

Figure 3.4 Natural sampled single edge PWM waveform and harmonic spectrum

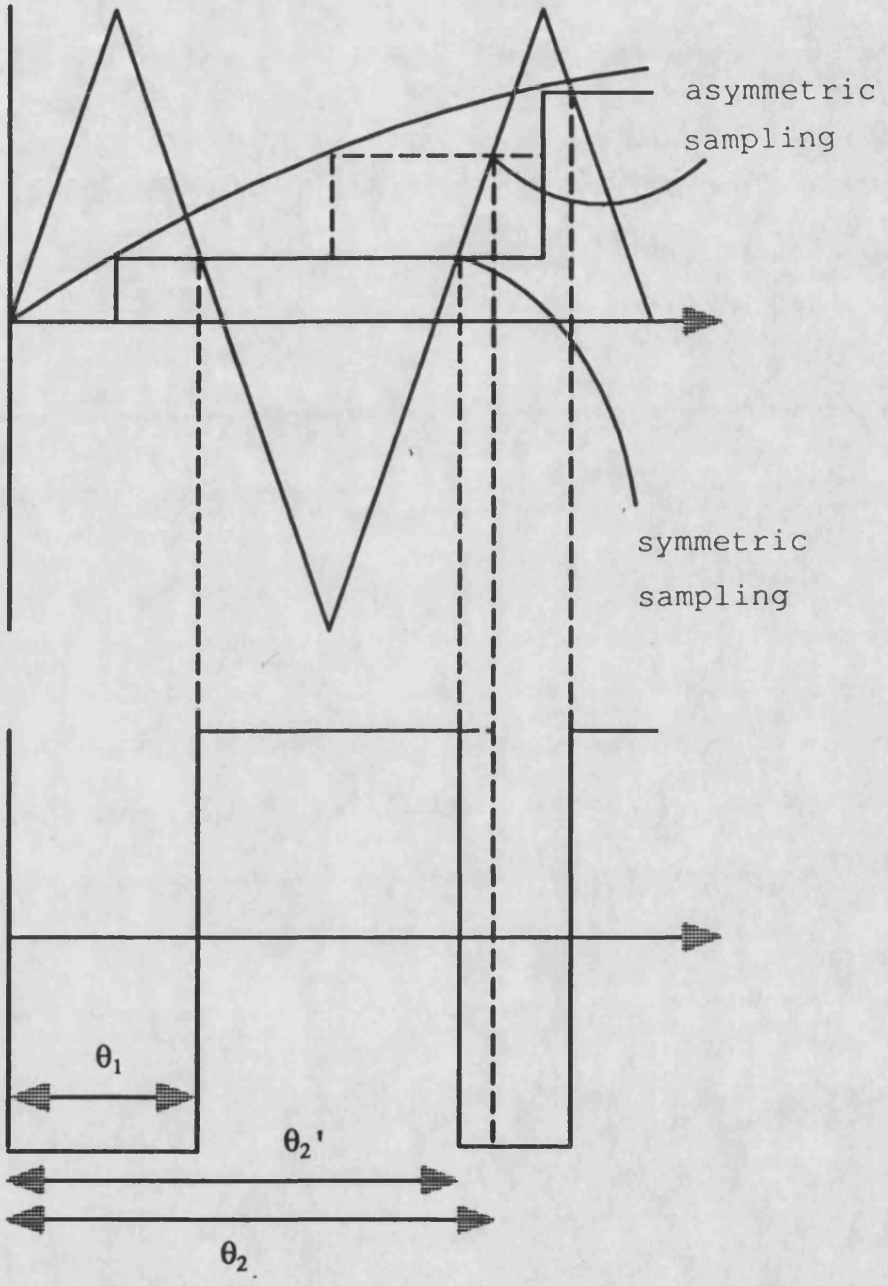

Figure 3.5 Regular sampling process

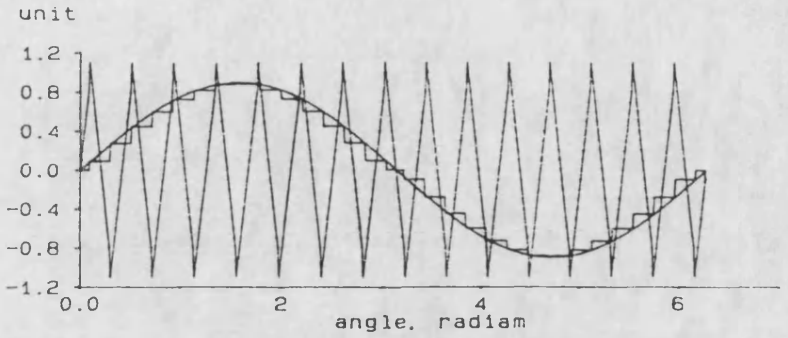

(a) sampling process

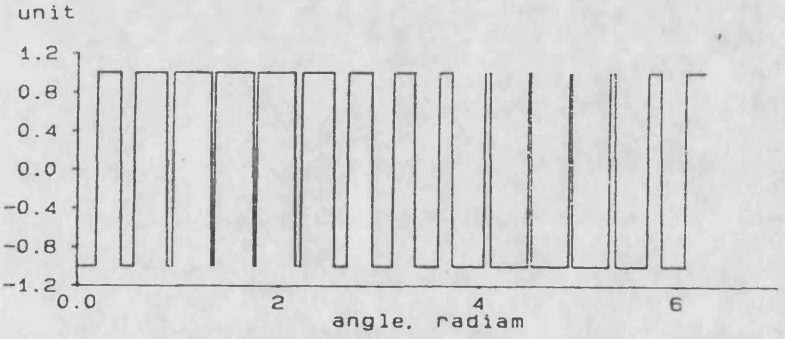

(b) pole switching waveform

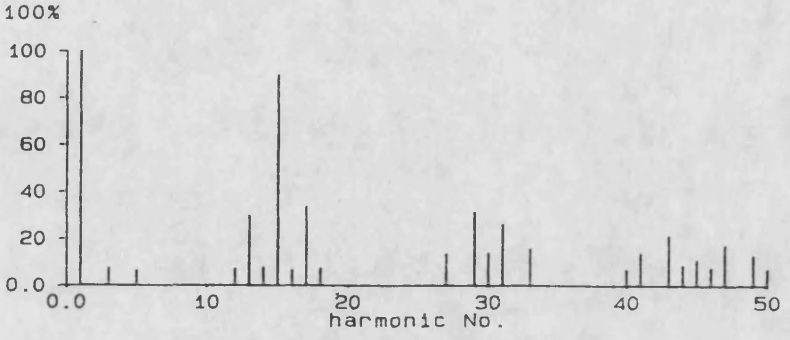

(c) harmonic spectrum

Figure 3.6 Regular sampled asymmetrical PWM waveform and harmonic spectrum

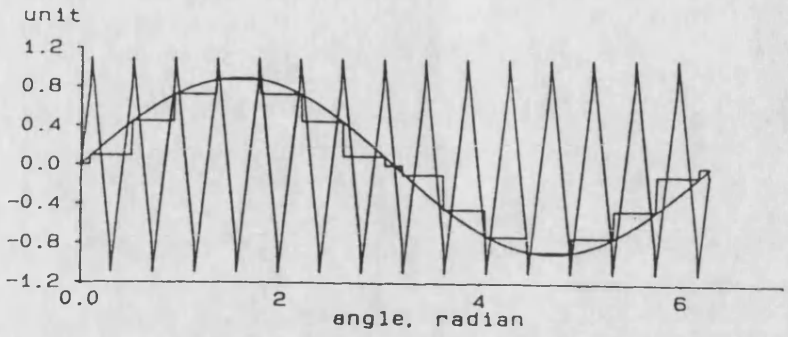

(a) sampling process

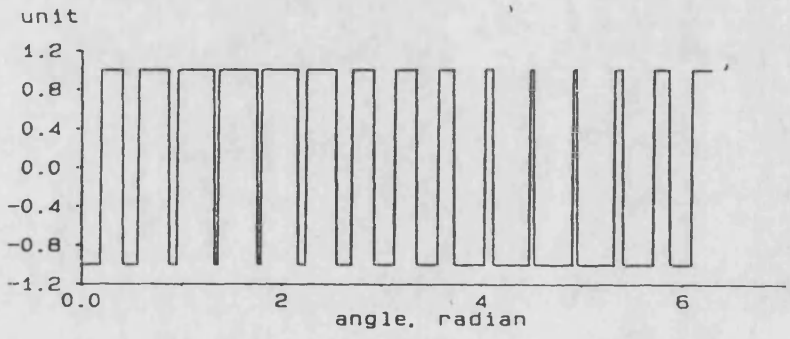

(b) pole switching waveform

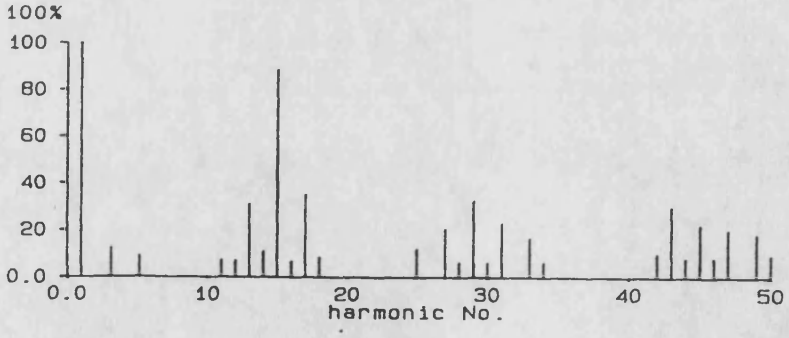

(c) harmonic spectrum

Figure 3.7 Regular sampled asymmetrical PWM waveform and harmonic spectrum

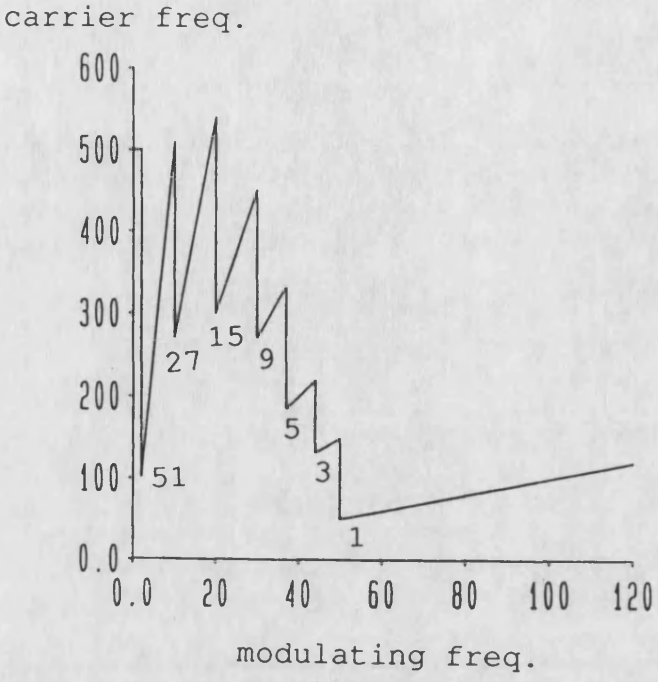

Figure 3.8 Gear change pattern

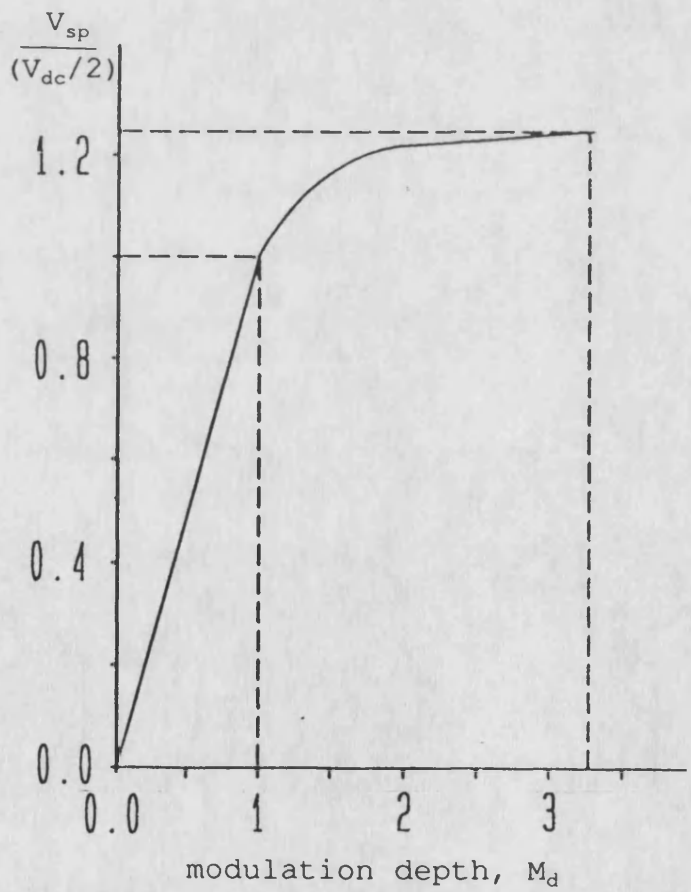

Figure 3.9 Relationship between V_{sp} and M_d

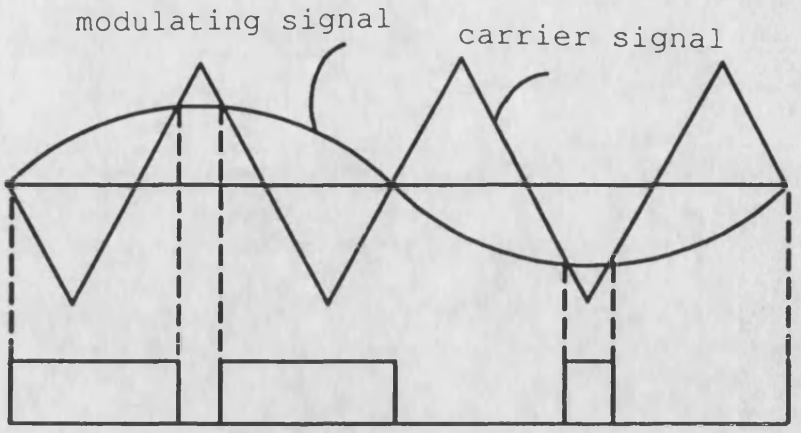

(a). conventional method

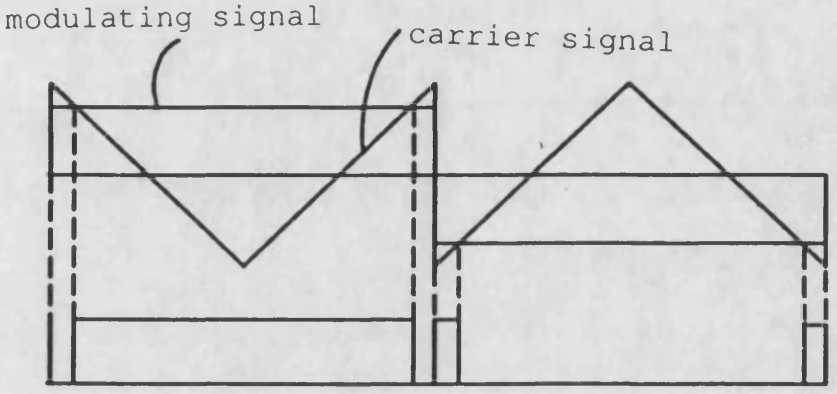

(b). modified method

Figure 3.10 Transition from three-pulse mode to one-pulse mode

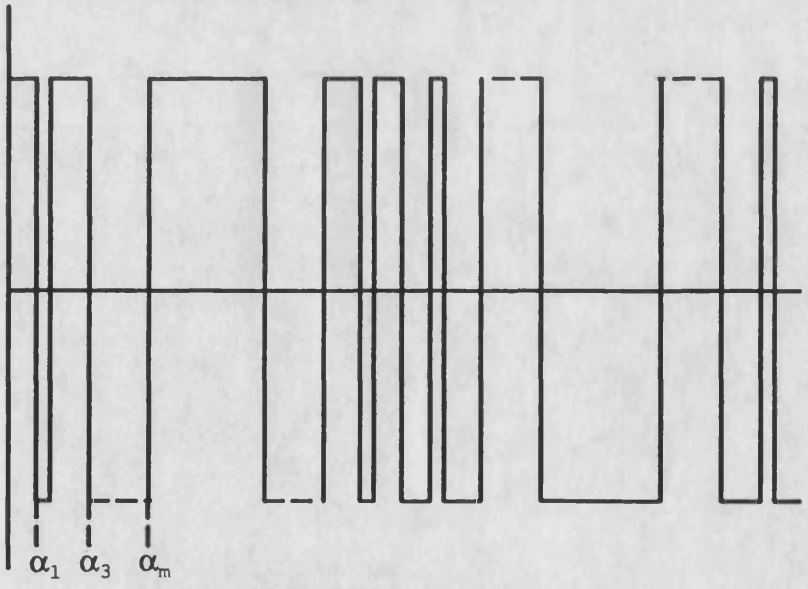

Figure 3.11 Generalised quarter-wave symmetric PWM waveform

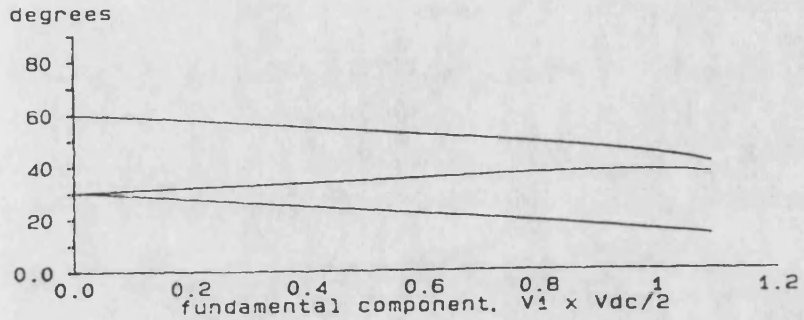

(a) three angles per quarter cycle

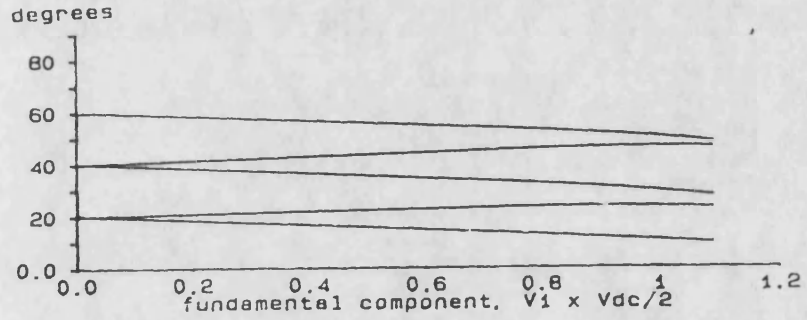

(b) five angles per quarter cycle

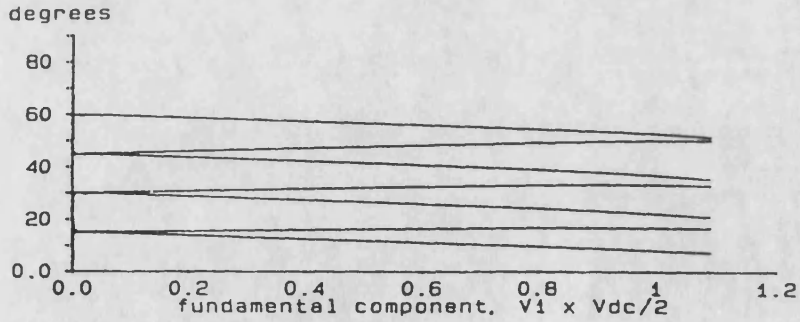

(c) seven angles per quarter cycle

Figure 3.12 Harmonic elimination scheme

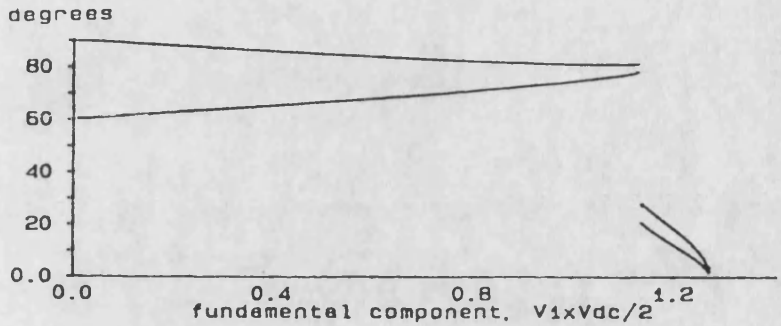

(a) two angles per quarter cycle

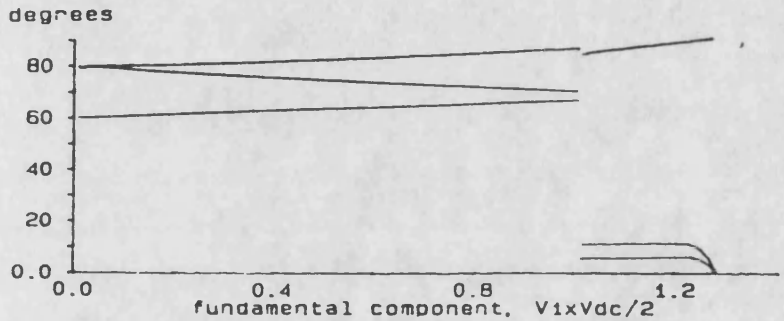

(b) three angles per quarter cycle

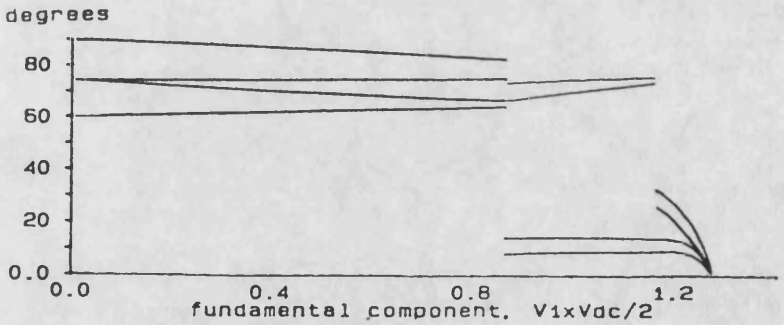

(c) four angles per quarter cycle

Figure 3.13 Harmonic minimisation scheme

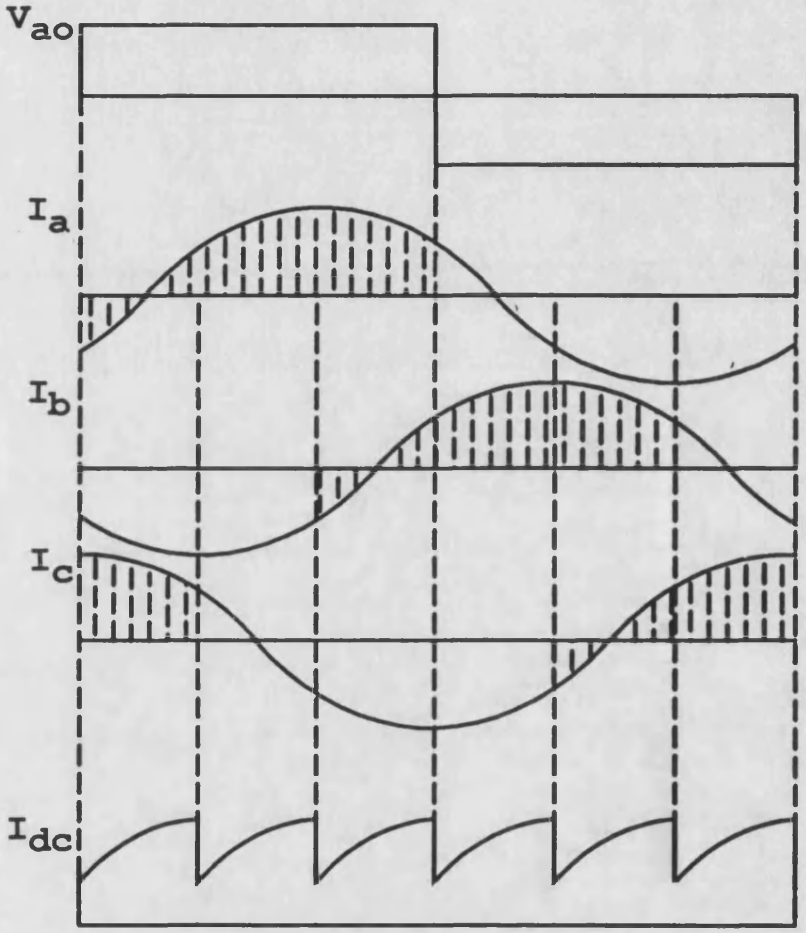

Figure 3.14 Composation of DC link current

Chapter 4 : System modelling

4.1 Introduction

The performance of a DC-fed VSI-SCIM drive system can be simulated either in the frequency domain or in the time domain. To predict the general performance of the system, the frequency domain model is a simple and useful tool. However, the time domain model is more effective for the transient analysis of the system performance.

In frequency domain modelling, the simple transformer equivalent circuit for the induction motor can be used to predict the motor currents and torques under different harmonic voltages. These individual components can then be summed to give the response to a non-sinusoidal supply voltage. The simplicity of this model is particular clear when only the fundamental component of the supply voltage is considered. However, if a transient analysis is required, this model can be very inconvenient.

In time domain modelling, the system variables are related by a set of differential equations. By solving these differential equations using a numerical method, the system transient response to different input signals can be explicitly expressed. Compared with frequency

domain modelling, where the total response is the summary of individual responses, time domain modelling is extremely convenient and accurate, particularly if the system transient response is required.

In this chapter, both frequency domain and time domain models of a DC-fed inverter-induction motor drive are presented

4.2 Frequency domain model

Frequency domain modelling of a DC-fed inverter-induction motor drive is carried out in three steps corresponding to the three drive regions of Figure 2.11. The objective of the model is in predicting the system general performance. In constructing the model, certain limitations and assumptions are required as follows

a) Only the fundamental component of the inverter output voltage is considered;

b) Only steady state performance is considered;

c) The efficiencies of both electrical and mechanical parts are assumed to be 100%.

Throughout this section, the per-phase equivalent circuit of the induction motor, shown in Figure 2.1, is

used as the machine model. A block diagram of the system is shown in Figure 4.1. The frequency-time table derived in section 2.7 is used to determine the required supply frequency at any specific instance by using interpolation. The basic variables used to describe the VSI-SCIM system are stator voltage, current, and rotor slip. These three variables are considered for each of the different drive regions.

Under constant torque operation, the motor supply voltage is determined by

$$V_1 = k_1 f \qquad (4.1)$$

where k_1 is the ratio of rated voltage to rated frequency, f is the supply frequency. Note that V_1/f = constant means that the flux is constant. In order to have a constant torque, the motor slip frequency must also be kept constant (eqn. 2.7). This slip frequency is calculated by applying rated voltage and frequency to the equivalent circuit, in which rated output torque occurs at rated slip frequency. Once the supply voltage and the slip frequency are known, the motor line current is given by

$$I_1 = \frac{V_1}{Z_1 + Z_m Z_2/(Z_m+Z_2)} \qquad (4.2)$$

Under constant power operation, the stator voltage is kept at the rated value and the power, which is the product of torque and speed, is maintained constant. This constant is equal to the product of rated torque and the base speed. In order to keep the value of $T_e\omega_r$ constant, the output torque (T_e) must be reduced with increase of speed. The motor output power is

$$P = k_2(V_1/\omega)^2\omega_{s1}\omega_r \qquad (4.3)$$

Since $\omega_{s1} = \omega_s - \omega_r = s\omega_s$, $\omega = p/2*\omega_s$, and $s << 1$, eqn. 4.3 can be simplified as

$$P = k_3V_1^2s \qquad (4.4)$$

This equation indicates that with increase of supply frequency, the slip frequency should also be increased, so as to keep the slip (ω_{s1}/ω_s) or the power constant. For a given supply frequency, the slip frequency can be determined and hence the motor line current can be calculated using eqn. 4.2.

Under high-speed operation region, $T_{em}\omega^2$ is constant. Combining this condition with eqn. 2.7, it can be seen that the above condition can be satisfied only when ω_{s1} is kept constant. Again the motor line current can be calculated from eqn. 4.2 at rated voltage and the constant slip frequency.

Thus the stator voltage, current, and rotor slip are known for each of the different drive regions. From the power balance, the system input DC current is calculated from

$$I_{dc}V_{dc} = I_{dc}^2R_f + 3V_1I_1\cos\phi \qquad (4.5)$$

where cos ϕ, the motor power factor, varies with rotor slip. The motor output torque is given by eqn. 2.7. Using eqn. 2.7 together with the resistance torque calculated in section 2.5, the train acceleration, speed, and distance can be determined by eqns. 2.17 and 2.18. From these considerations, a total steady state simulation has been carried out with the practical system parameters given in Appendix B. The simulated results are presented in appendix I-1.

4.3 Time domain model

In the last section, a frequency domain system model was constructed by using the per-phase equivalent circuit of the induction motor. This model is valid only for steady state operation. In an adjustable speed drive system, the dynamic behaviour is important and therefore must be taken into consideration.

The dynamic performance of an induction motor is complex because of the coupling effect between the stator and the rotor phases. Since the coupling coefficients vary with rotor position, the machine model described by differential equations will have time-varying coefficients, if A-B-C phase is used as a set of three axes.

By applying Park's two-axis theory, the state variables may be expressed in terms of orthogonal or mutually decoupled direct (d) and quadrature (q) axes. This d-q model can be expressed in either a stationary or a rotating reference frame. In the stationary reference frame, the reference d and q axes are fixed on the stator, whereas in the rotating reference frame these are rotating. The rotating frame may either be fixed on the rotor or move at synchronous speed.

In the next few subsections, machine model based on Park's theory will be presented with the following assumptions

a) The stator and rotor windings are balanced.
b) The air-gap flux is spacially sinusoidal.
c) No core losses.
d) No skin effects.
e) No saturation effects.

4.3.1 Induction motor axis transformation

To implement Park's two-axis model, the three axes in the three-phase induction motor must first be transformed to a two axis set. If the as-bs-cs axes and ds-qs axes are both in the stationary reference frame, and there is an arbitrary angle θ between the two sets of axes, as shown in Figure 4.2, the motor phase voltages in terms of the ds-qs voltages can be written in matrix form as

$$\begin{bmatrix} V_{as} \\ V_{bs} \\ V_{cs} \end{bmatrix} = \begin{bmatrix} \cos\theta & \sin\theta & 1 \\ \cos(\theta-120^\circ) & \sin(\theta-120^\circ) & 1 \\ \cos(\theta+120^\circ) & \sin(\theta+120^\circ) & 1 \end{bmatrix} * \begin{bmatrix} V_{qs} \\ V_{ds} \\ V_{os} \end{bmatrix} \quad (4.6)$$

and the corresponding inverse relationship is,

$$\begin{bmatrix} V_{qs} \\ V_{ds} \\ V_{os} \end{bmatrix} = \begin{bmatrix} \cos\theta & \cos(\theta-120^\circ) & \cos(\theta+120^\circ) \\ \sin\theta & \sin(\theta-120^\circ) & \sin(\theta+120^\circ) \\ 0.5 & 0.5 & 0.5 \end{bmatrix} * \begin{bmatrix} V_{as} \\ V_{bs} \\ V_{cs} \end{bmatrix} \quad (4.7)$$

where V_{os} is the zero-sequence component. For a balanced three-phase condition, this component does not exist. Here it is considered only to obtain a unique matrix transformation.

In eqns. 4.6 and 4.7, if θ is set to zero, so that the qs-axis is coincident with the as-axis, and ignoring the zero-sequence component, the transformation relationships can be simplified as

$$
\begin{aligned}
V_{as} &= V_{qs} \\
V_{bs} &= -1/2*V_{qs} - 3/2*V_{ds} \\
V_{cs} &= -1/2*V_{qs} + 3/2*V_{ds}
\end{aligned}
\qquad (4.8)
$$

and

$$
\begin{aligned}
V_{qs} &= V_{as} \\
V_{ds} &= -1/3*V_{bs} + 1/3*V_{cs}
\end{aligned}
\qquad (4.9)
$$

Thus the motor phase voltages have been transformed between original 3-axes and an equivalent 2-axes representation. Other quantities, such as current and flux, can be transformed in a similar manner. Note that, if required, the stationary reference frame can be easily converted to a rotating reference frame.

4.3.2 Induction motor two-axis model

The three-phase stator equation set of the induction motor may be easily expressed in stationary coordinates as, bs, and cs. The stator equation in vector form is

$$\bar{V}_s = R_s\bar{I}_s + d\bar{\psi}/dt \qquad (4.10)$$

where $\bar{V}_s$, $\bar{I}_s$, and $\bar{\psi}$ are vectors of the instantaneous voltage, current and flux. Each of these vectors can be expressed in terms of component unit vectors in the form

$$X = X_{as}U_{as} + X_{bs}U_{bs} + X_{cs}U_{cs} \qquad (4.11)$$

where X is either $\bar{V}_s$, $\bar{I}_s$ or $\bar{\psi}$ and U_{as}, U_{bs}, U_{cs} are unit

vectors. If the coordinate axes rotate at the synchronous speed ω_s, eqn. 4.10 can be written as

$$\bar{V}_s = R_s\bar{I}_s + d\bar{\psi}/dt + \bar{\omega}_s\times\bar{\psi} \qquad (4.12)$$

where $\bar{\omega}_s$ is speed vector and the added cross product $\bar{\omega}_s\times\bar{\psi}$ is defined as the "speed voltage" due to rotation of the reference frame.

The above idea can also be applied using the ds-qs axes. Each vector is now in the form

$$X = X_{ds}U_{ds} + X_{qs}U_{qs} \qquad (4.13)$$

The performance of the cross product can be understood through Figure 4.3. If the axes rotate in the counter-clockwise direction, according to the right hand rule, the direction of the speed vector $\bar{\omega}_s$ is pointing out of the d-q plane. Again, using the right hand rule, vector $\bar{\omega}_s\times\bar{\psi}_{ds}$ is in the same direction as the q-axis and the vector $\bar{\omega}_s\times\bar{\psi}_{qs}$ is in the opposite direction to the d-axis. Hence the d-q voltage components for the synchronous rotating frame can be written in separated form

$$\begin{aligned} V_{qs} &= R_sI_{qs} + d\psi_{qs}/dt + \omega_s\psi_{ds} \\ V_{ds} &= R_sI_{ds} + d\psi_{ds}/dt - \omega_s\psi_{qs} \end{aligned} \qquad (4.14)$$

In a similar way, if the rotor is not moving, the rotor equations are in the form

$$V_{qr} = R_r I_{qr} + d\psi_{qr}/dt + \omega_s \psi_{dr}$$
$$V_{dr} = R_r I_{dr} + d\psi_{dr}/dt - \omega_s \psi_{qr} \qquad (4.15)$$

where all the variables and parameters are referred to the stator. Since the rotor moves at speed ω_r, the d-q axes fixed on the rotor move at a speed $\omega_s - \omega_r$ relative to the synchronous rotating reference frame. Therefore, eqn. 4.15 should be modified as

$$V_{qr} = R_r I_{qr} + dF_{qr}/dt + (\omega_s - \omega_r)\psi_{dr}$$
$$V_{dr} = R_r I_{dr} + dF_{dr}/dt - (\omega_s - \omega_r)\psi_{qr} \qquad (4.16)$$

So far, both stator and rotor equations have been derived under the assumption that the d-q axes rotates at synchronous speed ω_s. In fact, the d-q axes can rotate at any speed ω. In particular,

$$\omega = \begin{cases} 0\ ; & \text{for stationary frame model} \\ \omega_s; & \text{for synchronous rotating frame model} \\ \omega_r; & \text{for rotor fixed frame model} \end{cases}$$

Combining eqns. 4.14 and 4.16 with $\omega_s = 0$, the dynamic model of an induction motor in the stationary reference frame is given by

$$\begin{bmatrix} V_{qs} \\ V_{ds} \\ V_{qr} \\ V_{dr} \end{bmatrix} = \begin{bmatrix} R_s+pL_s & 0 & pL_m & 0 \\ 0 & R_s+pL_s & 0 & pL_m \\ pL_m & -\omega_r L_m & R_r+pL_r & -\omega_r L_r \\ \omega_r L_m & pL_m & \omega_r L_r & R_r+pL_r \end{bmatrix} * \begin{bmatrix} I_{qs} \\ I_{ds} \\ I_{qr} \\ I_{dr} \end{bmatrix} \qquad (4.17)$$

where p is the differential operator. For a squirrel cage induction motor, V_{qr} and V_{dr} are zero. The corresponding equivalent circuits are shown in Figure 4.4. The flux linkage expressions in terms of the currents can be written from Figure 4.4 as

$$\begin{bmatrix}\psi_{qs}\\ \psi_{ds}\\ \psi_{qr}\\ \psi_{dr}\end{bmatrix} = \begin{bmatrix}L_{ls}+L_m & 0 & L_m & 0\\ 0 & L_{ls}+L_m & 0 & L_m\\ L_m & 0 & L_{ls}+L_m & 0\\ 0 & L_m & 0 & L_{ls}+L_m\end{bmatrix} * \begin{bmatrix}I_{qs}\\ I_{ds}\\ I_{qr}\\ I_{dr}\end{bmatrix} \tag{4.18}$$

To solve eqn. 4.17 with continuous variation of the speed ω_r, an extra differential equation must be introduced. The speed can be related to the torque as

$$T_e - T_l = J_m d\omega_r/dt \tag{4.19}$$

where T_l is the load resistance torque and J_m is the motor-load inertia.

As mentioned in section 2.1, the motor developed torque is the result of the interaction of air-gap flux and rotor current. This torque can be given in a general vector form as

$$\begin{aligned} T_e &= 3/2*p/2*\bar{\psi}_m \times \bar{I}_r \\ &= 3/2*p/2*(\psi_{qm}, \psi_{dm}) \times (I_{qr}, I_{dr}) \\ &= 3/2*p/2*(\psi_{dm} I_{qr} - \psi_{qm} I_{dr}) \end{aligned} \tag{4.20}$$

The flux ψ_{dm} and ψ_{qm} is given by

$$\psi_{qm} = L_m(I_{qs}+I_{qr})$$
$$\psi_{dm} = L_m(I_{ds}+I_{dr}) \qquad (4.21)$$

Combining eqn. 4.19, 4.20, and 4.21, the relationship between speed and motor currents can be written as

$$d\omega_r/dt = 1/J_m*[3/2*p/2*L_m(I_{qs}I_{dr}-I_{ds}I_{qr}) - T_l] \qquad (4.22)$$

Eqns. 4.17 and 4.22 describe the total model for the induction motor with its load.

4.3.3 VSI-SCIM system model

In this sub-section, the model will be extended to include the VSI as the motor drive converter. In addition, the effect of the DC source impedance and the system input filter will be taken into account (Figure 4.5). The VSI-SCIM model takes account of the different inverter drive switching modes. In each mode, the DC-link impedance is transformed to the stator fixed two-axis model by introducing two extra state variables, the DC input current and the DC link voltage.

The system to be modelled is shown in Figure 4.5, together with the polarities and directions of all voltages and currents. As shown, the inverter consists of six ideal switches. The effect of the GTO snubber

circuits is not included. The motor is assumed to be in delta connection. For a balanced three-phase motor, a delta-star transformation can be made if required by multiplying all the impedances by a factor of three.

If each of the six switches conduct for 180° under quasi-square wave operation, then there are three switches on at any moment, but never two in any single phase. Hence, there are eight possible combinations of switch closures. The cases, when the upper three (1,3,5), or the lower three switches (2,4,6) are on together correspond to the same mode electrically. Therefore, there are totally seven different modes, mode 7 and 8 being identical.

The following relates the DC variables (DC input current and DC link voltage) with the motor phase voltages and currents for all the switching modes, as shown in Figure 4.6 (a-h). The operational equations for each mode are

Mode 1:
$$\begin{aligned} V_{in} &= (R_f+pL_f)I_{in} + V_{dc} \\ 0 &= I_{in} - pC_fV_{dc} - I_a + I_b \\ 0 &= 1/pC_f(I_a-I_b-I_{in}) + V_{as} \\ 0 &= 1/pC_f(I_b-I_a+I_{in}) + V_{bs} \\ 0 &= V_{cs} \end{aligned} \qquad (4.23)$$

Mode 2:
$$\begin{aligned} V_{in} &= (R_f+pL_f)I_{in} + V_{dc} \\ 0 &= I_{in} - pC_fV_{dc} - I_a + I_c \\ 0 &= 1/pC_f(I_a-I_c-I_{in}) + V_{as} \\ 0 &= 1/pC_f(I_c-I_a+I_{in}) + V_{cs} \\ 0 &= V_{bs} \end{aligned} \qquad (4.24)$$

Mode 3:
$$\begin{aligned} V_{in} &= (R_f+pL_f)\,I_{in} + V_{dc} \\ 0 &= I_{in} - pC_fV_{dc} - I_b + I_c \\ 0 &= 1/pC_f(I_c-I_b+I_{in}) + V_{cs} \\ 0 &= 1/pC_f(I_b-I_c-I_{in}) + V_{bs} \\ 0 &= V_{as} \end{aligned} \qquad (4.25)$$

Mode 4:
$$\begin{aligned} V_{in} &= (R_f+pL_f+)\,I_{in} + V_{dc} \\ 0 &= I_{in} - pC_fV_{dc} + I_a - I_b \\ 0 &= 1/pC_f(I_a-I_b+I_{in}) + V_{as} \\ 0 &= 1/pC_f(I_b-I_a-I_{in}) + V_{bs} \\ 0 &= V_{cs} \end{aligned} \qquad (4.26)$$

Mode 5:
$$\begin{aligned} V_{in} &= (R_f+pL_f)\,I_{in} + V_{dc} \\ 0 &= I_{in} - pC_fV_{dc} + I_a - I_c \\ 0 &= 1/pC_f(I_c-I_a-I_{in}) + V_{cs} \\ 0 &= 1/pC_f(I_a-I_c+I_{in}) + V_{as} \\ 0 &= V_{bs} \end{aligned} \qquad (4.27)$$

Mode 6:
$$\begin{aligned} V_{in} &= (R_f+pL_f)\,I_{in} + V_{dc} \\ 0 &= I_{in} - pC_fV_{dc} + I_b - I_c \\ 0 &= 1/pC_f(I_b-I_c+I_{in}) + V_{bs} \\ 0 &= 1/pC_f(I_c-I_b-I_{in}) + V_{cs} \\ 0 &= V_{as} \end{aligned} \qquad (4.28)$$

Mode 7:
$$\begin{aligned} V_{in} &= (R_f+pL_f)\,I_{in} + V_{dc} \\ 0 &= I_{in} - pC_fV_{dc} \\ 0 &= V_{as} \\ 0 &= V_{bs} \\ 0 &= V_{cs} \end{aligned} \qquad (4.29)$$

Using eqn. 4.8, the stator voltages can be converted from three-axes to a two-axis representation. For the stator currents, the transform matrix is similar. Substituting (V_{as}, V_{bs}, V_{cs}) and (I_a, I_b, I_c) by (V_{ds}, V_{qs})

and (I_{ds}, I_{qs}) in modes 1-7 gives the system model based on a stationary frame machine model

$$\begin{bmatrix} V_{in} \\ 0 \\ 0 \\ 0 \\ 0 \\ 0 \end{bmatrix} = \begin{bmatrix} R_f+pL_f & 1 & 0 & 0 & 0 & 0 \\ 1/C_f & -p & K_1 & K_2 & 0 & 0 \\ 0 & K_1 & R_s+pL_s & 0 & pL_m & 0 \\ 0 & K_2 & 0 & R_s+pL_s & 0 & pL_m \\ 0 & 0 & pL_m & -\omega_r L_m & R_r+pL_r & -\omega_r L_r \\ 0 & 0 & \omega_r L_m & pL_m & \omega_r L_r & R_r+pL_r \end{bmatrix} * \begin{bmatrix} I_{in} \\ V_{dc} \\ I_{qs} \\ I_{ds} \\ I_{qr} \\ I_{dr} \end{bmatrix} \qquad (4.30)$$

where K_1 and K_2 vary from mode to mode. In the case of mode 7, K_1 and K_2 are zero. The values of K_1 and K_2 under the different modes are shown in Figure 4.7.

By rearranging the differential terms in eqn. 4.30, the equations can be written in the standard state space form

$$[X]' = [A][X] + [B][V] \qquad (4.31)$$

where $[X] = [I_{in}, V_{dc}, I_{qs}, I_{ds}, I_{qr}, I_{dr}]^t$

$[V] = [V_{in}, 0, 0, 0, 0, 0]^t$

$[A] = -[L]^{-1}\{[R]+\omega_r[G]\}$

$[B] = [L]^{-1}$

The matrices [L] and [G] are given by

$$\mathbf{[L]} = \begin{bmatrix} L_f & 0 & 0 & 0 & 0 & 0 \\ 0 & -1 & 0 & 0 & 0 & 0 \\ 0 & 0 & L_s & 0 & L_m & 0 \\ 0 & 0 & 0 & L_s & 0 & L_m \\ 0 & 0 & L_m & 0 & L_r & 0 \\ 0 & 0 & 0 & L_m & 0 & L_r \end{bmatrix} \qquad (4.32)$$

$$[G] = \begin{bmatrix} 0 & 0 & 0 & 0 & 0 & 0 \\ 0 & 0 & 0 & 0 & 0 & 0 \\ 0 & 0 & 0 & 0 & 0 & 0 \\ 0 & 0 & 0 & 0 & 0 & 0 \\ 0 & 0 & 0 & -L_m & 0 & -L_r \\ 0 & 0 & L_m & 0 & L_r & 0 \end{bmatrix} \qquad (4.33)$$

The matrices in eqns. 4.32 and 4.33 apply to all seven modes. Matrix [R] varies from mode to mode and can be written in a general form

$$[R] = \begin{bmatrix} R_f & 1 & 0 & 0 & 0 & 0 \\ 1/C_f & 0 & K_1 & K_2 & 0 & 0 \\ 0 & K_1 & R_s & 0 & 0 & 0 \\ 0 & K_2 & 0 & R_s & 0 & 0 \\ 0 & 0 & 0 & 0 & R_r & 0 \\ 0 & 0 & 0 & 0 & 0 & R_r \end{bmatrix} \qquad (4.34)$$

Eqn. 4.22, together with eqn. 4.31, gives the complete dynamic model of the DC-fed inverter induction motor drive system in the stationary frame machine model. The stability of this system model is discussed in the following section.

4.4 System stability

The system model described by eqns. 4.22 and 4.31 can be expressed in the form

$$x' = f(x,u) \qquad (4.35)$$

where x is a state vector and u is an input vector. As shown in the last subsection, this system model represents a 7-dimensional time-varying nonlinear system.

For general purpose applications, the stability analysis of VSI-SCIM systems involving mechanical effects is well known [80,81]. Information about the stability limits may be obtained by linearising the system equations about an operating point and investigating the stability of the resulting linear perturbation equations.

For railway traction applications, the speed of the induction motor can be assumed to be constant throughout an inverter output cycle, due to the large load inertia. With this assumption, the system model can be linearised with a constant speed for a limited time interval.

An effective method to analyse the stability of the simplified system is to used the Routh-Hurwitz technique [82]. Using this method the total system input impedance is required. Based on synchronous rotating frame machine model, the induction motor equivalent impedance may be described as

$$Z_m = \frac{a_4p^4+a_3p^3+a_2p^2+a_1p^1+a_0}{b_3p^3+b_2p^2+b_1p^1+b^0} \qquad (4.36)$$

where p is the differential operator and a_i and b_i are coefficients related to motor speed and parameters. The coefficient (k) used to transform the system input filter components into the machine equivalent circuit is

$6/\pi^2$. The total system equivalent impedance as shown in Figure 4.8 is given by

$$Z_{in} = kR_f + pkL_f + \frac{kZ_m}{pC_f+Z_m+k}$$

$$\text{or} \quad Z_{in} = \frac{c_6p^6+c_5p^5+c_4p^4+c_3p^3+c_2p^2+c_1p^1+c_0}{d_5p^5+d_4p^4+d_3p^3+d_2p^2+d_1p^1+d^0} \qquad (4.37)$$

Calculations of all the coefficients a_i, b_i, c_i and d_i are given in Appendix C.

Applying the Routh-Hurwitz technique on the coefficients c_0-c_6, the system becomes unstable if any of the elements in the first column of the Routh-Hurwitz array are negative.

Using this technique, the system stability boundaries for the 140 kW and 3.0 kW induction motors are shown in Figures 4.8 (a) and (b). Figure 4.8 (c) shows the stability boundary with the laboratory-based system used later.

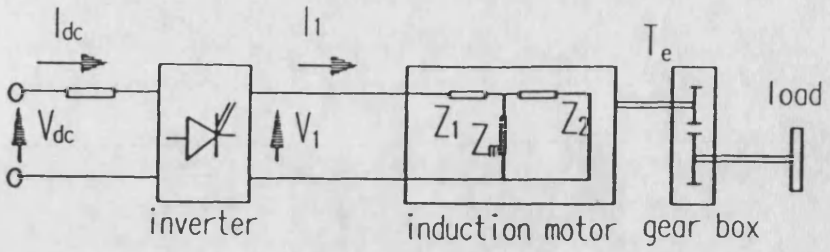

Figure 4.1 System block diagram

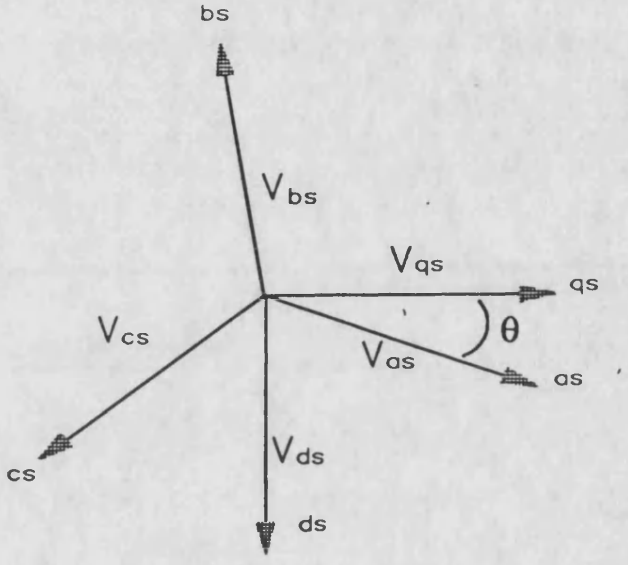

Figure 4.2 Transformation between as-bs-cs axes and d-q axes

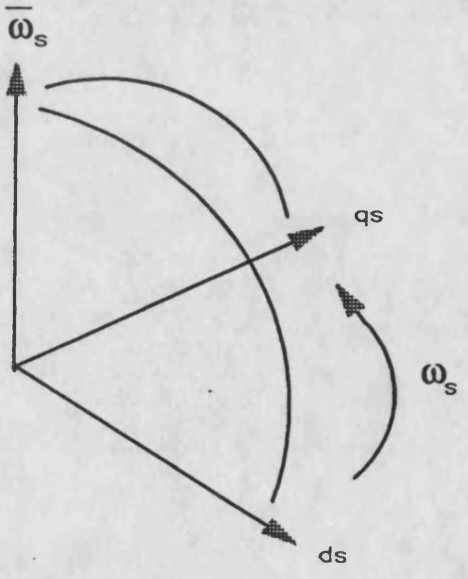

Figure 4.3 cross product operation

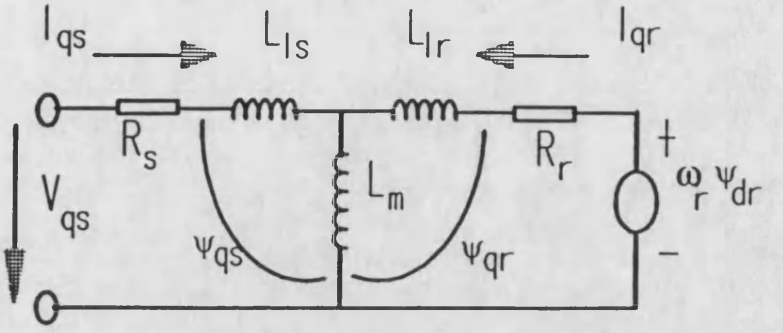

(a) qs-circuit

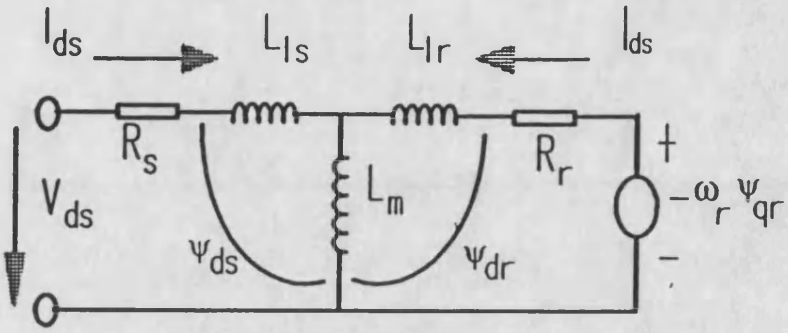

(b) ds-circuit

Figure 4.4 D-Q equivalent circuits in stationary reference frame

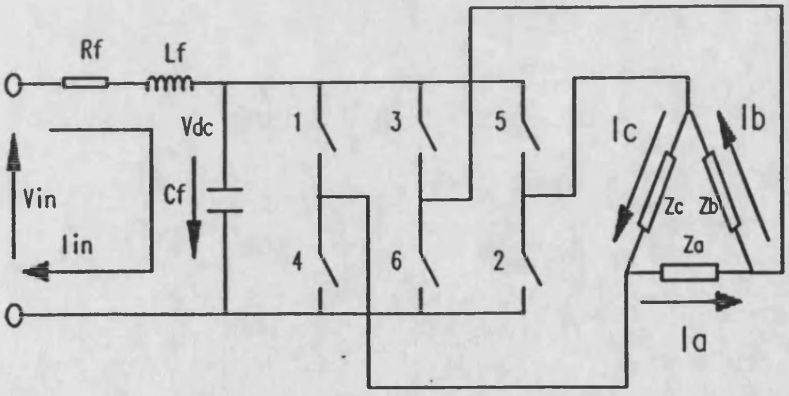

Figure 4.5 System equivalent circuit

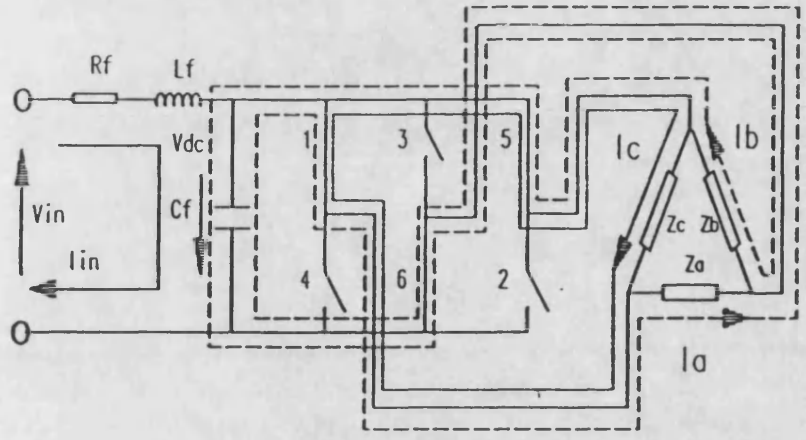

(a). mode 1

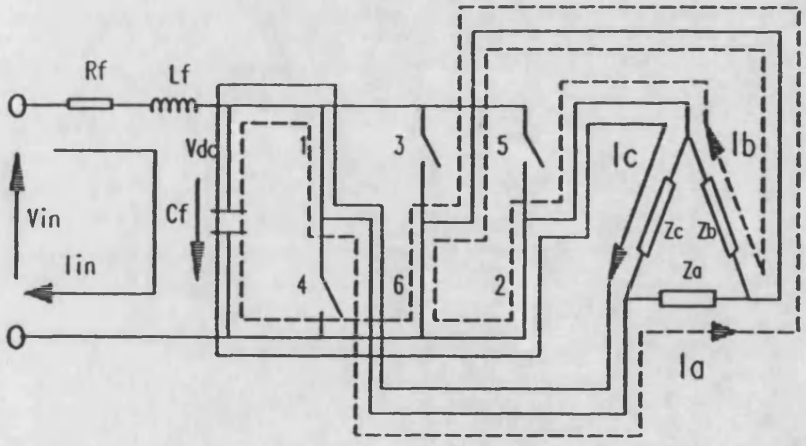

(b). mode 2

Figure 4.6 Inverter switching mode 1-2

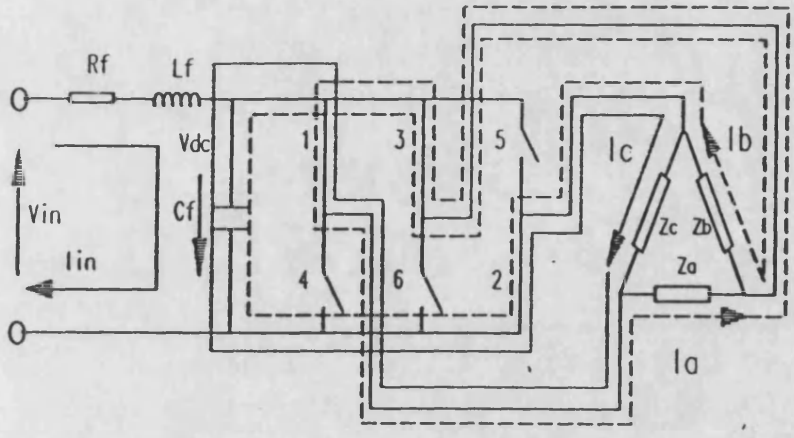

(c). mode 3

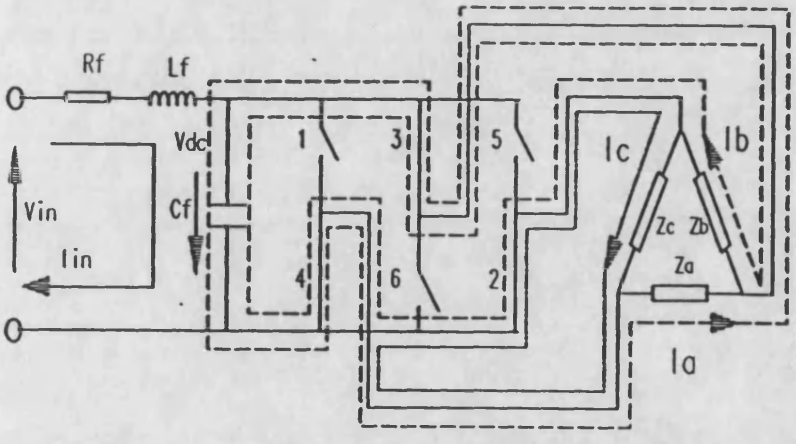

(d). mode 4

Figure 4.6 Inverter switching mode 3-4

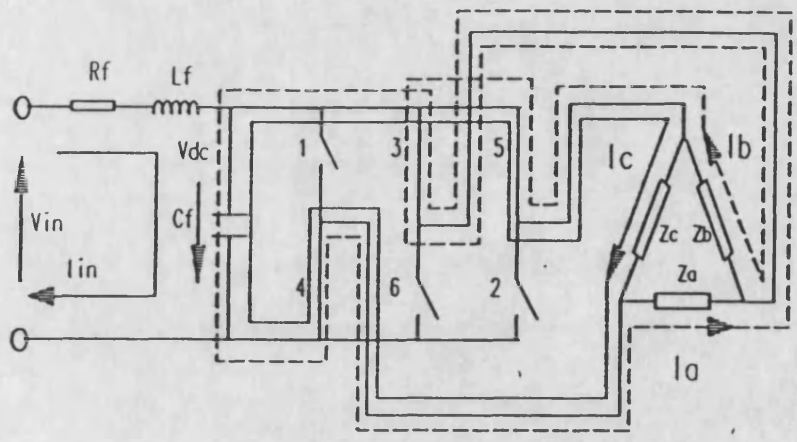

(e). mode 5

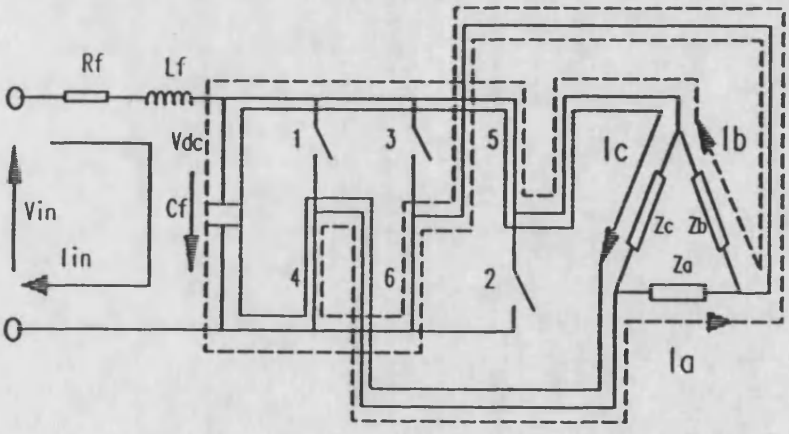

(f). mode 6

Figure 4.6 Inverter switching mode 5-6

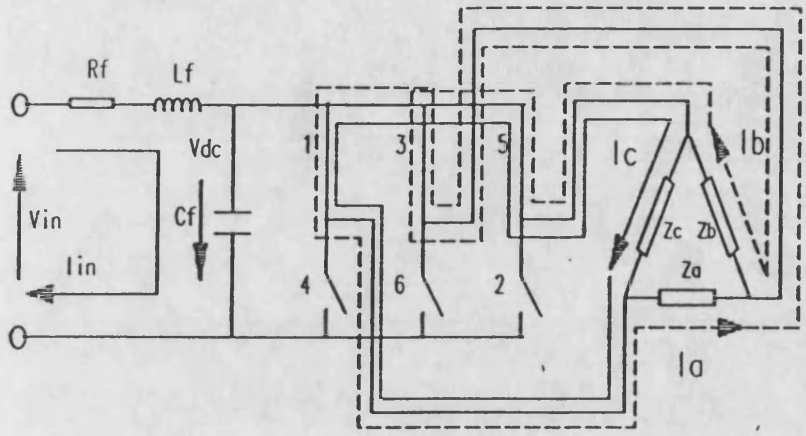

(g). mode 7

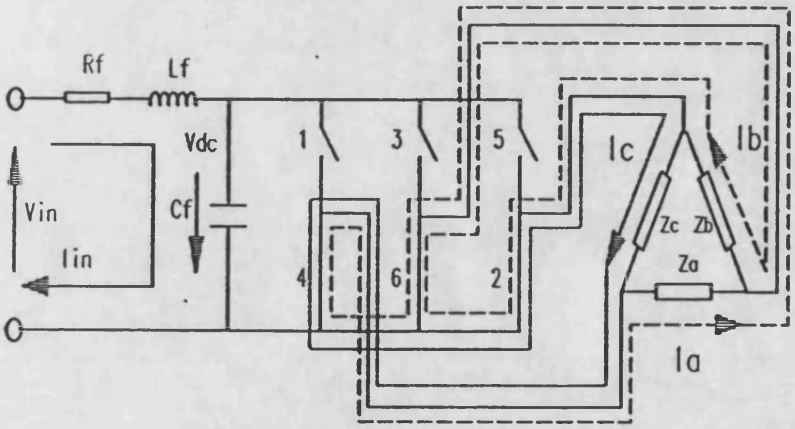

(h). mode 8

Figure 4.6 Inverter switching mode 7-8

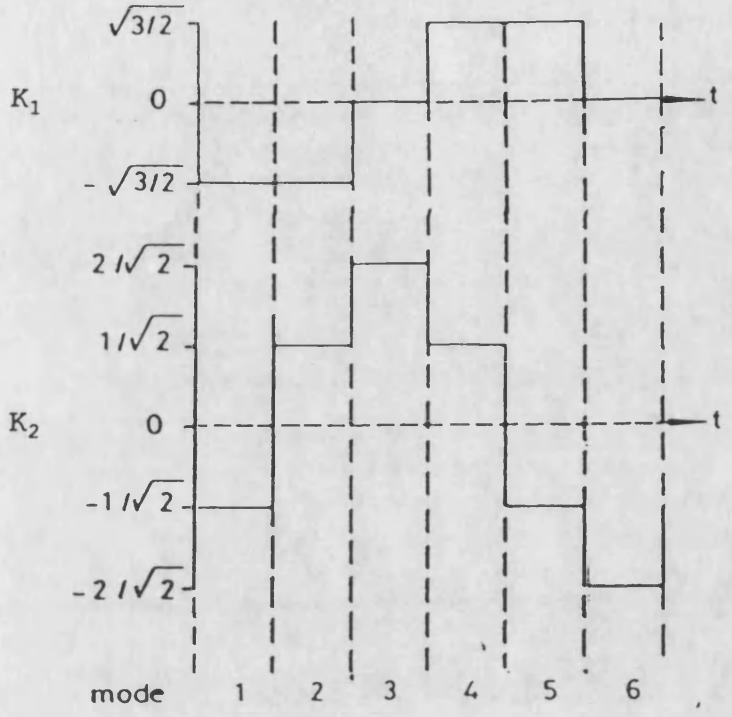

Figure 4.7 Variation of K_1 and K_2

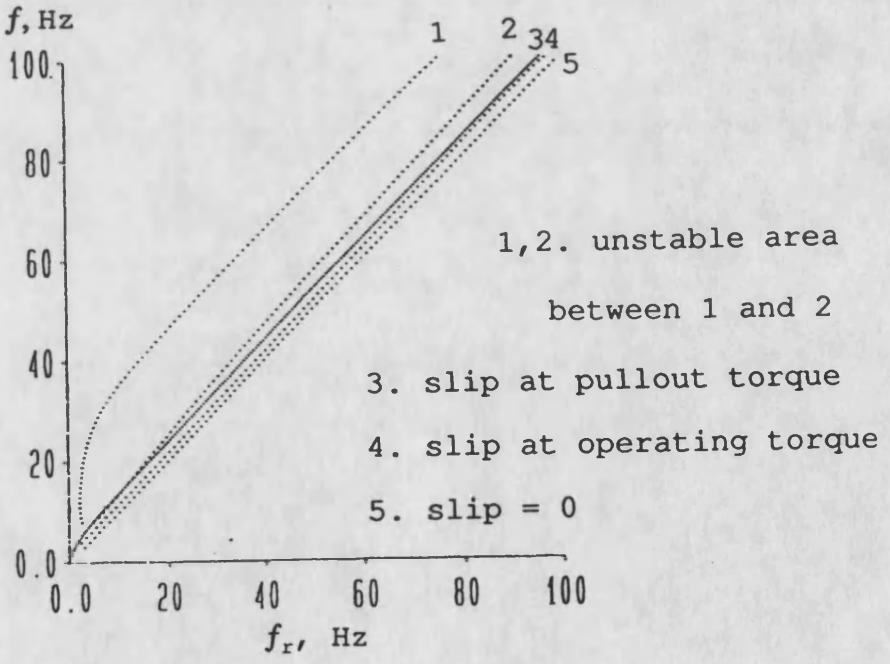

(a). simulation system with 140 kW motor

Figure 4.8 System stability boundary

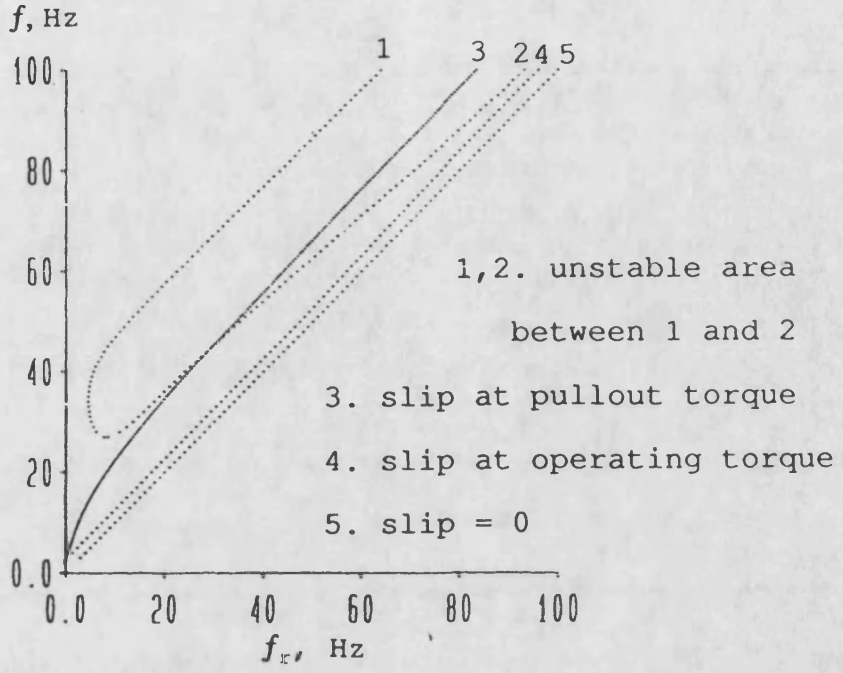

(b). simulation system with 3 kW motor

Figure 4.8 System stability boundary

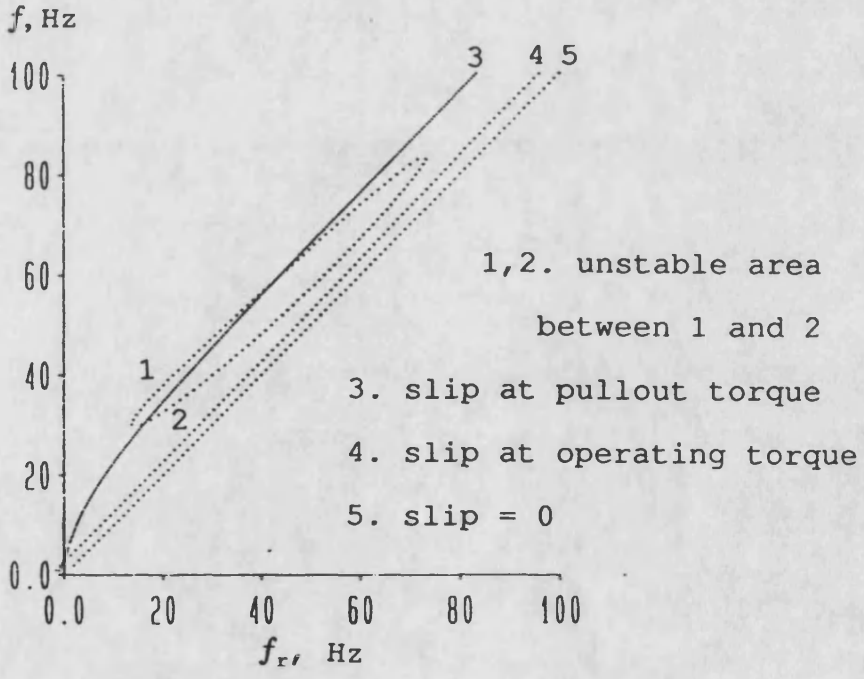

(c). experiment system with 3 kW motor

Figure 4.8 System stability boundary

Chapter 5 : System model implementation

5.1 Introduction

In chapter 4, the total model of a DC-fed voltage source inverter-induction motor drive system was constructed. The computer simulation of this system model was implemented on a MC68000 based multi-processor computer.

In this chapter, the computer hardware and software will be described. This is followed by consideration of the simulator input. The final form of the input is a look-up table which contains a sequence of mode-period pairs. To solve the differential equations of the system, different numerical methods are reviewed. In particular, the 4th-order Runge-Kutta method is investigated in detail. Also, an on-line FFT facility is described which was written by the author as one of the local library packages for system variable harmonic analysis.

The simulation is a two-stage procedure. The first stage, implemented using a single task, shows the general behaviour of the system performance. The intermediate simulation results are then stored and used as the initial conditions for the second stage which is implemented as a multi-task simulation. The multi-task

implementation gives a defined window view of certain system variables together with their harmonic content.

5.2 Description of multi-processor computer

The multi-processor computer used for the simulator is as designed by Dale [55] and modified by Berry [56] for the real-time simulation of power systems. No hardware modification were necessary, although considerable software development was required.

The system hardware consists of a number of MC68000 single board computers (SBC) sharing a common backplane. A block diagram of the system is shown in Figure 5.1 [55]. Each SBC had its own processor, memory, backplane interface and optional input/output circuitry. One SBC is configured to handle all input and output functions. This "master" SBC permits the user to control the tasks running on the other SBCs configured as "slave" processors. In addition to the SBCs, the system also has a high resolution colour graphics controller board. This board supports the on-line display of the simulation results. The shared common backplane is controlled by a system arbiter board. The communication to other computers or printers or plotters are carried out through a multi-link local area network board. A quarter megabyte dynamic RAM memory board is used for general

purpose workspace by simulation programs. More details of this system are given in [55,56].

The operating system of this computer was developed by Dale [55] from single processor multi-tasking TRIPOS to a multi-processor version (MP-TRIPOS). The system software consists of a number of segments in executable binary code produced by assemblers and compilers. The assembly code sections are concerned with the hardware specific functions and the rest of the system software are coded in BCPL (Basic Combined Programming Language).

The standard TRIPOS system has at least four tasks. Task one is the command line interpreter (CLI). This task reads command names and attempts to execute them. All commands and user programs run under a particular invocation of the CLI. The second task is the debug task. The terminal may be connected directly to the debug task by the user, or it may be called into action automatically by the system if something goes wrong. When the system is under debugging, the state of the machine can be examined or altered, and the program execution can be continued if required. The third and fourth tasks handle the terminal and the filing system on a disc unit.

The system programming language is BCPL. This is an unusual high-level language because it is typeless. The

BCPL compiler translates the BCPL code into object code which is executable by the machine.

Once a program is running under the CLI task, more tasks can be created or deleted on line as desired. The one which creates other tasks is also known as the master task, and the ones created as the slave tasks. The slave tasks can be created either on the same processor where the master task resides or on slave processors. When more than one tasks reside on one processor, a priority is assigned to each task.

The communication between tasks is realized by sending data packets. A packet is a vector which contains information such as the packet.ID, packet.link and packet.type. Packet.ID contains the ID number of the destination task to which this packet is sent. Packet.link is used to link this packet with others on the work queue. Packet.type tells the destination task what actions it is required to take. In addition, a packet also contains two result fields and ten argument fields. Each field could be a vector itself. These fields are used to transfer information which the destination task required.

The whole system bootstrap proceeds by first loading the TRIPOS kernel into the master processor from disk using a bootstrap program residing in EPROM. Once the

master processor is running, a system load command is executed in the initialisation sequence to download the operating system from disk. After the system is set up, a simulation can be run by loading the program object code under the CLI task.

5.3 Simulator input implementation

5.3.1 General design

In chapter 2, it is recalled that in the voltage source inverter induction motor drive, the system input is described by two variables, the stator supply voltage and the stator supply frequency. Under PWM operation, the former is represented by the modulation depth, and the latter by the modulation frequency.

The objective in designing the system input is to determine the relationships between the above two variables and the operating time. These relationships are described as a look-up table. This table contains the information which specifies, at any instant, the inverter switching mode (one out of seven) and the period which this mode takes.

The design of the table is illustrated in Figure 5.2. A three-bit binary code is used to represent the on-off states of the inverter switching modes. Phase A-B-C

corresponds to the three bits from left to right. If the top switch in a phase is on, the corresponding bit is logic one. If the bottom switch is on the corresponding bit is zero. Under quasi-square wave operation as shown in Figure 5.2, the total number of modes is six. The period for all six modes is the same (1/6 cycle). Under PWM operation, two extra modes exist. These correspond to the cases when all three top or bottom switches are on. In this case, the periods are no longer identical, but vary from mode to mode. The mode-period look-up table is used as the system input for both the simulation and the experimental verification.

With a particular traction drive duty-cycle (in the form of a speed-time relationship), the mode-period look-up table can be determined by the following procedure. The relationship between slip frequency (f_{sl}) and time is determined according to a specific application requirement. The supply frequency is determined by the sum of f_{sl} and f_r where f_r, rotor electrical speed frequency, corresponds to the train speed and is determined by a specific train operating duty-cycle as shown in section 2.7. Under constant torque operation, the supply voltage is calculated such that the ratio of V_s/f is constant. The modulation depth is then related to the supply voltage for the different PWM schemes. Finally, the switching angles for a given modulation frequency and modulation depth are

calculated. These angles are used to determine the mode-period look-up table. The following sub-sections present each procedure in detail.

5.3.2 Determination of slip frequency

As discussed in section 2.7, the stator frequency and motor speed are related by slip frequency. At startup, the motor speed is zero, and the slip frequency is equal to the stator frequency.

Constant torque operation requires the slip frequency to be kept constant. If the stator frequency starts at 0.1 Hz, the slip frequency should increase up to the rated value, i.e. that at which rated torque is obtained with rated voltage and frequency. For simplicity, the slip frequency is assumed to linearly increase from 0.1 to rated value within the stator frequency range of 0.1 to 2.0 Hz. Above this stator frequency, it is kept constant until the end of constant torque operation.

As shown in section 2.7, to obtain constant power operation, the slip frequency should be increased with increase of stator frequency so as to keep the ratio ω_{sl}/ω constant. In the high-speed operation region, the slip frequency is kept constant at the last obtained value in the constant power region.

The relationship between slip frequency and time can be determined as follows. For a given train speed, the corresponding time is known from the duty-cycle. If the parameters for a specific machine are known, the rated slip frequency can be calculated. The first turning point in the slip frequency is made at the transition between asynchronous PWM and synchronous PWM. This occurs when the sum of rated slip frequency and rotor speed frequency is equal to the stator frequency (2 Hz). The second turning point corresponds to the start of quasi-square operation. This is made when the sum of rated slip frequency and rotor speed frequency is equal to the rated stator frequency (50 Hz). The third turning point is the end of constant power operation. This is at the time when the sum of slip frequency and rotor speed frequency is equal to 85 Hz. A total view of slip frequency for the 140 kW motor is shown in Figure 5.3.

5.3.3 Determination of supply frequency

The maximum supply frequency is determined by the required maximum train speed and the corresponding slip frequency. The minimum supply frequency is mainly determined by the maximum allowed stator current, if constant torque operation is required at startup. Figure 5.4 (a) and (b) shows the required stator supply voltage and the corresponding stator current, as a function of starting frequency, with rated and half rated starting

torque. It can be seen that the stator current increases rapidly when the supply frequency is reduced below 0.1 Hz. Therefore, 0.1 Hz is used as the starting frequency throughout the simulation for the practical system.

For a given train speed, the supply frequency can be calculated using the above requirements for slip frequency. The starting and terminating supply frequency for the three operating regions are set at 0.1, 50, 85, and 120 Hz. From 0.1 to 2 Hz, asynchronous PWM is used, and from 2 to 50 Hz synchronous PWM is used. Above 50 Hz, quasi-square wave is used. The method for updating the supply frequency for both PWM operations will be presented later.

5.3.4 determination of supply voltage

Under constant torque operation, the supply voltage varies in proportion to the supply frequency so as to keep the voltage/frequency ratio constant. At low frequencies, the supply voltage is boosted to compensate the dominating voltage across the stator resistance. At the end of constant torque operation, the supply voltage reaches its rated value and thereafter is kept constant. Figure 5.5 shows the relationship between the required supply voltage and the required operation time at supply frequencies under 2 Hz.

For PWM operations, the relationship between the required supply voltage and the modulation depth must be determined. When the modulation depth is less than unity, the relationship is linear [$M_d = V_{sp}/(V_{dc}/2)$, where V_{sp} is peak fundamental component]. When M_d is greater than unity, the linear relationship no longer holds. This is because over-modulation results in pulse dropping. A sudden increase in the supply voltage can occur during pulse dropping. As discussed in section 3.6, one method to overcome this is to introduce a modified PWM scheme

An asynchronous PWM scheme is applied with the supply frequency in the range of 0.1 to 2.0 Hz. From 2.0 to 37.0 Hz, the conventional synchronous PWM scheme is used. After this, a modified synchronous PWM is applied up to 50 Hz. The transition point (37 Hz) is made where the modulation depth is just below unity. Figure 5.6 shows the relationship between the peak value of the supply voltage and the modulation depth. This was calculated for a fixed V_{sp}, f, and M_r, by varying M_d and finding where the fundamental component peak value equalled V_{sp}. It was confirmed from the figure that with $M_d < 1$, V_{sp} and M_d are linearly related. Also it is evident that the relationship between V_{sp} and M_d can be approximated by two linear equations. This linear approximation is adopted throughout this simulation.

5.3.5 Asynchronous PWM input

Under asynchronous PWM operation, the sinusoidal PWM schemes described in sections 4.3 and 4.4 can be used. The following explains how the asymmetric regular sampled PWM scheme is implemented. The carrier frequency is assumed to be 500 Hz, and the modulation frequency is increased from 0.1 to 2.0 Hz. The length of time for this operation was calculated as 0.396 second. This is equivalent to 198 carrier cycles. The modulation depth and modulation frequency are updated for each carrier cycle.

Calculation of the triggering times for phase A is explained by Figure 5.7. At the end of the i^{th} carrier cycle, the sine wave is sampled as A_i, The absolute value of A_i is taken as the initial value of the $(i+1)^{th}$ carrier cycle. This can be expressed as

$$M_{di+1} \sin(2\pi f_{i+1}t + \varphi_{i+1}) = A_i \qquad (5.1)$$

Note that the first value of A_1 is given by $M_{d0}\sin 2\pi f_0 T$, where T is the period of the carrier and $\varphi_0 = 0$.

It is clear that for any given A_i, there are two corresponding values of φ_{i+1}. If only the value of $(0° < \varphi_{i+1} < 90°)$ is considered, then

$$\varphi_{i+1} = \sin^{-1}(A_i/M_{di+1}) \qquad (5.2)$$

The values of φ_{i+1} for the other three quadrants are determined by the values of the total phase angle (θ). This angle is given as

$$\theta = 2\pi T\sum f_i \qquad (5.3)$$

The relationship between φ_i' and θ is given as

$$\begin{aligned} \varphi_i' &= \varphi_i && 0° < \theta \leq 90° \\ &= \pi - \varphi_i && 90° < \theta \leq 180° \\ &= \pi + \varphi_i && 180° < \theta \leq 270° \\ &= 2\pi - \varphi_i && 270° < \theta \leq 360° \end{aligned} \qquad (5.4)$$

Once the initial phase angle for each carrier cycle is given, the switching times for each cycle are defined by the down-slope and up-slope crossing times, t_d and t_u. These times are given by

$$\begin{aligned} t_{di} &= T[i+1/4(1-A_{i-1})] \\ t_{ui} &= T[i+1/4(3+A_i')] \end{aligned} \qquad (5.5)$$

where $A_i' = M_{di}\sin(2\pi f_i T/2 + \varphi_i)$. The timings of t_d and t_u correspond to the moment of switch-on of the top and bottom switching devices in each phase. If a logic 1 represents the on-stage of the top device and 0 for the bottom device, the firing sequence for the switching devices can be defined by a set of mode-period pairs.

The period corresponds to t_d and t_u and the mode corresponds to logic values 1 and 0.

The above has shown how the switching times of the phase A are calculated. By setting the initial phase angle $\varphi = 120°$ and $\varphi = -120°$, the timings for phases B and C are obtained. The total modes for all three phases can be described by three-bit binary codes shown in Figure 5.2. By comparing the time sequence between the three sets of switching times, the timings in sequence together with the corresponding mode are put into a look-up table and used as the system input.

5.3.6 Synchronous PWM input

The distinction between asynchronous and synchronous PWMs is that the latter must have an integer modulation ratio. If the extreme case, where a non-integer carrier cycle and non-integer modulation cycle give an integer ratio, is excluded, the modulation frequency must have at least one complete cycle. Within a certain operation time, a decision should be made on the number of supply frequency steps, the value for each step frequency and its repetition. The following presents one method which can solve the above problem.

The basic idea is that an equal time interval, say 0.5 second (2Hz), is added from the beginning of the

synchronous PWM operation at 0.396 second. For a given time, the supply frequency is determined as stated in sub-section 5.3.3. If the period of this frequency is larger than the time interval, then the difference is added to the time interval. If the time interval is several times bigger than the period of the frequency, the time interval is divided by the period. The integer value is kept as the number of repeats for that frequency and if the remainder is more than half of the period, the time interval is extended. If the remainder is smaller than half of the period, the time interval is reduced until the remainder is smaller than the pre-decided value. Using the above method, a set of time-frequency-repeat data is obtained.

Generally, the length of the time interval determines the smoothness of the frequency update. After several tries, it was found that 0.4 second interval gave frequency steps in about one Hz intervals.

With the above modulation frequencies, five modulation ratios were adopted: 51, 27, 15, 9, and 9'. The first four correspond to conventional PWM schemes, and the last corresponds to a modified PWM scheme. Selection of the modulation ratio is made with a trade-off between the harmonic content and the switching loss in the inverter. With the natural sampled PWM scheme,

Figure 5.8 gives the total harmonic distortion with the above modulation frequencies and modulation ratios.

Throughout the five modulation ratios, any of the sinusoidal PWM schemes described in sections 3.3 and 3.4 can be used. The switching angles can be calculated using the corresponding equations described in chapter 3. The mode-period look-up table can be produced in a similar way to that described in the last sub-section.

5.4 System model calculation

5.4.1 Introduction

The system model described in section 4.3.3 can be summarized as an initial-value problem:

$$x' = f(t,x) \qquad a < t < b,$$
$$x(a) = x_o \qquad (5.6)$$

where x are the vector of the state variables.

In general, it is impossible to obtain a functional (analytical) solution of (5.6). Instead, the interval [a,b] is divided into subintervals or steps. The solution is then approximated at n+1 evenly spaced values, i.e., $t_i = t_o + ih$, $h = (b-a)/n$, i varying between 0 and n.

One method of approximating these solutions numerically is to express the solution $x(t_{i+1})$ about the point t_i by using a Taylor expansion

$$x_{i+1} = x_i + x_i'*h + x_i''/2*h^2 + \cdots\cdots \qquad (5.7)$$

It is clear that only finite items in the series can be calculated. The drop out of the remainder introduces a local truncation error. If the first n items are retained, the error is given in the form

$$O(h^{n+1}) = x^{(n)}(\xi)/(n+1)!*h^{n+1} \qquad (5.8)$$

where $t_i \leq \xi \leq t_{i+1}$. In this case, the local truncation error is of the order h^{n+1}. It can be proved that the total truncation error is of the order h^n.

If only the first two items in eqn. (5.7) are employed as

$$x_{i+1} = x_i + x_i'*h \qquad (5.9)$$

the method becomes Euler's method. Obviously, the accuracy in using this method is poor due to the low order of the truncation error. To improve the accuracy, more items must be employed. This means there is a need to calculate the complicated high-order derivatives.

One way to gain high accuracy without involving high order derivative evaluations, is to use the Runge-Kutta method. A general form of the Runge-Kutta method is

$$x_{i+1} = x_i + hF \qquad (5.10)$$

where F is an approximation to f(t,x) during the interval $[t_i,t_{i+1}]$. Theoretically, a truncation error order O(h) can be achieved as high as one desires. In practice, a 4th-order method has proved to be sufficient for most applications. The following presents one of the 4th-order Runge-Kutta algorithms

$$x_{i+1} = x_i + h/6(k_1+2k_2+2k_3+k_4) \qquad (5.11)$$

where $k_1 = f(t_i,x_i)$

$k_2 = f(t_i+h/2,x_i+h/2*k_1)$

$k_3 = f(t_i+h/2,x_i+h/2*k_2)$

$k_4 = f(t_i+h,x_i+h*k_3)$

Using this algorithm, a 5th-order truncation error can be achieved with four evaluations of the function f(t,x).

The above methods are one-step methods, i.e., the integration at each point needs only information at one

previous point. A multi-step method makes use of information at more than one previous point.

A typical 4th-order multi-step formula, known as the Adams-Bashforth method, is given as

$$x_{i+1} = x_i + h/24(55f_i - 59f_{i-1} + 37f_{i-2} - 9f_{i-3}) \quad (5.12)$$

where $f_i = f(t_i, x_i)$ and so on. This method is an explicit method, since it gives an explicit expression for x_{i+1} in terms of the preceding values.

An implicit 4th-order multi-step formula, known as the Adams-Moulton method, is given as

$$x_{i+1} = x_i + h/24(9f_{i+1} + 19f_i - 5f_{i-1} + f_{i-2}) \quad (5.13)$$

where $f_{i+1} = f(t_{i+1}, x_{i+1})$ etc..

The combined use of eqns. 5.12 and 5.13 is known as the predictor-corrector method. Eqn. 5.12 is used first to obtain a predicted value x_{i+1}, which then serves on the right-hand side of eqn. 5.13 as the initial approximation. For each step, the function f(t,x) is evaluated twice with a local 5th-order error.

In general, the Runge-Kutta method has the advantages that it is self-starting, stable, and provides good

accuracy. One disadvantage is that no local-error estimation is provided. The user has to find whether the step length h being used is adequate by some other way. Moreover, it requires twice as many function evaluations as the predictor-corrector method. Considering that each of the individual inverter switching modes can themselves be an integration step, the multi-step methods are excluded. The single step 4th-order Runge-Kutta method is thus selected to calculate the system model.

5.4.2 The Runge-Kutta method

Before using the Runge-Kutta method, a number of points should first be considered. These are the determination of the integration step-size, minimisation of errors from all sources, making sure of convergence and retaining stability in the calculation.

The convergence of a numerical method is defined as: if x^* is the true solution and x is the integrated value, then as the step-size h -> 0, the term (x^*-x) -> 0. It has been shown that all Runge-Kutta methods are convergent [82].

A numerical method is called A-stable (absolute), if the solution is stable with any step-size h. When the time constants in a system are significantly different

(say by a factor of 10), the system has stiff differential equations. Under this condition, some of the numerical methods such as the one-step Runge-Kutta method may be unstable, if the step-size is close to or larger than the smallest time constant of the system.

In addition to the truncation error, there are two other types of errors - original data error and round-off error. The former is due to the inexact values of the initial conditions, and the latter due to the finite word length in the computer. All these three errors are subject to propagating or accumulating problems. Normally, the accumulated error is not simply the sum of the local errors, because each local error may either grow or decay as the computation proceeds. A detailed discussion on round-off error propagation problem is given in reference [83]. It has been shown [84] that if the local truncation error for a one-step method is $O(h^{n+1})$, then the accumulated truncation error will be $O(h^n)$.

In general, the accuracy of a numerical integration will depend upon both the truncation error and the round-off error. To keep the truncation error small, the step-size h should also be small. However, the smaller h is taken, the more integration steps have to be performed, and the greater the round-off error is likely to be. Moreover, with small step-size, an excessive

numbers of functions have to be evaluated which requires substantial computing time. In order to reduce the computing time, the step-size must be increased. Even when the accuracy criterion is satisfied, the largest step-size should not exceed the smallest time constant of the system with the Runge-Kutta method.

5.4.3 Determination of step-size

In section 5.4.1, the integration step-size h for the Runge-Kutta method is assumed to be fixed over the entire interval [a,b]. In fact, the step-size h can be varied with the criteria of accuracy. In an extreme case, h can be the whole interval [a,b]. Ideally, the variation of step-size h should be controlled on-line according to the estimated error. In reality, this is impractical because the error estimation is complicated and requires substantial extra computing time [85].

For specific system differential equations, one way to solve the above problem is to make several step-size trials, and to select that which is reasonable for both the error criteria and computing time.

Since most step lengths in the mode-period look-up table are of the order of 10^{-4} second, it seems that this length of time is small enough from the accuracy point of view, though this length of time can be halved at a

sacrifice of nearly doubling the computing time. The following gives three trials for the integration step-sizes of a whole period, 1/4 period, and 1/8 period for each mode.

3.0 kW laboratory based system was used for the trials. The simulation was performed by the system input designed previously until f = 18.6 Hz, M_r = 27, using the period of each mode as an integration step-size. The results were stored as initial conditions for the three trials. Table 5.1 shows the sampled output of the system input current, motor line current, and the motor speed. The differences are seen to be reasonably small considering that the simulation model itself is an approximation of the real system.

From software inspection of the complete look-up table, a few larger step-sizes of the order of 3.0×10^{-3} are seen to be present. This happens only in special cases at modes 000 and 111 where f = 2.89 Hz, M_r = 51. Integration with these large step-sizes is subject to the condition of numerical stability.

It has been shown [86] that a one-step 4th-order Runge-Kutta method is A-stable if the step-size h < 2.78*lm, where lm is the smallest time constant of the system. By linearising the system about the points where the largest step-sizes occur, the system time constant

can be found by solving the system eigenvalues. However, a quick method to check the numerical stability at these points is to apply this technique and determine if the result is convergent. When this was done, the simulation result did show the method to be stable at those points.

5.5 FFT facility

A major task in the simulation of AC traction drives is to display the harmonic contents of the simulated variables. In the standard TRIPOS library, a FFT facility is not available. Therefore, a FFT algorithm has been implemented in BCPL as one of the local library programs.

The theory of the Fast Fourier Transform is well established in the literature [87] and it will not be repeated here. There are many implementation techniques, from which the Cooley-Tukey FFT algorithm has been adopted [88]. Normally, the input of a standard FFT program is a complex time function. If the input is a real time function, the imaginary part of the input must be set to be zero. With this treatment, the computation effort spent on the transformation is not less than that spent on the complex time function. One way to halve the computation time [87] is to separate the odd number of input data as the imaginary part and leave the even number as the real part. The program based on Cooley-

Tukey algorithm for real time function as input written in BCPL is shown in Apperdix D.

In using the FFT program to calculate the harmonic contents of the simulation output variables, aliasing and spectral leaking errors occur. The former is introduced when the sampling frequency is less than twice the largest frequency component of the sampled function (from sampling theory). The latter occurs when the length of sampling time (truncation) is not an exact multiple of the period of the sampled function (here only periodical functions are considered).

One method to reduce the aliasing error is to increase the sampling rate. However, the extra sampled points require more computing time. In reality, the dominating harmonic components are at low frequency, and the harmonics at high frequency are smaller. Since aliasing error exists at high frequencies, by keeping the sampling frequency at a reasonable rate, the aliasing error can be controlled at an acceptable level.

Intuitively, the second error can be eliminated by setting the length of truncation as the same as the period of the sampled function. In practice, however, the period of the sampled function is not always known. An effective method to reduce this error is to apply weighting functions or windows to the sampled function.

A thorough review of various window methods is given in [89]. Since the length of sampling time (truncation) is not an integer multiple of the period of the sampled function, this results in discontinuity at the boundary. The idea of using a window is to reduce the order of the discontinuity at the boundary of the periodic function.

5.6 Simulator implementation

5.6.1 Input generation

The simulation input is generated by three main programs: F-V program, PWM program, and M-P program. The F-V program is for generating the supply frequency and supply voltage. The PWM program is for generating the firing angles using one of the PWM schemes. The M-P program is for sorting out the sequence in the three-phase PWM firing angles, and putting the mode-period pairs into a look-up table.

The F-V program contains five sub-routines which are SUB.TS for calculating the train speed, SUB.RSF for the slip frequency, SUB.SF for the supply frequency, SUB.SV for the supply voltage, and SUB.MD for the modulation depth. All these variables are related to each other through time. The PWM programs consist of asynchronous PWM and synchronous PWM sub-routines. Asynchronous PWM (ASYN.PWM) uses the asymmetrical regular sampled PWM

scheme. The synchronous PWM sub-routines are single-side natural sampled PWM (SSNS.PWM), double-side natural sampled PWM (DSNS.PWM), symmetrical regular sampled PWM (SRS.PWM), asymmetrical regular sampled PWM (ARS.PWM), and modified asymmetrical regular sampled PWM (MARS.PWM). In addition, there are two optimisation sub-routines. They are harmonic elimination PWM (HE.PWM) and harmonic minimisation PWM (HM.PWM). The M-P program contains a sorting program (S.PROG) which produces the look-up table using the output of PWM programs. Appendix E outlines the input and output of each of the above programs.

The look-up table used for the system simulation has a total of 7557 points. The first 1188 points correspond to asynchronous PWM operation. Each point contains a mode and its period. The remaining 6228 points are for synchronous PWM operation. For a particular supply frequency with its modulation ratio, the number of points are fixed. For example, if M_r = 15, the number of points is 15×6 = 90, since each carrier cycle produces two firing angles and there are three phases. At the end of each cycle, an extra point is added which terminates the total number of points for this supply frequency with its repeating times. Square-wave operation requires 141 points. Each point contains the value of the supply frequency and the repeat times for that frequency. Under square-wave operation, the frequency in the pointer is

first converted into a period (T) and then divided by 6. The result is the length of each mode.

5.6.2 Single task implementation

The simulator is first implemented using a single task which is the system CLI task. The program is first coded in the BCPL language. Then it is compiled into object code. To start the simulation, the operator needs to invoke the object code of the program through the key board.

At the beginning, the simulator displays the system initial parameters on the screen and prompts the operator to make a decision whether to change the parameters. Then the simulator asks for:

a) The length of time which will be used for screen display or plot;

b) the number of sampling points within the above length of time;

c) The number of intermediate values to be stored as initial conditions for the multi-task simulation.

Having completed the above, the simulator sets up three checking pointers for the above requests and begins to fetch the information from the look-up table.

Completion of the total simulation requires several hours. The output of this simulation consists two sets of data - one for display or plot and the other for initialising the multi-task simulation.

5.6.3 Multi-task implementation

The multi-task structure is shown in Figure 5.9. The master task, console task and display task are performed by a 68000 SBC (the local processor) and the calculator task and FFT task are performed by a 68020 SBC (the remote processor).

The sequence for one processor to work on different tasks is arranged according to the priority. On the local processor, the master task has the highest priority, and the display has the lowest. The priority for the calculator task is higher than that for the FFT task on the remote processor. Communication between tasks is carried out by sending a data packet. If one task receives more than one packet simultaneously, that with higher priority will be processed first. Note that the tasks on the local processor have higher priority than that on the remote processor.

At the beginning, the master task is invoked by running OBJ.MASTER. This command is accepted by the Tripos command line interpreter (CLI). After initialising its own conditions, the master task creates and initialises the other four tasks. When the console task is ready to run, control of the console is passed from the master task to the console task. Now the console task is ready to interact with the operator.

The console task will receive different instructions from the operator and then pass them to the master task. In turn, the master task tells the other three tasks to take certain actions as required by the operator. If the instruction is simulation, then the master task sends a packet to the calculator task. When one display page or window has calculated, the calculator task sends the results to the FFT task and then carries on for another display window. After the FFT analysis, the display task receives the information for on-line display.

At any moment, if more than one group of data is under store, the FFT or display task will refuse to accept the packet sent by the calculator or FFT task. In this case, the calculator or FFT task has to wait until the packet is accepted.

On each on-line display page, one system variable and its harmonic spectrum are displayed. The screen also indicates resolution of the spectrum, DC level of the system variable, value of the maximum harmonic amplitude and its harmonic number, frequency of the fundamental component, calculation time for this page, and the real time of the system operation.

The console task is always ready to receive any instructions available from the operator regardless of the stage of master task. Once the console task receives QUIT, it then passes this command to the master task. The master task takes over the control of the console and then terminates all the other four tasks and stops the simulation.

The programs for each tasks are first coded in the BCPL language, after which they are compiled into object code. The object code for the master task is loaded when the command, OBJ.MASTER, is input by the operator at the beginning of the simulation. The object codes for the other four tasks are loaded when the master task creates the corresponding tasks.

Appendix F outlines the program structures for the master and console tasks. The other three tasks take the actions dictated by the master task.

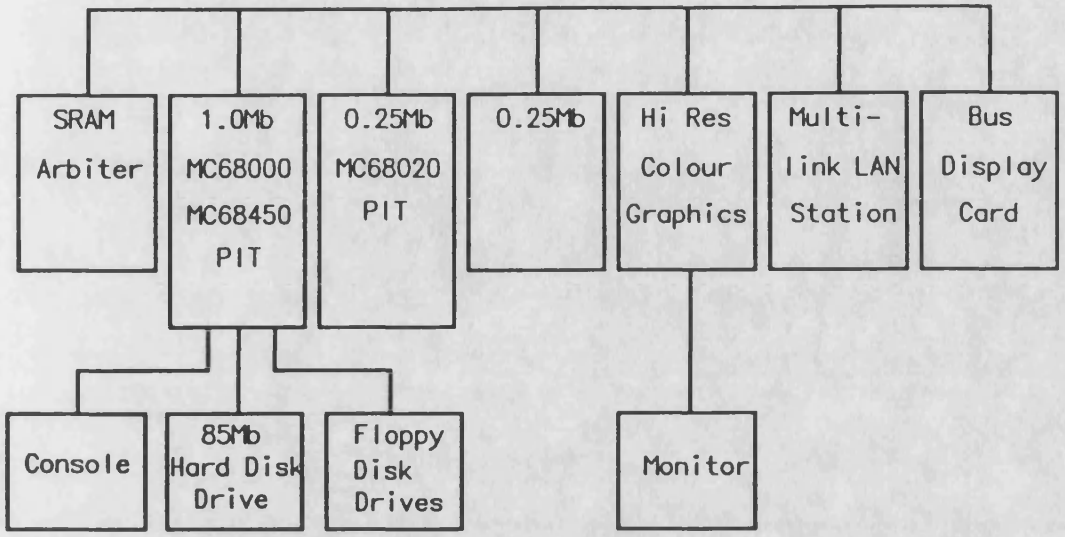

Figure 5.1 Block diagram of simulator hardware

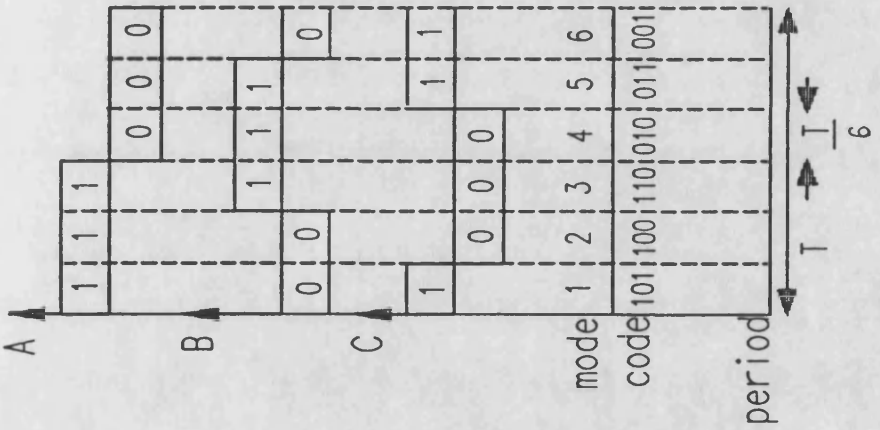

Figure 5.2 Inverter switching modes

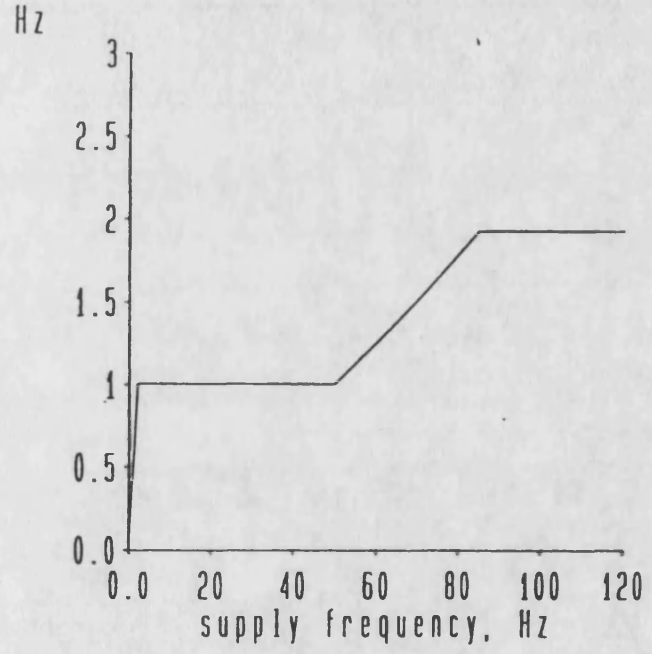

Figure 5.3 Variation of slip frequency

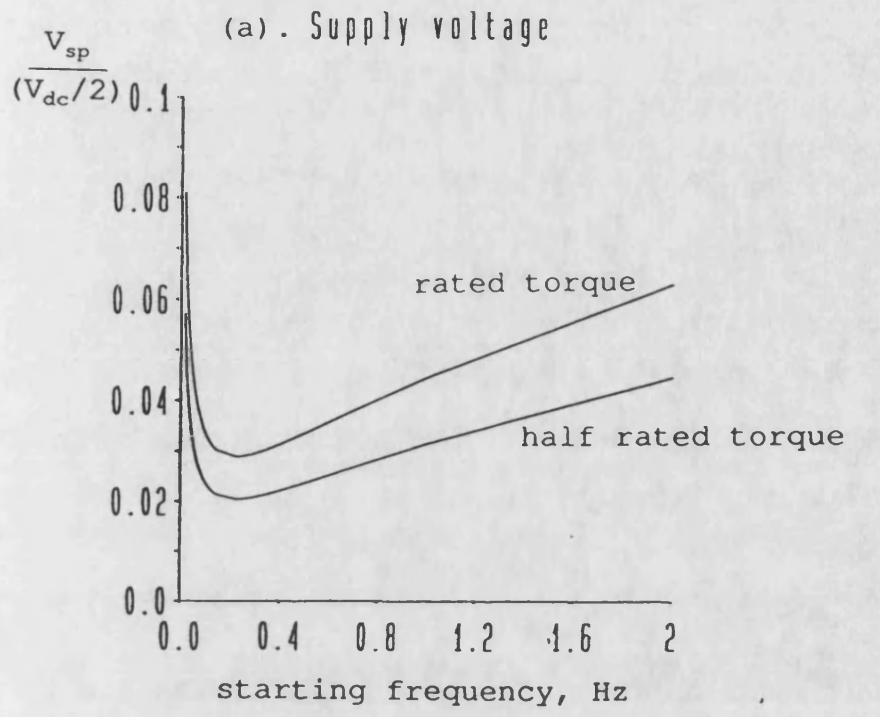

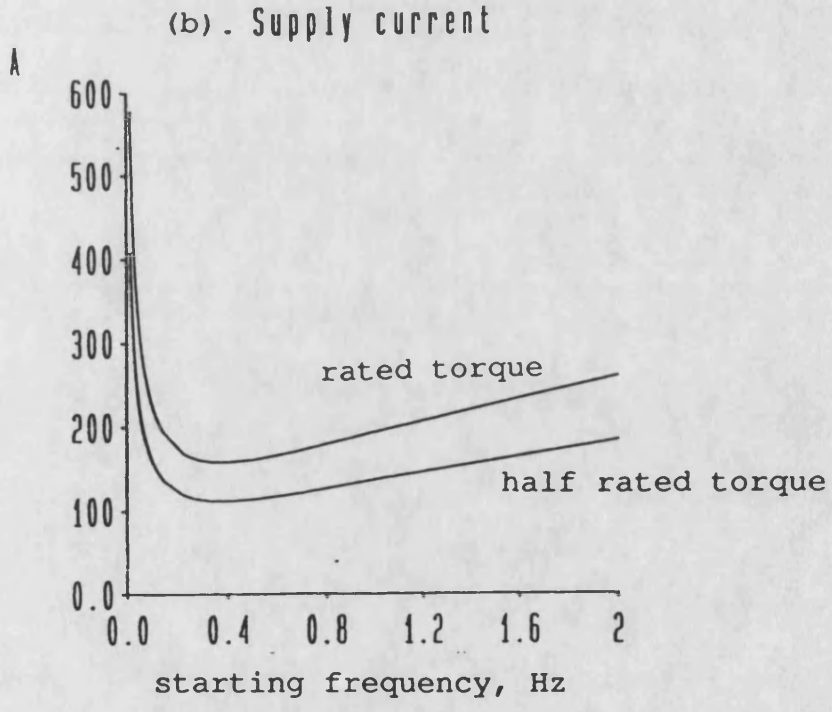

Figure 5.4 Starting voltage and current with different supply frequencies

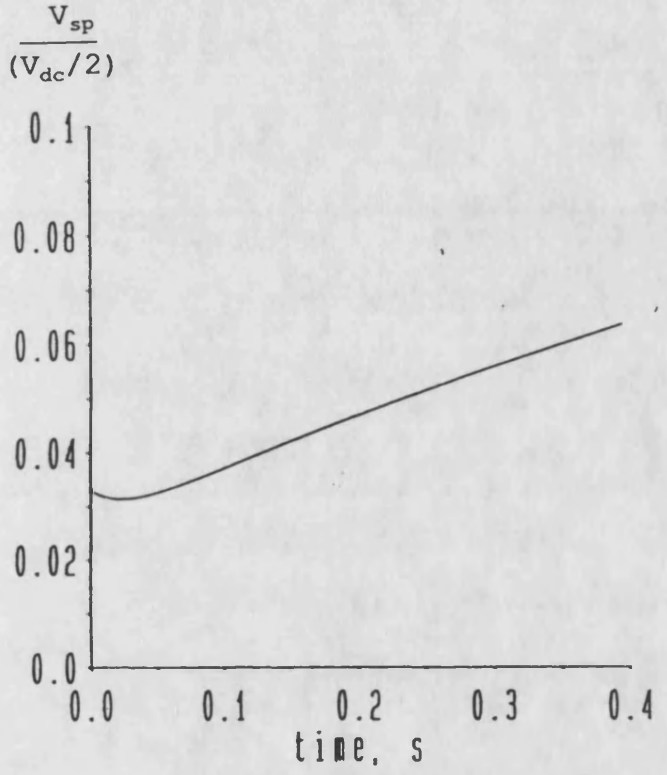

Figure 5.5 Supply voltage at low frequencies

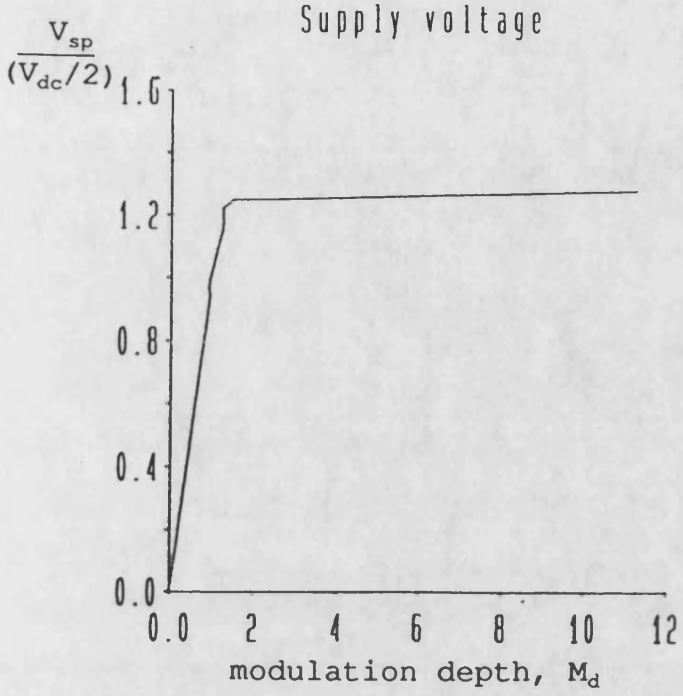

Figure 5.6 Relation between stator peak voltage and modulation depth

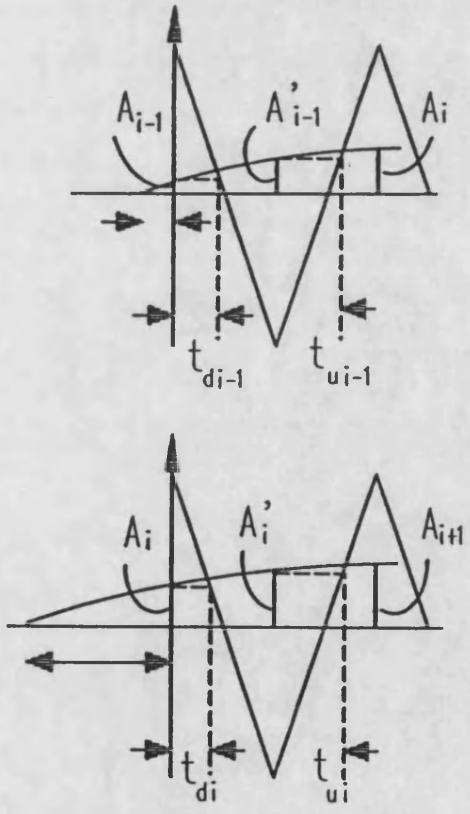

Figure 5.7 Calculation of asynchronous PWM switching angles

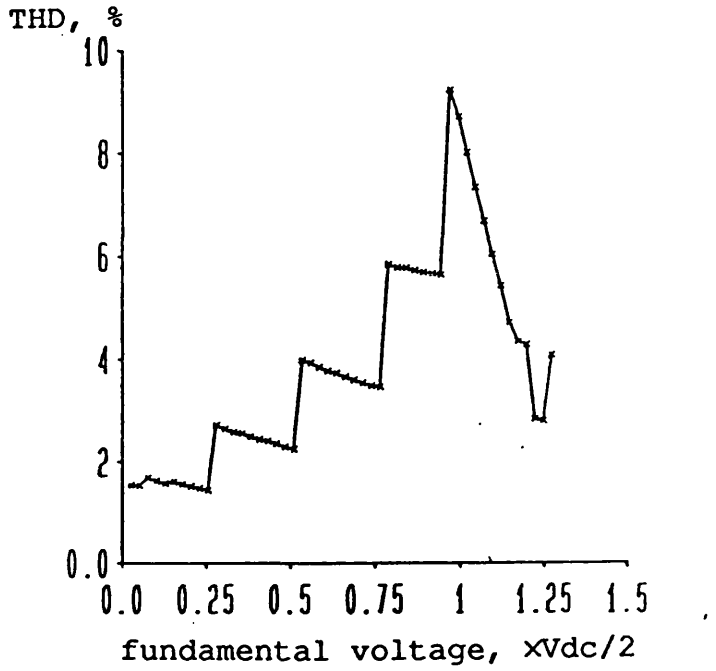

Figure 5.8 Total Harmonic Distortion

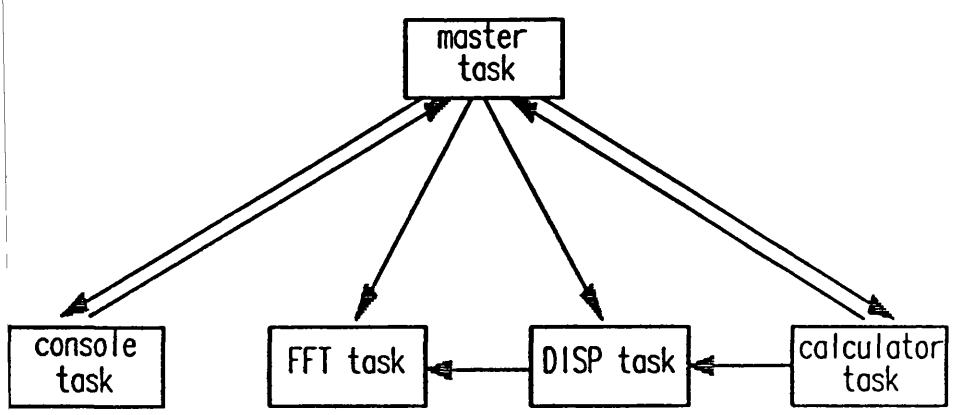

Figure 5.9 Diagram of multi-task scheme

Table 5.1 Simulation results using different integration step-sizes,

<A> step = the length of each mode

No.	Iin (A)	I-line (A)	speed (rad/s)
1	4.71598,	0.917,	55.25
2	5.08369,	-10.08,	55.35
3	5.76895,	-12.05,	55.46
4	6.38445,	-10.18,	55.56
5	6.90797,	-7.257,	55.68
6	7.39125,	4.123,	55.8
7	7.80467,	14.46,	55.91
8	8.20853,	23.11,	56.04
9	8.60938,	12.55,	56.16

<B> step = 1/4 length of each mode

No.	Iin (A)	I-line (A)	speed (rad/s)
1	4.716,	0.9169,	55.25
2	5.08374,	-10.08,	55.35
3	5.76898,	-12.05,	55.46
4	6.38449,	-10.18,	55.56
5	6.90806,	-7.257,	55.68
6	7.39133,	4.123,	55.8
7	7.80473,	14.46,	55.91
8	8.20855,	23.11,	56.04
9	8.60934,	12.55,	56.16

<C> step = 1/8 length of each mode

No.	Iin (A)	I-line (A)	speed (rad/s)
1	4.71599,	0.9169,	55.25
2	5.08372,	-10.08,	55.35
3	5.76901,	-12.05,	55.46
4	6.38454,	-10.18,	55.56
5	6.90807,	-7.257,	55.68
6	7.39129,	4.123,	55.8
7	7.8047,	14.46,	55.91
8	8.20856,	23.11,	56.04
9	8.60934,	12.55,	56.16

CHAPTER 6: Experimental implementation

6.1 Introduction

The objective of constructing the laboratory based traction drive system is to validate the simulator before the practical traction drive system is simulated. It has been assumed that the practical system is a three-car train with two motored cars and one trailer. Each car has four axles. Each motored axle is driven by a 140 kW induction motor. The total resistance is divided by 8, the number of motored axles. The simulation, however, is only concerned with one of the motored axles. For the laboratory system, a single low power drive was used.

The laboratory drive is shown in Figures 6.1 and 6.2. It consists of a 3kW induction motor with load comprising train resistance (simulated by a 3.5 kW DC machine) and the train inertia (simulated by a heavy flywheel linked between the induction motor and the DC machine). The DC supply for the inverter was obtained by rectifying a three-phase supply through an auto-transformer. The inverter was built with GTO thyristors. The drive circuits for the GTOs were controlled by a 68000 SBC through a logic unit.

The look-up table, similar to that used as the simulation input for the practical system, was first generated by the parallel computer. It was then down loaded to the 68000 SBC through a PC. Software written in assembly language was used to fetch information from the look-up table and send it to the logic control unit through a 68230 PIT (Parallel Interface / Timer).

The total drive up performance from 2.667 Hz to 48.12 Hz takes 99.95 seconds. The experimental results were measured and recorded by the instrumentation given in Appendix B.

6.2 68000 SBC and 68230 PIT

The Andelos 68000 single board computer hardware consists of a 16-bit 68000 microprocessor running at 10 MHz, 16Kb EPROM and 64Kb RAM (expanded from 4Kb), a serial interface, a parallel interface, and an optional EPROM programmer (EProg) board. The system bus can be extended to a satellite board through two DIL sockets. The serial interface, 8250, was used to link this SBC to a host computer, AMSTRAD PC, through a RS232 link. The parallel interface, 8255, was used to link the EProg board. A layout of the 68000 SBC, its memory map and other details are presented in [90].

A 68000 native code assembler (SEKA) was stored in EPROM. The main features of SEKA are the text editor, 68000 assembler, symbolic debugger, line disassembler, an EPROM programmer handler and formatted listing output. Further details are given in [91].

A 68230 parallel interface timer (PIT) was used to interface the 68000 SBC with the peripheral logic control unit. The PIT consists of two independent sections, three ports (A,B,C) and a timer. Further details are given in [92]. Only port A is used for output data and the timer is not considered further.

The 68230 has three byte-wide I/O ports located on the lower eight data bus lines (D0-D7). Data transfers between the 68000 SBC and these three ports are performed by reading from or writing to a corresponding data register within the 68230. The read/write operation is directed by the 68230 internal registers. The 68230 has a total of 23 registers. To fully address these registers, five address bus lines are required (2^5=32). From the 68000 SBC memory map [90], it can be seen that the 68230 is positioned at the hexadecimal location of 800000. An address bus line (EXSEL) is provided by 68000 SBC. Address bus lines A1-A5 are used together with the EXSEL line to cover all 23 registers within the 68230. Since the 68230 is located at the lower eight data bus lines, the LDS (lower byte data strobe) line has to be

ANDed with the EXSEL line to give a chip select (CS) line. Figure 6.3 shows the interface between the 68000 SBC and 68230 PIT through the two sockets on the 68000 SBC board. The pin assignment of the sockets is from the 68000 SBC buses, and the arrows indicate the destinations on the 68230 chip.

6.3 Download of look-up table

The look-up table used for the laboratory system input was generated in a similar way as that for the practical system. However, only synchronous PWM schemes were applied with a modulation frequency starting at 2.667 Hz and ending at 48.12 Hz. The sequence of gear ratio change was the same as for the simulation, i.e., M_r = 51 for f < 10 Hz; M_r = 27 for f < 20 Hz; M_r = 15, for f < 30 Hz; M_r = 9, for f < 37 Hz; and M_r = 9', for f < 50 Hz; where M_r = 9' corresponds to the modified PWM scheme.

To transfer the look-up table from the parallel computer to the AMSTRAD PC, a program written in BCPL language called TRANSLUT was used. This program first gets the look-up table from a data.file and then opens another data.file and writes the data into this data.file in a hexadecimal form. Each data occupies four bytes space. For example, the decimal value $(3061)_{10}$ is converted into the four byte hexadecimal $(0BF5)_{16}$. This

data.file is then copied to the AMSTRAD PC. Another program written in GW-BASIC called CONVTLUT inputs the four bytes of each data separately. The first two bytes were put together as one value and the second two bytes as another, i.e., $(0B)_{16}$ => $(0*16+11)_{10}$, $(F5)_{16}$ => $(15*16+5)_{10}$. When the values are output into a file, the GWBASIC program stores this data.file in ASCII code. Since the maximum value of one byte (containing 8 binary bits) is 256, two bytes have the value of 65536. Considering the maximum period for all the different modes is less than 5000 microseconds, a two byte-space is sufficient for each period. Thus each mode-period point occupies four bytes, with the first two bytes for the period and the second two for the mode. The maximum value of any mode is not greater than 7. The reason that two bytes are assigned to each mode is to make each period-mode point as a long-word so that the program count down is simple.

Finally, a program also written in GW-BASIC called DOWNLOAD was used to download the data.file from the AMSTRAD PC to the 68000 SBC through a RS232 serial interface. The main commands used are 'open' and 'shell'. The former links the PC and the SBC together, and the latter copies files from the PC to the SBC. The addresses where the look-up table will be stored in the 68000 SBC memory are at hexadecimal 602000 onwards.

The look-up table used for the experimental system was arranged into two areas, the step-rpt (repeat) area and the mode-period area. The step-rpt area consists of 22 long-words. The first long-word contains the number of supply frequency steps (21 steps have been used). Each of the remaining long-words contain the number of modes and the number of repeat times of the corresponding supply frequency step. The mode-period area starts at hex 602058 ($22*4_{10}$ => 58_{16}) and each mode-period point occupies a long-word.

6.4 System control program

The system control program was used to generate a three-phase PWM waveform using the information in the down loaded look-up table. This program was first written in assembly language using word processor software. Then it was down loaded from the AMSTRAD PC to the 68000 SBC memory, located from hex 400400 onwards, by the DOWNLOAD program. Finally, the 68000 assembler (SEKA) translates this program into machine code, after which it is ready to run.

To fetch data from the 68000 SBC memory and send it to port A of the 68230 PIT, certain internal registers of 68230 PIT must be initialised. This includes the port general control register (PGCR), the port A data direction register (PADDR), and the port A control

register (PACR). The values for the initialisation of these ports can be obtained from ref[92].

Figure 6.4 shows the flowchart of the control program. The first step in the program is to define the labels. The labels used are POINTER1, the starting address of the step-rpt area, POINTER2, the starting address of the mode-period area, PGCR, PADDR, PACR, and PADR (port A data register). After initialisation of the related ports, the program sends out a signal to indicate the port is ready. The main part of the control program is given in Appendix G. In this program, address register A3 contains the address of PADR through which the PWM information is sent to the logic control unit. Address registers A4 and A5 contain pointer1 and pointer2.

At the beginning, the program loads the required number of steps into D7 using pointer1, after which pointer1 is incremented. The new value of pointer1 gives the location at which the number of modes for the first step is stored, and the following location contains the number of repeat times for this step. This continues for the remaining steps. After the number of modes for a new step is loaded to D0 and the number of repetition for this step is loaded to D2, a new cycle is started. First, the number of modes is stored in a temporary data register D1 for subsequent count down, then pointer2 in

A5 is stored in A6 as a temporary pointer. In each mode, after the mode and the period of the mode have been loaded, the temporary pointer (A6) is increased by 2. When the mode is output to the port, the period of this mode is counted down to zero. After each mode, D1 is decremented and is checked to see if it contains -1. If the check is negative, the program goes back to the label (MODE), and the next mode is continued. Otherwise, the number of repeat times in D2 is checked. If D2 does not contain -1, the program goes back to the label CYCLE and the same step is repeated. Otherwise, the temporary pointer (A6) is saved to A5 as the starting pointer of a new step. Finally, the number of step in D7 is checked. If it does not contain -1, then the program goes back to the label REPEAT. Otherwise, PWM generation is completed, and the program sends out a signal to indicate the port is closed.

Note that the numbers followed by each instruction in the quoted program indicate the execution time of that instruction in machine cycle (10MHz). The execution time for each mode is T_m = 5.6 us, for each cycle it is T_c = T_m + 3.2 us and for each step it is T_s = T_c + 5.8 us. All these times have been deduced at the appropriate position when the look-up table was transferred by the program TRANSLUT.

6.5 Logic control unit

As shown in section 5.3, the on-off states of the three-phase inverter switching devices are described by three binary bits. Each bit corresponds to one phase. These three bits are output through the PA1-3 lines of the 68230 port A. In order to control all six switching devices in the inverter, these three signals must be separated into six. Moreover, each switching device has a switching, or delay, time. For safety reasons, before one device is fully switched off, the other on the same phase leg should not be switched on. The main task of the logic control unit is to solve the above problem.

The signal separation can be carried out by using SN74LS04 inverters. The switching time problem was solved by using monostable multivibrators (SN74121). The SN74121 device features negative transition triggered inputs. Once triggered, the outputs are independent of further transitions at the inputs and are a function only of the timing components. By choosing appropriate timing components, the output pulse length may be varied from 40 nanoseconds to 28 seconds. Figure 6.5 shows a SN74121 circuit with its timing diagram. With the timing components as shown, the maximum pulse length of 33 microseconds can be achieved (T = 0.7RC). This pulse is long enough to cover the GTO switching time.

Figure 6.6 shows the diagram for the logic control unit. The corresponding timing waveform is shown in Figure 6.7. The output lines PA1-3 of 68230 port A are used for the phases A-C. These three signals are first buffered by a SN7404 which protects the 68230 PIT. The first three inverters in the SN74LS04 ensure that the outputs A1, B1, and C1 of the control unit are in the same phase sequence as the outputs PA1, PA2, and PA3. Label A is used to mark the input of the delay device (SN74121). Since this device has a switching time, an even number of inverters in the 74LS04 which are located in parallel with 74121 are used to make up the time losses. Therefore, the phase at point A is the same as at point A22, and the phase at point $\overline{A}$ is the same as at point A12. The output phase A1 of the control unit is the AND of the signals at A11 and A12, and phase A2 is the AND of those at A21 and A22.

At power-on of the 68000 SBC, the 68230 PIT and the logic control unit, the red and yellow LEDs are on. The yellow LED indicates the power-on of the 68230 PIT and the logic control unit. Since at power-on, the data register of the 68230 port contains logic '0', the red LED is on. Once the port ready signals (switching between logic '0' and '1') are sent out to PA0, the red LED flashes for 10 seconds. Normally, the gate locker K2 is kept closed. This ensures that all the output gates of the logic control unit are closed. Hence, no firing

to the GTO inverter by accident can occur. When the red LED is flashing, the locker K2 should be opened to open the output gates. This is indicated by the on state of a green LED. At the completion of PWM generation, the red LED flashes again for 10 seconds. During this time, the locker K2 should be closed.

Note that the port line PA7 is used as the triggering signal line when measurement is required. This will be described in the next section.

6.6 GTO inverter and gate driver

The selection of the GTO devices is determined by the load which the GTOs are required to drive. The load used is a 3kW delta-connected induction motor. When 220 V is applied to the terminals, the rated line current is 11.77A. Considering the maximum operating duty-cycle of a GTO in a three-phase inverter is less than 50%, the rated current of the required GTO must be greater than 6A (rms). Amongst the standard general purpose devices, the current rating of the BTW58 is 6.5A (average); BTV58 is 10A; and BTV59 is 13.5A. The voltage ratings of these GTOs are in the range of 600-1500V (repetitive peak off-state voltage). In selecting the voltage ratings, a trade-off must be made between the costs of GTOs and the snubber circuits. From the above considerations, the BTV58-1000 device was selected.

In constructing a GTO inverter circuit, two important GTO characteristics must be considered. The first is the reverse characteristic, since the device is incapable of blocking voltage, even a few volts, or conducting significant current. When reverse conduction is required, such as in AC drives, a diode must be connected in anti-parallel with the GTO. The second point is that the rate of rise of the voltage between anode and cathode (dV/dt) must be limited to a maximum value. Normally, the higher the peak anode current that must be switched off, the lower the allowable dV/dt. To limit the dV/dt value, a snubber capacitor must be connected across the GTO. For the laboratory system, the type of the diode is BY329, and the parameter of the snubber capacitor is 22nF. Full details are given in [93]. Note that unlike thyristors, due to the internal gate structures, low power GTOs do not require the maximum di/dt value to be controlled.

The GTO operates with very short switching times for both turn-on and turn-off (less than 2 us for the BTV58). To achieve this performance in practice, the GTO gate drive circuit must be designed correctly.

To turn the GTO on, a positive current must be injected into the gate for the duration of the turn-on time. Each GTO component has its own required gate

current. Once turned on, the GTO gate current can be removed. Continuous present of the gate current, however, ensures that when the GTO anode current reduces below the latch current, the GTO remains on

GTO turn-off is achieved by drawing from the gate a current pulse between 20 and 100% of the anode current for a few hundred nanoseconds. This is done by applying a negative voltage between -5 and -10V directly between gate and cathode, normally with a charged capacitor. The highest controllable anode current is determined by the highest gate turn-off current. To obtain a high gate turn-off current with a suitably charged capacitor voltage, the impedance in the turn-off loop must be kept as low as possible. In particular, the stray series inductance must be minimised.

Depending on the specific application, the GTO gate drive circuit can be either non-isolated or isolated. A practical non-isolated gate drive circuit is shown in Figure 6.8. The main features of this circuit are that it is simple and low cost. However, being non-isolated, it is unsuitable for A.C. drive application. A simple isolated gate drive circuit using a pulse transformer may only be used in applications in which the switching frequency is in the range of 10-40kHz. An isolated gate drive circuit with wide switching frequency range (DC-

5kHz) can be constructed with much higher cost and is more complex [94].

Instead of using a pulse transformer, the input control signal of the gate drive circuit can be isolated by an opto-isolator. Figure 6.9 shows one of such devices (TIL111) together with its TTL interface. The simple non-isolated gate drive circuit shown in Figure 6.8 can then be used for A.C. drives when such an opto-isolator is applied to the input of the drive circuit. In addition, the supplies for each of the top three GTO drive circuits in the inverter must also be isolated. The bottom three GTO drive circuits can use a common supply. Thus four isolated supplies are required. Figure 6.10 shows the circuit diagram for such supplies. Since the input current rating of the gate drive circuit is less than 200 mA, the regulators in the top three supplies are rated at 500 mA (78M15) and the regulator in the fourth supply is rated at 2 A (78S15). The fifth supply is used for the triggering circuit, as explained later.

The TTL signals (A1-A6,PA7), together with a 5V supply from the output of the logic control unit, are sent to the input of the isolating circuits as shown in Figure 6.9. The output of this circuit leads to the input of the gate drive circuits as shown in Figure 6.8. The supplies for the output of the isolating circuits

are 5V isolated supplies as shown in Figure 6.10. The 15V terminals in the isolated supplies are used for the gate drive circuits.

6.7 Simulation of train inertia

The design of the flywheel used to simulate the train inertia is based on the ratio of the motor output torque to the equivalent train inertia referred to the motor axle. The motor rated output torque for the practical system is 890 Nm. The total inertia of the three-car train referred to the wheel axle is 18,000 kgm^2 (neglecting the wheelset and axle inertia). This inertia divided by eight, the number of motored axles, giving 2,250 kgm^2.

Conversion of inertia from wheel axle to motor shaft can be made with regard to the constant power value before and after the conversion. If T_e and T_w are the torques at motor and wheel shafts, then the power is given by

$$P = \omega_r T_e = \omega_w T_w \qquad (6.1)$$

where ω_r and ω_w are motor and wheel speeds. From dynamic equations

$$T_e = J_m d\omega_r/dt$$

$$T_w = J_w d\omega_\omega/dt \qquad (6.2)$$

it can be shown that

$$T_e = J_w/G^2 * d\omega_r/dt$$
$$J_m = J_w/G^2 \qquad (6.3)$$

where J_m, J_w are train inertias referred to motor and wheel shafts, and $G = \omega_r/\omega_w$, the motor/wheel speed ratio. Using eqn. 6.3, J_m = 105.6 kgm^2 is obtained. Hence, the torque/inertia ratio is 890/106 = 8.4 for the practical system. If the rated output torque of the 3 kW induction motor is 20 Nm, then the equivalent flywheel inertia is 2.38 kgm^2.

A flywheel with 1.0 kgm^2 inertia was selected. The value of 1.0 kgm^2, which is less than half of the equivalent inertia, accounts for the wound DC machine inertia. The conservative design is also due to the mechanical safety reason, since the maximum motor speed can reach near 1500 rpm.

6.8 Simulation of train resistance

The train resistance is simulated by a DC machine. The value of the resistance torque produced by the machine may be calculated from the ratio of the rated torque to the equivalent resistance torque referred to

the motor shaft in the case of the practical system. The train resistance calculated in section 2.5 multiplied by the wheel radius gives the resistance torque referred to the wheel axle. The torque convertion from wheel axle to motor shaft is shown in eqn. 2.16.

As shown in Figure 2.10, the train resistance varies with train speed. For simplicity, the maximum resistance from the practical system was converted to the small system resistance at the rated motor speed. The maximum total train resistance is about 5000 N and when divided by 8 (the number of motored axles) the value is 625 N. The resistance torque referred to the wheel is 625*0.4 = 250 Nm. The resistance torque referred to the motor shaft is 500*13/60 = 54 Nm. So the ratio of the rated torque to the resistance torque is 890/54 = 16.5. If the rated torque of the 3 kW induction motor is 20 Nm, the resistance torque required is 20/16.5 = 1.2 Nm.

The machine used to produce the resistance torque is a separately-excited DC generator, the equivalent circuit of which is shown in Figure 6.11. The ratings and parameters of this machine are in Appendix B.

The open circuit armature voltage (the induced electromotive force, EMF) is given by

$$E_a = k_1 \psi \omega_r \qquad (6.4)$$

where k_1 is constant, ψ is the flux produced by the field current, and ω_r is the rotor speed. The magnetisation curve of the machine is shown in Figure 6.12, with the rotor speed kept constant at the rated value of the induction motor. The rated field current, I_f = 1.25 A, was measured at E_a = 240 V.

If T is the resistance torque produced by the machine, the supplied mechanical energy is equal to the consumed electrical energy

$$T\omega_r = E_a I_a \qquad (6.5)$$

where $T = k_2 \psi I_a$, k_2 is constant. The armature equation is

$$I_a = E_a/(R_a+R_1) \qquad (6.6)$$

Substituting (6.6) into (6.5)

$$T = (k_1\psi)^2\omega_r/(R_a+R_1) \qquad (6.7)$$

At rated speed, $k_1\psi$ (= E_a/ω_r) was measured to be 1.53 [V/(rad/s)]. Thus in order to produce 1.2 Nm resistance torque, R_1 should be 304 ohms.

6.9 VSI-SCIM drive and instrumentation

The voltage source inverter - squirrel cage induction motor drive consists of an induction motor, a GTO inverter, a DC input filter, a power diode rectifier, and an auto-transformer. The detailed system circuit diagram is shown in Figure 6.13. In order to reduce the operating voltage, the stator of the induction motor is delta-connected. Therefore, if the rated line voltage is 220V, the DC link voltage should be 282V, and the output of the auto-transformer should be 209V. The output ratings of the auto-transformer are 20A and 240V. The ratings of the power diode for the rectifier are 40A (maximum mean forward current) and 1200V (repetitive reverse mean voltage). The 4.2 mF capacitor is used to stabilise the rectifier output. The parameters of the LC filter components are 9 mH and 1.8 mF.

The system variables to be measured are the electrical and mechanical. Both DC and AC voltages are directly measurable and recorded by an oscilloscope. The DC and AC currents are measured through a current transducer using a Hall effect device. The output of the transducer is sent to the oscilloscope. The mechanical variables are the induction motor output torque and the motor shaft speed.

When measuring the electrical variables, the trigger signal from the logic control unit (PA7) is isolated first as shown in Figure 6.9. After the initialisation,

port line PA7 contains logic '0'. At the beginning of the output of the first PWM signal, PA7 is set to logic '1'. This positive slope signal is used to trigger the oscilloscope.

A torque transducer was used to measure the induction motor output torque. This transducer was first calibrated by an AVERY torsion machine. The details of the transducer are given [95,96]. The motor speed was measured by a DC tacho-generator [97]. The calibration of this tacho-generator was carried out by installing a metal disc along the motor shaft, with 30 small holes equally located round the edge. The signal from a slotted opto-switch (TIL138) was recorded by a digital pulse counter. By reading the number of pulses, the tacho-generator output voltage can be calibrated.

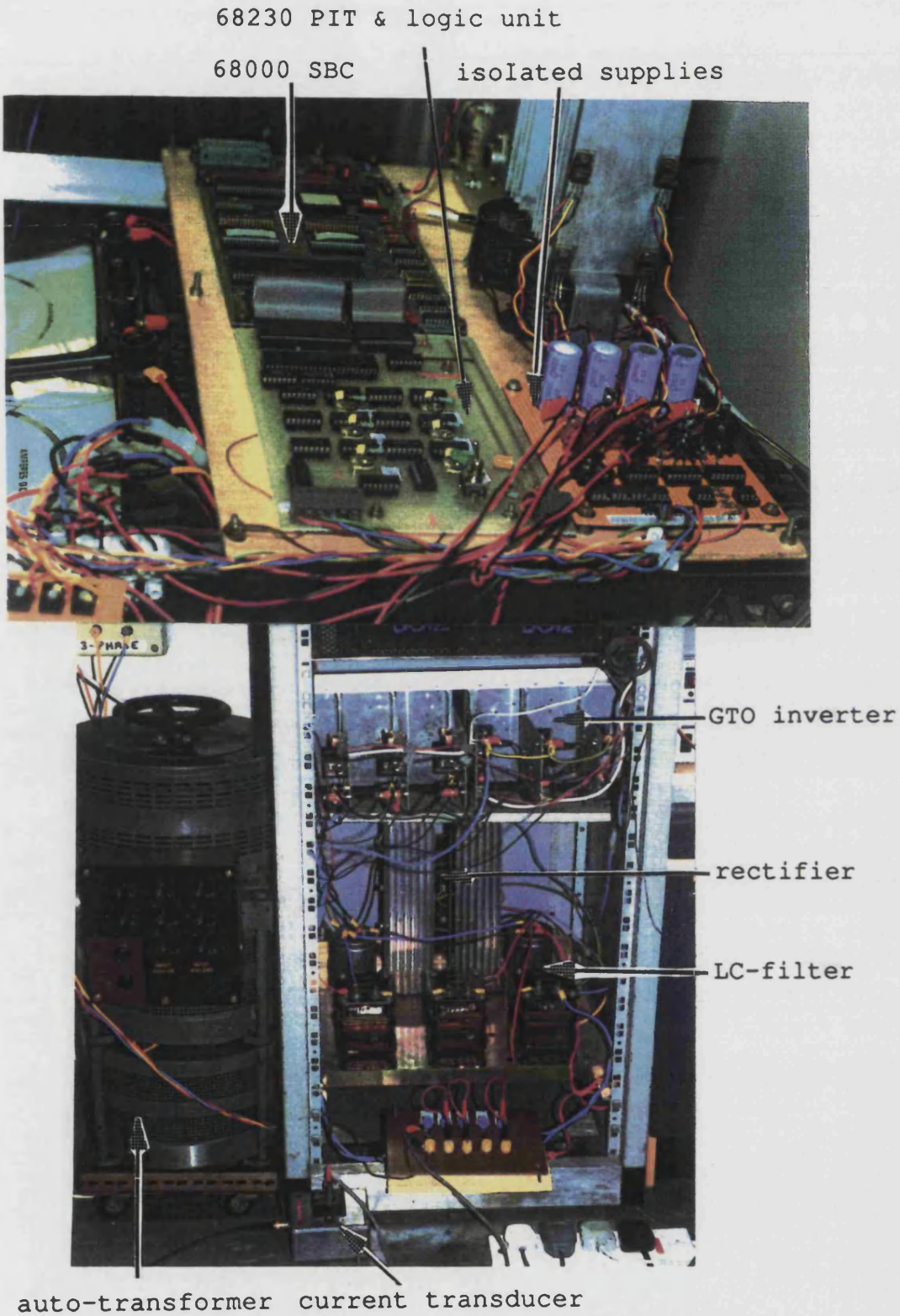

(a) control section

Figure 6.1 Photograph of VSI-SCIM drive

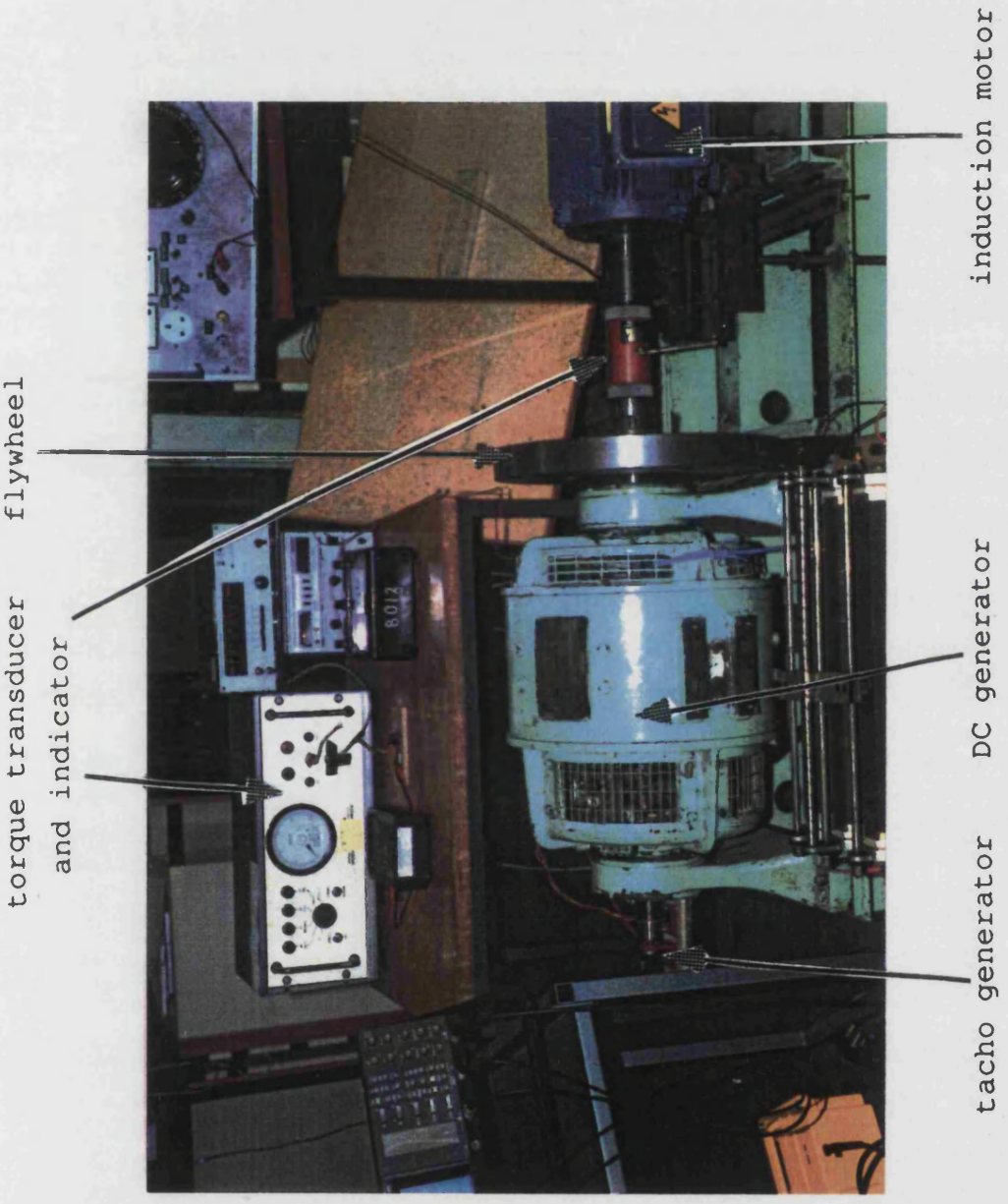

(b) driving section

Figure 6.1 Photograph of VSI-SCIM drive

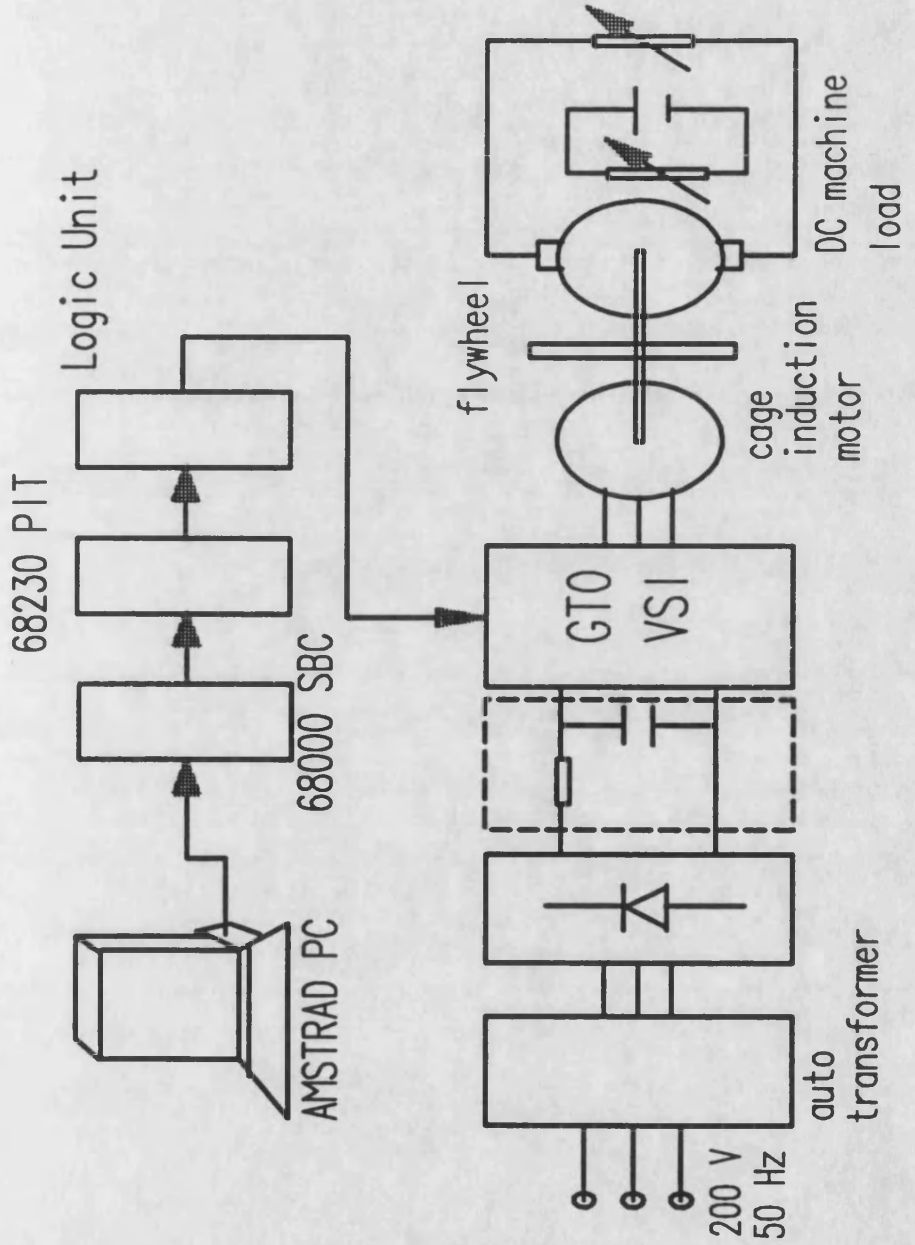

Figure 6.2 Block diagram of VSI-SCIM drive

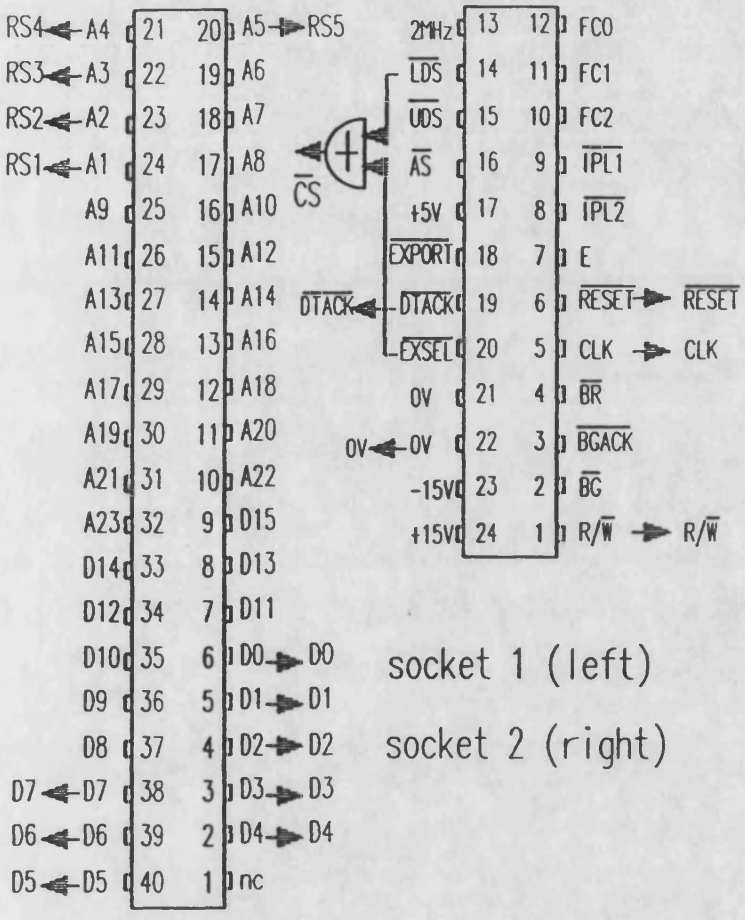

Figure 6.3 Interface between
68000 SBC and 68230 PIT

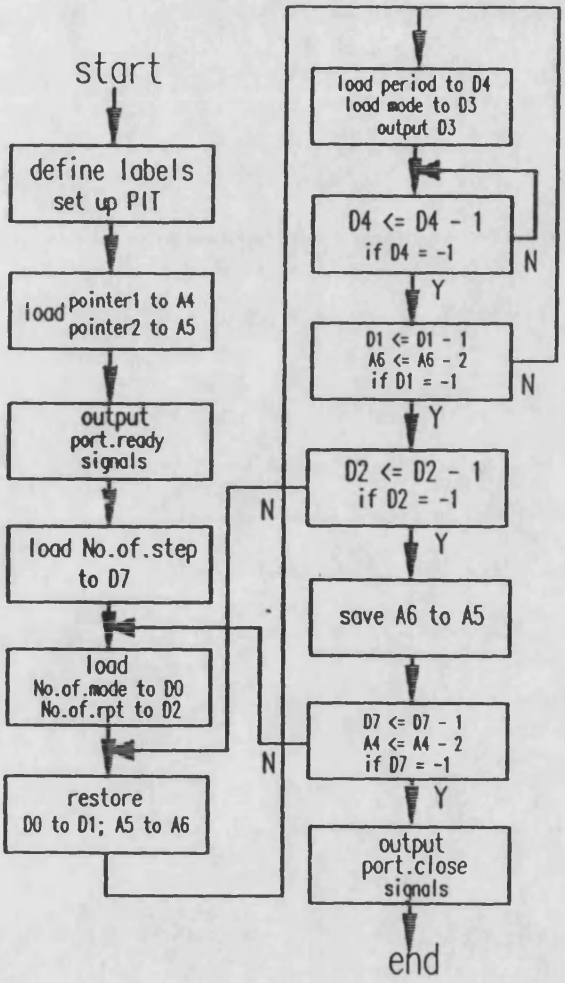

Figure 6.4 Flowchart of control program

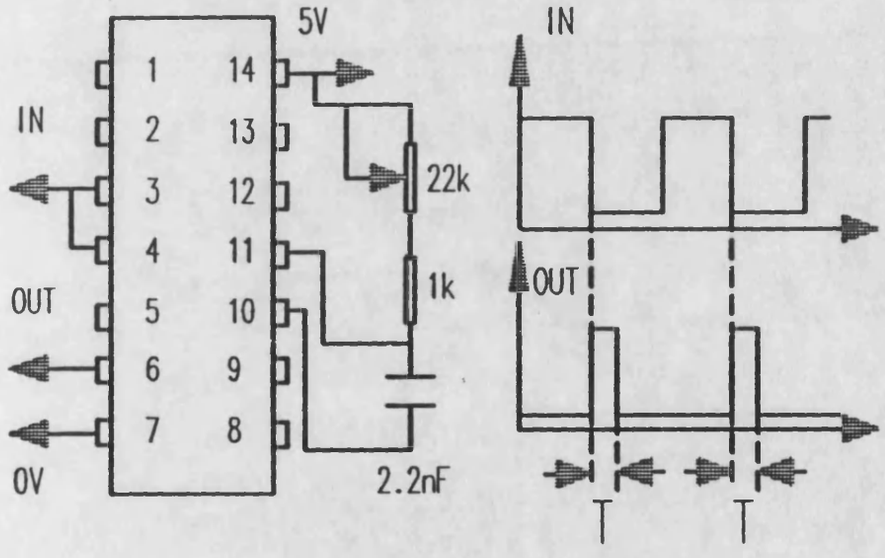

Figure 6.5 74121 circuit and timing

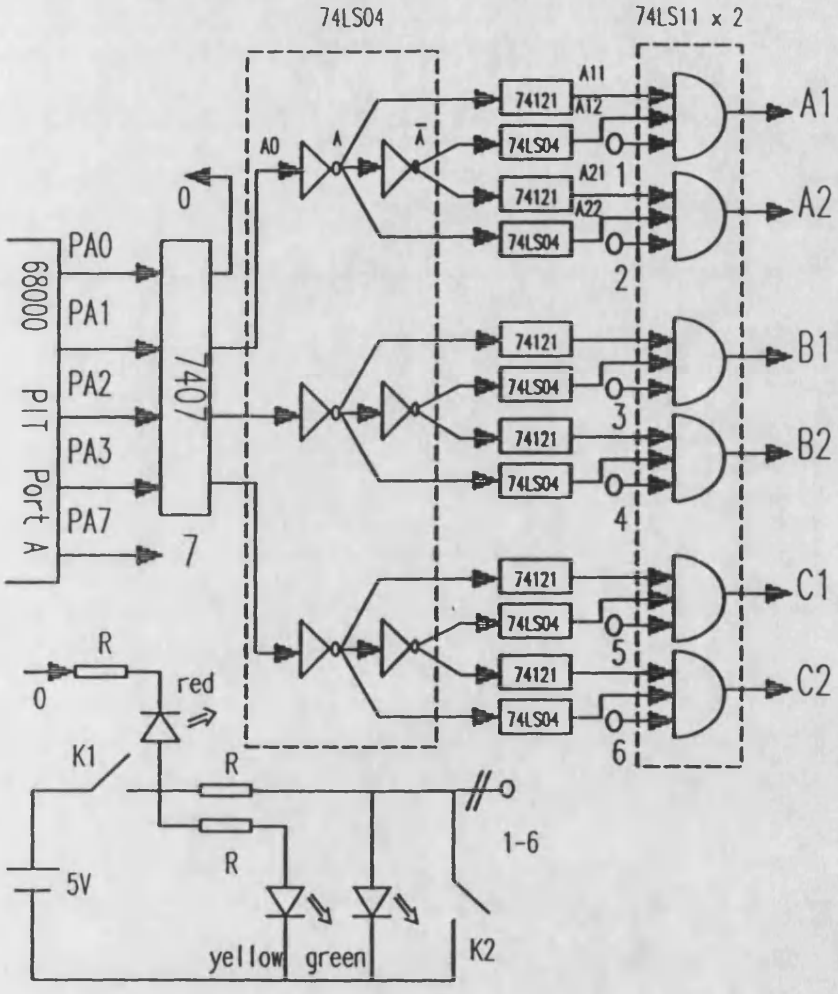

Figure 6.6 Logic control unit diagram

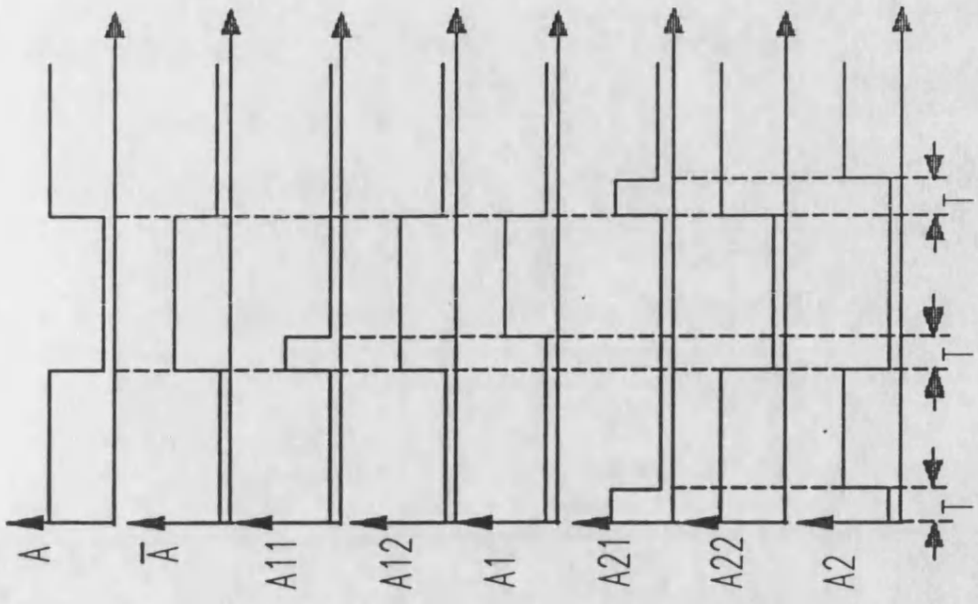

Figure 6.7 Generation of switch-on delay

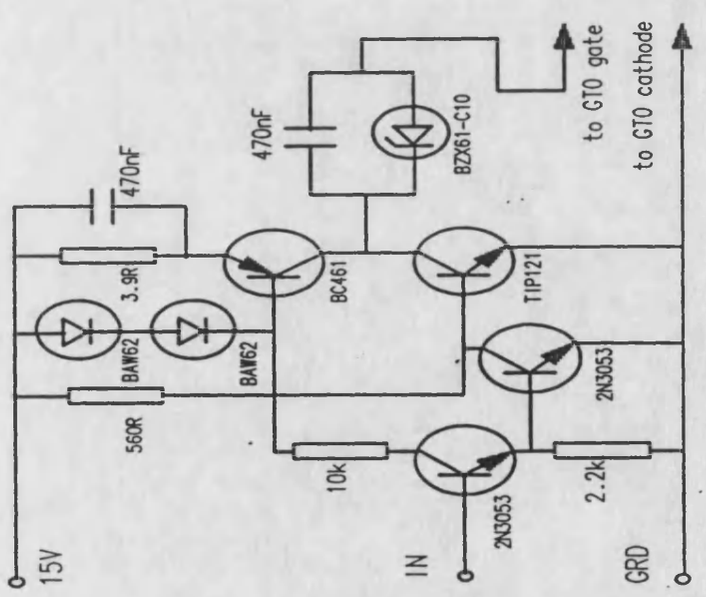

Figure 6.8 GTO gate drive circuit

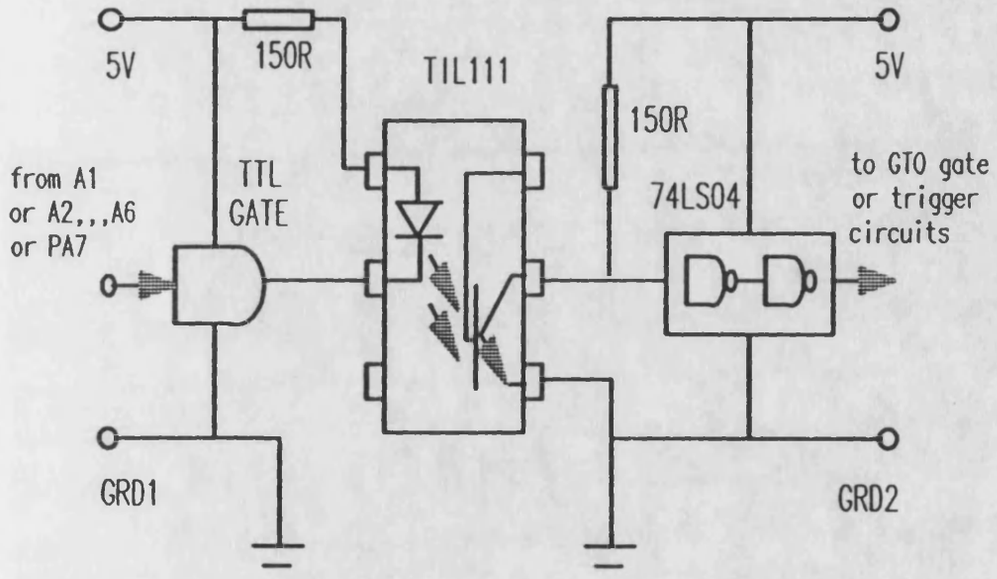

Figure 6.9 Signal isolating circuit

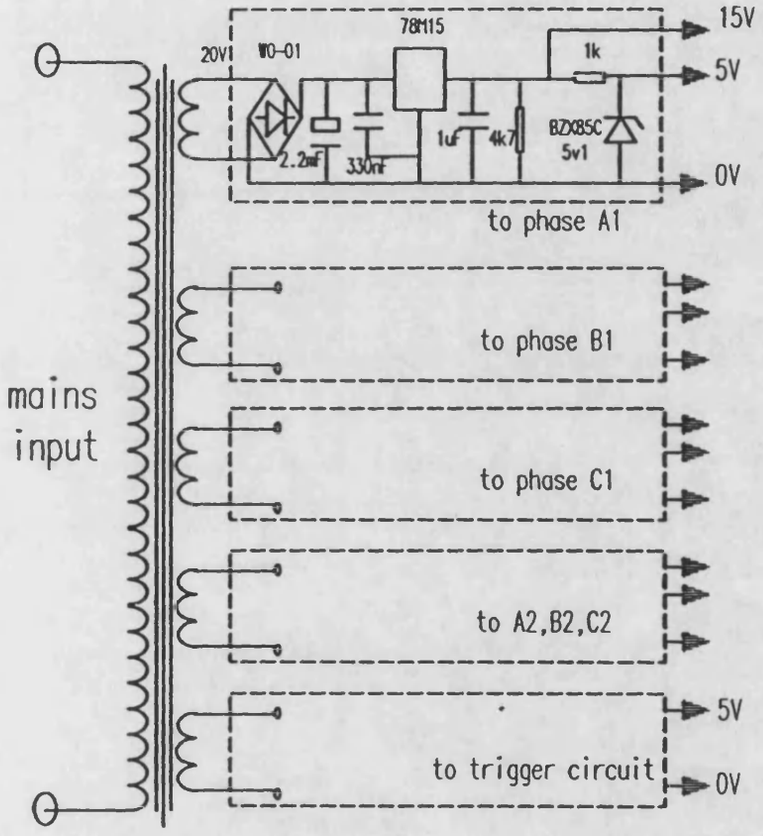

Figure 6.10 Isolated supply circuits

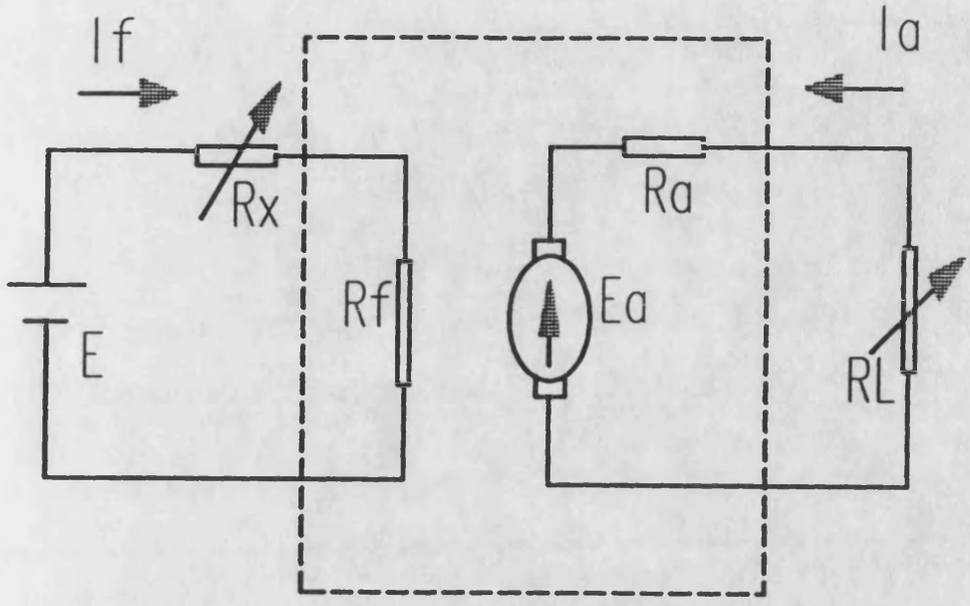

Figure 6.11 DC generator equivalent circuit

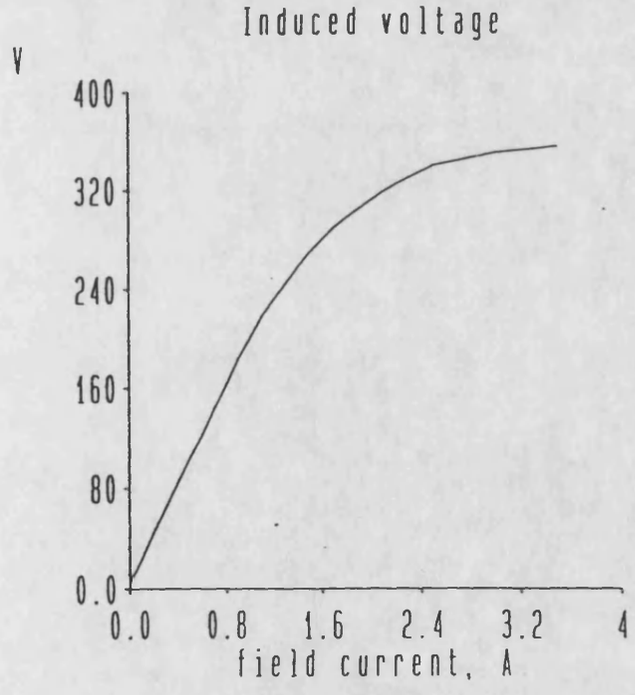

Figure 6.12 Magnetisation curve

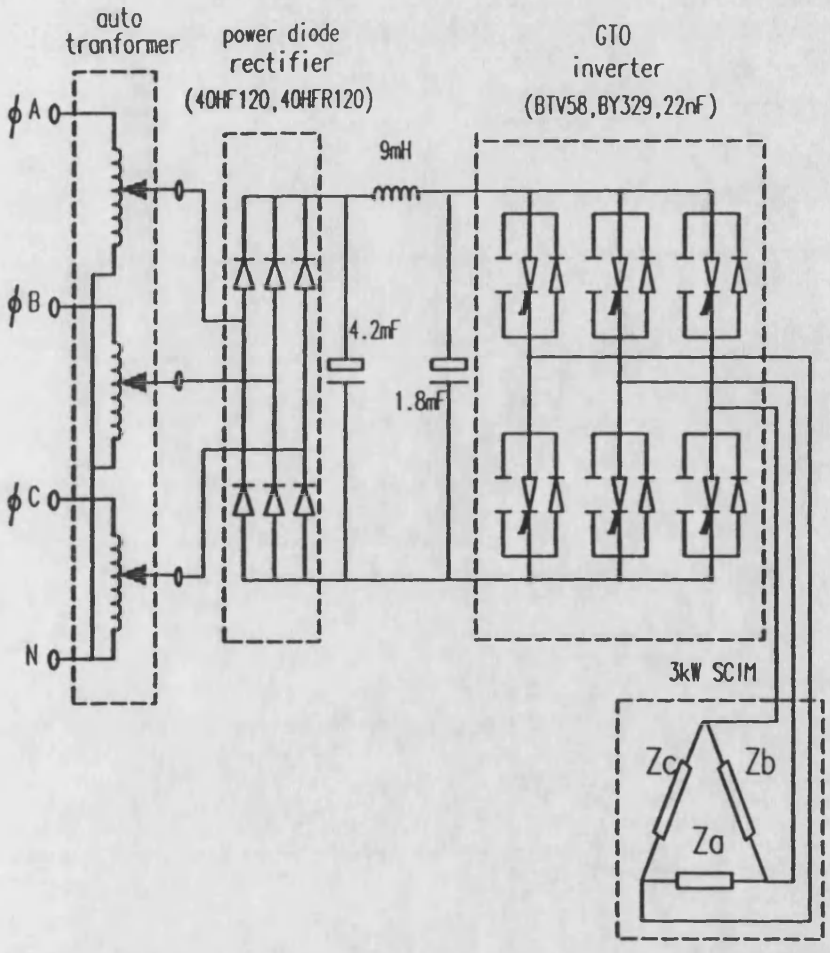

Figure 6.13 Laboratory based

VSI-SCIM system circuit

Chapter 7 : Simulator verification

7.1 General

In this chapter, the simulator is verified by comparing simulated and experimental results for the 3 kW laboratory based system. The system parameters are given in Appendix B. For both the simulation and the experimental verification, the induction motor was delta-connected, and only synchronous PWM scheme was used with the frequency varying from 2.667 Hz to 50 Hz.

The system input look-up tables for the simulation and the experimental verification are given in Tables 7.1 and 7.2 respectively. The columns in the table give the number of frequency steps, the terminating time for each frequency step, the frequency and the number of repetitions for each step.

For the simulation, the system DC supply voltage was 282 V, the rated motor line voltage was 220 V, the rated line current was 11.78 A and the rated motor output torque was 20 Nm. The train inertia was assumed to be 2.0 kgm^2 and the train resistance was designed to increase from zero to 2.0 Nm (10% of 20 Nm).

In the experiment, the system DC supply voltage was 75 V which was obtained from a three-phase auto-

transformer through a three-phase rectifier. The reduced DC supply voltage takes account of the flywheel (1.0 kgm^2) which has an inertia less than half of that calculated. It is also reduced because the dV/dt controlled by the simple capacitor snubber circuit is at a critical value. Otherwise, a more complex snubber circuit must be employed.

With 75 V DC supply, the equivalent motor line voltage was 58.5 V, the expected line current was 3.13 A and the expected motor output torque was 1.43 Nm. The total mechanical system inertia was about 1 kgm^2 and the system load produced by the DC machine was designed to increase from zero to 0.5 Nm. Note that the system friction was about 0.2 Nm at no load. The total system resistance torque was about 50% of the tractive torque. The acceleration rate was about a factor of 10 smaller than that designed for the simulation. Therefore, the operation time for the experiment was about 10 times longer than the simulation time.

7.2 Comparison between simulated and experimental results

Comparison between experiment and simulation was carried out for three aspects of operation: the system general performance, the behaviour at gear changing and

pulse dropping, and the harmonic content of certain system variables.

Figure 7.1 - 7.6 present the general waveforms of the system variables. If the ripple on the system input current in Figure 7.1-b is ignored, the waveform pattern of the system input current from the experiment is in agreement with that from the simulation given in Figure 7.1-a. The ripple is due to the introduction of inductance from the auto-transformer and the rectifier output capacitor. This was verified by additional simulation results obtained with the addition of an inductor and a capacitor (Appendix H). Moreover, it seems that the system input current in the experimental results shows instability at certain frequencies. The reason may be because at certain transition points, the supply frequency increases but the rotor speed cannot follow instantaneously, with the result that the operating point may enter the unstable region as indicated in Figure 4.8-c.

The same phenomenon can be observed from the DC link voltage as shown in Figure 7.2-a and -b. Since the source output impedance of the experimental drive is larger than that of the simulation system, the drop in DC link voltage at each frequency step is greater.

Figure 7.3-a and -b shows the DC link currents. The minimum current from the simulation results during the last five steps is greater than zero. This may be because during this period, the number of pulses per cycle is reduced. Consequently, the number of times the inverter operates in mode 7 is reduced per cycle. In the extreme case, for square wave operation, no mode 7 at all appears. Note that only in the case of mode 7 can the DC link current be zero, in which case the machine is totally separated from the inverter. Since the GTOs are controlled such that the switch-on time is always delayed by a certain time to avoid short circuit in a single phase, this results in the possibility that on some occasions, even though there is no actual mode 7, the machine will become separated from the inverter.

Figure 7.4-a and -b shows the motor line current. Due to the large number of repeat times at high supply frequency, only the first five frequency steps from the experimental result are presented together with expansion of the first few cycles. For the first few frequency steps, the experimental current variation patterns are almost the same, while the simulated patterns are irregular. This is because the number of repeat times for each frequency step in the experiment is much larger than that in the simulation as shown in Tables 7.1 and 7.2.

Figure 7.5-a and -b shows the motor output torque. In measuring the experimental torque, a large number of harmonics were observed. The result shown is that which was "filtered" by the oscilloscope. However, the general pattern is still in agreement with that simulated. Like the case of motor line current, for the first few frequency steps, the simulated torque pattern is irregular due to the limited number of repetitions for each step. With the increase of frequency, the harmonic current decreases due to increase of motor reactance. Consequently, the harmonic torque is reduced. This is verified in the simulated result. Since the torque transducer introduces mechanical noise harmonics, it is not capable of measuring the harmonic torque produced electrically.

Figure 7.6-a and -b shows the motor output speed. Again the experiment result is in agreement with the simulated case. From Figure 7.6-b, it can be seen that there is mechanical noise on the speed signal. This noise may be produced by mechanical bearings and friction, or by mechanical resonance. It is also seen that during each frequency step, the motor speed reaches a maximum value and keeps this value for the rest of the step. This means that the total driving time is longer than required. The extra time ensures that the motor slip is always under control. Hence the motor current will not exceed the limit.

Figure 7.7 shows the simulation results of a gear change at time = 4.669 s where the modulation ratio M_r changes from 15 to 9. Figure 7.8 shows the experimental results of a gear change at time = 59.17 s with M_r changing from 15 to 9. These figures give an expended view of the general waveforms of the system variables at gear change points.

Figure 7.9-a gives the simulated inverter output phase voltage and its harmonic spectrum at time = 3.13 s where the supply frequency $f = 21.7$ Hz and M_r = 15. The harmonic number with the largest amplitude is 15, and the numbers with second largest amplitude are 29 and 31. This is as predicted in chapter 3.

The experimental results of inverter output phase voltage and its harmonic spectrum are shown in Figure 7.9-b, with f = 20.53 Hz and M_r = 15. As shown, the harmonic frequency with the largest amplitude is about 300 Hz which corresponds to harmonic number 15, and the those with second largest amplitude are about 600 Hz equivalent to harmonic number of 30±1. Figure 7.9-c gives the inverter line voltage and its harmonics. Comparing with Figure 7.9-b, the difference is that the dominating harmonic numbers at carrier frequency and its multiples (in triplen numbers) are cancelled in the line voltage.

Figure 7.10-a and -b shows the simulated and experimental DC link currents together with their harmonic spectra. The supply frequency and modulation ratio are the same as those in the inverter voltage case. The simulated result shows that the harmonic number with the largest amplitude is 30. This is in agreement with that from the experiment which is about 600 Hz. It is also shown that the DC link current harmonics always occur at harmonic number 6 and its multiples. The harmonic number with the largest amplitude is 30 which may be produced by the largest pair of motor line current harmonics at number 29 and 31, as predicted in chapter 3.

Figure 7.11-a and -b gives the motor line current and its harmonic spectrum. Again the condition is the same as above. It is clear that the fundamental component in both results is well above the harmonics. It is also shown that the harmonic amplitudes and their sequences from both results are in agreement. A detailed harmonic comparison between the simulated and measured motor line current is given in Tables 7.3 - 7.7.

Table 7.1 Time-Freq.-Repeat
for laboratory based system simulation
(synchronous PWM operation)

No.	Time	Freq.	Rpt.	No.	Time	Freq.	Rpt.
1	0.37495,	2.667,	1;	2	0.7735,	5.018,	2
3	1.03998,	7.505,	2;	4	1.47665,	9.16,	4
5	1.89828,	11.86,	5;	6	2.31347,	14.45,	6
7	2.72542,	16.99,	7;	8	3.08439,	19.5,	7
9	3.49961,	21.68,	9;	10	3.87185,	24.18,	9
11	4.28834,	26.41,	11;	12	4.66901,	28.9,	11
13	5.05417,	31.16,	12;	14	5.44302,	33.43,	13
15	5.835,	35.72,	14;	16	6.22965,	38.01,	15
17	6.62664,	40.3,	16;	18	7.02569,	42.6,	17
19	7.40434,	44.9,	17;	20	7.80804,	47.06,	19
21	8.2323,	49.5,	21				

Table 7.2 Time-Freq.-Repeat
for laboratory based system experiment
(synchronous PWM operation)

No.	Time	Freq.	Rpt.	No.	Time	Freq.	Rpt.
1	4.49944,	2.667,	12;	2	8.77555,	4.911,	21
3	13.4677,	7.033,	33;	4	17.9597,	9.35,	42
5	22.631,	11.56,	54;	6	27.183,	13.84,	63
7	31.853,	16.06,	75;	8	36.3836,	18.32,	83
9	40.9135,	20.53,	93;	10	45.5391,	22.7,	105
11	50.1155,	24.91,	114;	12	54.6576,	27.08,	123
13	59.1751,	29.22,	132;	14	63.4813,	31.35,	135
15	68.0498,	33.49,	153;	16	72.5978,	35.62,	162
17	77.1312,	37.72,	171;	18	81.7281,	39.81,	183
19	86.3093,	41.91,	192;	20	90.8775,	44,	201
21	95.4368,	46.06,	210;	22	99.9463,	48.12,	217

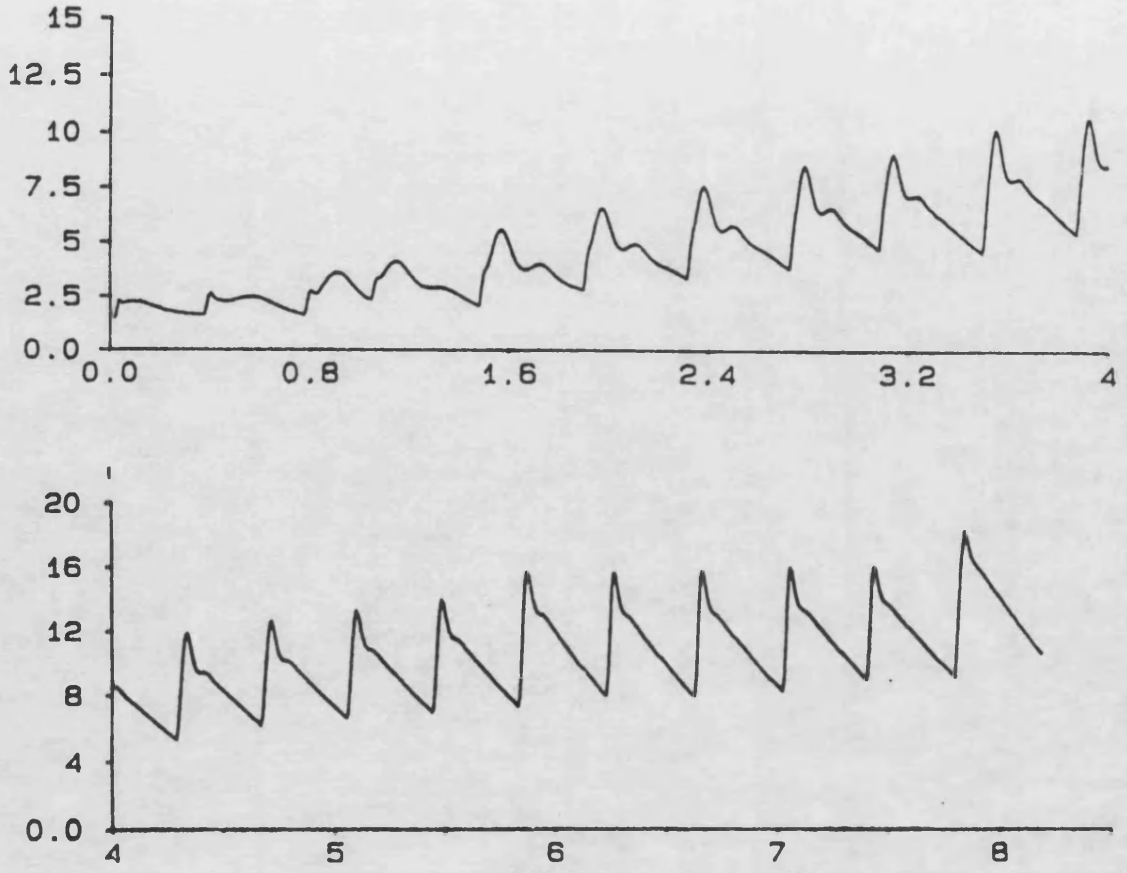

Figure 7.1-a System general performance simulation results

(system input current: A; time: s)

Figure 7.1-b System general performance experiment results

(system input current: 1 A/div; time: 5 s/div)

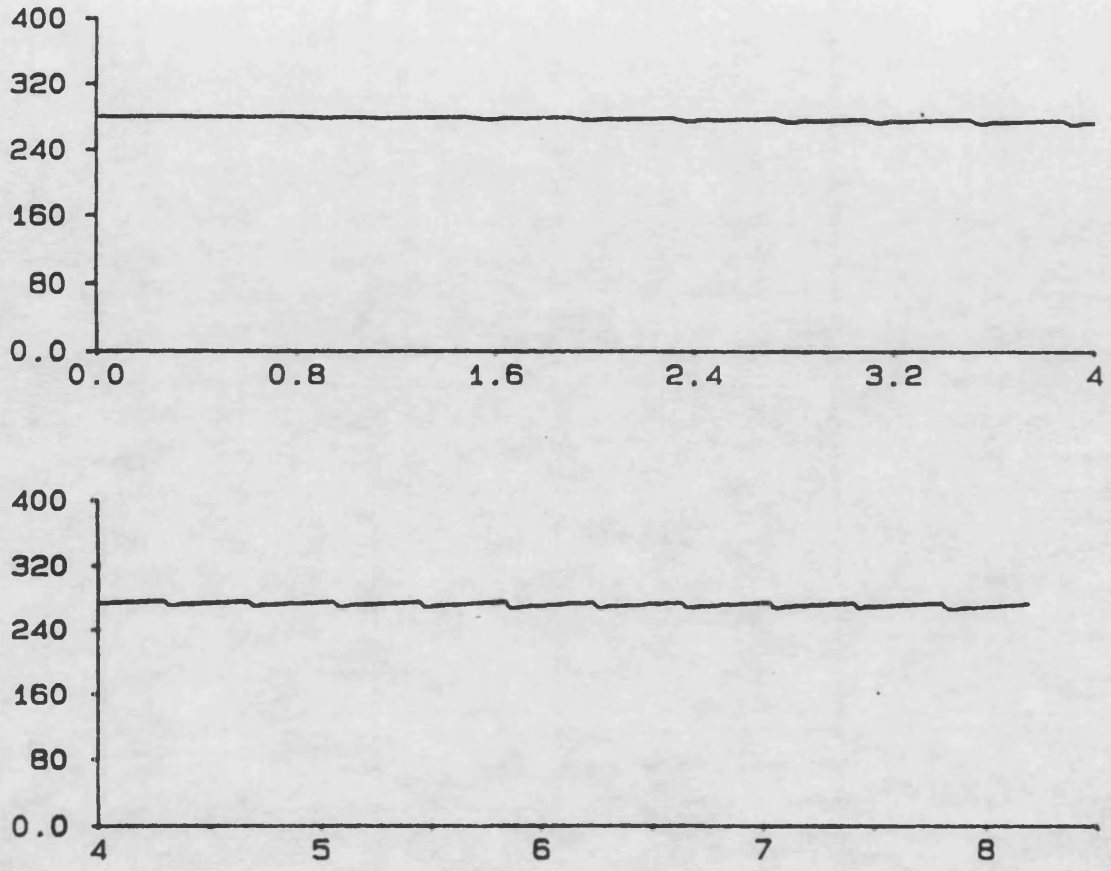

Figure 7.2-a System general performance simulation results

(DC link voltage: V; time: s)

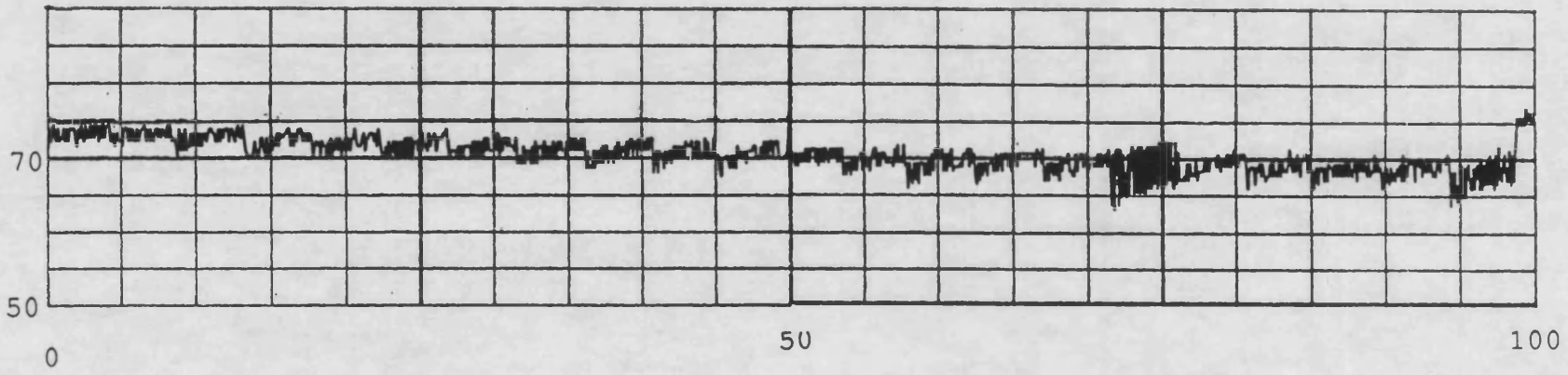

Figure 7.2-b System general performance

experiment results

(DC link voltage: 5 V/div; time: 5 s/div)

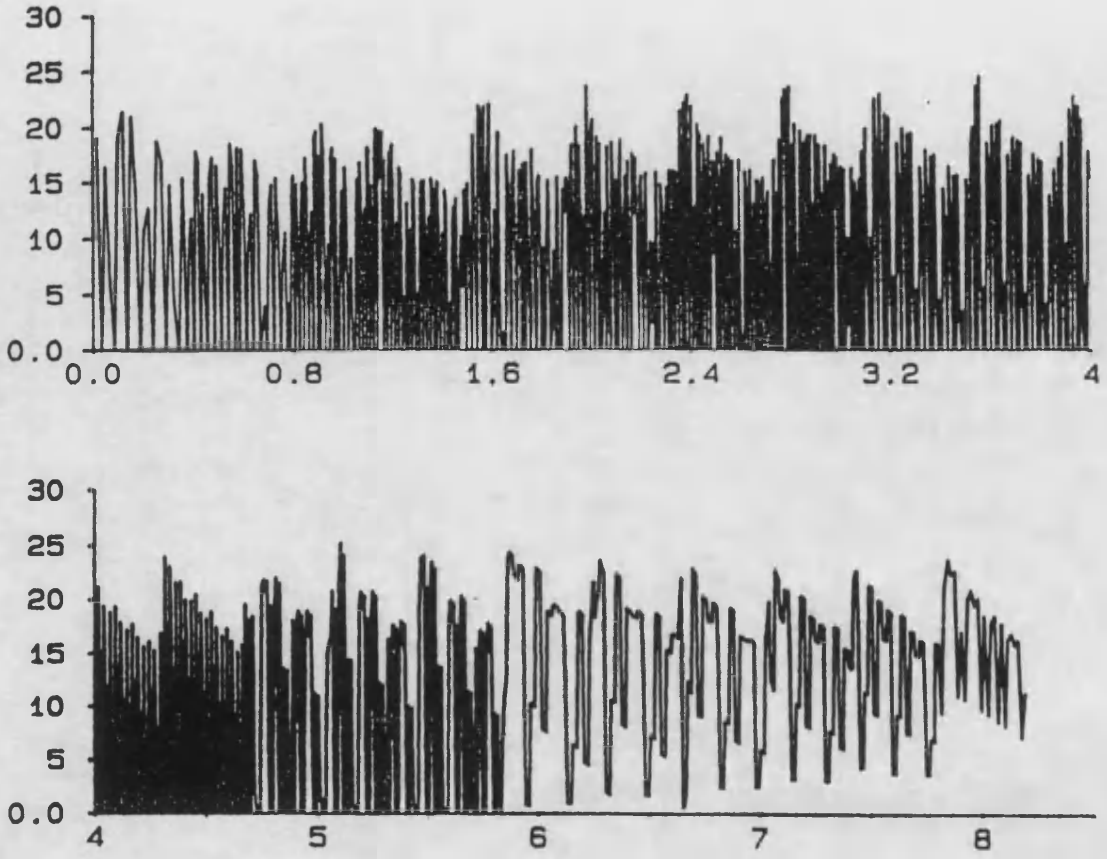

Figure 7.3-a System general performance simulation results

(DC link current: A; time: s)

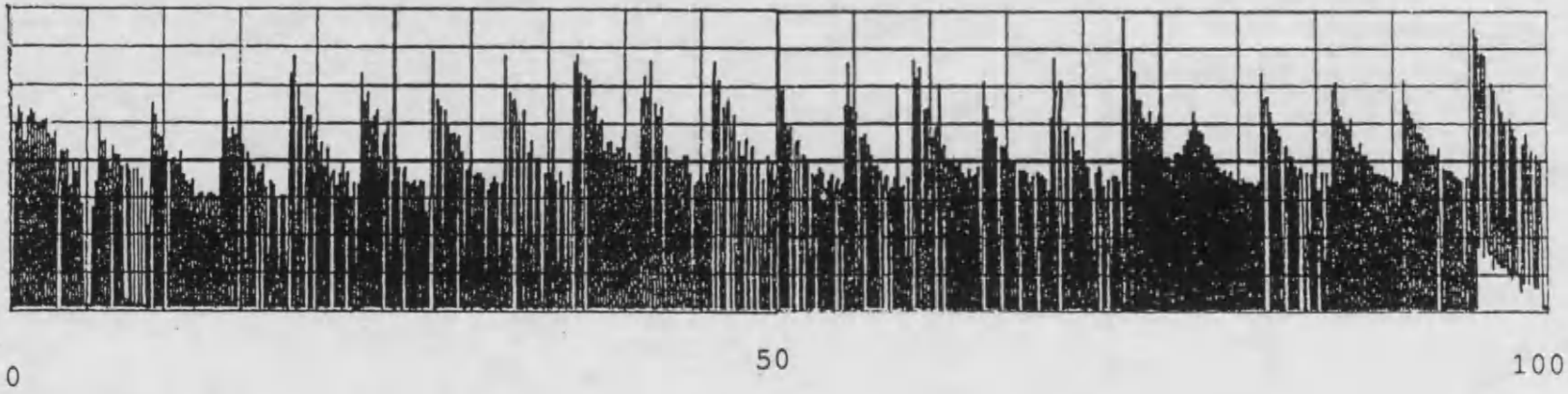

Figure 7.3-b System general performance experiment results

(DC link current: 1 A/div; time: 5 s/div)

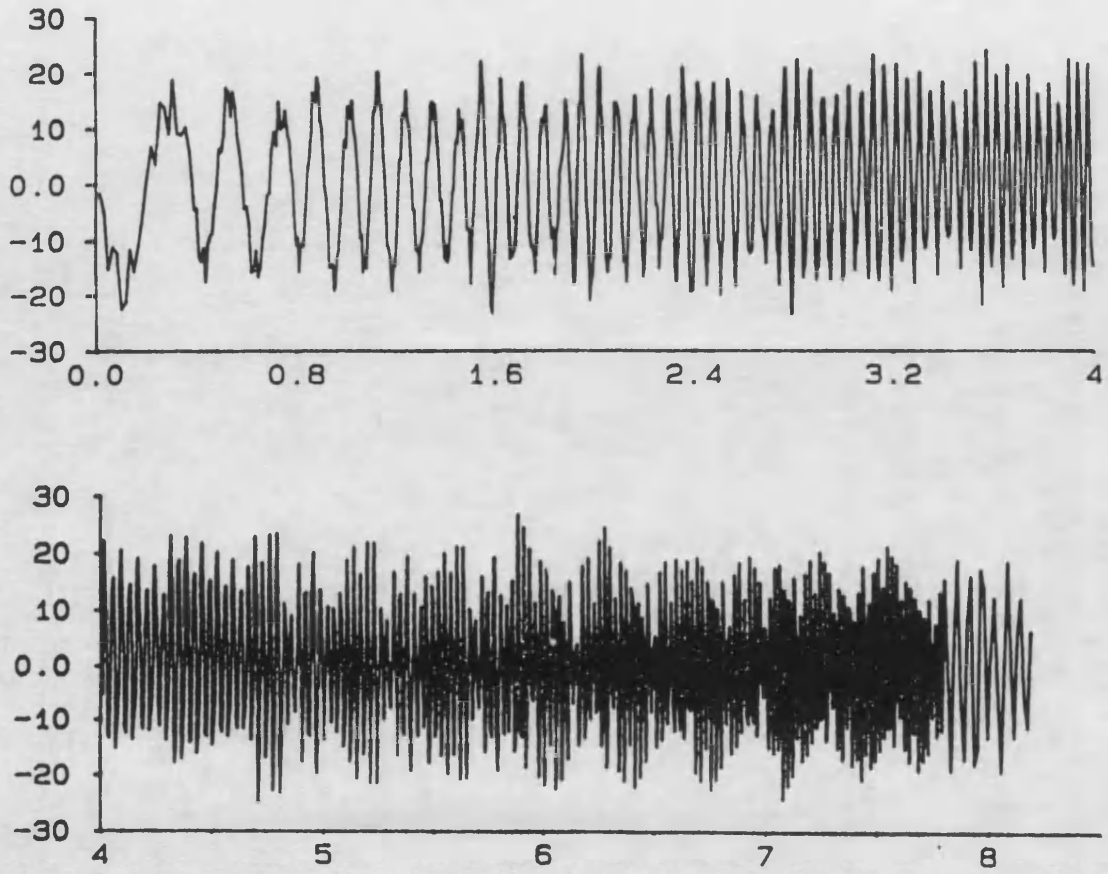

Figure 7.4-a System general performance simulation results

(motor line current: A; time: s)

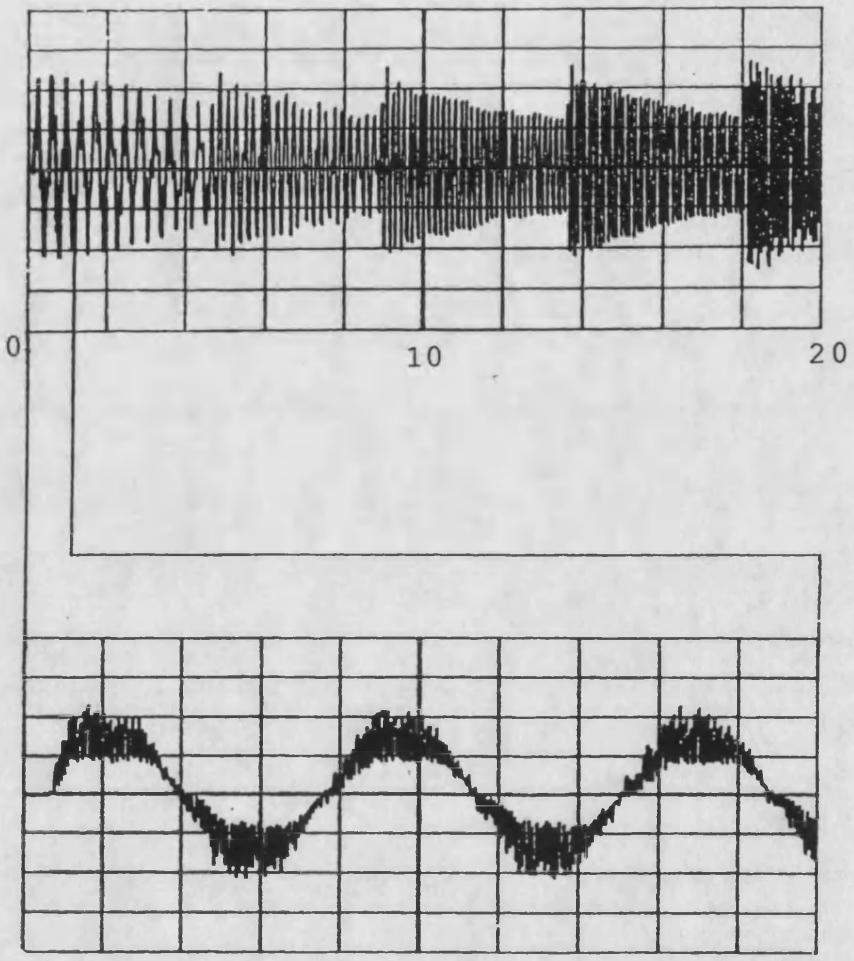

(expansion of the first few cycles)

Figure 7.4-b System general performance experiment results

(motor line current: 2 A/div; time: 2 s/div)

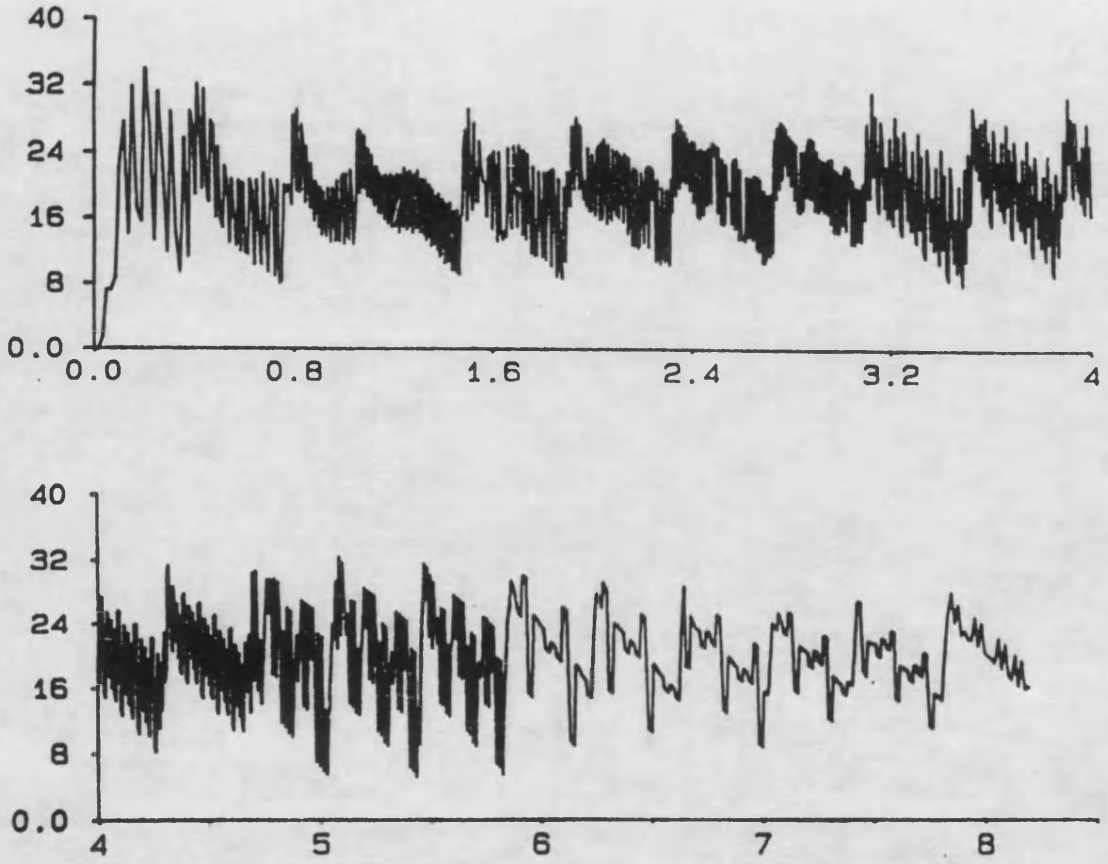

Figure 7.5-a System general performance simulation results (motor output torque: Nm; time: s)

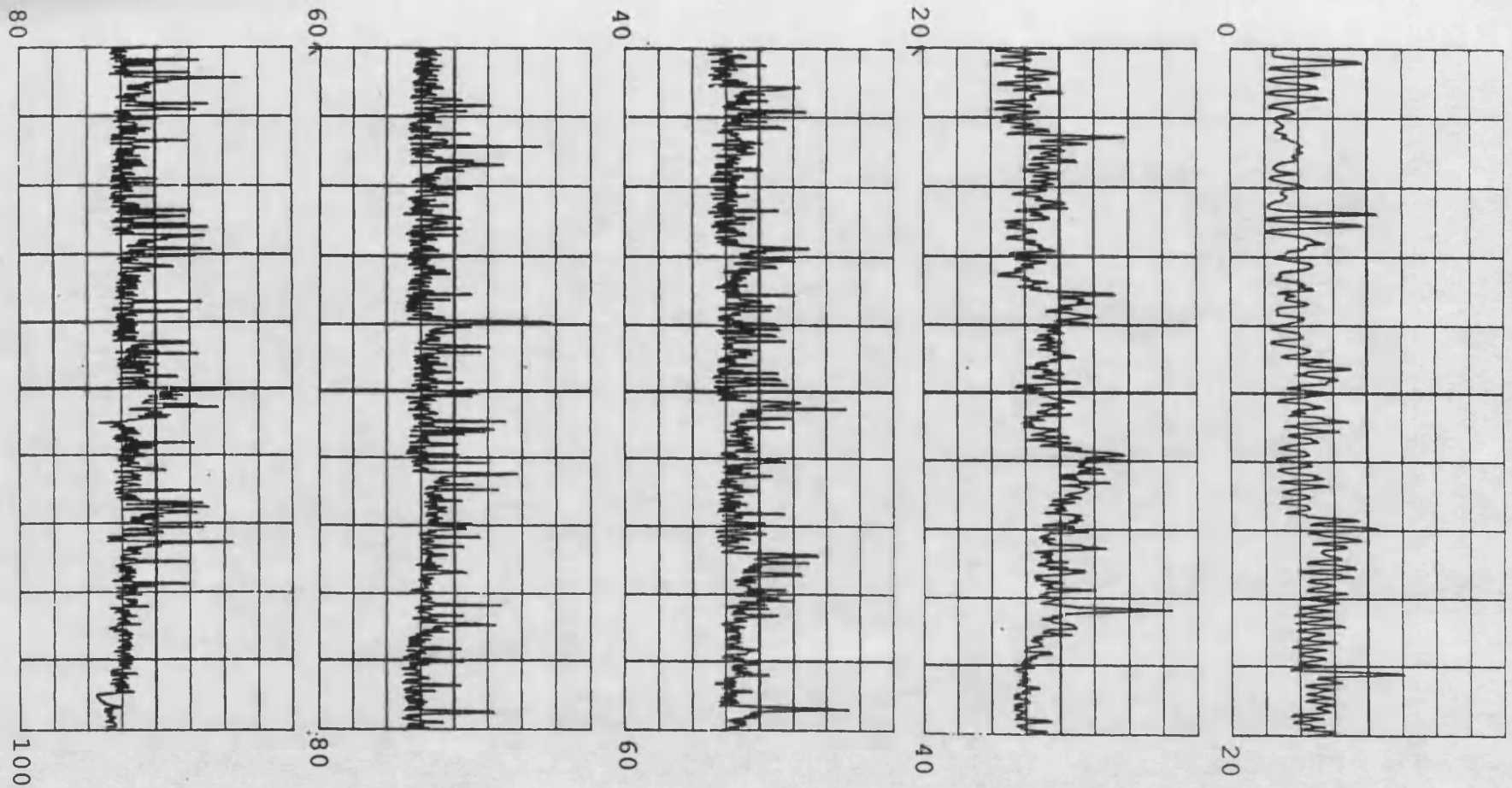

Figure 7.5-b System general performance

experiment results

(motor output torque: 0.48 Nm/div; time: 2 s/div)

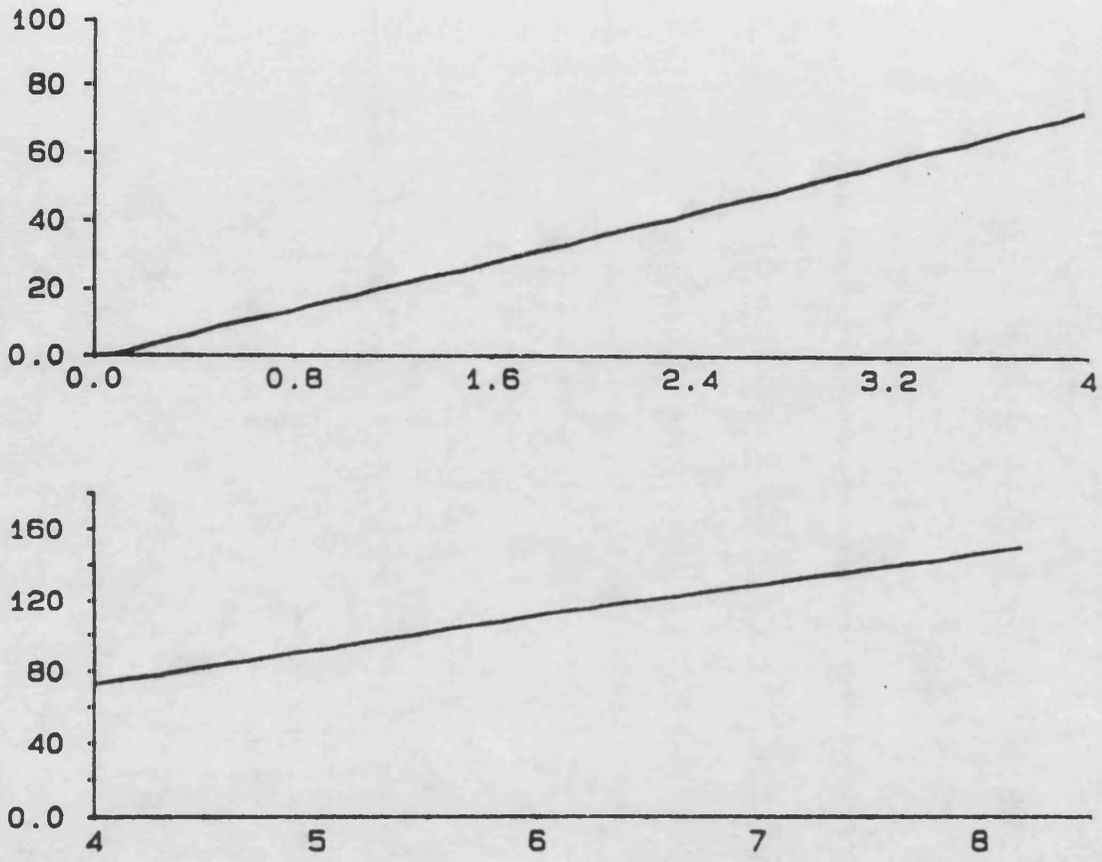

Figure 7.6-a System general performance simulation results

(motor speed: rad/s; time: s)

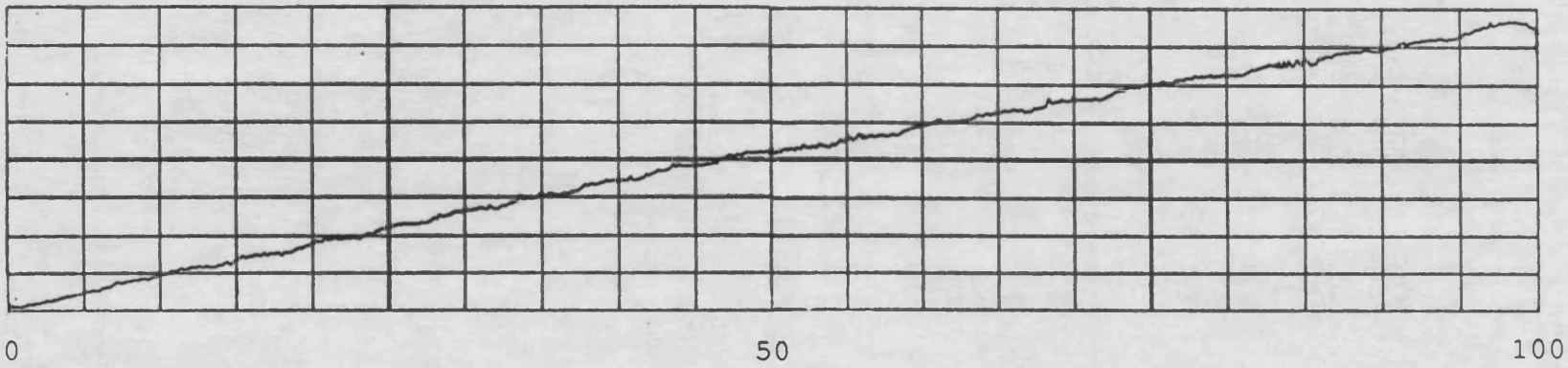

Figure 7.6-b System general performance

experiment results

(motor speed: 19.8 (rad/s)/div; time 5 s/div)

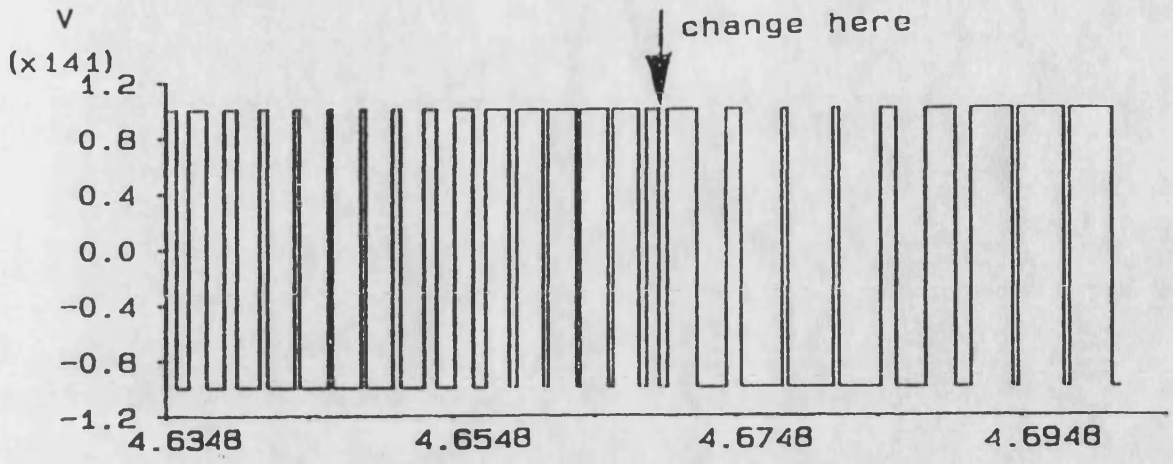

<1>. inverter phase voltage

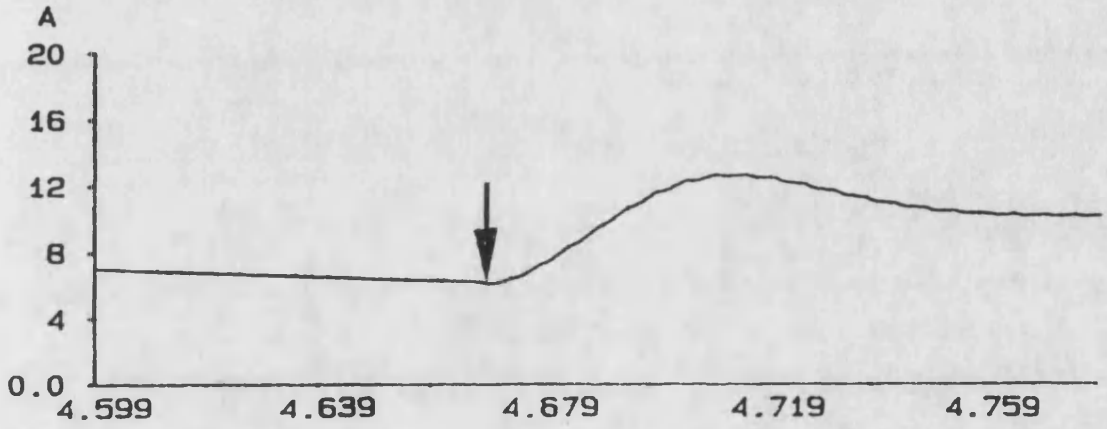

<2>. system input current

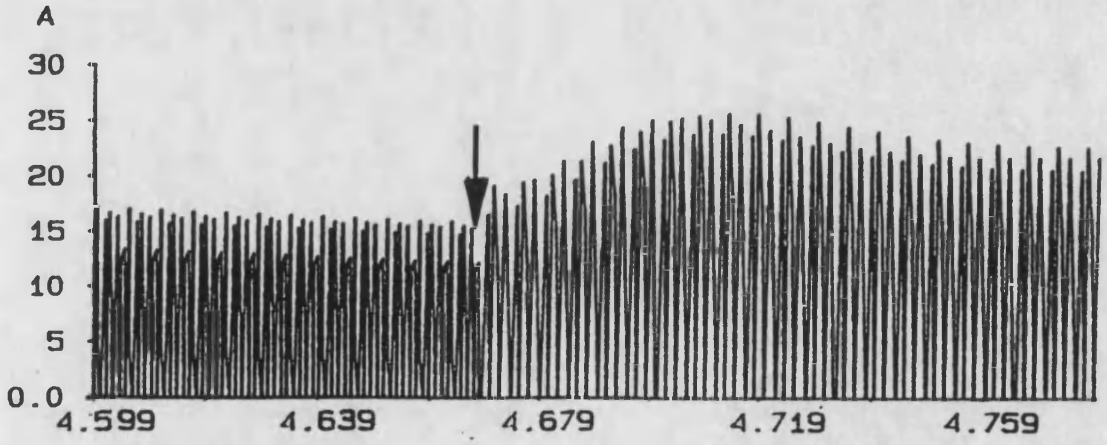

<3>. DC link current

Figure 7.7-a Gear change

simulation results

t = 4.669 s, Mr = 15 -> 9

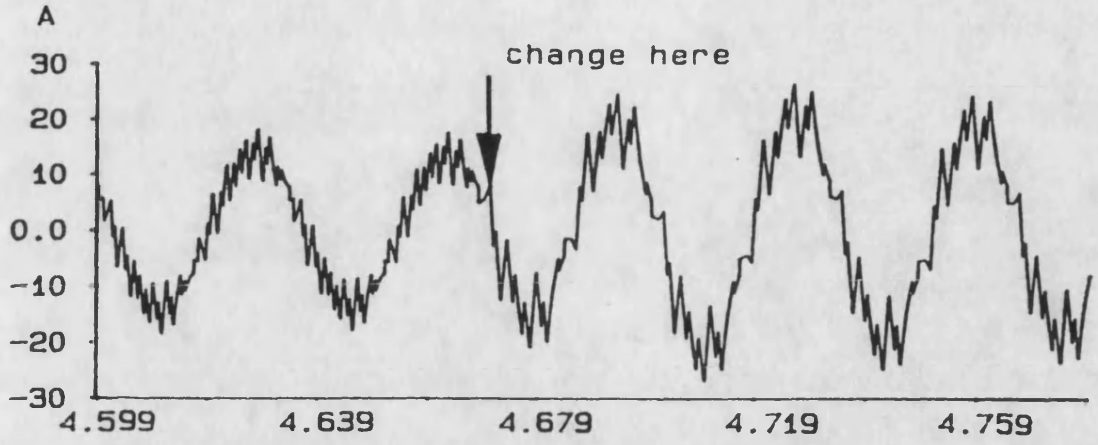

<1>. motor line current

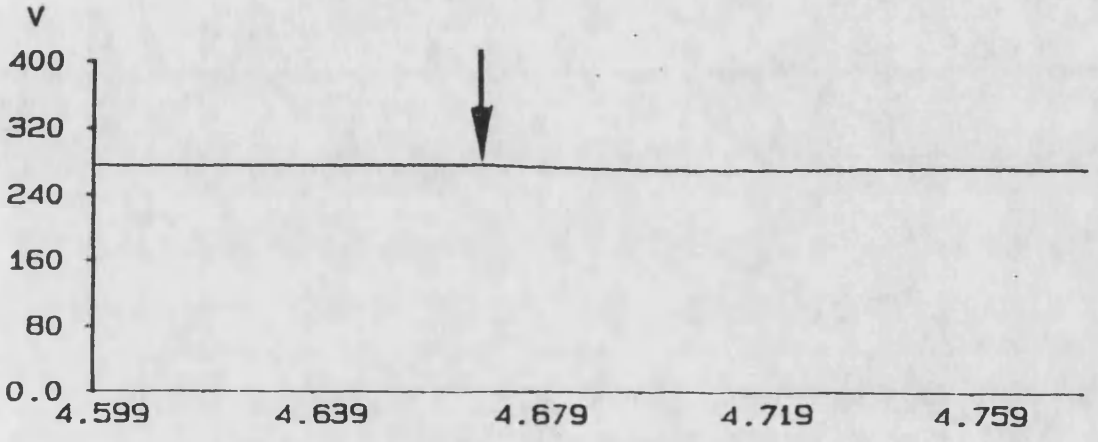

<2>. DC link voltage

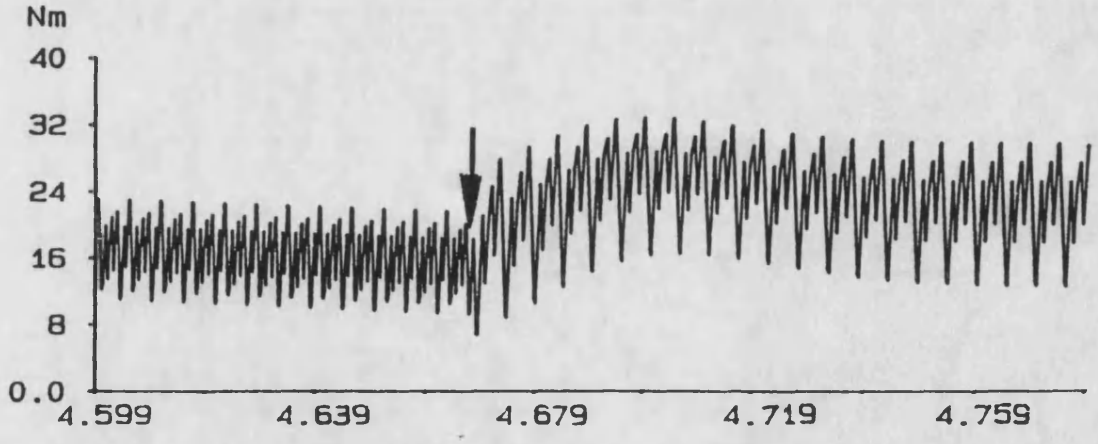

<3>. motor output torque

Figure 7.7-b Gear change

simulation results

t = 4.669 s, Mr = 15 -> 9

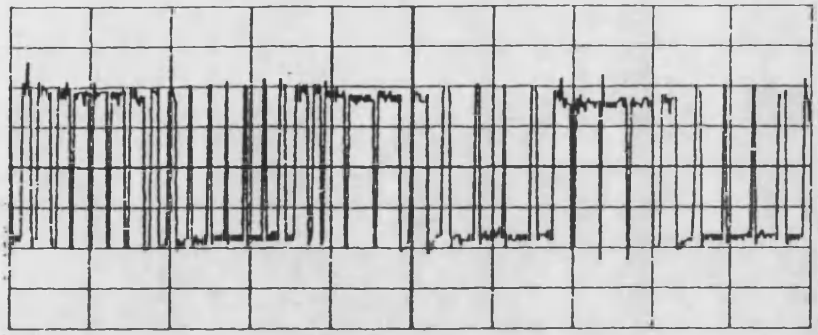

59.13

1. inverter phase voltage: 18.75 V/div
time: 10 ms/div

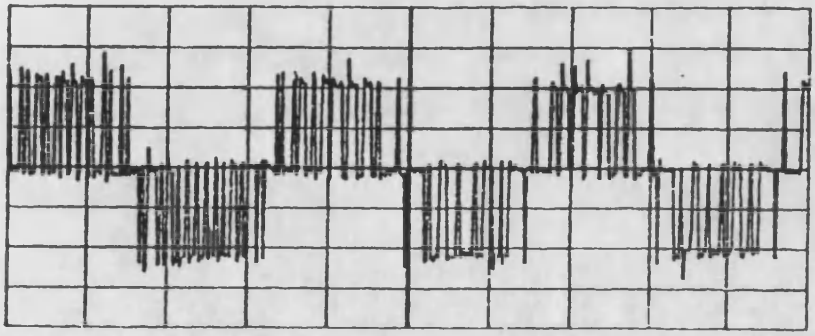

59.13

2. inverter line voltage: 32.48 V/div
time: 10 ms/div

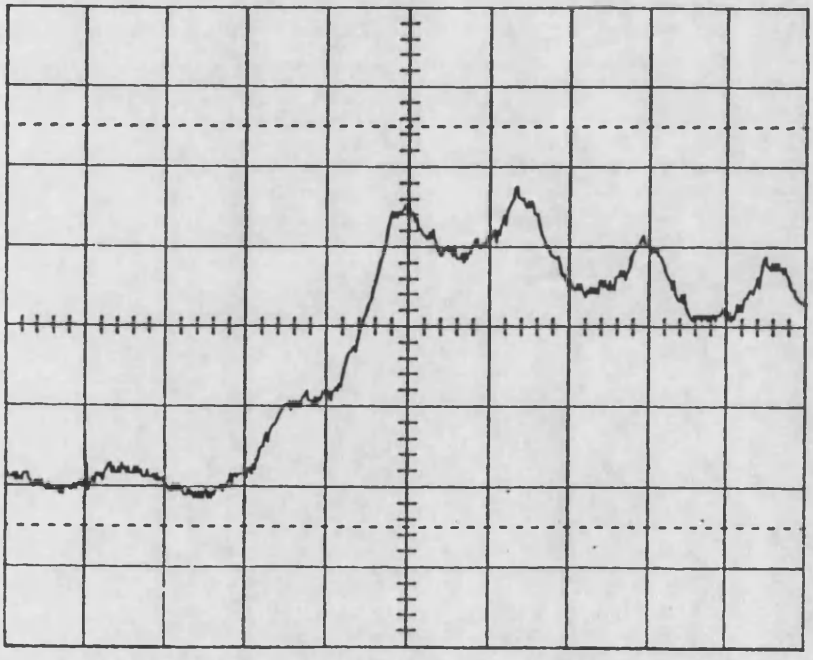

0.14

59.11

3. system input current: 0.93 A/div
time: 20 ms/div

Figure 7.8-a Gear change experiment results

t = 59.17 s, Mr = 15 -> 9

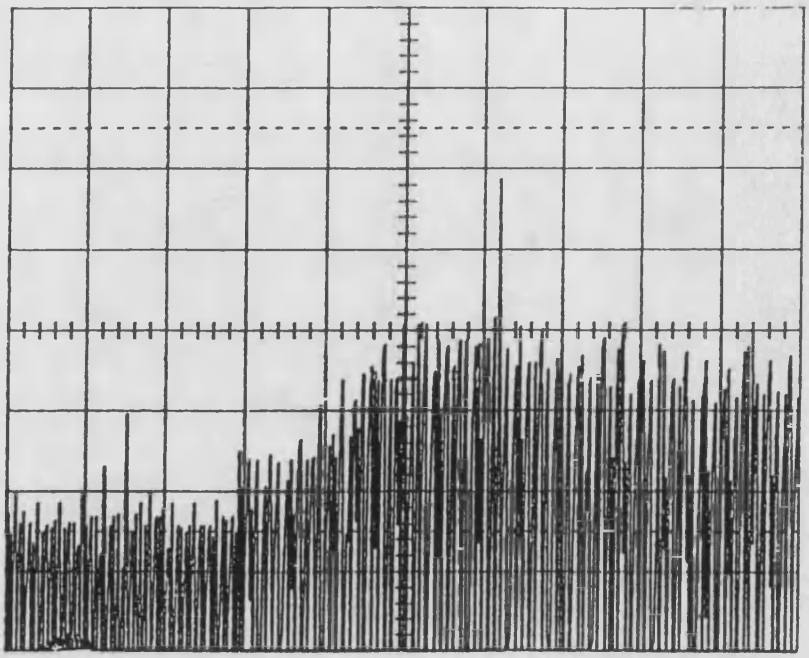

<1>. DC link current: 1.32 A/div
time: 20 ms/div

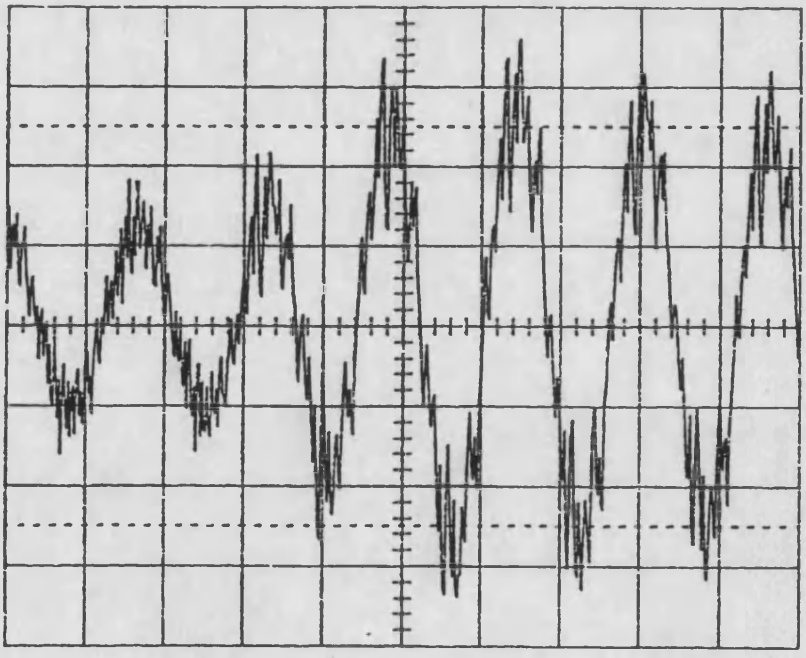

<2>. motor line current: 2 A/div
time: 20 ms/div

Figure 7.8-b Gear change

experiment results

t = 59.17 s, Mr = 15 -> 9

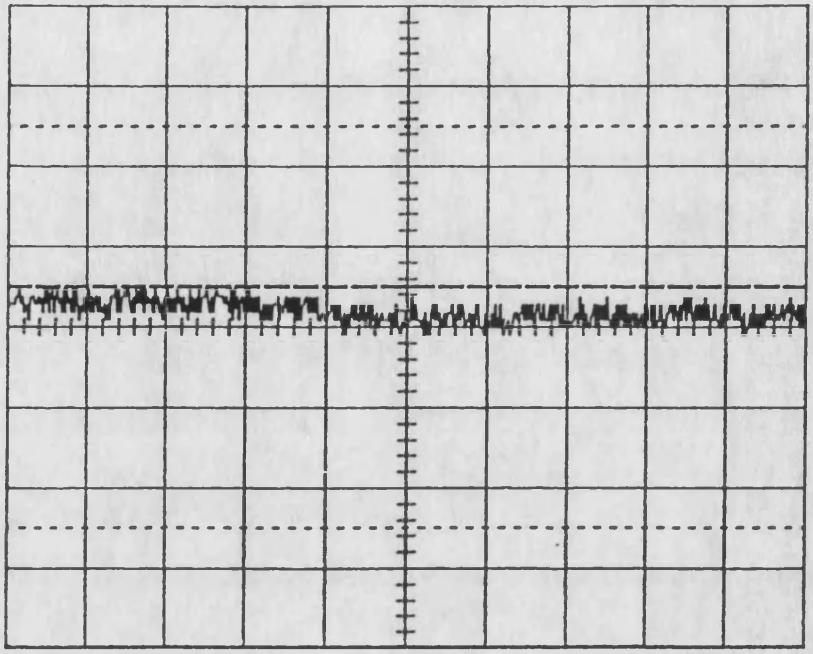

<1>. DC link voltage: 5 V/div
time: 20 ms/div

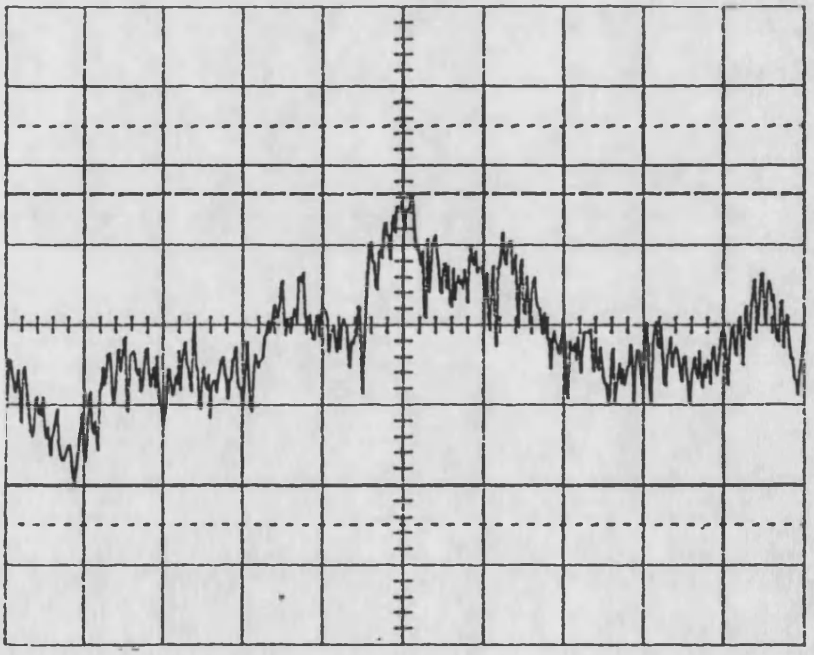

<2>. motor output torque: 0.52 Nm/div
time: 20 ms/div

Figure 7.8-c Gear change

experiment results

t = 59.17 s, Mr = 15 -> 9

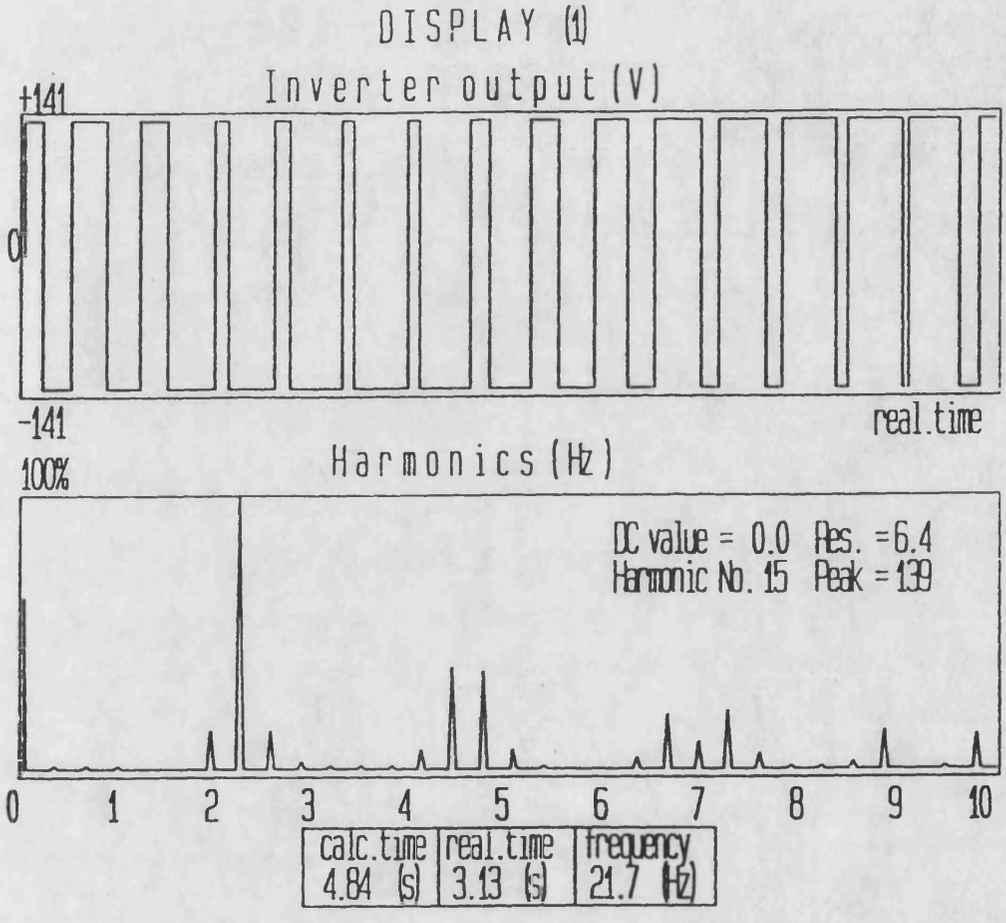

Figure 7.9-a Inverter phase voltage and its harmonic spectrum, Mr = 15 simulation results

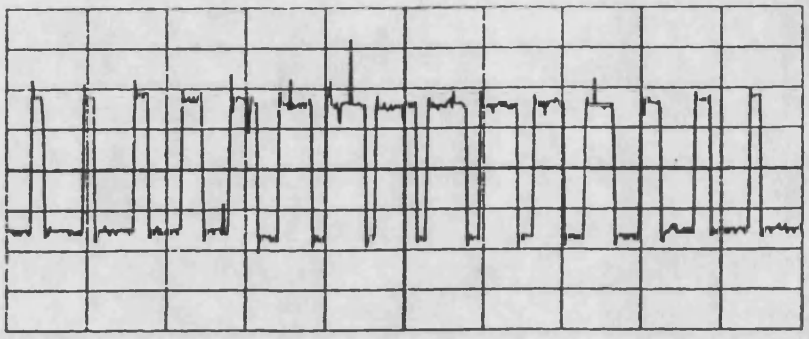

36.39

(Y: 20 V/div; X: 5 ms/div)

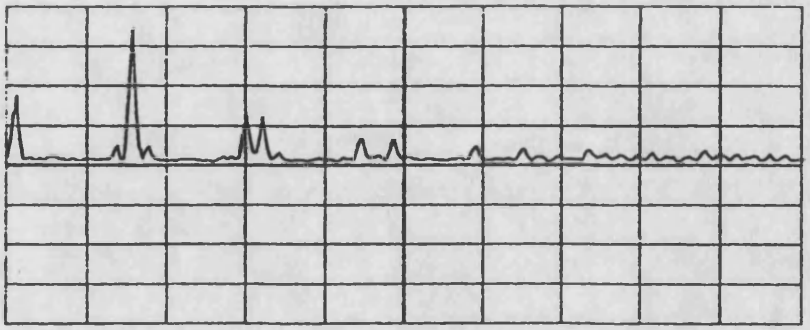

(Y: 10 V/div; X: 200 Hz/div)

Figure 7.9-b Inverter phase voltage and its harmonic spectrum, f = 20.53 Hz, Mr = 15

experiment results

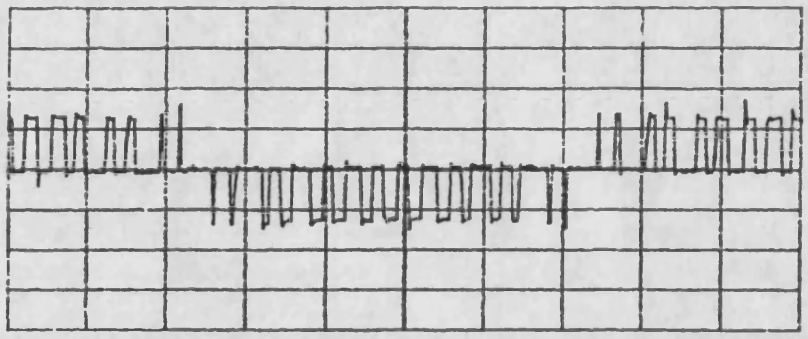

36.39

(Y: 50 V/div; X: 5 ms/div)

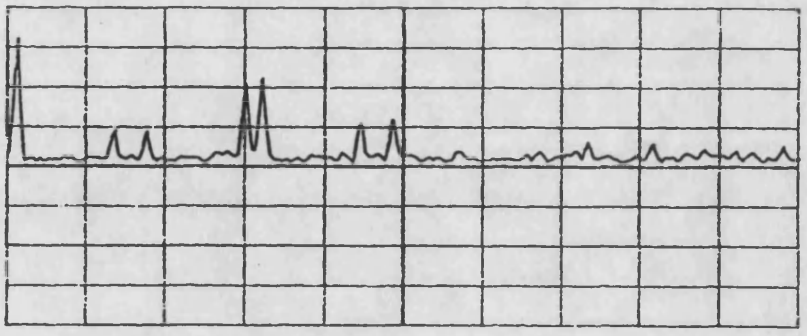

(Y: 10 V/div; X: 200 Hz/div)

Figure 7.9-c Inverter line voltage and its harmonic spectrum, f = 20.53 Hz, Mr = 15

experiment results

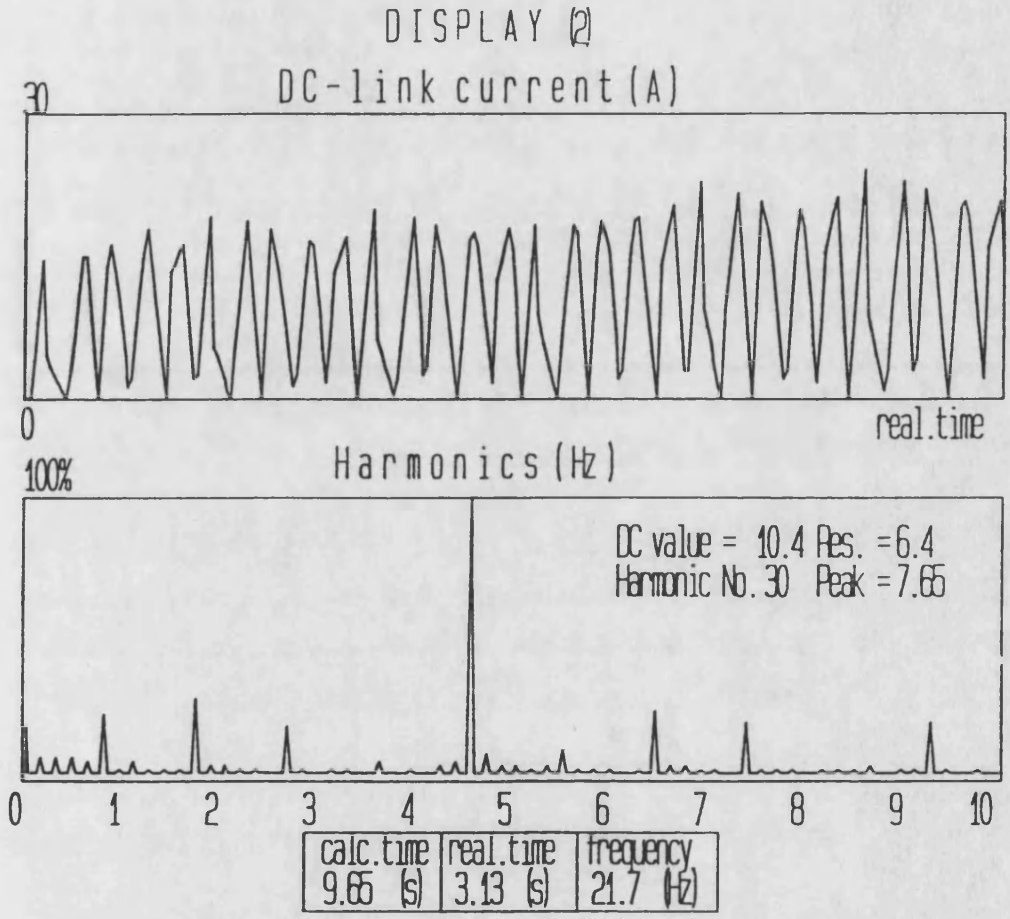

Figure 7.10-a DC link current and its harmonic spectrum, Mr = 15 simulation results

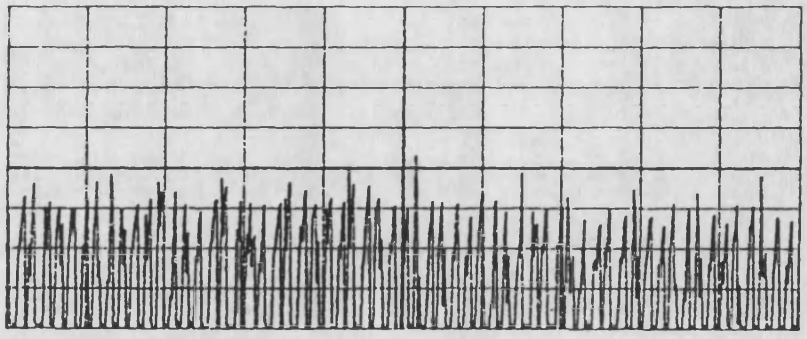

36.39

(Y: 2 A/div; X: 10 ms/div)

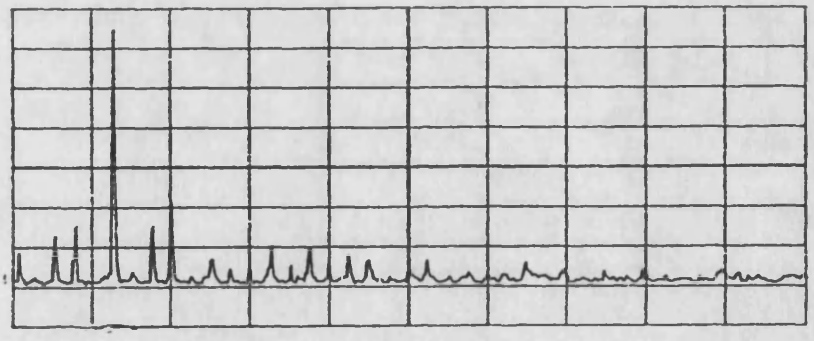

(Y: 0.4 A/div; X: 500 Hz/div)

Figure 7.10-b DC link current and its harmonic spectrum, f = 20.53 Hz, Mr = 15 experiment results

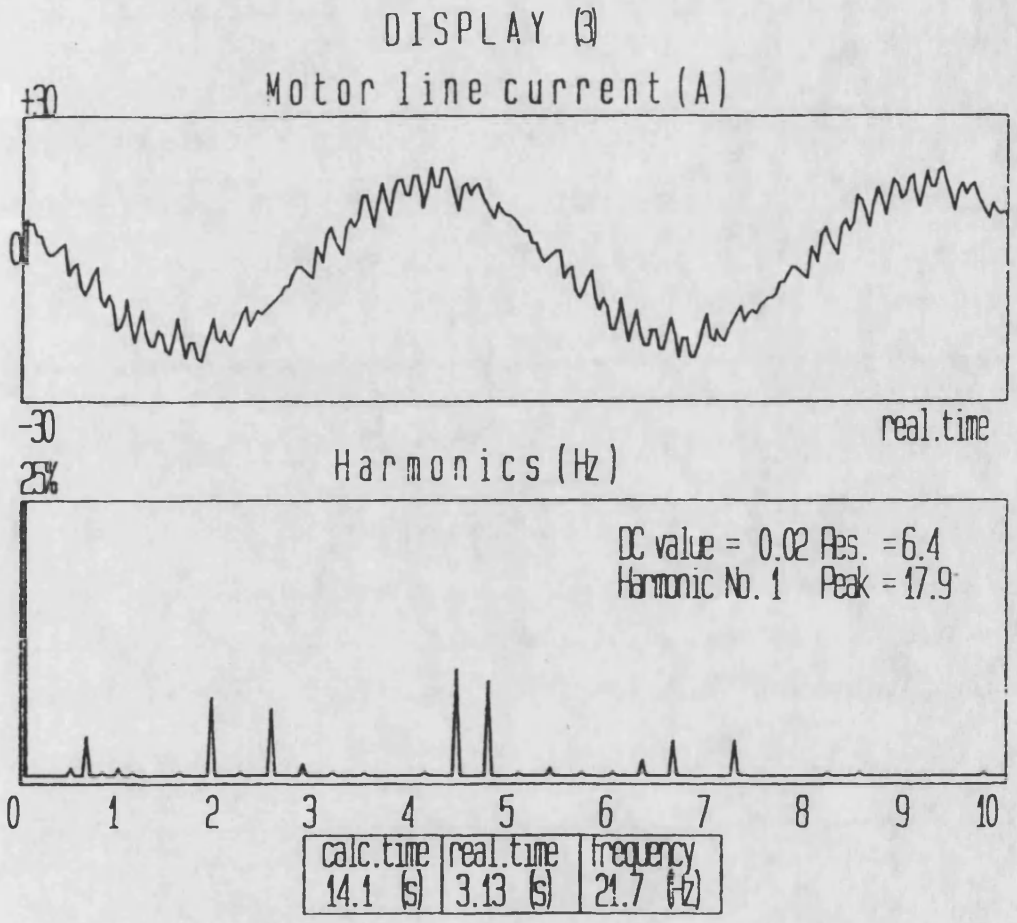

Figure 7.11-a Motor line current and its harmonic spectrum, Mr = 15 simulation results

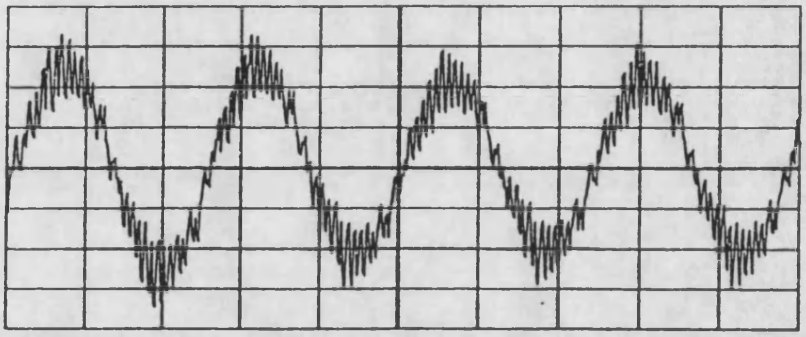

36.39

(Y: 2 A/div; X: 20 ms/div)

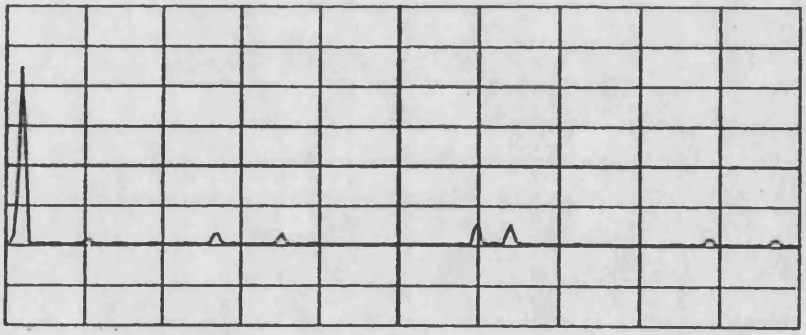

(Y: 1 A/div; X: 100 Hz/div)

Figure 7.11-b Motor line current and its harmonic spectrum, f = 20.53 Hz, Mr = 15 experiment results

Table 7.3 Motor line current harmonic spectrum

(a) simulation results

Mr = 27, $f = 11.9$ Hz

Harmonic No.	Frequency	Amplitude	Percentage
1,	11.9,	15.12,	100.0
5,	59.3,	0.1598,	1.057
7,	83.0,	0.1827,	1.209
25,	296.5,	0.5079,	3.359
29,	343.9,	0.5296,	3.503
39,	462.5,	0.357,	2.362
53,	628.5,	1.429,	9.456
55,	652.2,	1.398,	9.245
79,	936.8,	0.3986,	2.637
83,	984.3,	0.3267,	2.161

(b) experimental results

Mr = 27, $f = 11.6$ Hz

Harmonic No.	Frequency	Amplitude	Percentage
1,	11.6,	3.8,	100.0
5,	57.8,	0.045,	1.2
7,	80.9,	0.034,	0.9
11,	127.2,	0.041,	1.05
25,	289.0,	0.114,	3.01
29,	335.2,	0.103,	2.71
53,	612.7,	0.42,	11.05
55,	635.8,	1.448,	11.78
79,	913.2,	0.086,	2.25
83,	959.5,	0.076,	2.02

Table 7.4 Motor line current harmonic spectrum

(a) simulation results

Mr = 15, f = 21.7 Hz

Harmonic No.	Frequency	Amplitude	Percentage
1,	21.68,	17.94,	100.0
5,	108.4,	0.6709,	3.73
7,	151.7,	0.1842,	1.027
13,	281.8,	1.305,	7.27
17,	368.5,	1.104,	6.152
19,	411.8,	0.2234,	1.245
29,	628.6,	1.755,	9.783
31,	671.9,	1.539,	8.579
41,	888.7,	0.2685,	1.496
43,	932.0,	0.6331,	3.528

(b) experimental results

Mr = 15, f = 20.5 Hz

Harmonic No.	Frequency	Amplitude	Percentage
1,	20.5,	4.55,	100.0
5,	102.5,	0.128,	2.76
7,	143.5,	0.028,	0.63
13,	266.6,	0.286,	6.28
17,	348.5,	0.278,	6.11
19,	389.5,	0.057,	1.25
29,	594.5,	0.486,	10.67
31,	635.5,	0.478,	10.51
41,	840.5,	0.014,	0.31
43,	881.5,	0.157,	3.45

Table 7.5 Motor line current harmonic spectrum

(a) simulation results

Mr = 9, $f = 31.2$ Hz

Harmonic No.	Frequency	Amplitude	Percentage
1,	31.2,	19.44,	100.0
7,	218.1,	3.075,	15.82
11,	342.7,	1.962,	10.09
17,	529.7,	1.551,	7.981
19,	592.0,	1.317,	6.777
23,	716.6,	0.4132,	2.126
25,	778.9,	0.6963,	3.582
29,	903.5,	0.4532,	2.331

(b) experimental results

Mr = 9, $f = 31.4$ Hz

Harmonic No.	Frequency	Amplitude	Percentage
1,	31.4,	5.25,	100.0
5,	156.7,	0.143,	2.72
7,	219.4,	0.571,	10.88
11,	344.8,	0.386,	7.35
17,	532.9,	0.414,	7.89
19,	595.6,	0.286,	5.44
23,	721.0,	0.114,	2.18
25,	783.7,	0.121,	2.31
29,	909.1,	0.072,	1.36

Table 7.6 Motor line current harmonic spectrum

(a) simulation results

Mr = 9', f = 38.0 Hz

Harmonic No.	Frequency	Amplitude	Percentage
1,	38.0,	20.53,	100.0
5,	190.0,	4.271,	20.8
7,	266.1,	2.124,	10.35
11,	418.1,	2.741,	13.35
13,	494.1,	0.2594,	1.264
17,	646.1,	1.572,	7.657
19,	722.2,	1.551,	7.556
23,	874.2,	0.2622,	1.277
25,	950.2,	0.5258,	2.561

(b) experimental results

Mr = 9', f = 37.7 Hz

Harmonic No.	Frequency	Amplitude	Percentage
1,	37.7,	5.73,	100.0
5,	188.5,	0.857,	14.96
7,	263.9,	0.314,	5.48
11,	414.7,	0.571,	9.97
13,	490.1,	0.0	---
17,	640.9,	0.286,	4.98
19,	716.3,	0.305,	5.32
23,	867.1,	0.128,	2.24
25,	942.5,	0.121,	2.12

Table 7.7 Motor line current harmonic spectrum

(a) simulation results

Mr = 9', f = 49.5 Hz

Harmonic No.	Frequency	Amplitude	Percentage
1,	49.5,	21.85,	100.0
5,	246.8,	1.052,	4.814
7,	345.5,	0.2656,	1.216
11,	543.0,	0.7173,	3.283
13,	641.7,	0.9157,	4.191
17,	839.2,	0.5015,	2.295
19,	937.9,	0.4518,	2.068

(b) experimental results

Mr = 9', f = 48.1 Hz

Harmonic No.	Frequency	Amplitude	Percentage
1,	48.1,	7.1,	100.0
5,	240.6,	0.357,	5.11
7,	336.8,	0.0714,	1.02
11,	529.3,	0.214,	3.06
13,	625.6,	0.243,	3.47
17,	818.1,	0.143,	2.04
19,	914.3,	0.129,	1.84

Chapter 8 : Simulation of a practical traction drive

8.1 Introduction

In this chapter, the simulation results for a practical traction drive are presented. The system parameters are given in Appendix B. The system input voltage, 668 V, is assumed to be DC with no ripple. This is not realistic, practical values being the standard traction voltages of 600, 750, 1500 and 3000 V, with AC ripple from traction rectifier substations. The value of 668 V was chosen to produce a motor line voltage at the correct rated value of 520 V.

All three drive regions are operated in the simulation. Under constant torque operation, the stator supply frequencies, or modulation frequencies, vary from 0.1 Hz to 2.0 Hz using the asynchronous PWM scheme and from 2.0 Hz to 49.16 Hz using the synchronous PWM scheme. With synchronous PWM operation, the double-size natural sampled PWM scheme was used and five modulation ratios were adopted. These are M_r = 51 for f < 10 Hz, M_r = 27 for f < 20 Hz, M_r = 15 for f < 30 Hz, M_r = 9 for f < 37, and M_r = 9' for f < 49.16 Hz. The last M_r (= 9') implies that the modified PWM scheme was used. From 50 Hz to 85 Hz, the constant power region was operated, and

above this frequency, the high speed region was entered, up to 120 Hz.

The system input look-up tables for the simulation are given in Tables 8.1-8.3. Each table gives the number of frequency steps, the terminating time for each step, the frequency, and the number of repetitions for each frequency.

For the first 0.396 seconds of motion, asynchronous PWM was used, with a carrier frequency of 500 Hz. The modulation frequency, between 0.1 Hz and 2.0 Hz, and modulation depth are updated during each carrier cycle. From 0.396 to 18.157 seconds, natural sampled synchronous PWM was used. As shown in Table 8.1, the frequency in the first step was 2.897 Hz. The number of repeats for this frequency is one. Therefore, the period T of this frequency is 0.345 seconds, and the terminating time for this step is at 0.741 seconds.

The following presents the simulation results with the above conditions. In section 8.2, the total system performance is given. The gear change and pulse dropping behaviours at different points are presented in section 8.3, and the harmonic content of certain system variables is presented in 8.4.

8.2 System total performance

Figures 8.1 - 8.6 show the waveforms of the system variables against operating time. In each figure, six variables are presented. At the beginning of each frequency step, the motor output torque suffers a step increase. This can be understood from the motor torque-speed curve. Since at the instant of step change of frequency, the motor speed cannot suddenly rise, the increased torque accelerates the motor. The increase of speed, then, causes the motor torque to decrease. Consequently, the motor line current, DC link current, and system input current all have to vary with variation in the motor torque. The following gives a brief description of the behaviour of each of the six variables simulated.

In the constant torque region, the system input current increases steadily from zero to the maximum value of about 400 A, while the motor output torque and the motor line current are kept constant. This is because the pre-designed constant torque operation requires the rotor current and the magnetising current to be constant. Hence, the line current is also constant. From the power relationship, $V_{in}I_{in} = T_e\omega_r + k$, the input current can only vary with variation of the motor speed. In reality, the tractive torque is much greater than the resistance torque. Therefore, the acceleration is nearly constant. Hence, both the speed

and the input current increase linearly. Again, from power balance consideration, $V_{dc}I_{dc} = kV_1I_1$. Neglecting variation in the power factor, since V_{dc} and I_1 are constant, I_{dc} increases with increase in V_1. At longer times, the ripple on the DC link voltage grows due to the increased current drawn from the capacitor. At the end of this region, the motor speed is $2\pi(49.16-1.005)/2$ = 151.28 rad/s.

In the constant power region, the motor torque decreases proportionally to $1/f$. The constant slip keeps the rotor current constant. The magnetising current is reduced with increase in supply frequency. Note that the magnetising current is much smaller than the rotor current. Therefore the stator current, DC link current and system input current all decrease slowly. The large step increase in the system variables at the beginning of the constant power region is due to the transition from PWM to square-wave operation. At the end of the region, the motor speed is $2\pi(85-1.96)/2$ = 262 rad/s.

In the high-speed region, the motor torque decreases proportionally to $1/f^2$. Due to both magnetising current and rotor current decreasing with increase of supply frequency, the motor line current, and hence also the DC link current and system input current, decreases rapidly. At the end of this region, the motor speed is $2\pi(120-1.96)$ = 372 rad/s.

8.3 Gear change and pulse dropping behaviour

In this section, two gear change points and two pulse dropping points will be shown. The gear change points selected are at times of 10.8s and 13.49s. The first point corresponds to the frequency transition from 29.72 Hz to 31.76 Hz with the modulation ratio M_r changing from 15 to 9. The second point corresponds to the transition from 36.86 Hz to 37.91 Hz with M_r changing from 9 to 9'. Note that the second point in the gear change is also involved with the first pair of pulses being dropped. The two pulse dropping points corresponding to the second and the third pair of pulses being dropped are at time = 17.38s, f = 48.14 Hz and M_r = 9', and at time = 17.77s, f = 49.16 Hz and M_r = 9'. Note that the dropping of the third pair of pulses results in the transition from PWM to square wave operation.

Figure 8.7 shows the inverter output PWM waveforms at the two gear changing points. Figures 8.8 and 8.9 show the behaviour of the corresponding system variables. The inverter output PWM waveforms at the two pulse dropping points are shown in Figure 8.10. The behaviour of the corresponding system variables is shown in Figures 8.11 and 8.12. Note that in all these figures, the

transitions are made at the time indicated by the arrows.

8.4 Harmonic analysis

Four system variables, each corresponding to one on-line display page, are presented in this section together with their harmonic content. The four variables are inverter output PWM voltage, DC link current, motor line current, and motor output torque. Other system variables such as the system input current are not displayed. Since the exact frequencies are not known, to analyse these signals is not in the capability of the FFT routine written by the author.

The information given on each display page includes the waveform of the system variable and its harmonic content, the value of the DC component and the peak value of the harmonic component with the largest amplitude, the harmonic number corresponding to the largest amplitude harmonic component, and the frequency resolution. In addition, the frequency of the fundamental component, the real-time at the start of the display and the calculation time for the display page are also shown.

Figures 8.13 - 8.16 present the simulation results at four different time instants. Each contains four display

pages. The supply frequencies at the four points are 20.6, 30.8, 37.9, and 49.16 Hz with the modulation ratios M_r = 15, 9, 9', and 9'.

In Figure 8.13-a, the fundamental component is 20.6 Hz. The largest harmonic component number is 15 (resolution 6.4 times scale 2.34) with peak value of 349 V. The second largest harmonic component numbers are 29 and 31. These are as predicted in section 4.2, i.e., the harmonic amplitudes are in the sequence of M_r, $2M_r \pm 1$, etc. This prediction is also true in Figure 8.14-a where the first three harmonic numbers with the largest amplitude are 9, 17, and 19. When over-modulation is introduced, the prediction is no longer valid, as shown in Figures 8.15-a and 8.16-a.

In Figures 8.13-c - 8.16-c, it can be seen that the motor line current has the same harmonic components as the inverter PWM voltage except for the triplen harmonics. Moreover, the harmonic amplitudes are much smaller than those in the inverter PWM voltage due to the filter effect from the motor reactance. With increase in harmonic number, the harmonic amplitudes decreases.

Figures 8.13-b - 8.16-b show the DC link current, and Figures 8.13-d - 8.16-d show the motor output torque, together with their harmonic spectra. As predicted, the

harmonic numbers are always multiples of six. The largest harmonic component for both the DC link current and the motor output torque has the harmonic number $2M_r$ under the condition of $M_r > 9$. This is clearly shown in Figures 8.13-b and -d. The reason is because the largest pair of motor line current harmonics exist at harmonic number $2M_r-1$ and $2M_r+1$. The prediction is not true when $M_r < 9$ or with over-modulation operation ($M_d > 1$). As can be seen in Figures 8.16-b and -d, the harmonics tend to move towards lower frequencies.

Table 8.1 Time-Freq.-Repeat
(synchronous PWM operation)

No.	Time	Freq.	Rpt.	No.	Time	Freq.	Rpt.
1	0.74122,	2.897,	1;	2	1.01717,	3.624,	1
3	1.25256,	4.248,	1;	4	1.63266,	5.262,	2
5	1.9587,	6.135,	2;	6	2.24815,	6.91,	2
7	2.62673,	7.925,	3;	8	2.96633,	8.834,	3
9	3.27673,	9.666,	3;	10	3.65168,	10.67,	4
11	3.99679,	11.59,	4;	12	4.39216,	12.65,	5
13	4.7591,	13.63,	5;	14	5.10288,	14.55,	5
15	5.48871,	15.57,	6;	16	5.85093,	16.54,	6
17	6.24865,	17.6,	7;	18	6.62493,	18.61,	7
19	6.98284,	19.56,	7;	20	7.37132,	20.6,	8
21	7.74199,	21.58,	8;	22	8.13951,	22.64,	9
23	8.51999,	23.66,	9;	24	8.88544,	24.63,	9
25	9.2751,	25.67,	10;	26	9.65018,	26.67,	10
27	10.0471,	27.72,	11;	28	10.4299,	28.74,	11
29	10.8001,	29.72,	11;	30	11.1903,	30.76,	12
31	11.5682,	31.76,	12;	32	11.9645,	32.81,	13
33	12.3488,	33.83,	13;	34	12.7223,	34.82,	13
35	13.1128,	35.86,	14;	36	13.4928,	36.86,	14
37	13.8886,	37.91,	15;	38	14.274,	38.93,	15
39	14.6498,	39.92,	15;	40	15.0406,	40.95,	16
41	15.4221,	41.96,	16;	42	15.8175,	43.0,	17
43	16.2038,	44.02,	17;	44	16.6033,	45.07,	18
45	16.9939,	46.1,	18;	46	17.3761,	47.11,	18
47	17.7709,	48.14,	19;	48	18.1575,	49.16,	19

Table 8.2 Time-Freq.-Repeat
(constant power operation)

No.	Time	Freq.	Rpt.	No.	Time	Freq.	Rpt.
1	18.2956,	50.68,	7;	2	18.4324,	51.16,	7
3	18.5873,	51.66,	8;	4	18.7407,	52.16,	8
5	18.8927,	52.63,	8;	6	19.0433,	53.11,	8
7	19.1926,	53.58,	8;	8	19.359,	54.08,	9
9	19.5239,	54.58,	9;	10	19.6874,	55.06,	9
11	19.8495,	55.53,	9;	12	20.0279,	56.03,	10
13	20.2048,	56.53,	10;	14	20.3802,	57.03,	10
15	20.5541,	57.51,	10;	16	20.7265,	57.98,	10
17	20.9146,	58.48,	11;	18	21.1012,	58.98,	11
19	21.2861,	59.48,	11;	20	21.4695,	59.96,	11
21	21.668,	60.46,	12;	22	21.8649,	60.96,	12
23	22.0601,	61.46,	12;	24	22.2539,	61.93,	12
25	22.4621,	62.43,	13;	26	22.6687,	62.93,	13
27	22.8737,	63.43,	13;	28	23.0926,	63.93,	14
29	23.3099,	64.43,	14;	30	23.5256,	64.93,	14
31	23.7395,	65.43,	14;	32	23.967,	65.93,	15
33	24.1928,	66.43,	15;	34	24.4169,	66.93,	15
35	24.6542,	67.43,	16;	36	24.8898,	67.93,	16
37	25.1236,	68.43,	16;	38	25.3702,	68.93,	17
39	25.6151,	69.43,	17;	40	25.8582,	69.93,	17
41	26.1137,	70.43,	18;	42	26.3675,	70.93,	18
43	26.6195,	71.43,	18;	44	26.8836,	71.93,	19
45	27.146,	72.43,	19;	46	27.4065,	72.93,	19
47	27.6789,	73.43,	20;	48	27.9494,	73.93,	20
49	28.2181,	74.43,	20;	50	28.4984,	74.93,	21
51	28.7768,	75.43,	21;	52	29.0665,	75.93,	22
53	29.3544,	76.43,	22;	54	29.6403,	76.93,	22
55	29.9374,	77.43,	23;	56	30.2325,	77.93,	23
57	30.5385,	78.43,	24;	58	30.8426,	78.93,	24
59	31.1447,	79.43,	24;	60	31.4575,	79.93,	25
61	31.7683,	80.43,	25;	62	32.0896,	80.93,	26
63	32.4089,	81.43,	26;	64	32.7384,	81.93,	27
65	33.066,	82.43,	27;	66	33.4036,	82.93,	28
67	33.7392,	83.43,	28;	68	34.0848,	83.93,	29
69	34.4282,	84.43,	29;	70	34.7815,	84.93,	30
71	35.1326,	85.43,	30;				

Table 8.3 Time-Freq.-Repeat
(equivalent DC series motor operation)

No.	Time	Freq.	Rpt.	No.	Time	Freq.	Rpt.
1	35.5283,	85.93,	34;	2	35.9332,	86.43,	35
3	36.3358,	86.93,	35;	4	36.7476,	87.43,	36
5	37.1684,	87.93	37;	6	37.5981,	88.43,	38
7	38.0367,	88.93,	39;	8	38.4839,	89.43,	40
9	38.9287,	89.93,	40;	10	39.3821,	90.43,	41
11	39.844,	90.93,	42;	12	40.3143,	91.43,	43
13	40.7929,	91.93,	44;	14	41.2798,	92.43,	45
15	41.7748,	92.93,	46;	16	42.2778,	93.43,	47
17	42.7889,	93.93,	48;	18	43.3078,	94.43,	49
19	43.845,	94.93,	51;	20	44.3899,	95.43,	52
21	44.9424,	95.93,	53;	22	45.5024,	96.43,	54
23	46.0698,	96.93,	55;	24	46.6548,	97.43,	57
25	47.2471,	97.93,	58;	26	47.8465,	98.43,	59
27	48.4631,	98.93,	61;	28	49.0867,	99.43,	62
29	49.7171,	99.93,	63;	30	50.3643,	100.4,	65
31	51.0182,	100.9,	66;	32	51.6886,	101.4,	68
33	52.3656,	101.9,	69;	34	53.0587,	102.4,	71
35	53.768,	102.9,	73;	36	54.4931,	103.4,	75
37	55.2243,	103.9	76;	38	55.9713,	104.4,	78
39	56.7337,	104.9,	80;	40	57.5114,	105.4,	82
41	58.3044,	105.9,	84;	42	59.1125,	106.4,	86
43	59.9354,	106.9,	88;	44	60.7825,	107.4,	91
45	61.6442,	107.9,	93;	46	62.5203,	108.4,	95
47	63.42,	108.9,	98;	48	64.3338,	109.4,	100
49	65.2708,	109.9,	103;	50	66.2306,	110.4,	106
51	67.2132,	110.9,	109;	52	68.2184,	111.4,	112
53	69.2458,	111.9,	115;	54	70.2953,	112.4,	118
55	71.3668,	112.9,	121;	56	72.4688,	113.4,	125
57	73.5923,	113.9,	128;	58	74.7458,	114.4,	132
59	75.9292,	114.9,	136;	60	77.142,	115.4,	140
61	78.3841,	115.9,	144;	62	79.6639,	116.4,	149
63	80.9724,	116.9,	153;	64	82.3178,	117.4,	158
65	83.7085,	117.9,	164;	66	85.1355,	118.4,	169
67	86.6069,	118.9,	175;	68	88.1225,	119.4,	181
69	89.6817,	119.9,	187;	70	91.2926,	120.4,	194

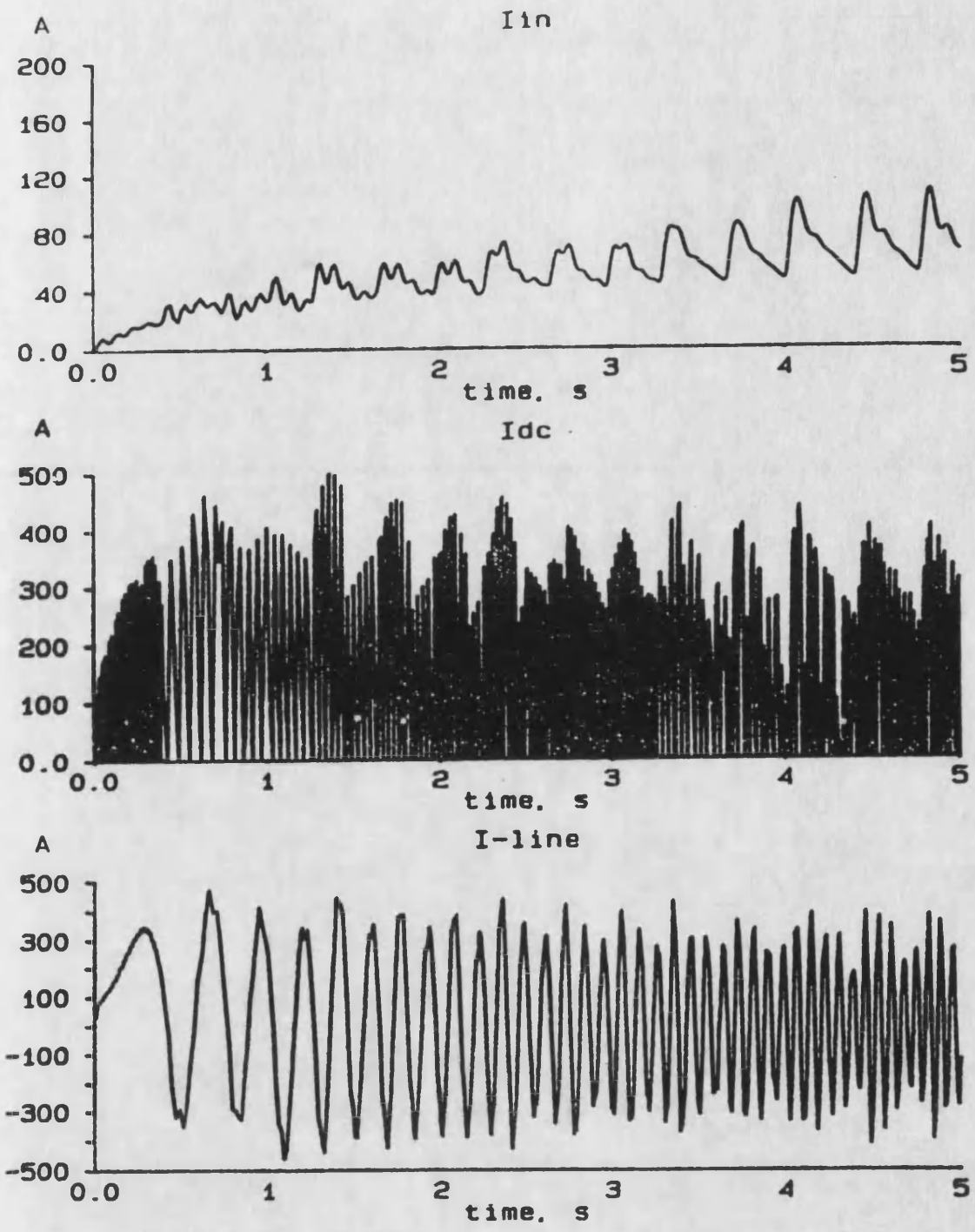

Figure 8.1-a System general performance

(system input-, DC link-, and motor line-current)

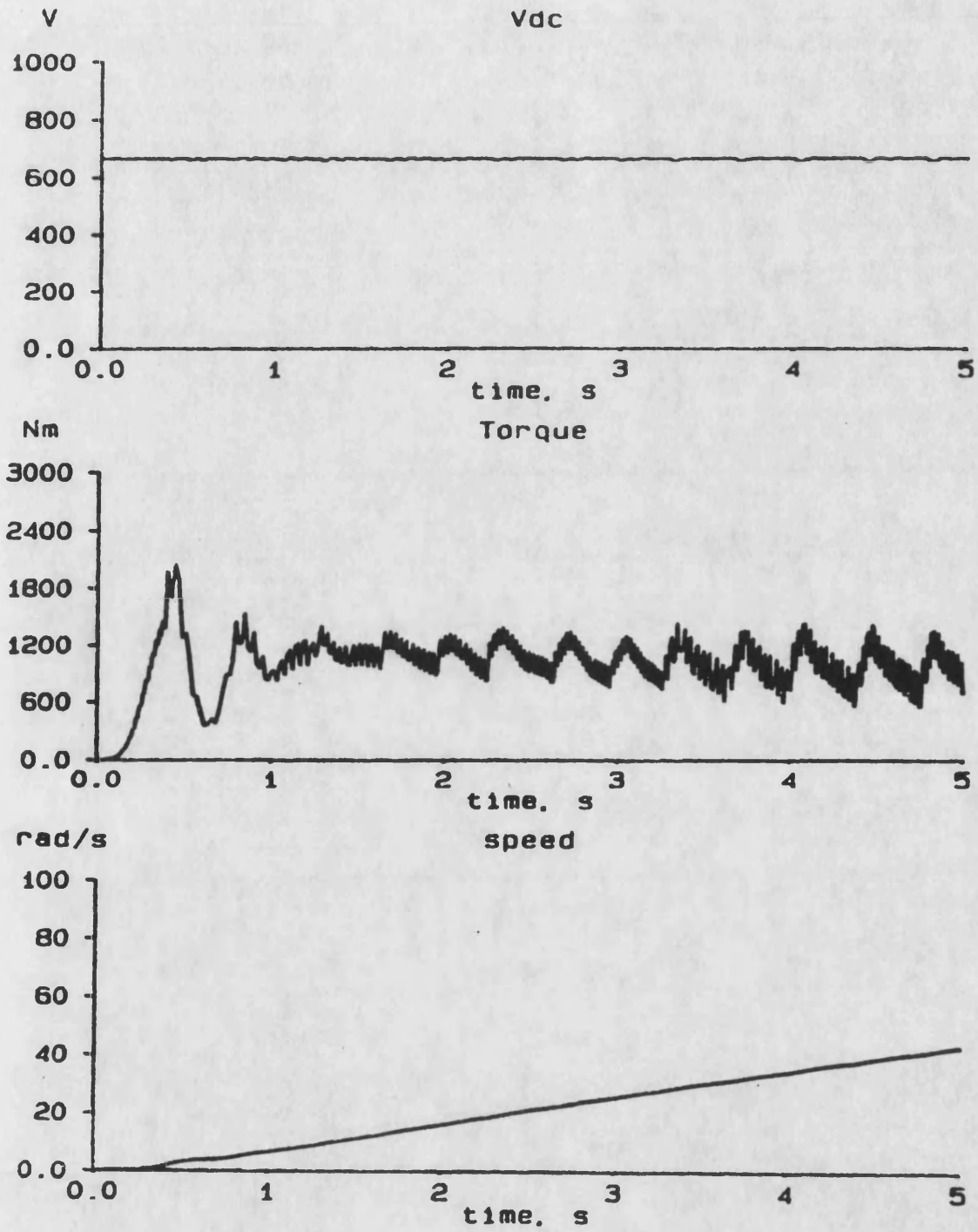

Figure 8.1-b System general performance

(DC link voltage, motor output torque, and motor speed)

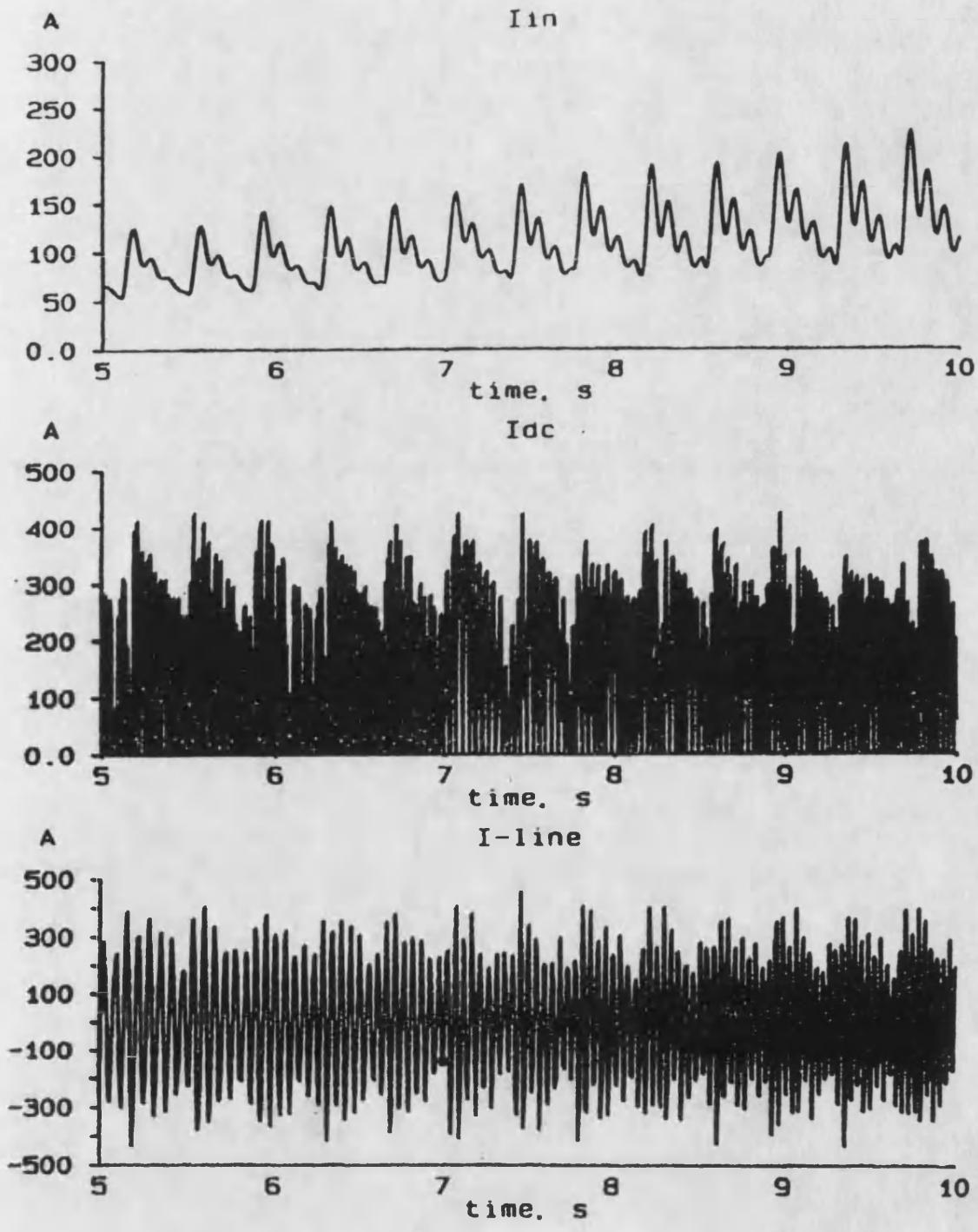

Figure 8.2-a System general performance

(system input-, DC link-, and motor line-current)

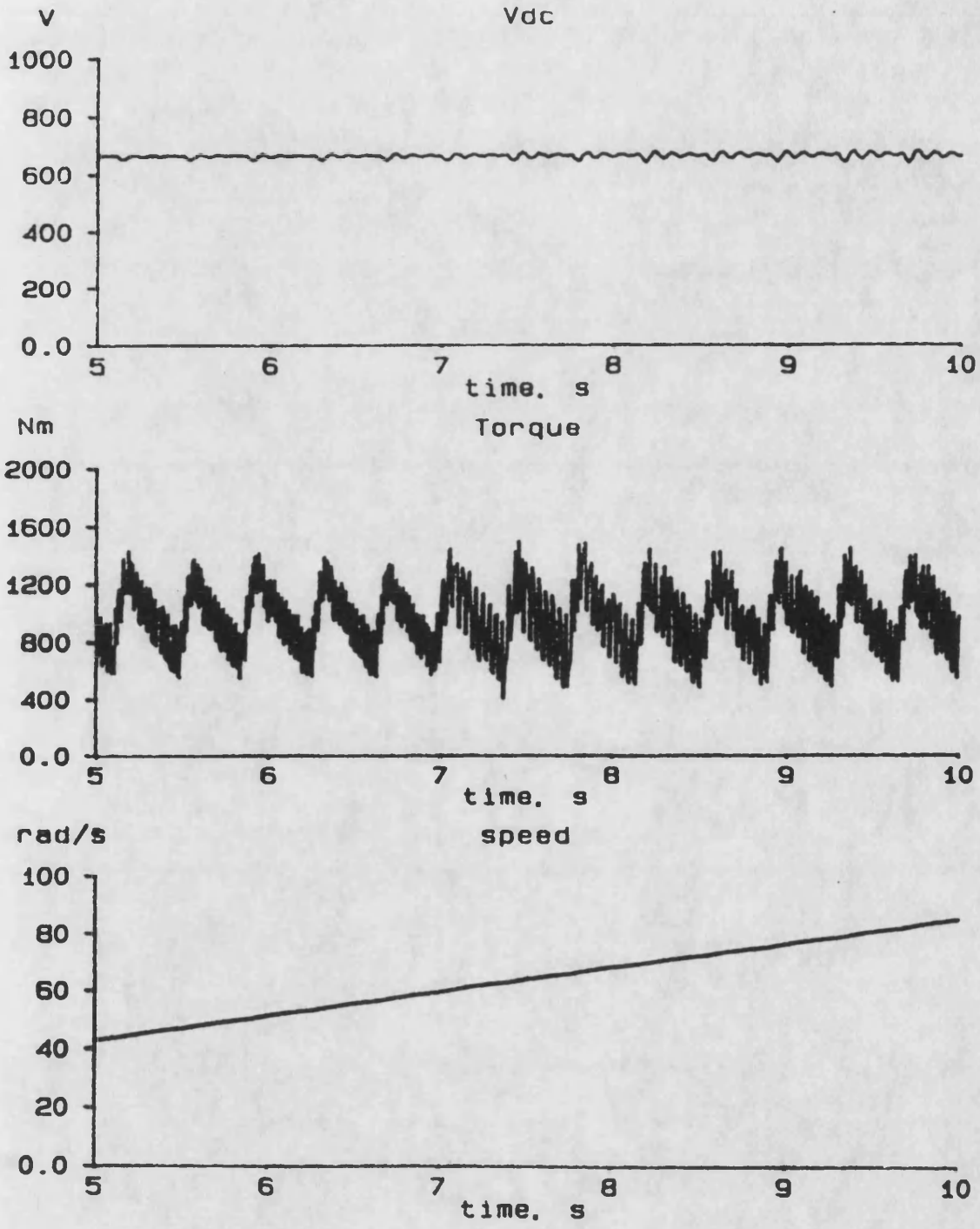

Figure 8.2-b System general performance

(DC link voltage, motor output torque, and motor speed)

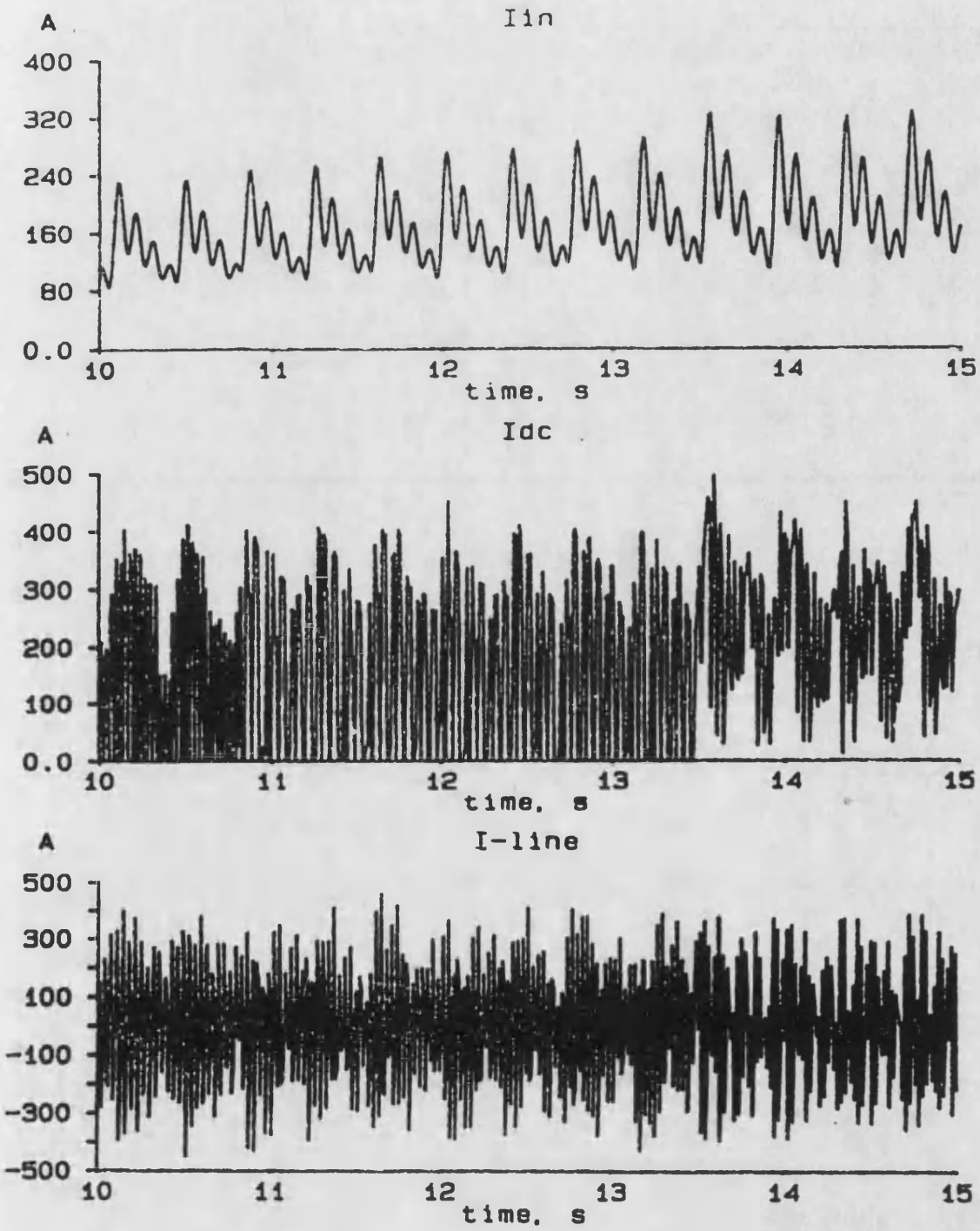

Figure 8.3-a System general performance

(system input-, DC link-, and motor line-current)

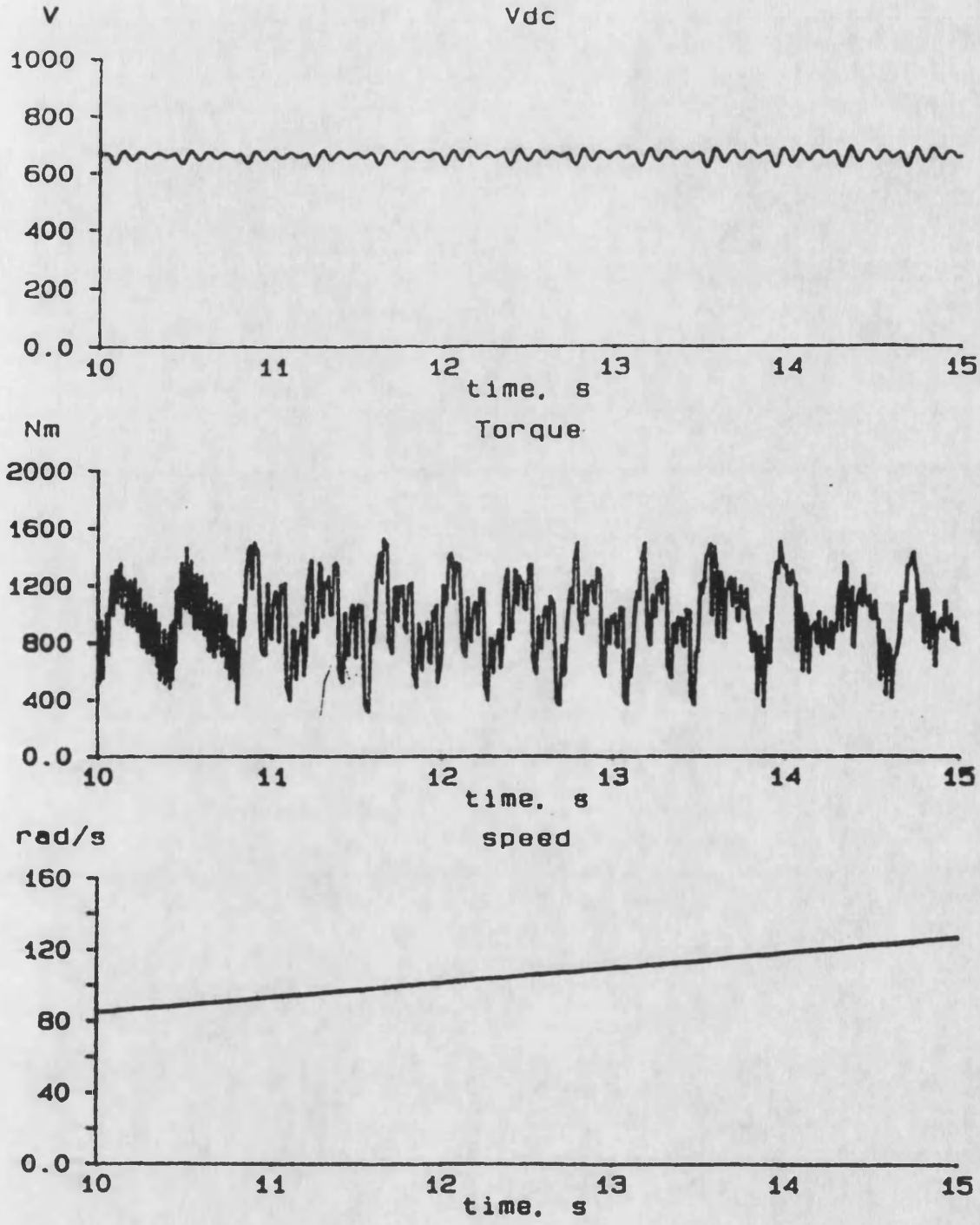

Figure 8.3-b System general performance

(DC link voltage, motor output torque, and motor speed)

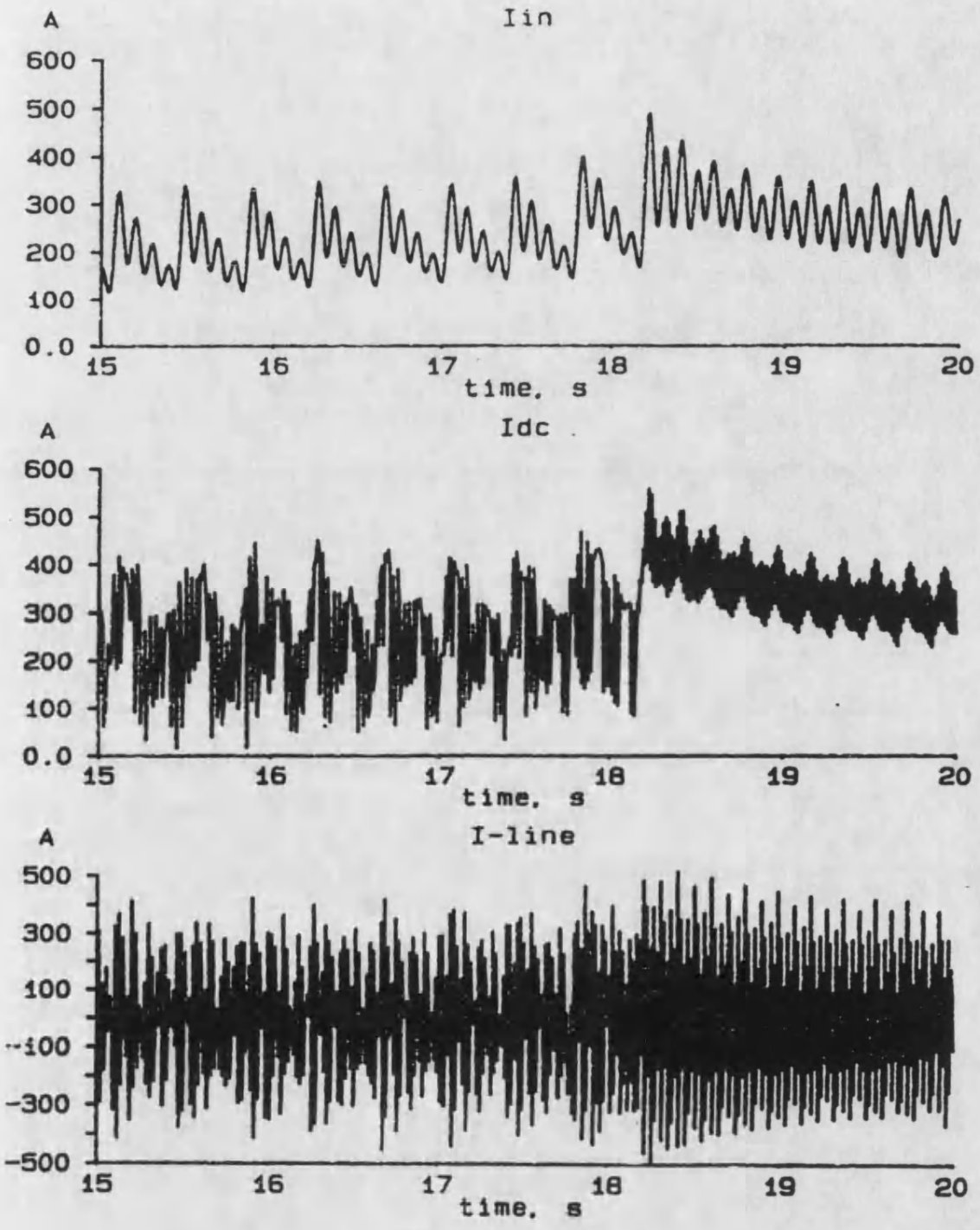

Figure 8.4-a System general performance

(system input-, DC link-, and motor line-current)

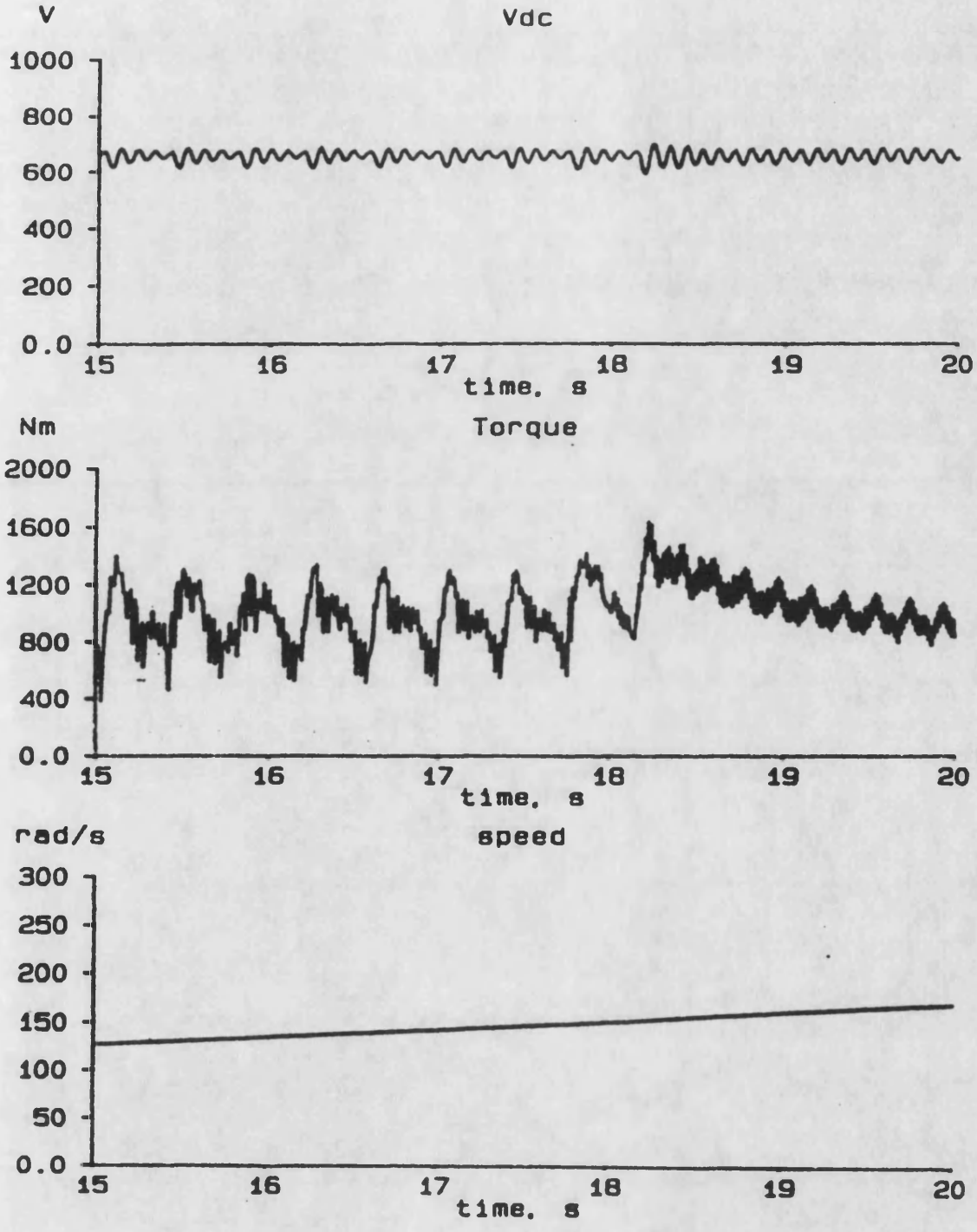

Figure 8.4-b System general performance

(DC link voltage, motor output torque, and motor speed)

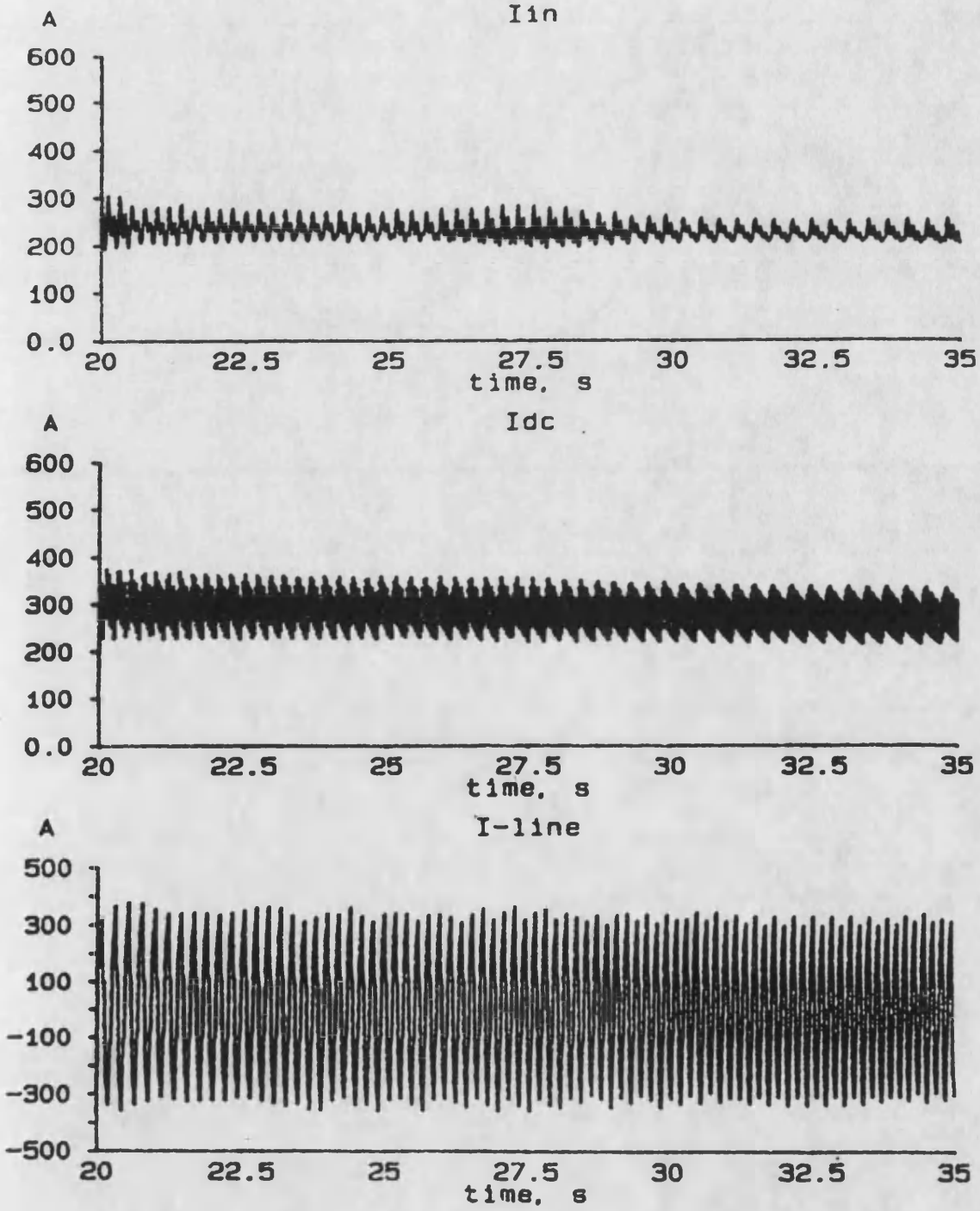

Figure 8.5-a System general performance

(system input-, DC link-, and motor line-current)

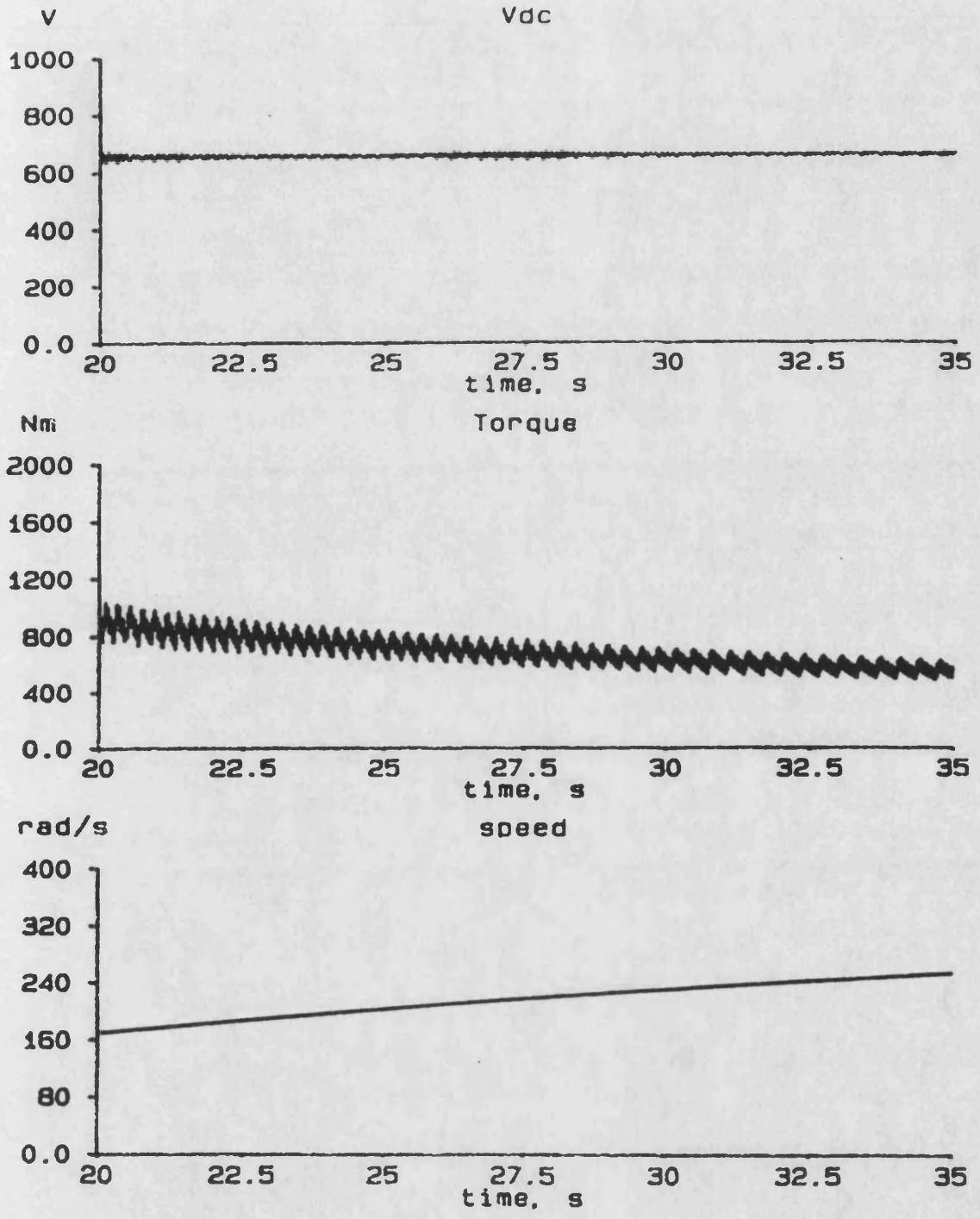

Figure 8.5-b System general performance

(DC link voltage, motor output torque, and motor speed)

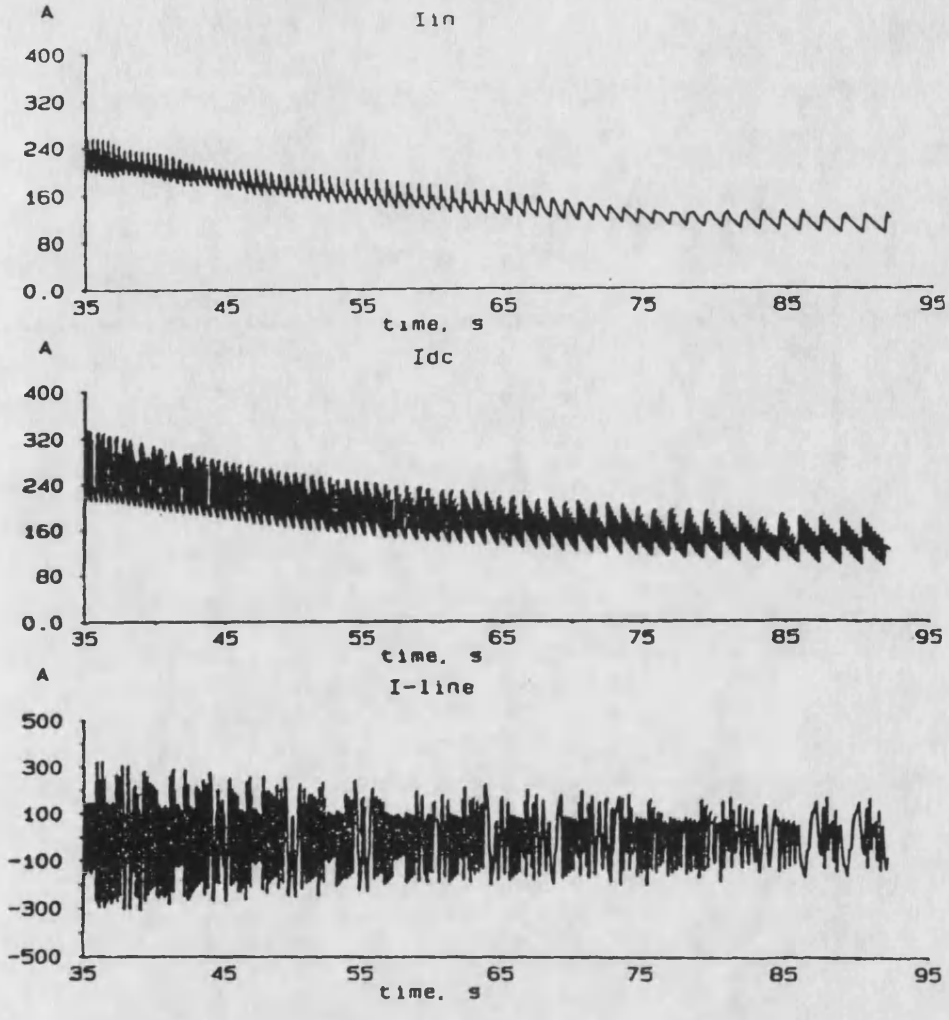

Figure 8.6-a System general performance
(system input-, DC link-, and motor line-current)

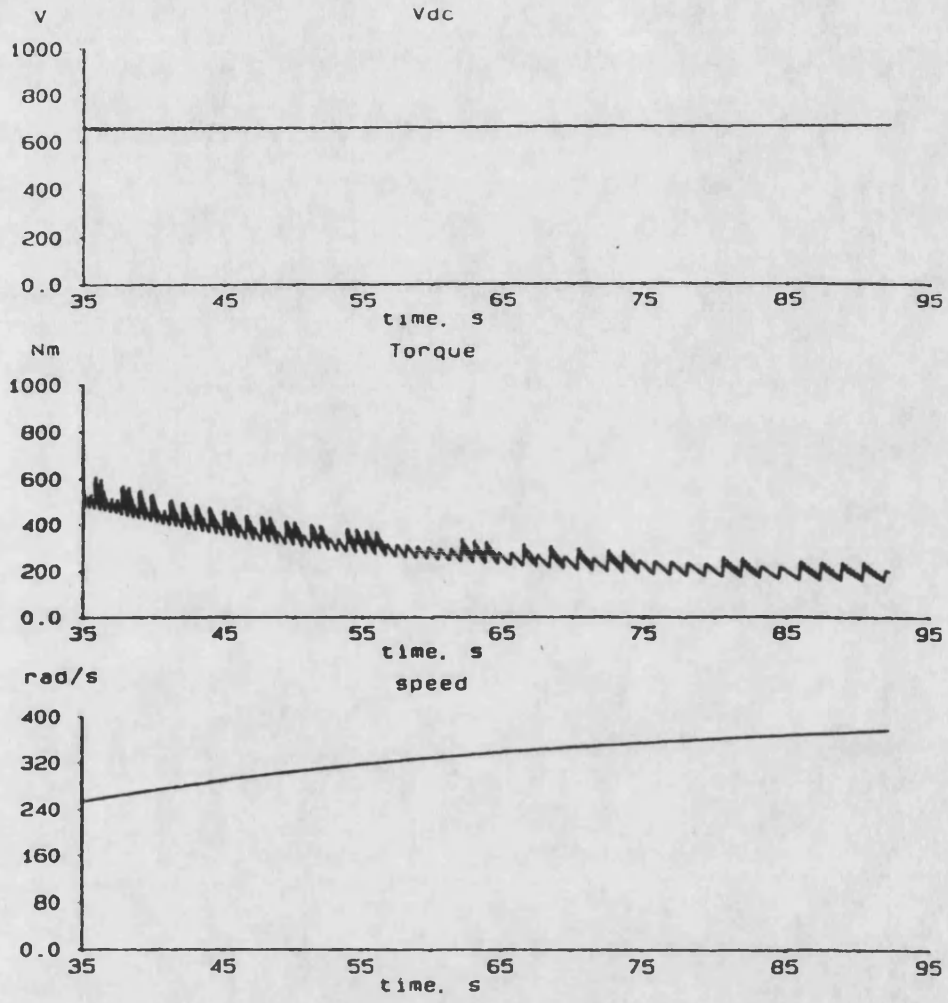

Figure 8.6-b System general performance

(DC link voltage, motor output torque, and motor speed)

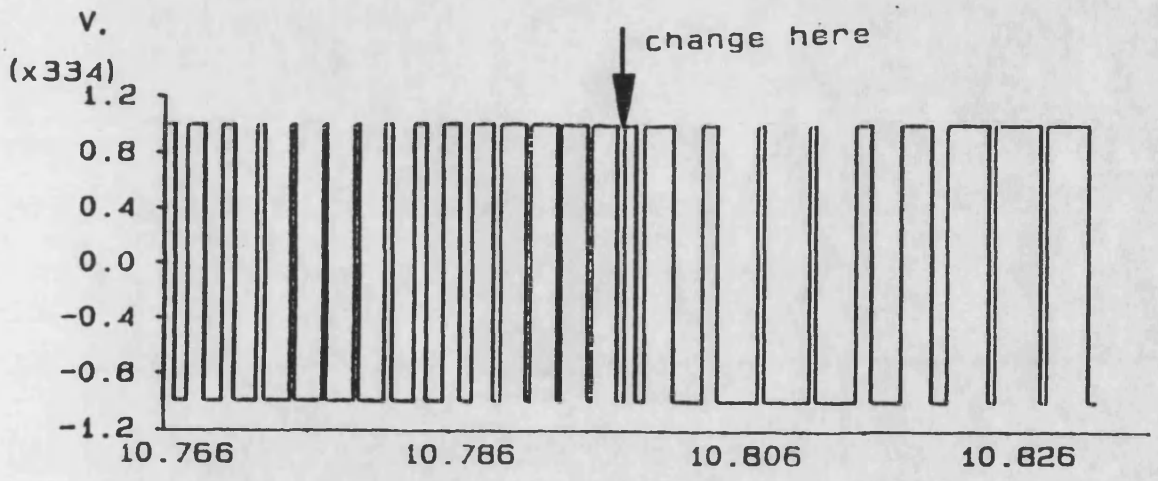

a). t = 10.8 s, Mr = 15 -> 9

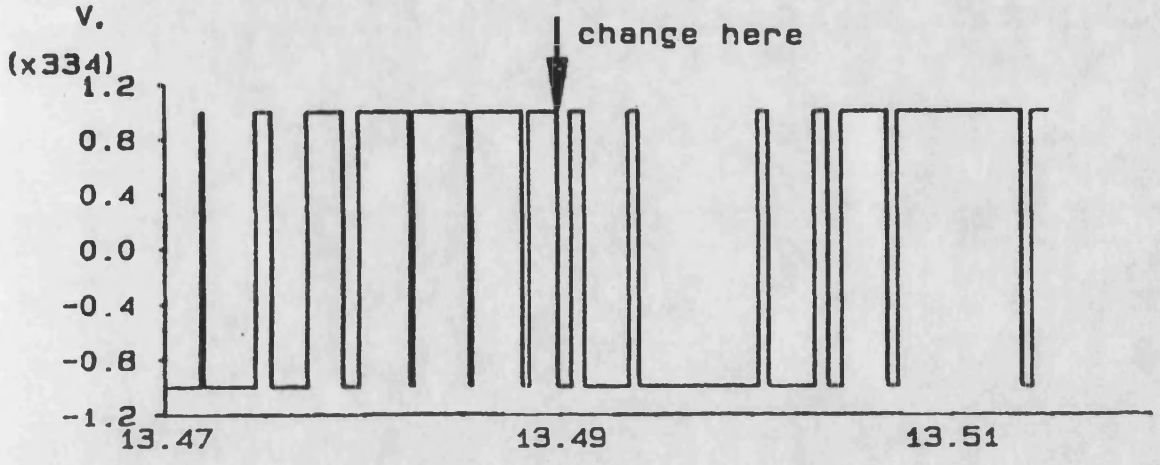

b). t = 13.49 s, Mr = 9 -> 9'

Figure 8.7 Gear change

(inverter output voltage)

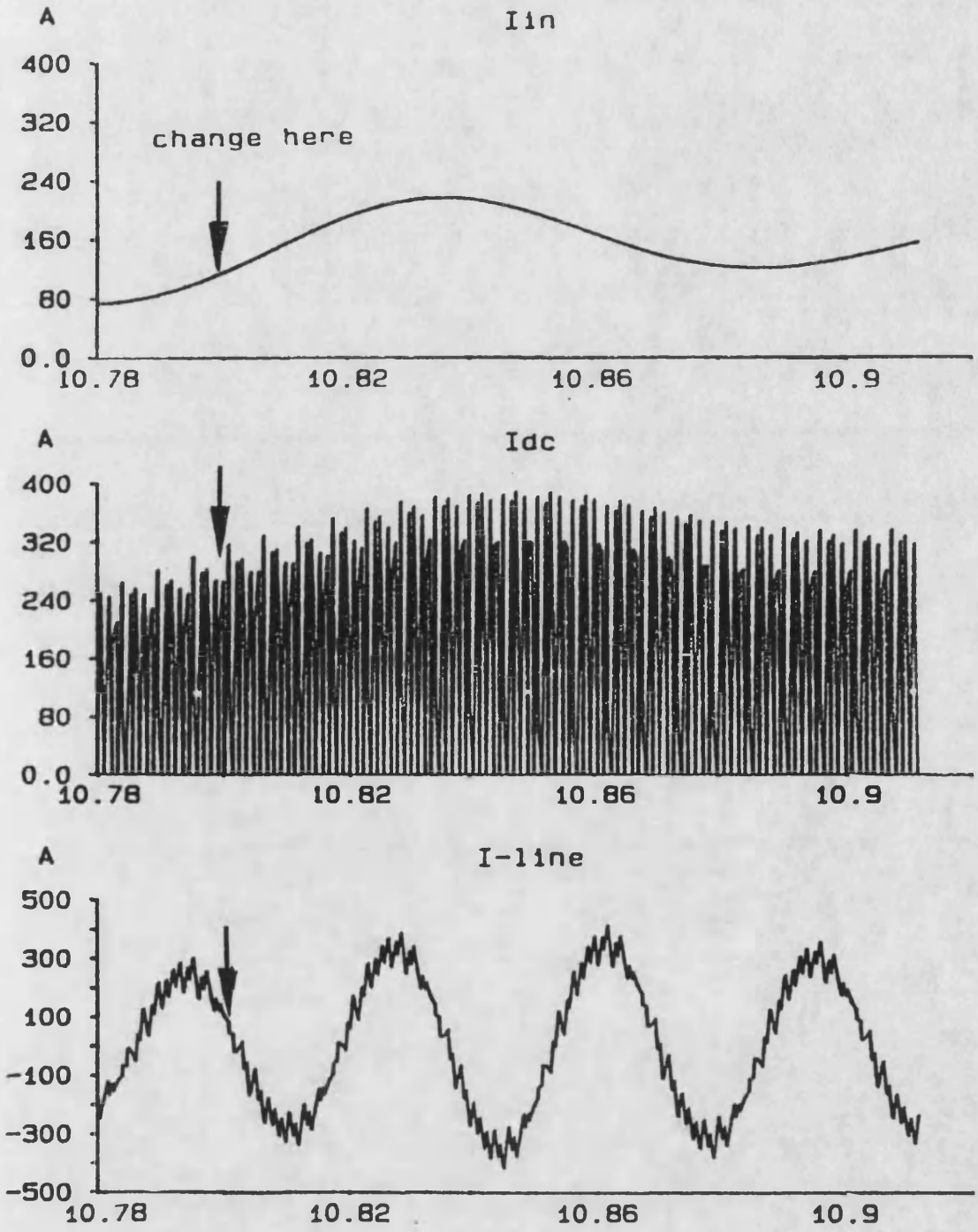

Figure 8.8-a Gear change

at: t = 10.8 s, Mr = 15 -> 9

(system input-, DC link-, and motor line-current)

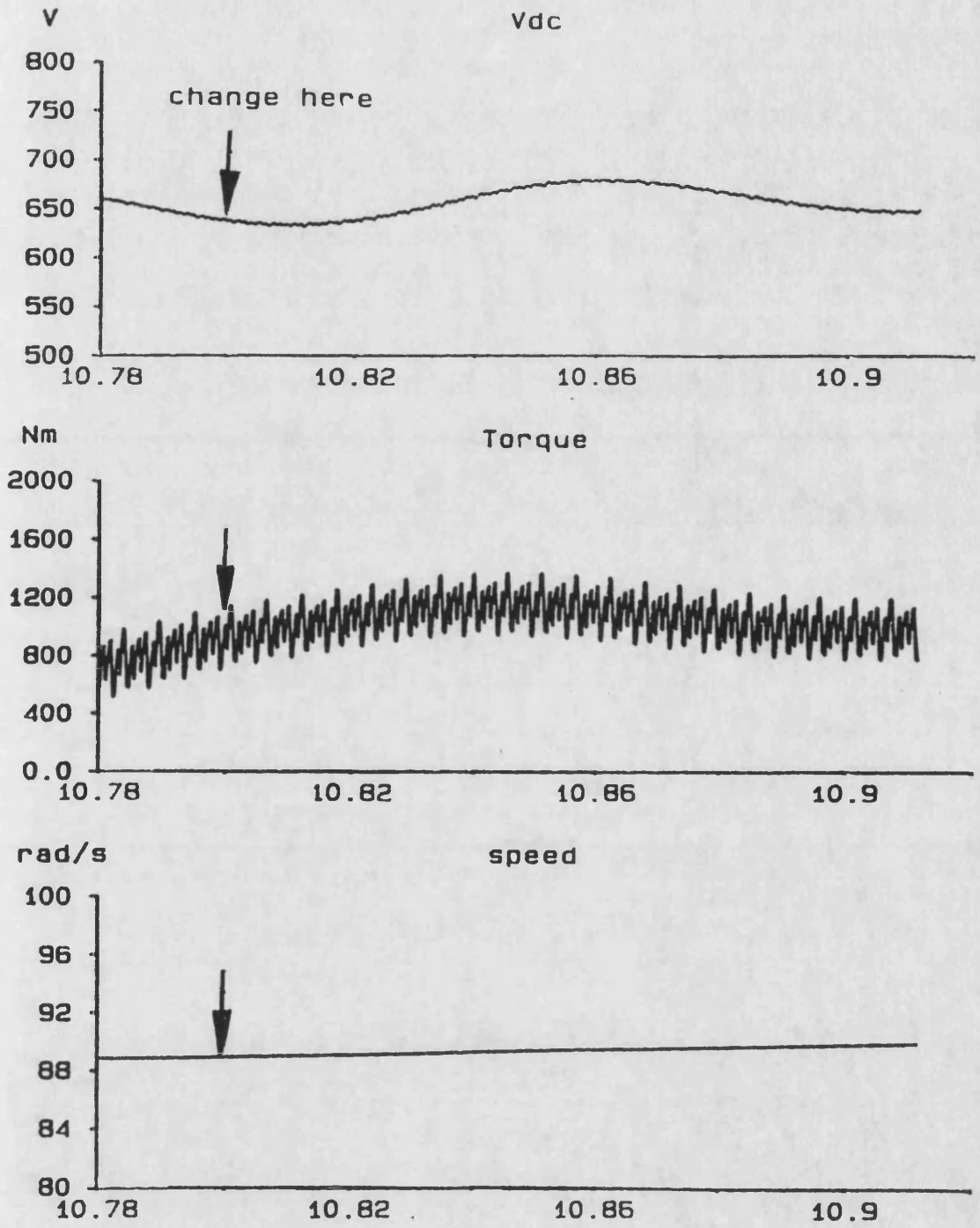

Figure 8.8-b Gear change

at: t = 10.8 s, Mr = 15 -> 9

(DC link voltage, motor output torque, and motor speed)

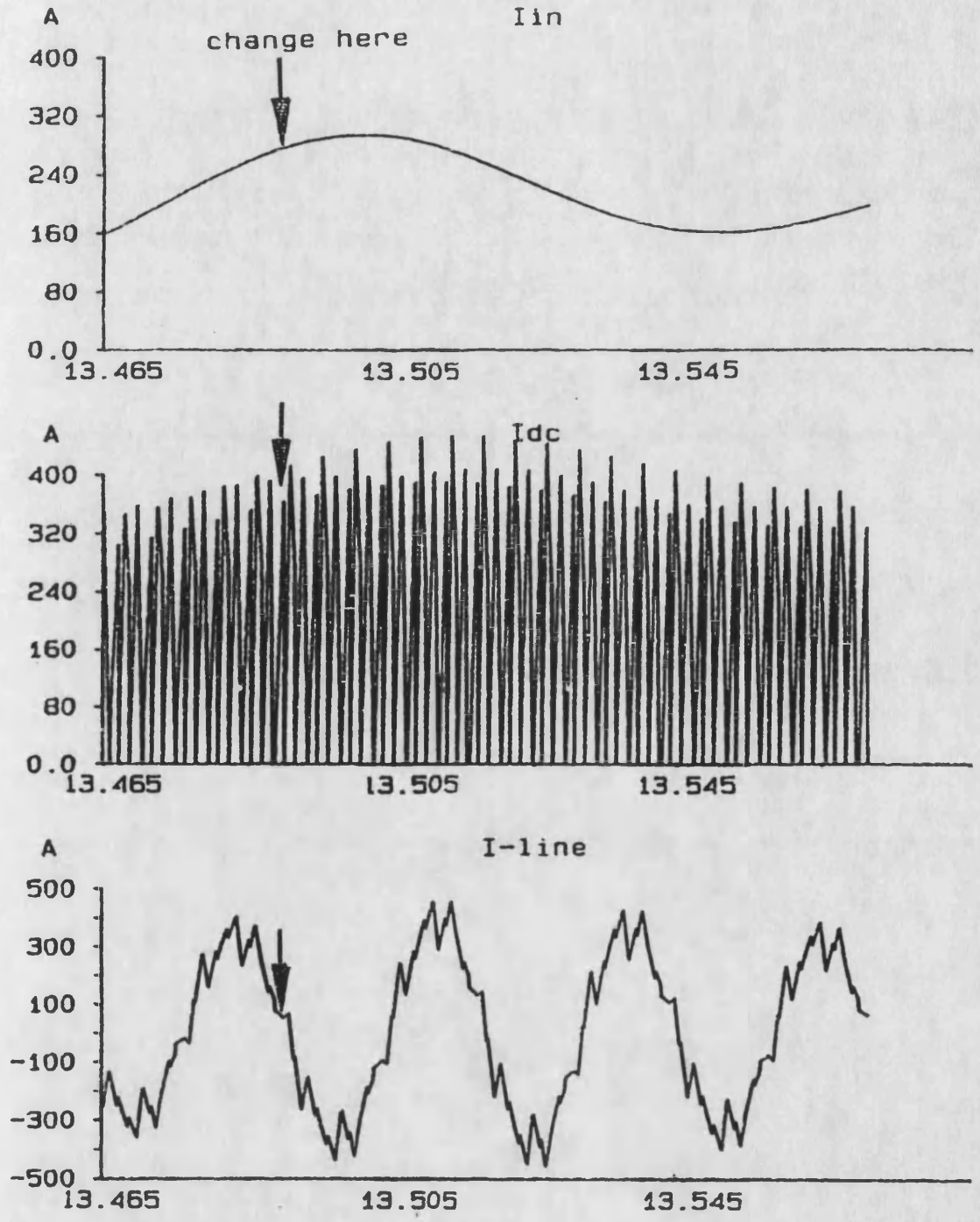

Figure 8.9-a Gear change

at: t = 13.49 s, Mr = 9 -> 9'

(system input-, DC link-, and motor line-current)

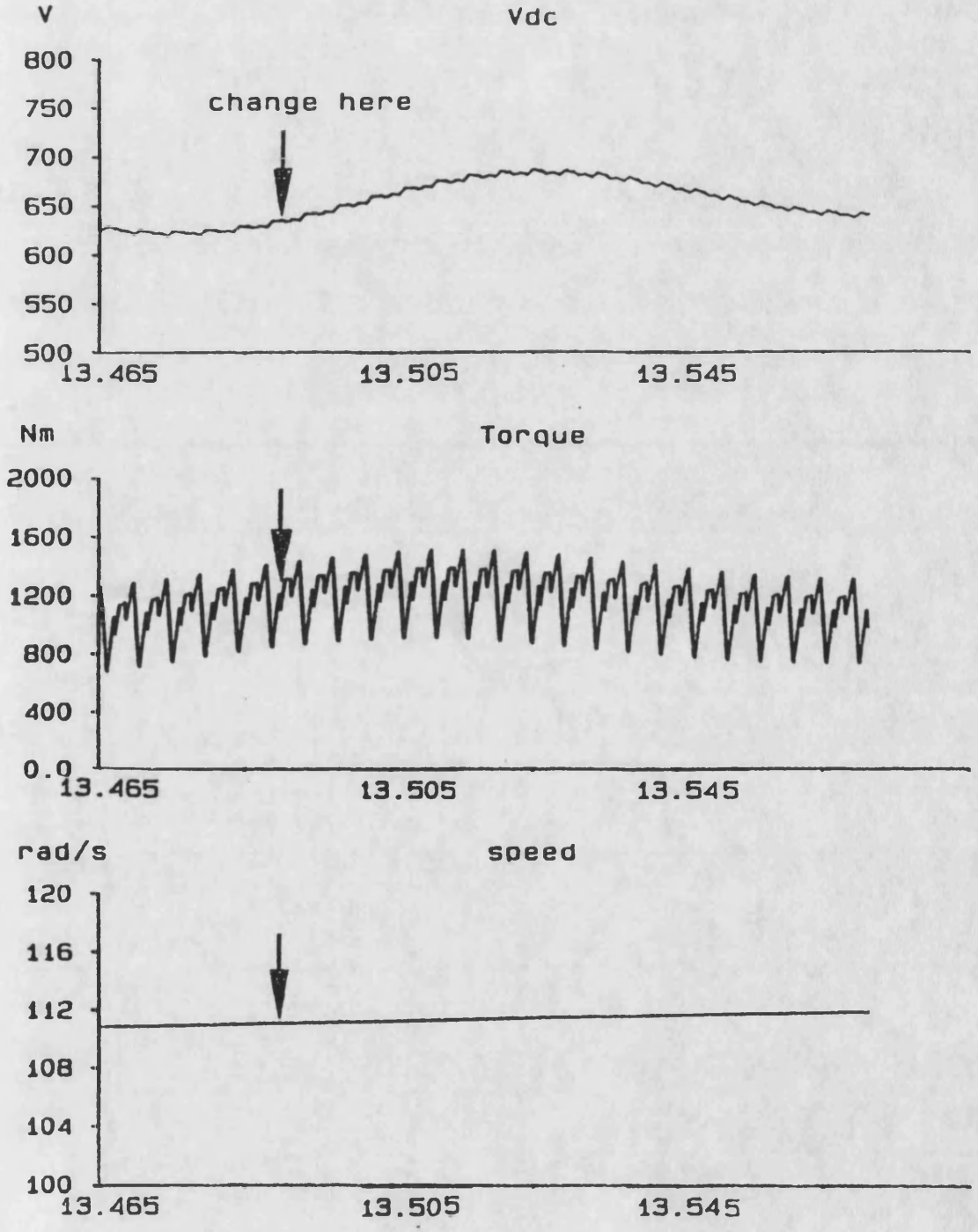

Figure 8.9-b Gear change

at: t = 13.49 s, Mr = 9 -> 9'

(DC link voltage, motor output torque, and motor speed)

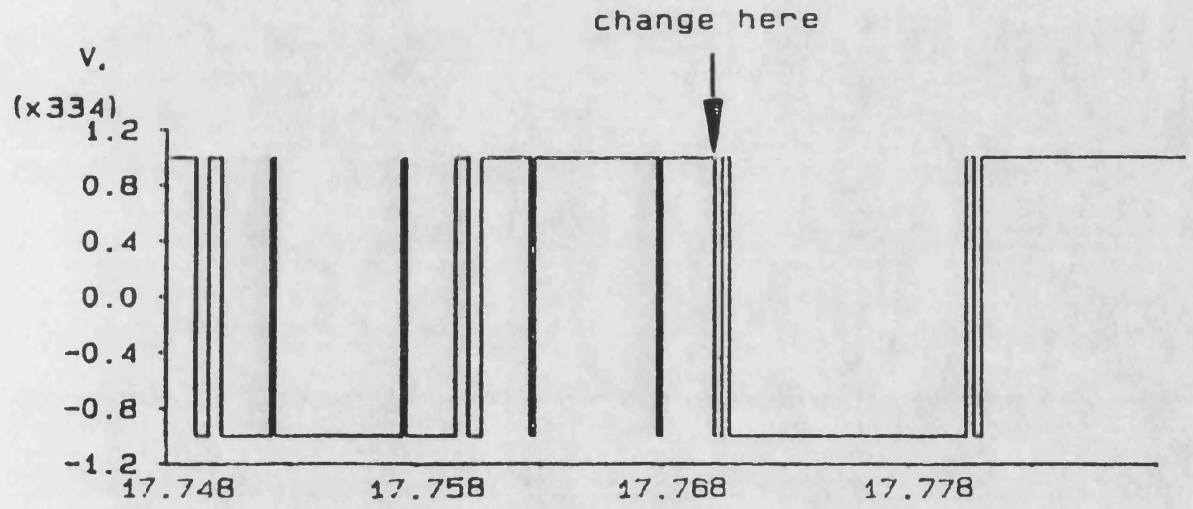

a). t = 17.77 s, Mr = 9'

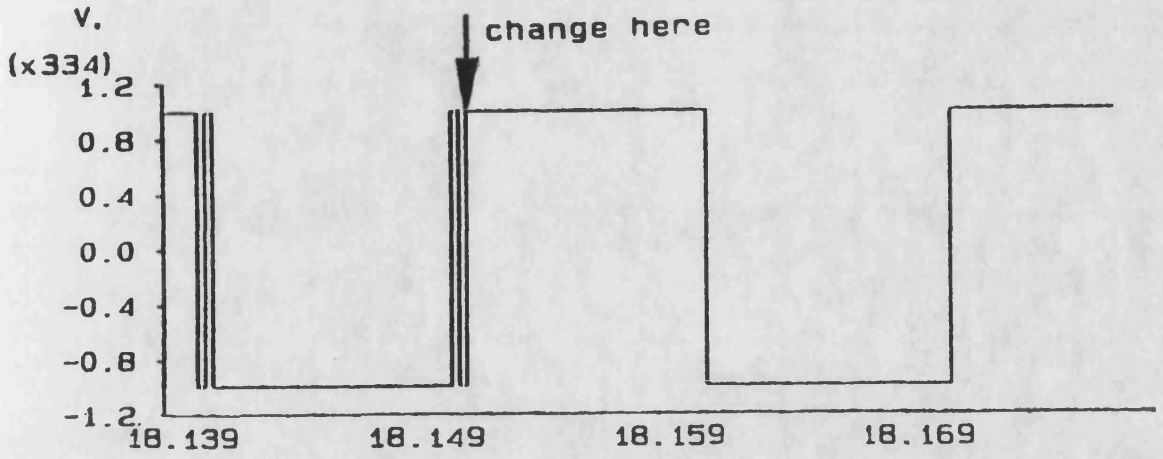

b). t = 18.16 s, square wave

Figure 8.10 Pulse dropping
(inverter output voltage)

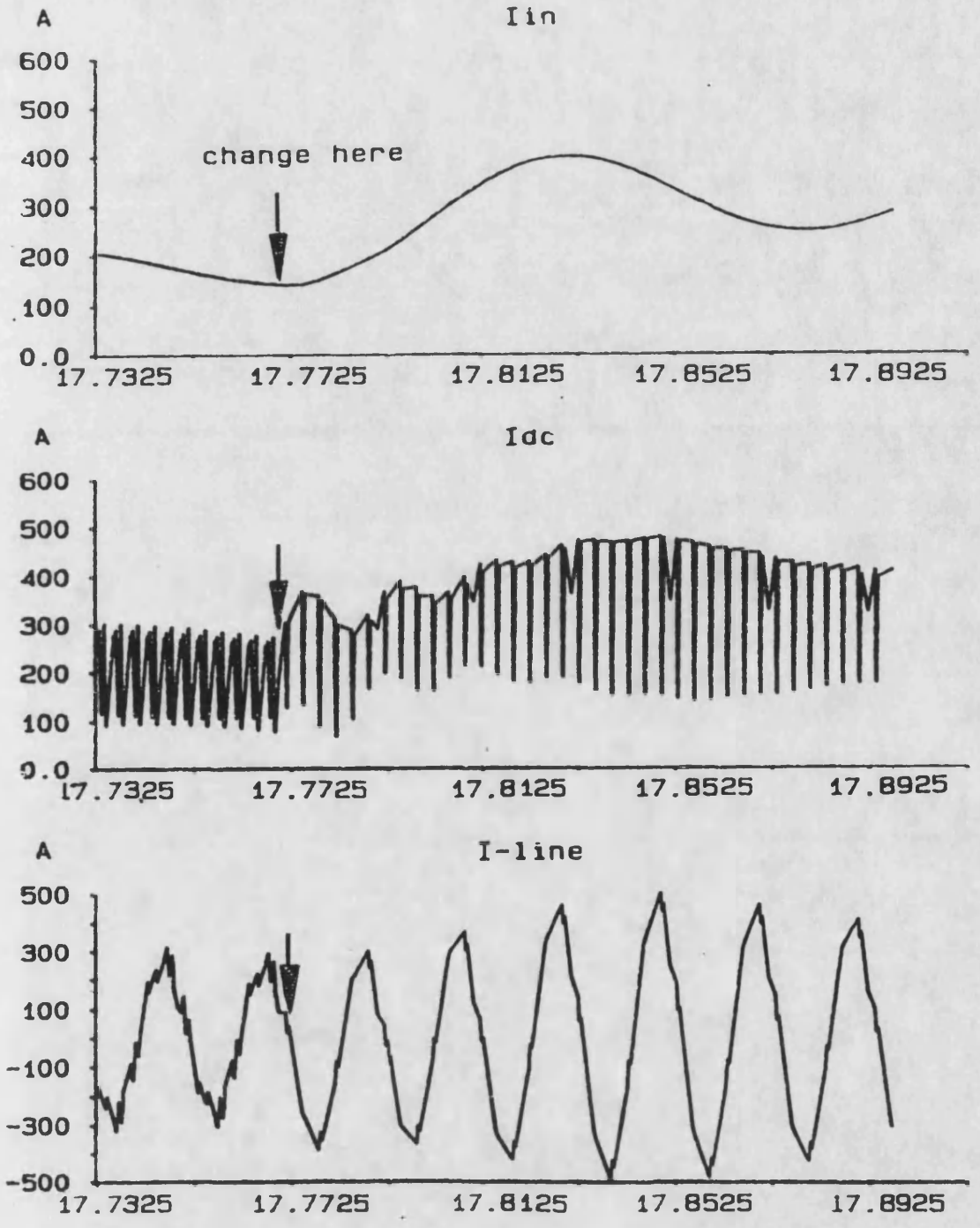

Figure 8.11-a Pulse dropping

at: t = 17.77 s, Mr = 9'

(system input-, DC link-, and motor line-current)

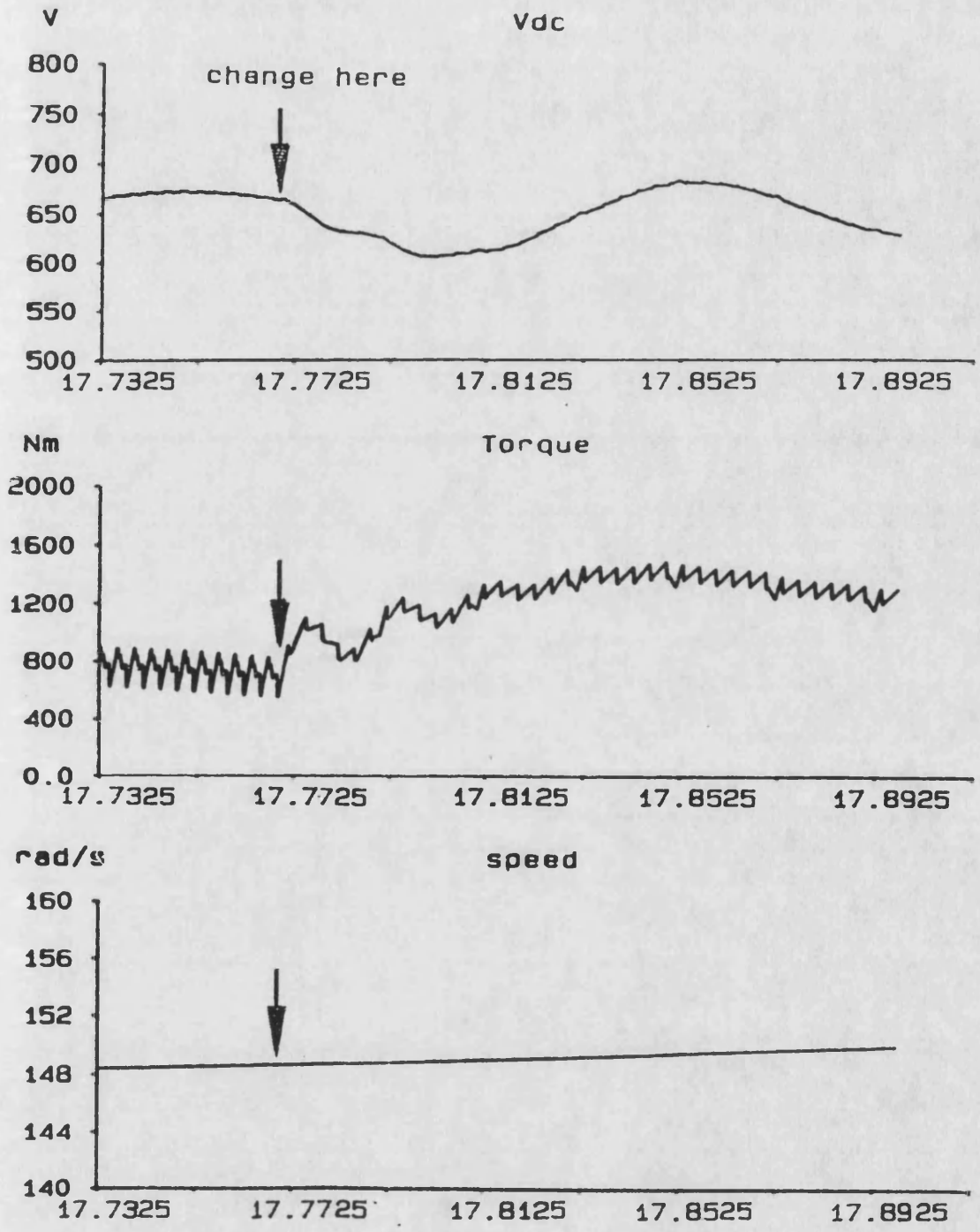

Figure 8.11-b Pulse dropping

at: t = 17.77 s, Mr = 9'

(DC link voltage, motor output torque, and motor speed)

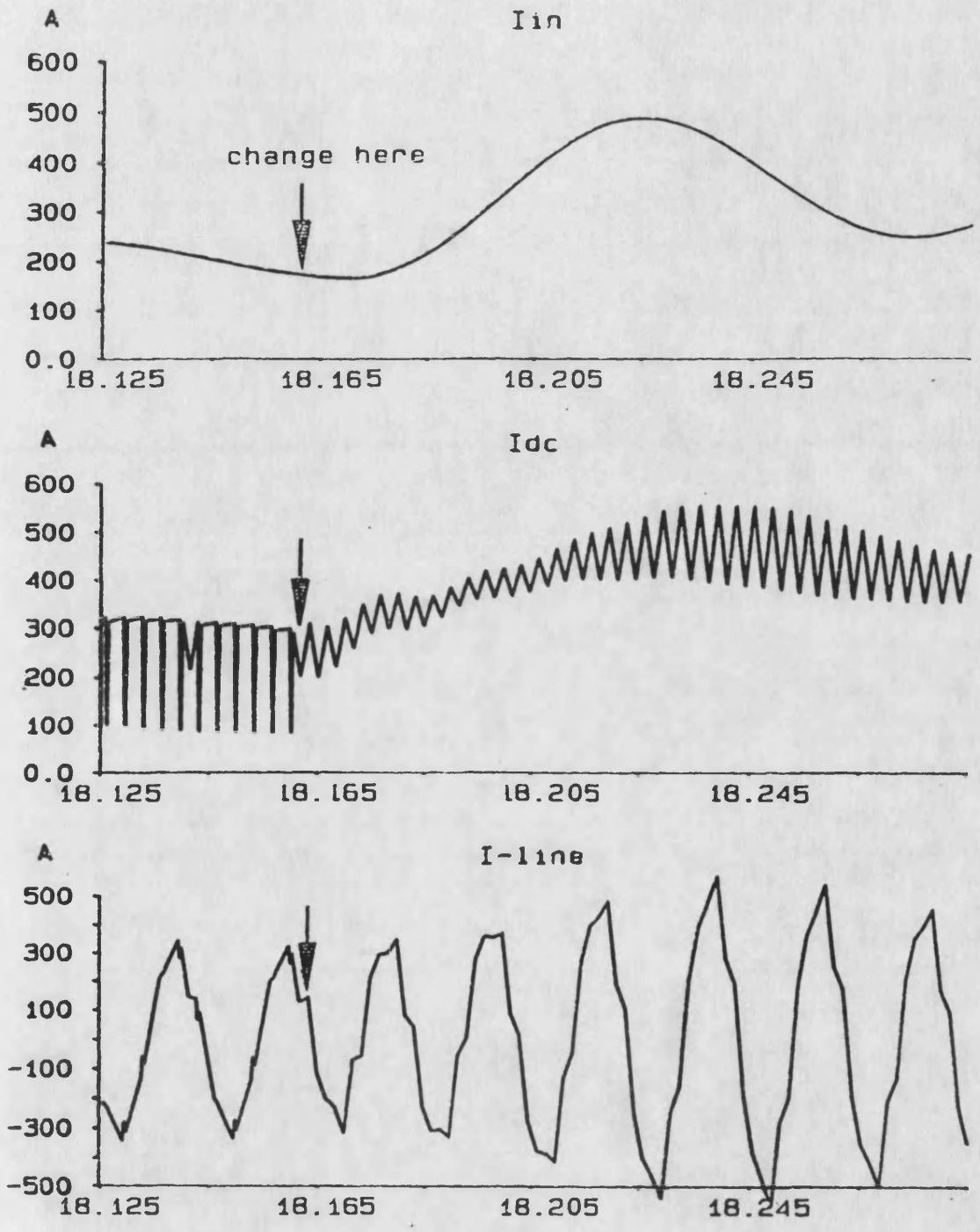

Figure 8.12-a Pulse dropping

at: t = 18.16 s, square wave

(system input-, DC link-, and motor line-current)

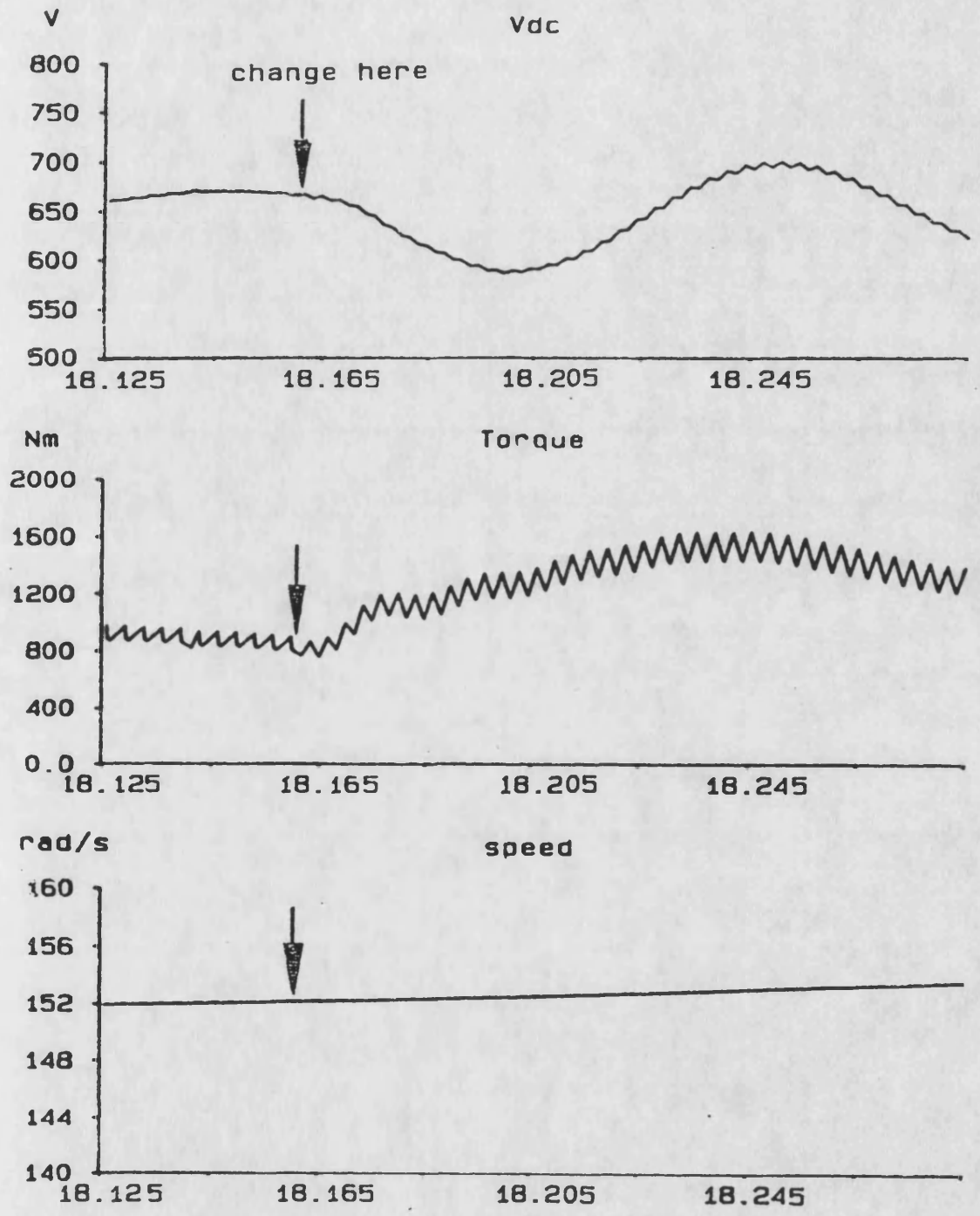

Figure 8.12-b Pulse dropping

at: t = 18.16 s, square wave

(DC link voltage, motor output torque, and motor speed)

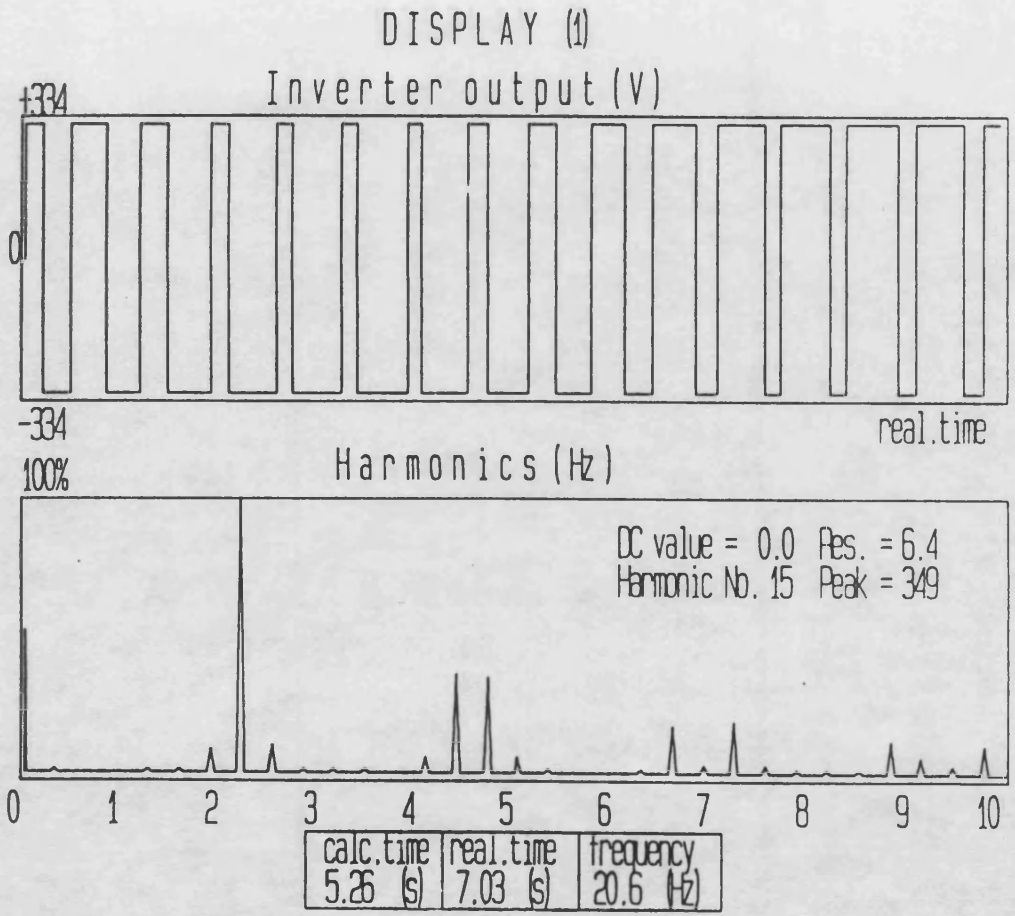

Figure 8.13-a PWM waveform and its harmonic spectrum, Mr = 15

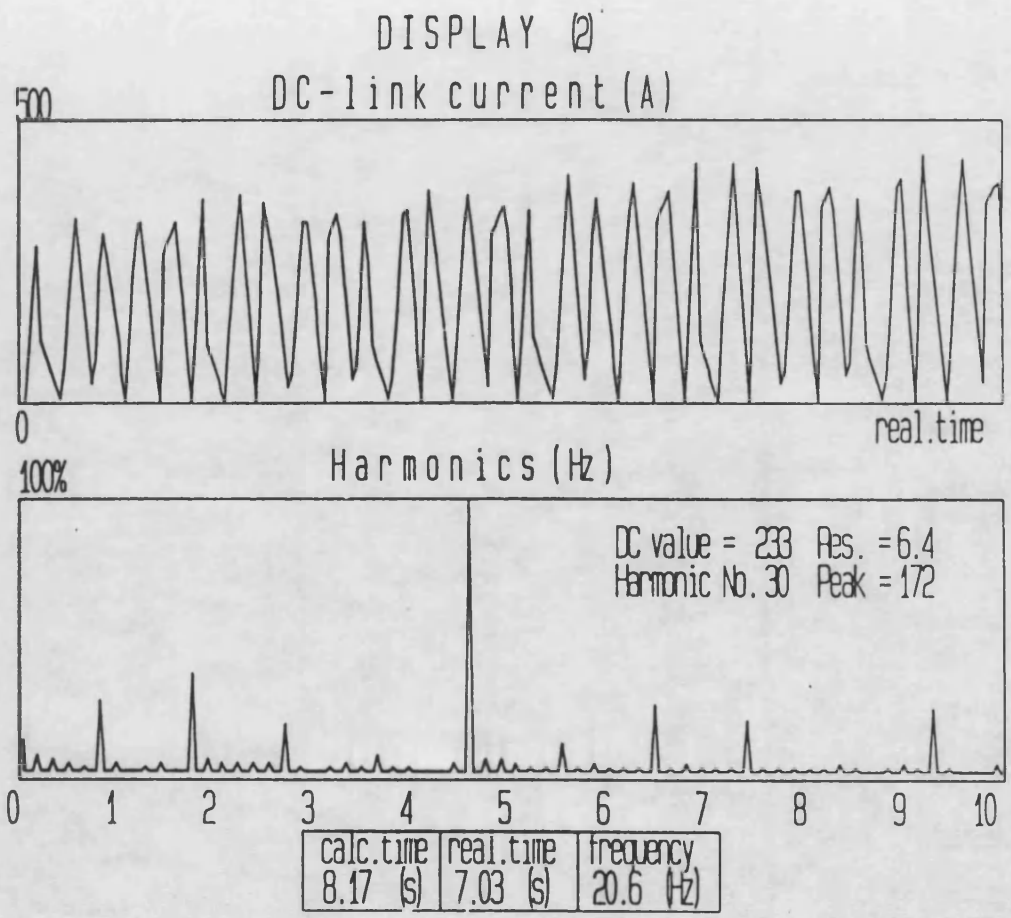

Figure 8.13-b DC link current and its harmonic spectrum, Mr = 15

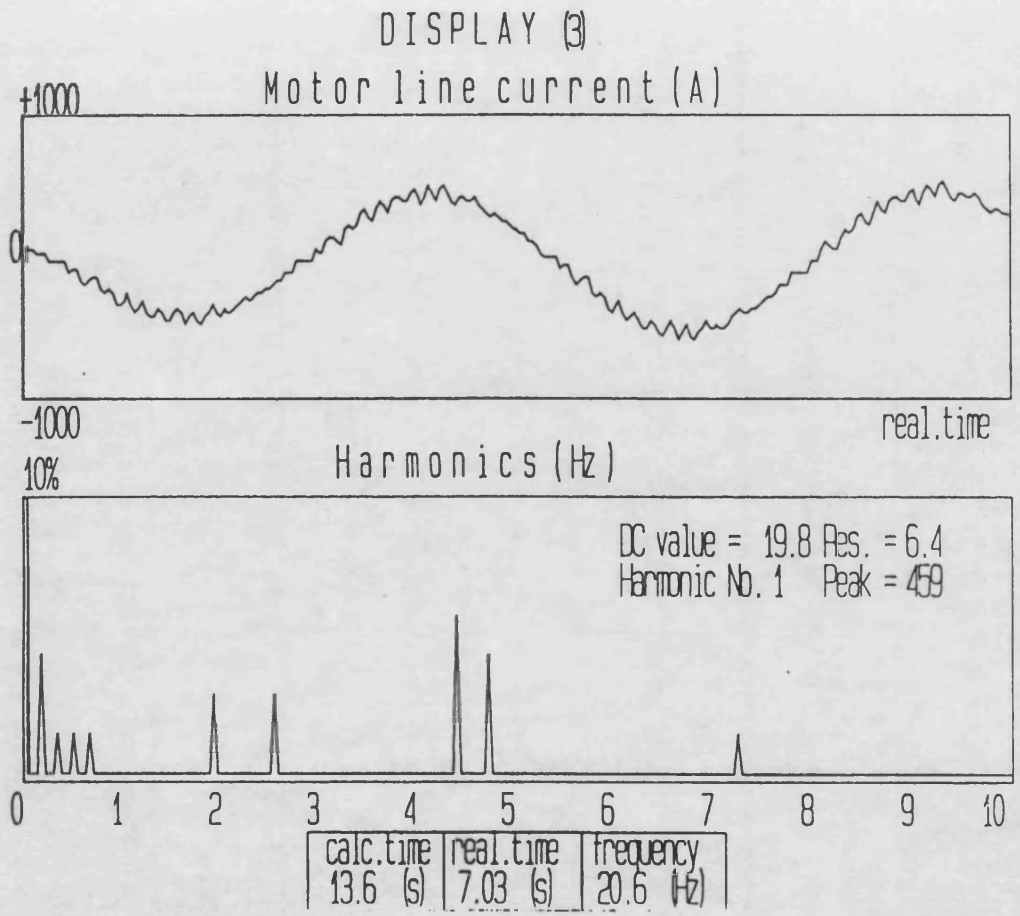

Figure 8.13-c Motor line current and its harmonic spectrum, Mr = 15

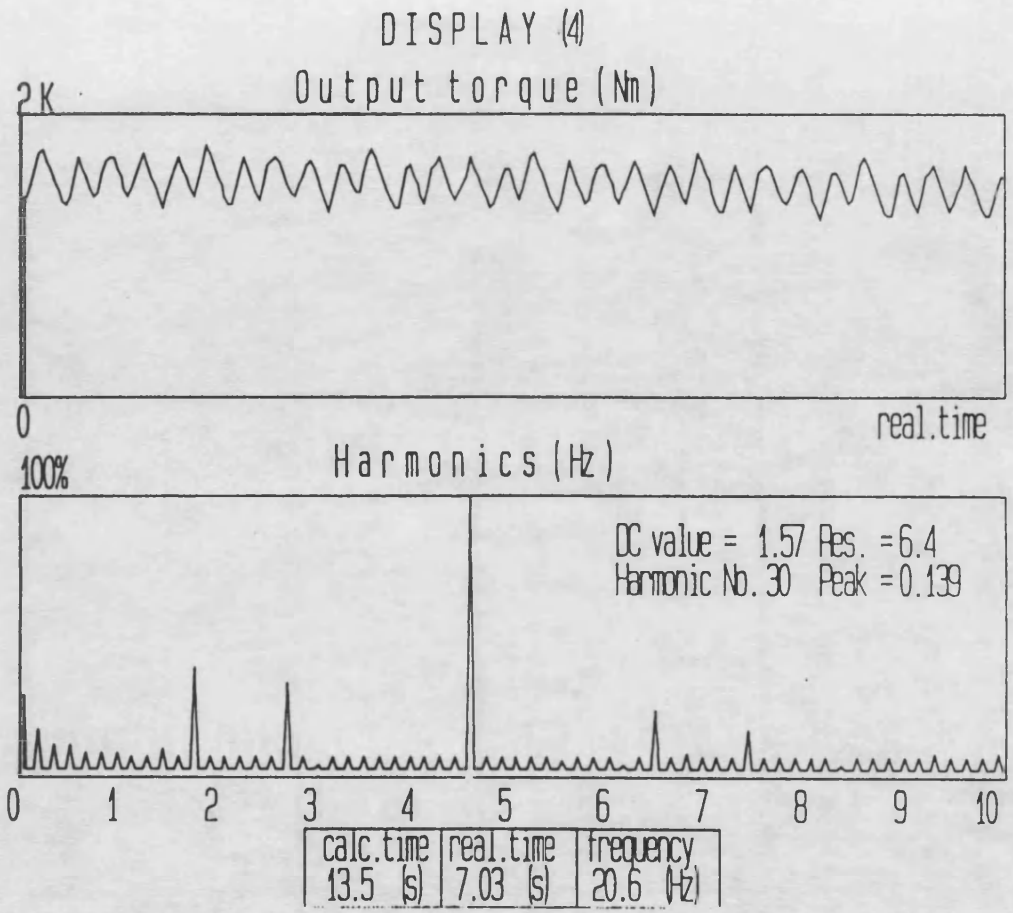

Figure 8.13-d Motor output torque and its harmonic spectrum, Mr = 15

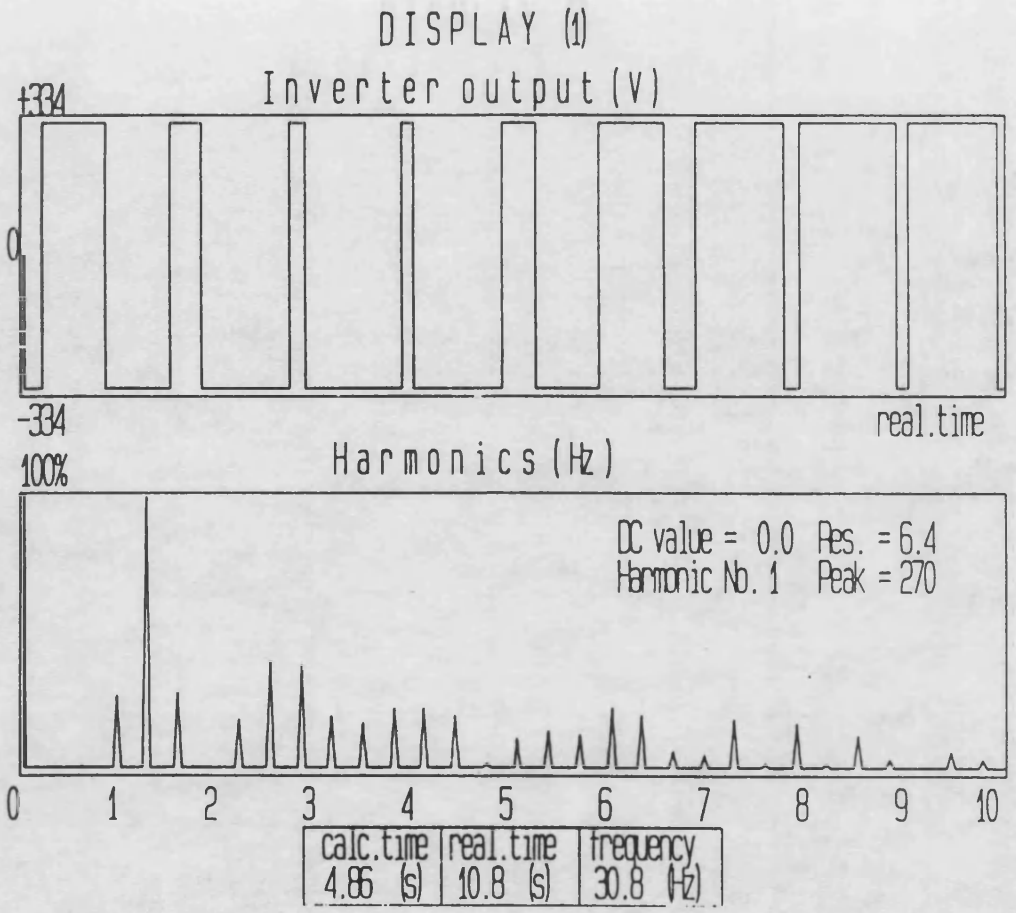

Figure 8.14-a PWM waveform and its harmonic spectrum, Mr = 9

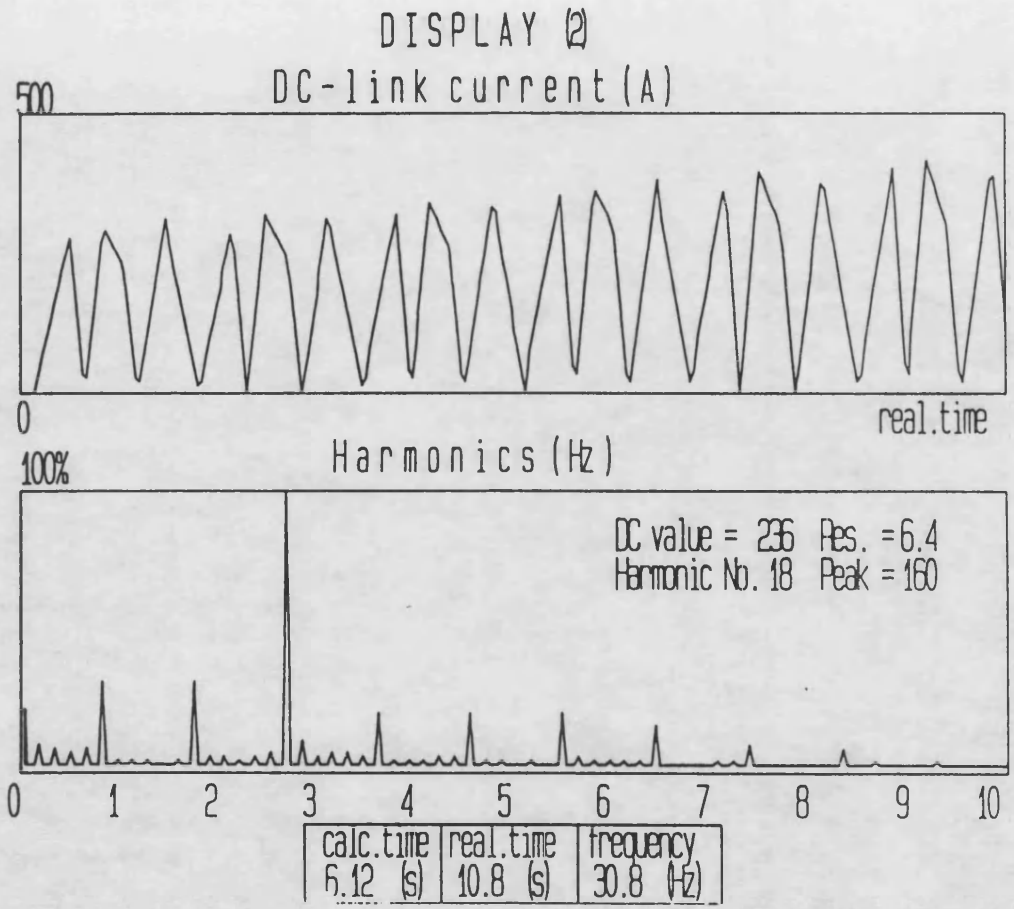

Figure 8.14-b DC link current and its harmonic spectrum, Mr = 9

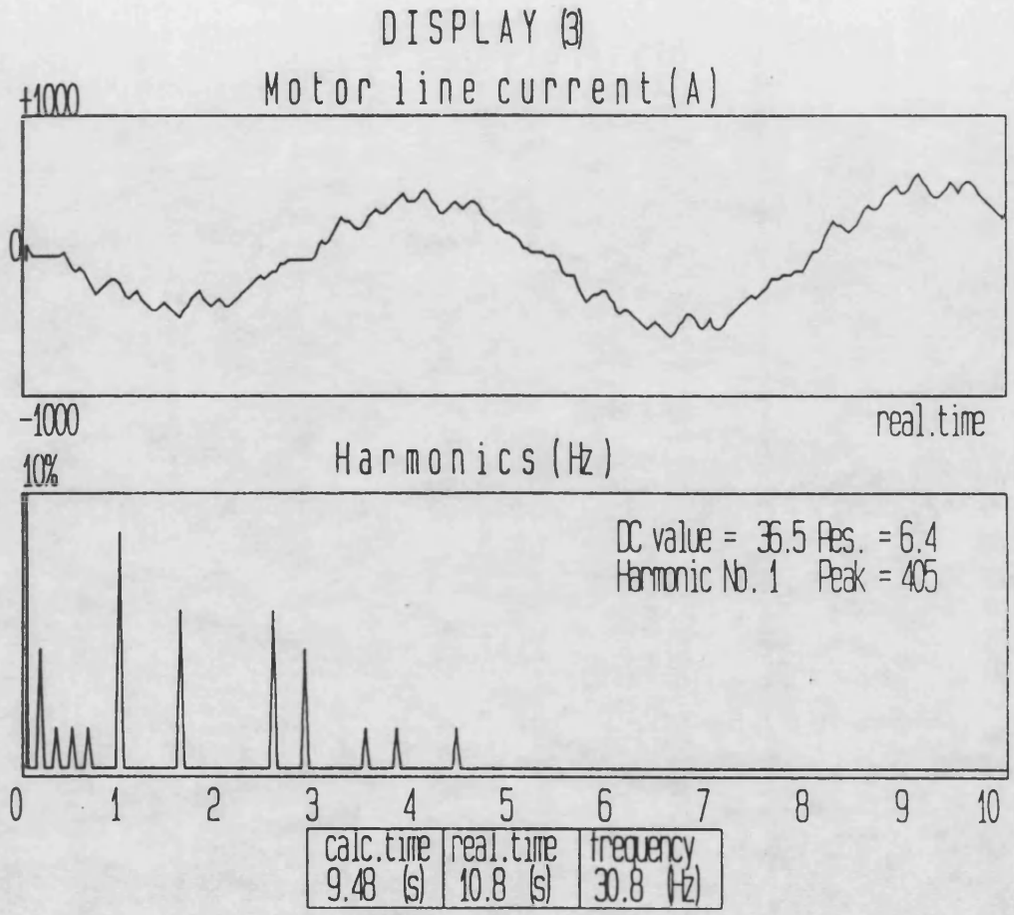

Figure 8.14-c Motor line current and its harmonic spectrum, Mr = 9

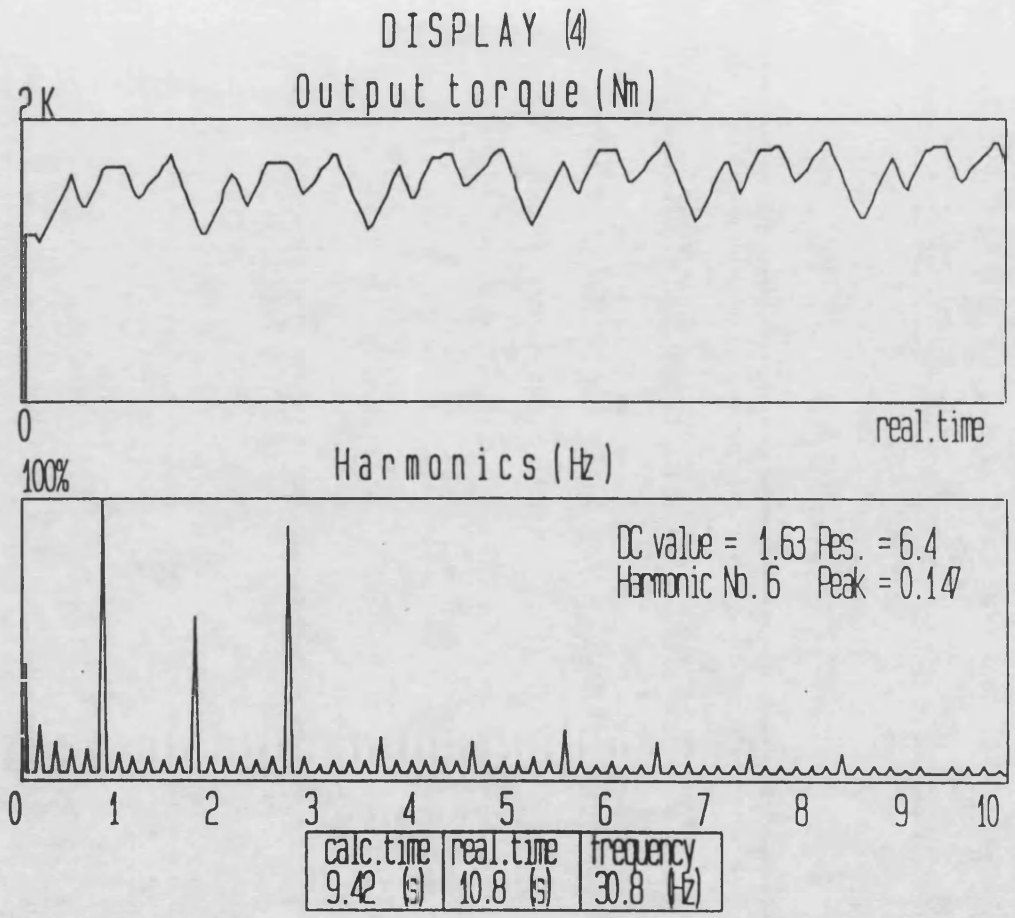

Figure 8.14-d Motor output torque and its harmonic spectrum, Mr = 9

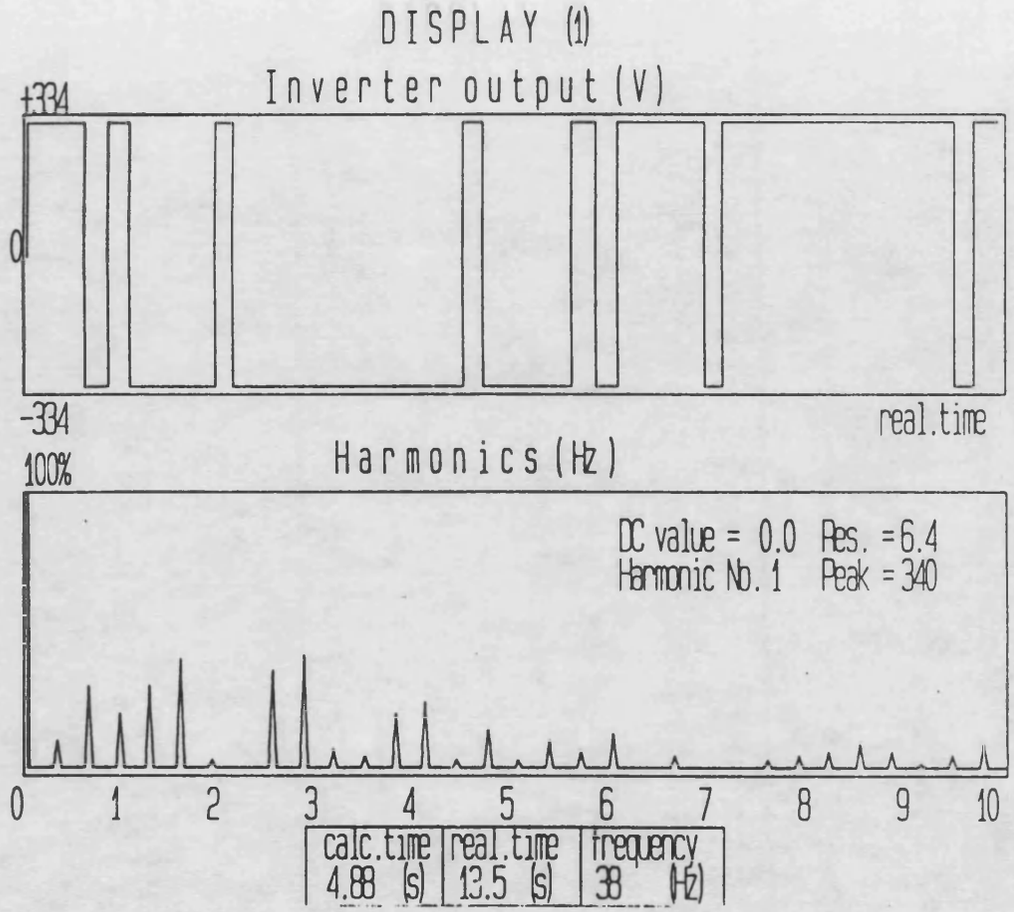

Figure 8.15-a PWM waveform and its harmonic spectrum, Mr = 9'

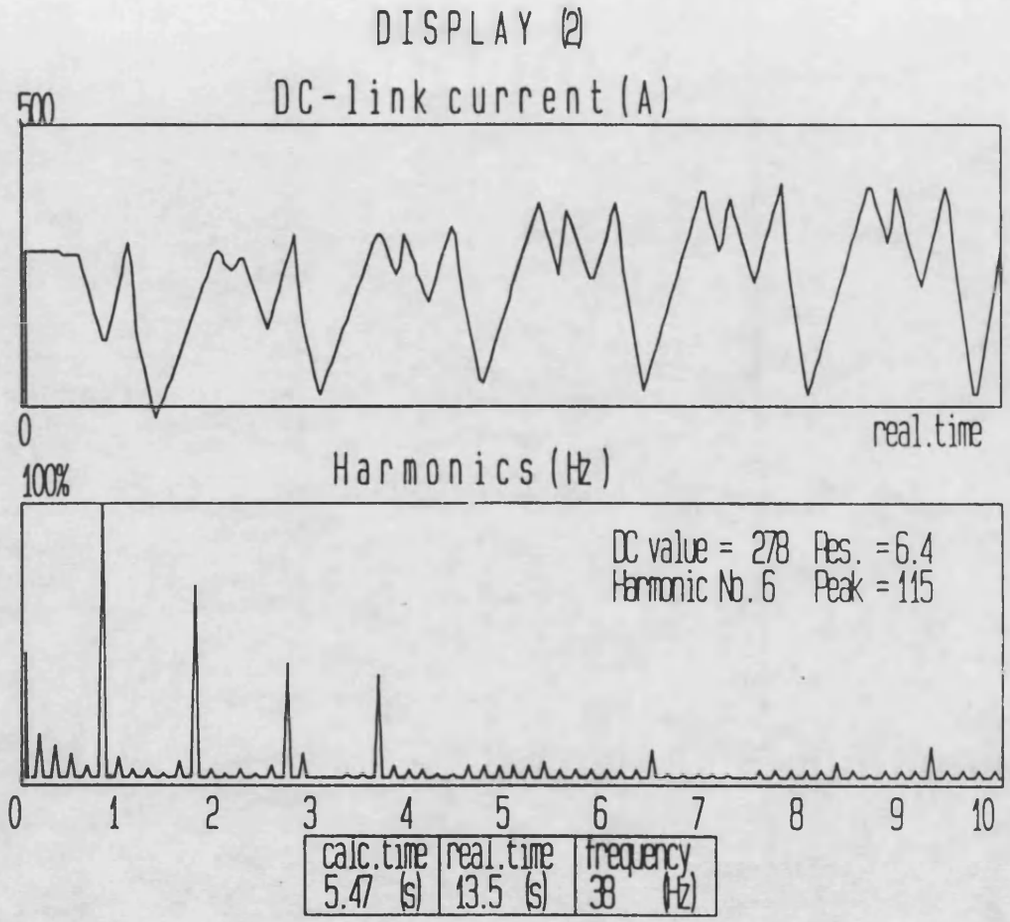

Figure 8.15-b DC link current and its harmonic spectrum, Mr = 9'

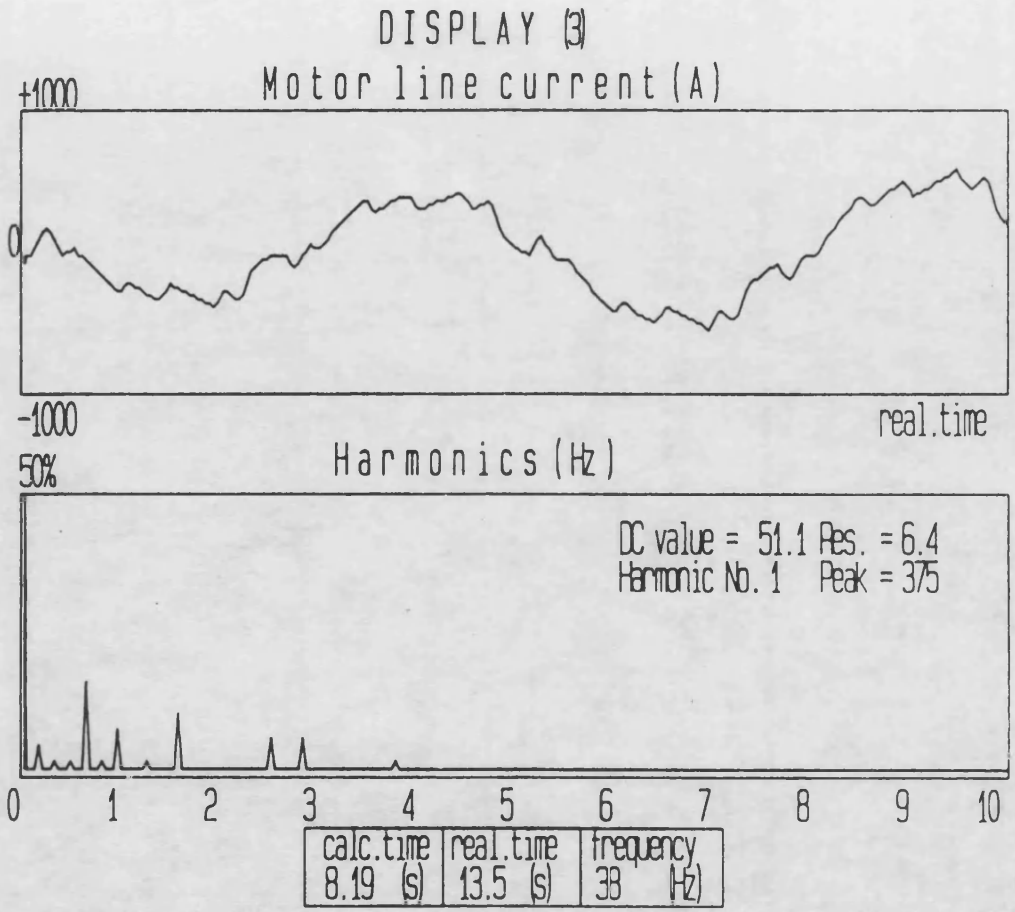

Figure 8.15-c Motor line current and its harmonic spectrum, Mr = 9'

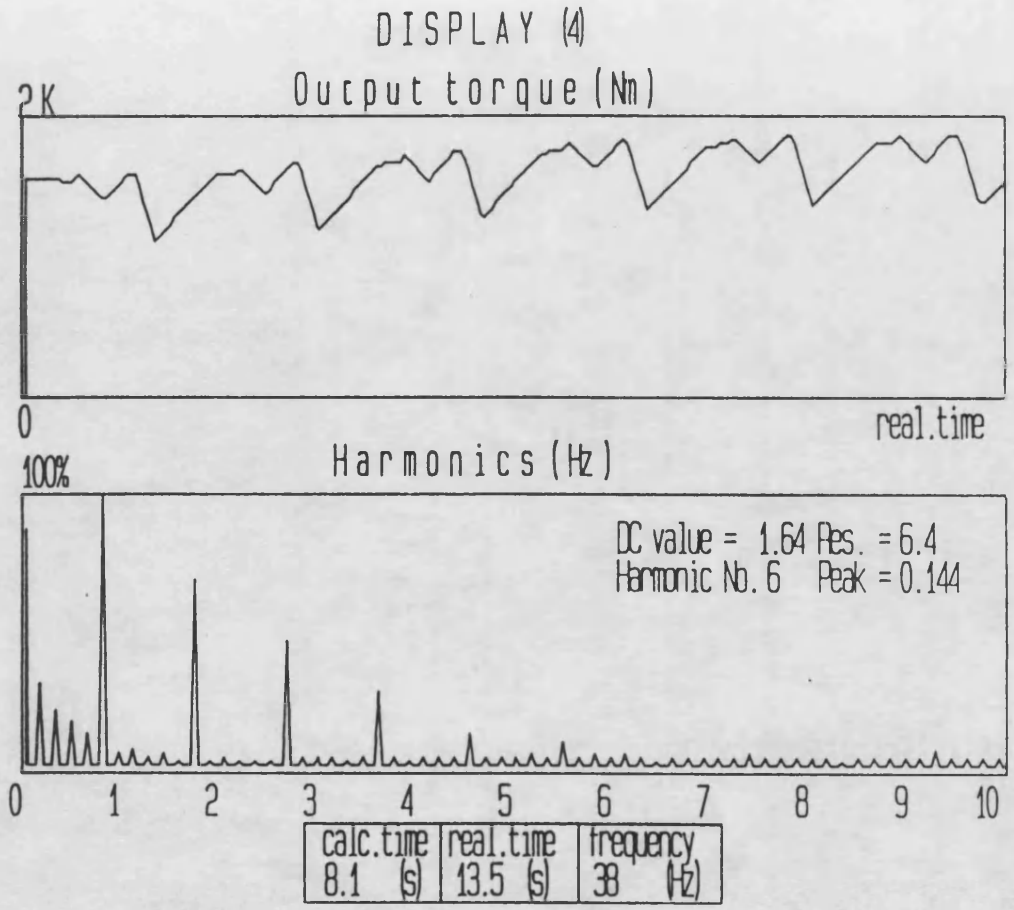

Figure 8.15-d Motor output torque and its harmonic spectrum, Mr = 9'

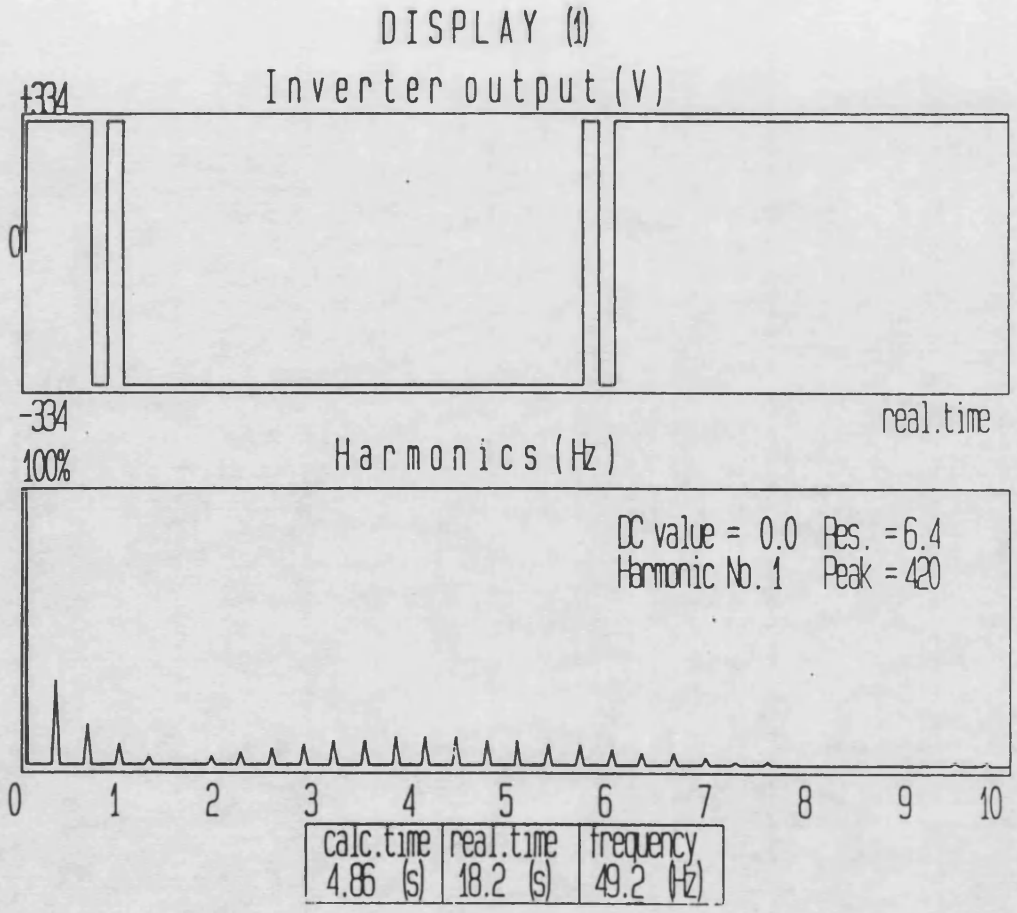

Figure 8.16-a PWM waveform and its harmonic spectrum, Mr = 9'

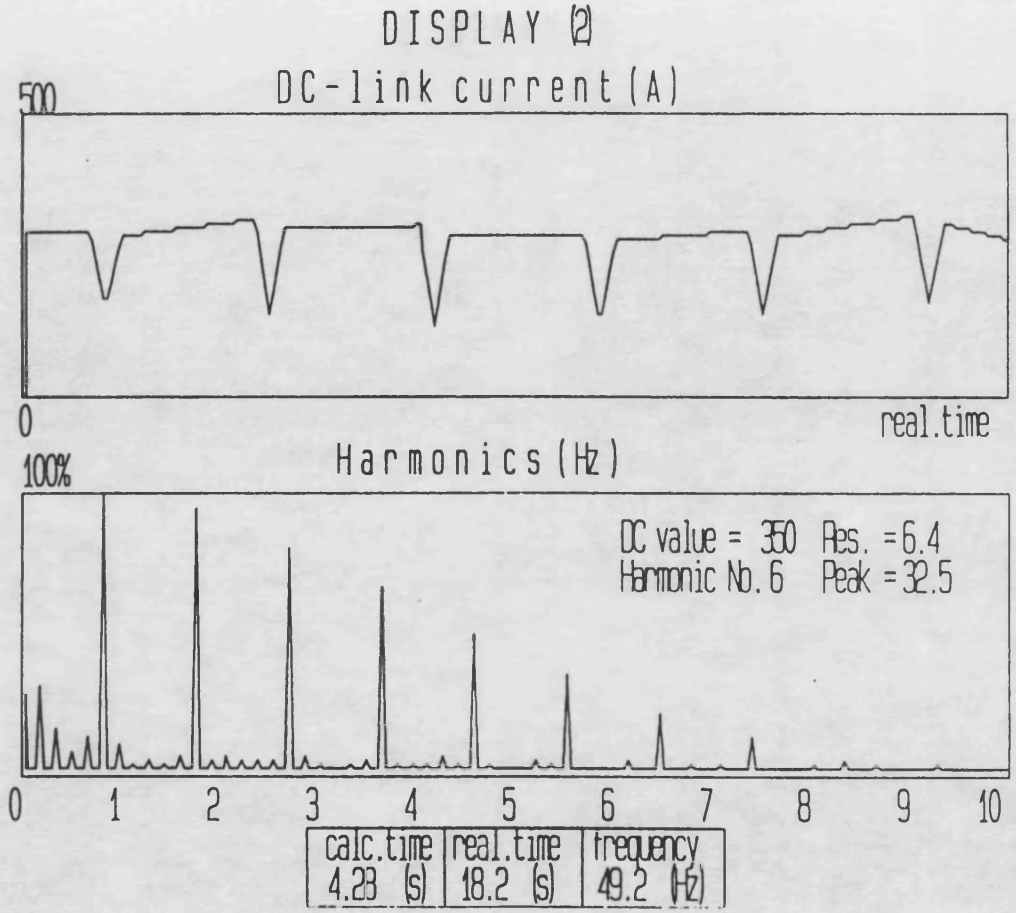

Figure 8.16-b DC link current and its harmonic spectrum, Mr = 9'

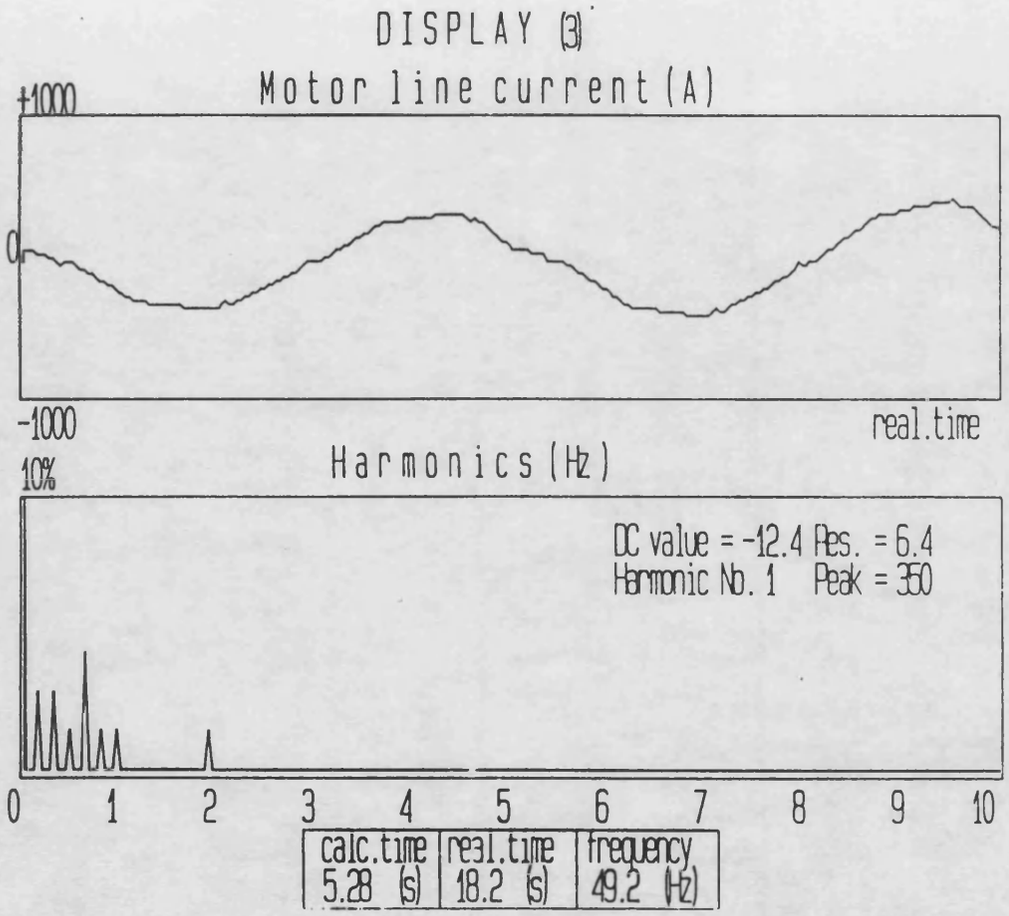

Figure 8.16-c Motor line current and its harmonic spectrum, Mr = 9'

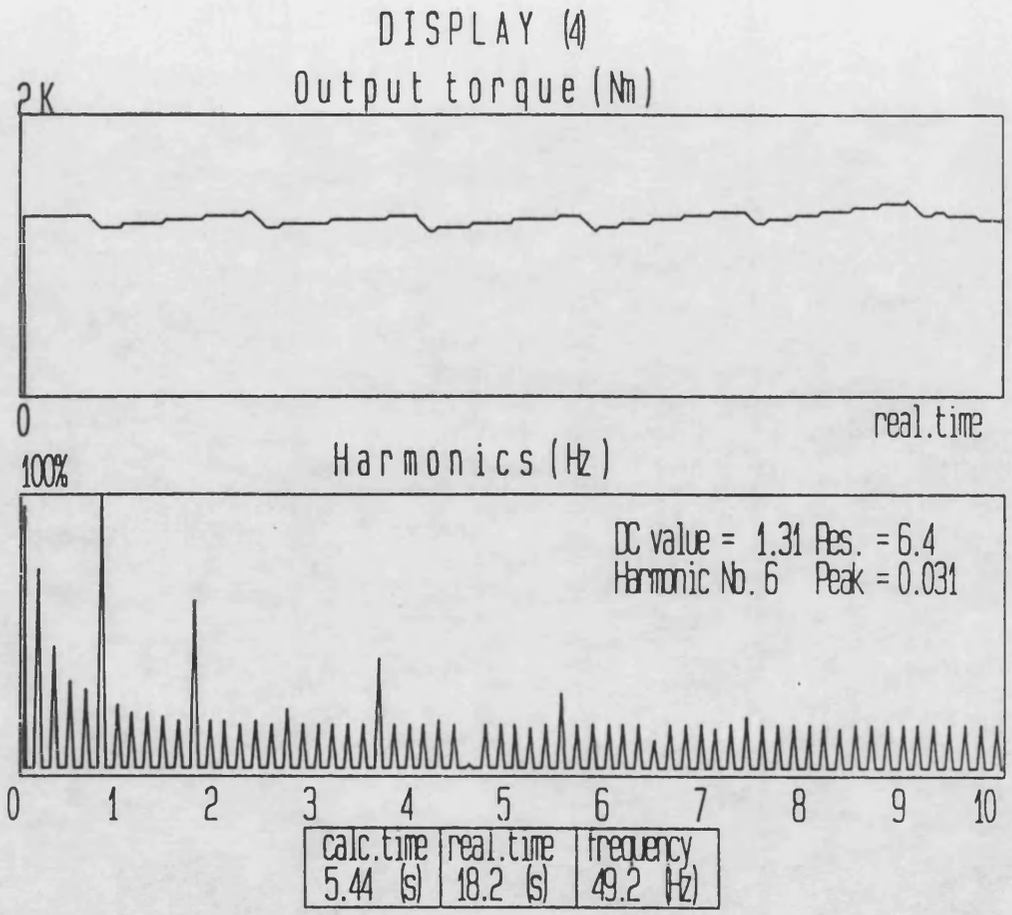

Figure 8.16-d Motor output torque and its harmonic spectrum, Mr = 9'

Chapter 9 : Conclusions and further work

9.1 Introduction

In this research, an on-line simulator for VSI-SCIM drives for rapid-transit has been implemented on a multi-processor computer. A laboratory based small scale traction drive has also been constructed and was used to verify the on-line simulator.

In this chapter, the presented work will be discussed. Some conclusions are drawn and suggestions for further work will also be given.

9.2 Conclusions

9.2.1 PWM schemes and signalling compatibility

Chapter 3 outlines various PWM schemes. Of the different schemes, the optimised PWM schemes are the most desirable from the point of view of railway signalling compatibility. The harmonic elimination technique can be used where some harmonics are particularly dangerous and must be eliminated. The application of the harmonic minimisation technique can also optimise the system performance and reduce the interference to the environment.

In the case of VSI-SCIM traction drives, the DC supply circuits include the rails themselves, which are also used by the signalling system. Therefore, if the signalling system uses power frequencies, (usually at 25, 50, 60, 75 or 125 Hz), power frequencies should ideally be completely eliminated to prevent harmonic current being injected from the AC to the DC side.

It is important to note that elimination of one harmonic component will result in increase of other, un-eliminated, components. If audio frequency is used in the signalling system, since harmonic rejection can be achieved by a properly tuned filter, a harmonic minimisation scheme would seem to be more suitable.

All the optimisation schemes suffer from the disadvantage of being unable to generate the PWM firing angles on-line. They are usually calculated off-line using a mainframe computer or PC and then stored in a microprocessor ROM for on-line generation of the PWM waveform.

The majority of traction drive systems use regular sampling PWM schemes. Since the equations defining the switching angles are analytical, the switching angles can be calculated using a microprocessor and the PWM waveform can be generated on-line. If power frequency is

used as the signalling frequency, one way to solve the interference problem is to use an active filter [98]. When audio frequency is used, an input LC-filter with a resonance frequency of approximately 50 Hz can completely block out harmonic current at the signalling frequencies [66].

The natural sampling PWM schemes were popular with the old analogue controllers where analogue devices were used to generate sine wave and triangular waveforms. Compared with analogue devices, digital computers are more accurate and efficient.

9.2.2 VSI-SCIM models

The frequency domain model of a VSI-SCIM drive is based on the per-phase equivalent circuit of the motor. It is a fast and simple method for the analysis of the system steady state performance. This model, however, is not suitable for system transient analysis.

In time domain modelling, the system may be described by 6-order time-varying linear differential equations. Using this model, the system performance can be simulated only at each individual motor speed, since the speed is assumed to be constant in the model. Moreover, the majority of the computer calculation time is spent on settling down the solutions.

By introducing an extra state variable, the motor speed, together with a mechanically related differential equation, the system may be described by a 7-order time-varying nonlinear model. The advantages in using this model are that the system continuous performance can be viewed and no computing time is required for settling down the solutions.

In particular, when this model is implemented on a multi-processor computer, it becomes very convenient to carry out system on-line simulation. With a colour graphic display unit, the operator has the flexibility to view either a specific operational point such as a gear change transition or the total performance under a certain operation time. The operator can also view the harmonic spectrum of certain system variables.

Using this simulator, a variety of tasks can be carried out. System performance under different PWM schemes can be compared, and the most suitable PWM scheme can be selected. The simulator can help system design engineers to choose the correct ratings of inverters and traction machines. The simulator can also be used to effectively design system control strategies such as voltage - frequency, current or torque control. By varying the above variables, certain system performance targets can be achieved. In an extreme case,

the tractive torque can be controlled to be larger than the maximum transmittable torque for the investigation of transient effects with wheel slip or slide.

9.2.3 Laboratory based traction drive

A microprocessor controlled laboratory based VSI-SCIM traction drive has been designed and constructed. This system has proved to be an effective tool in validating the simulation using an on-line simulation of the same system implemented by the multi-processor computer.

A 68000 SBC combined with the designed logic control unit was used to generate a three-phase PWM waveform in real-time. The use of a monostable multivibrator (SN74121) in the logic control unit is an effective method to control the time delay at switch on. GTO thyristors were used as the switching devices, which are also the devices being used in practical traction drives.

In setting the delay time for the six devices, two considerations must be made. Firstly, the duration of the delay time should be determined according to the devices used. Too long a delay time will result in "distortion" of the PWM waveform and the loss of operating voltage. Too short a delay time cannot ensure safe operation of the devices. The best way in setting

the delay time is to measure the turn-off time for each device and select the longest. Secondly, the delay times for all six devices must be the same, say 30 μs, so as to avoid unbalanced operation, especially at high modulation ratios.

In using the GTO devices, special precautions must be taken. When a simple capacitor snubber circuit is used, the devices could be easily destroyed even within the stated dV/dt range. In addition, the gate turn-off current should be sufficiently high. Otherwise, if one device fails to turn off, the inverter will be short-circuited. The gate turn-off current can be raised either by increasing the capacitor voltage, which is limited by the maximum value the GTO can accept, or by reducing the turn-off loop impedance.

9.3 Suggestions for further work

Two major areas are suggested for further work. They are concerned with the on-line simulator and the laboratory based simulator. Suitable further work for the on-line simulator is:

a) Modifying the existing FFT facility using the "window" technique [89], to enable a FFT analysis to be undertaken when the frequencies of the sampled functions

are not exactly known, such as in the case of system input current.

b) Standardising the on-line simulator using transputer processing devices and the C programming language. This work has already been started by Berry [99] for power system simulation applications.

c) Adding more multi-processors to the computer, say a total of 15 [56], and assigning them into groups. If the initial conditions are then stored for a small time step after single task operation, the on-line display task will then be performed more effectively.

d) Extending the simulation range. The simulation reported here is only concerned with single traction motor operation. In reality, several machines are fed by a single inverter. The simulation may be used to investigate the interacting effect between different motor currents on the system input current. The simulator may also be used to simulate the situation when wheels driven by different motors have different diameters.

The further work suggested for the laboratory based simulator includes:

a) Designing and constructing a single inverter fed multi-machine drive to verify the simulation suggested above.

b) Designing and constructing a microprocessor controlled train load simulator for which some work has already been done [100,101].

The combination of the above work schemes should be a great help to railway traction system design and control engineers.

References

1. Bertorelli, D.: "Three-phase power system in diesel electric locomotive", Ball Bearing Journal 222, March 1985 ISSN: 0308-1664, pp.20-24

2. Duffy, M.C.: "Mainline electrification and locomotive-electric systems", IEE Proc. Part A, Vol. 136 No. 6, 1989, pp. 279-289

3. Brenneisen, J., et al.: "A new converter drive system for a diesel-electric locomotive with asynchronous traction motors", IEEE Trans. on Industry Application, Vol. IA-9, No. 4, Aug. 1973, pp. 482-491

4. Cossie, A.: "SNCF apply the synchronous traction-motor to attain a robust truly-universal 5600-kW locomotive", Rail Eng. Int. Vol. 12, No. 1, 1983, pp. 7-10

5. Lacote, F.: "Second generation TGVs raise speed and comfort standards", Railway Gazette International, Vol. 142, 12, 1986, pp. 885-888

6. Brun, D.: "SNCF experience with power electronics - experiments of AC drives and their consequences on the choices made for the design of new electric units", IEE Conf. Publ. No. 279, 1987, pp. 21-25

7. Jonard, F.: "The new locomotives of French railways with synchronous motors", IEE Conf. Publ. No. 279, 1987, pp. 43-47

8. Petit, G.: "Evolution of the electrical equipment of TGV trainsets", IEE Conf. Publ. No. 279, 1989, pp. 403-407

9. Takehiko Katta, et al.: "Induction motor propulsion system for transit cars", Hitachi Review, Vol. 29, No. 1, 1980, pp. 19-24

10. Takashi Tsuboi, et al.: "GTO inverter controlled AC traction drives", Hitachi Review, Vol. 31, No. 1, 1982, pp. 23-27

11. Takashi Tsuboi, Takamasa Hori: "GTO inverter for AC traction drives", IEEE Trans. Vol. IA-19, No. 3, May/June 1983, pp.343-7

12. Kanzaki, T.: "High power GTO thyristor application to power electronic equipment used on railway vehicles", Toshiba Rev. Spring 1984, No. 147, pp. 8-12

13. Takashi Tsuboi, et al.: "Control system for traction drives", Hitachi Review, Vol. 35, No. 6, 1986, pp.311-6

14. Kaneda, J.: "The world's first VVVF inverter with 4500 V GTO thyristors", Mitsubishi Electr. Adv. (Japan) Vol. 34, 1986, pp. 6-8

15. Kawahira, K., et al.: "AC motor drive system for electric vehicles", Toshiba Rev., No. 159, 1987, pp. 14-19

16. Kiyoshi Nakamura, et al.: "Inverter drive system for AC electric rolling stocks", Hitachi Review, Vol. 37, No. 6, Dec., 1988, pp.371-6

17. Sone, S., et al.: "PWM converter-inverter system for AC supplied train", IEE Conf. Publ. No. 312, 1989, pp. 93-97

18. Sano, T., et al.: "VVVF inverter equipment for EMUS", IEE Conf. Publ. No. 312, 1989, pp. 98-102

19. Heider, H.J.: "Three-phase AC drive system at the Berlin underground", Proc. Int. Conf. on advanced propulsion systems for unban rail vehicles, Feb. 1980, pp. 119-132

20. Moschetti, A.: "Microprocessor-based PWM system for inverter-fed squirrel-cage motor traction systems", Conf. on Microelectronics in Power Electronics and Electrical Drives, Oct. 1982, pp. 425-431

21. Guldenpenning, A.U.W.: "German Federal Railway class 120 three-phase drive systems: service trials", Railw. Eng. (1981), No. 1, 1984, pp. 6-16

22. Korber, J. "Tractive vehicles in the coming decades - objectives, possibilities of resolving difficulties and examples from the point of view of the German railway industry", Rail International, April 1985, Vol. 16, No. 4, pp. 117-128

24. Winden, R.: "DB high-speed IC experimental train (ICE) with BBC three-phase drive system", Rail Eng. Int. Vol. 16, No. 3, 1987, pp. 9-12

25. Crome, R.: "West Berlin transforms the S-Bahn", Railw. Gaz. Int. Vol. 144, No. 3, 1988, pp. 159-162

26. Fischer, J.M.: "AC three-phase power transmission system for Amtrak's new locomotives F69PH-AC", IEEE/ASME Joint Railroad Conf. 1989, cat. n 89CH2749-0, pp.7-11

27. Klausecker, K.: "Modern control and power electronics for the AC drives of the German high-

speed train ICE", IEE Conf. Publ. No. 312, 1989, pp. 53-57

28. Voss, M.: "Application of the three-phase drive technique in electric motive power units of the German Federal Railways", IEE Conf. Publ. No. 312, 1989, pp. 58-62

29. Fischer, J.: "Diesel-electric locomotives with three-phase drive systems for Turkish State Railways", Brown Boveri Rev. Vol. 73, No. 12, 1986, pp. 689-697

30. Konno, N.: "25kV, 3000kW AC electric locomotive for Queensland Railways, Australia", Hitachi Rev. Vol. 35, No. 6 1986, pp. 343-348

31. Zhulev, O.N.: "Type VL86F electric locomotive with asynchronous traction motors", Sov. Electr. Eng. Vol. 57, No. 4, 1986, pp. 25-32 (Soviet)

32. Schmidt, D.: "Class EA3000 electric locomotives for Danish State Railways", Brown Boveri Rev. Vol. 74, No. 1, 1987, pp. 32-39

33. Kuehrer, F.: "The three-phase electric locomotives of the Austrian Federal Railways", Brown Boveri Rev. Vol. 74, No. 12, 1987, pp. 648-652

34. ---: "Netherlands Railways replaces electric and diesel loco fleet", Railw. Gaz. Int. Vol. 143, No. 4, 1987, pp. 219-221

35. Taufiq, J.A.: "AC traction in Finland", IEE Rev. Vol. 34 No. 10, 1988, pp. 381-383

36. Wojtas, B.J.: "Developments on British Railways traction and rolling stock", Power Eng. J. Vol. 3, No. 2, 1989, pp. 95-102

37. Ferrazzin, P.: "The electronic equipment of the group E402 locomotive for the Italian State Railways", IEE Conf. Publ. No. 312, 1989, pp. 82-87

38. -- "Converter locomotives with AC propulsion for Zurich's new 'S-Bahn'", ABB Review No. 10, 1990, pp.3-10

39. Gratzfeld, P.: "Lower running costs for diesel-electric locomotives with AC propulsion", ABB Review No. 1, 1991, pp.9-16

40. Giovanardi, G.: "Considering the asynchronous motor in the traction mode", Rail Eng. Int. 1978, Vol. 7, No. 3, pp. 87-88

41. Joshi, A.: "Comparison of AC traction drives using voltage and current source inverters", IEEE IAS Annual Meeting, 1978, pp. 781-788

42. ---: "Comparing synchronous and asynchronous traction motors", Railw. Gaz. Int. June 1982, Vol. 138, No. 6, pp. 458-9

43. Powers, W.F.: "Asynchronous traction motors will meet the synchronous challenge", Railw. Gaz. Int. March 1984, Vol. 140, No. 3, pp. 179-183

44. Nouvion, F.F.: "Considerations on the use of DC and three-phase traction motors and transmission system in the context of motive power development", Proc. Inst. Mech. Eng. Part D, Vol. 201, No. D2, 1987, pp. 99-113

45. Mouneimne, Z.S., Mellitt, B.: "Modelling of inverter-controlled asynchronous drives for system simulation in DC railways", IEE Proc. Part B. Vol. 135, No. 5, 1988, pp. 210-217

46. Hill, R.J., Huang, F.: "Performance prediction of inverter-induction motor drives for DC-fed railways", 4th Int. Conf. PEVSD, London, 17-19 July 1990, pp. 417-422

47. Lockwood, M.: "Simulation of inverter/induction machine systems including discontinuous phase currents", IEE Journal on Electric Power Applications, Vol. 1, No. 4, 1978, pp. 105-118

48. Giubergia, S.: "Computer simulation of inverter induction motor drives for electric locomotives", Int. Conf. on Numerical Control of Electrical Machines, France, 1980, pp.76-88

49. Denegri, G.B., at el.: "Dynamic performances of AC drives fed from power transistor-thyristor inverters", IEEE Trans. Ind. Appl. Vol. IA-21, No. 1, 1985, pp. 266-273

50. Taufiq, J.A., at el.: "Fast time domain modelling of inverter fed induction motor drive systems", 2th Int. Conf. on Power Electronics and Variable-Speed Drives, London, 1986, pp. 154-157

51. Taufiq, J.A., at el.: "Electrical instability in a voltage source inverter-fed induction motor drive at constant speed", IEE Proc. Part B, Vol. 133, No. 4, July 1986, pp. 299-307

52. Taufiq, J.A., at el.: "Computer simulation of AC/DC power converter fed inverter drives for traction", Int. Conf. on Electric Railway Systems for a new Century, London, Sep. 1987, pp. 230-234

53. Taufiq, J.A.: "Evaluating the step response of traction VSI drive", 3th Int. Conf. on Power Electronics and Variable-Speed Drives, London, July, 1988, pp. 340-342

54. Taufiq, J.A.: "Step response prediction for traction VSI drive with emphasis on signalling compatibility", 19th Annual IEEE Power Electronics Specialists Conference PESC'88 Vol. 2, 1988, pp. 1271-1275

55. Dale, L.A.: "Real time modelling of multimachine power systems", Ph.D thesis, University of Bath, 1985

56. Berry, T.: "Real time simulation of complex power systems using parallel processors", Ph.D thesis, University of Bath, 1989

57. Kanzaki, T., at el.: "High-power GTO thyristor application to power electronic equipment used on railway vehicles", Toshiba Rev. Spr. 1984, No. 147, pp. 8-12

58. Korber, J.: "From thyristor to GTO', Railway Gazette International, Sept. 1987, pp.601-604

59. Abraham, L.: "Power electronics in German railway propulsion", IEEE Proc. Apr. 1988, Vol. 76, No. 4, pp. 472-480

60. Kusko, A.: "Tuned filters for traction rectifier sets", IEEE Trans. on Ind. Appl. Vol. IA-21, No. 6, 1985, pp. 1571-1579

61. Rajashekara, K.S., at el.: "DC link filter design considerations in three-phase voltage source inverter-fed induction motor drive system", IEEE Trans. on Ind. Appl. Vol. IA-23, No. 4, 1987, pp. 673-680

62. Li, U.Z., at el.: "Optimisation design on series tuning filters used in traction systems", IEE Proc. Publ. No. 312, 1989, pp. 222-226

62. Bocchetti, G., at el.: "Dimensioning verify on an high power railway drive filtering system using EMTP", 18th EMTP Users Group Meeting Proceedings, France, 1990, p.N5/1-11

63. Press, W.H., et al.: "Numerical Recipes", Cambridge University Press, 1986

64. Bowler, P., et al.: "An inertia load simulator for traction systems", 2nd International Conference on

Electrical variable-speed drives, Sept. 1979, London, pp.165-70

65. Scott, M.: "Modern developments in wheelslip control on electric locomotives", Journal of Institution Loco. Eng., paper No. 719, 1969-70

66. Karvinen, J.: "Three-phase AC traction drives: design and service experience", IEE PROC., Vol. 134, Pt. B, No. 3, May 1987, pp.135-40

67. Mohan, N., et al., (1989) "Power electronics: convertors, applications, and design", New York, John Wiley & Sons

68. Barton, T.H.: "Pulse width modulation waveforms, the Bessel approximation", IEEE - IAS Conf. Rec. 1978, pp.1125-1130

69. Kanzaki, T., et al.: "Direct digital controlled PWM GTO inverter for DC 1500 V electric cars", Conference Record of the International Power Electronics Conference, 27-31 March 1983, Tokyo, Japan, pp.1587-98

70. Tsuboi, T., Nakamura, K.: "Control system for traction drives", Hitachi Review Vol. 35, No.6, 1986

71. Grant, D.A., Seidner, R.: "Ratio changing in pulse width modulated inverters", Proc. IEE Pr. B, Vol. 128, No. 5, pp.243-248

72. Patel, H.S., Hoft, R.G.: "Generalized techniques of harmonic elimination and voltage control in thyristor inverter: Part I- harmonic elimination", IEEE Trans. Vol. IA-9, May/June 1973, pp.310-317

73. Taufiq, J.A., et al: "Novel algorithm for generating near optimal PWM waveforms for AC traction", IEE Proc. Vol. 133, Pt.B, No.2, pp.85-94

74, Buja, G.S., et al.: "Optimal pulsewidth modulation for feeding AC motors", IEEE Trans. Vol. IA-13, No.1, 1977, pp.38-44

75. Takahashi, I., et al.: "A new control of PWM inverter waveform for minimum loss operation of an induction motor drive", IEEE Trans. Vol. IA-21, No.4, 1985, pp.580-7

76. Hoft, R.G., et al.: "GTO inverter optimal PWM waveform", IEEE Conference Record on IAS Annual Meeting, 1987, pp. 312-316

77. Bowes, S.R., et al.: "Suboptimal switching strategies for microprocessor-controlled PWM

inverter drives", IEE Proc. Vol.132, Pt.B, No.3, 1985, pp.133-148

78. Bowes, R.S., et al.: "New PWM switching strategy form microprocessor controlled inverter drives", ibid., Vol.133, Pt.B, No.4, 1986, pp.237-254

79. Evans, P.D.: "DC link current in PWM inverters", IEE Proc. Vol. 133, Part B, No. 4, July 1986, pp. 217-224

80. Fallside, F., Wortley, A.T.: "Steady-state oscillation and stabilisation of variable-frequency inverter-fed induction-motor drives", IEE Proc. 1969, 116(6), pp.991-999

81. Lipo, T.A., Krause, P.C.: "Stability analysis of a rectifier-inverter induction motor drive", IEEE Trans. 1969, PAS-88, (1), pp. 55-66

82. Henrici, P.: "Discrete variable methods in ordinary differential equations", Wiley, New York, 1962

83. Conte, S.D.: "Elementary numerical analysis", McGraw-Hill, New York, 1980

84. Hildebrand, F.B.: "Introduction to numerical analysis", McGraw-Hill, New York, 1965

85. Carnahan, B.: "Applied numerical methods", Wiley, New York, 1969

86. Johnson, L.W.: "Numerical analysis", Addison-Wesley, Reading, U.K., 1982

87. Brigham, E.O.: "The fast Fourier transform", Prentice-hall, New Jersey, 1974

88. Cooley, J.W., Tukey, J.W.: "An algorithm for machine calculation of complex Fourier series", Math. Computation, April 1965, Vol. 19, pp. 297-301

89. Harris, F.J.: "On the use of windows for harmonic analysis with the discrete Fourier transform", Proc. of IEEE, Vol. 66, No. 1, 1978, pp. 51-85

90. -- "68000 CPU Board and Eprom programmer", manual, Andelos system, 1984

91. -- "SEKA V1.0, 68000 Editor-Assembler-Debugger for Andelos 68000 SBC", manual, Andelos system, 1985

92. Motorola Data Sheet Device MC68230L10, 1981

93. Woodwerth, A., Burgum, F.: "Simple rules for GTO circuit design", Mullard Technical Publication M83-0137

94. Burgum, F.: "Basic GTO drive circuits", Mullard Technical Publication M81-0128

95. British Hovercraft Corporation Ltd., EEL 2400 Series Torque Transducers

96. British Hovercraft Corporation Ltd., EEL/ED/195/B operating Instructions for Indicator Unit TM9 and TM9/2

97. Evershed Powerotor, Group 3 - Tachogenerators

98. Hoogerwaard, Ir.A.: "The application of the voltage-source inverter in AC-drives for DC rail tractions", Institution of Engineers, Australia, Mechanical Engineering Transactions, 1986, pp.223-228

99. Berry, T: "Real time power system training simulator", Proc. of the 25th Universities Power Engineering Conf., Aberdeen, U.K., 12-14 Sept. 1990, Vol. 2, pp. 671-674

100. Bates, J.J. : "Simulation of massive inertia loads using feedback techniques", IEE Proc. Vol. 133, No. 3, 1966, pp. 509-516

101. Bowler, P. : "An inertia load simulator for traction systems", IEE Proc. Vol. 179, 1977, pp. 165-170

102. Limebeer, D.J.N. : Subsynchronous resonance of single-cage induction motors", IEE Proc. Vol. 128 Pt. B, No. 1, 1981, pp. 33-42

Appendix A
Practical data of EMU

The following information supplied by Brush Electrical Machines Ltd. presents practical data applicable to Electric Multiple Units for rapid transit railway applications.

The EMU data for a suburban service (typical of outer London operation) is

1. Train weight: 110 Tonnes (2x39 + 1x32)
2. Number of motored axles: 8
3. Number of trailer axles: 4
4. Train inertia: 18,000 kgm^2
5. Wheelset and axle inertia 170 kgm^2
6. Traction motor speed:
   Varies with design (typ max 3500-5500 rpm)
7. Maximum train speed: typ 80 mph (128 km/h)
8. Train wheel diameter: 840 mm new; 810 mm half worn
9. Motor/wheel gear ratio: 13/60
10. Weight transfer coefficient:
    15% with a max adhesion level of 26%
11. Max accelerating rate:
    0.9 m/s^2 for motoring; -1.1 m/s^2 for braking

The tractive resistance of an EMU with a 'flat' end profile is calculated from the formula

$$R = WR_m + NR_w + R_o$$

where R is total train resistance (N)

W is gross weight of train (tonnes)

R_m is specific mechanical and

track resistance (N/ton)

N is number of vehicles in train

R_w is specific wind resistance (N/car)

R_o is head and wake resistance (N/train)

Values of R_m, R_w and R_o are given in the following table.

Speed	R_m	R_w	R_o
(km/h)	(N/t)	(N/car)	(N/train)
0	66.0	--	--
5	11.09	38.31	590.0
10	11.64	54.81	606.93
20	12.8	90.79	620.37
30	14.03	131.55	696.66
40	15.34	178.05	835.79
50	16.72	231.26	1037.56
60	18.17	292.14	1302.56
70	19.70	361.64	1630.20
80	21.3	440.73	2020.68
90	22.97	530.37	2473.99
100	24.72	631.52	2990.15
110	26.54	745.14	3569.15
120	28.43	872.19	4210.97
130	30.4	1013.63	4915.64
140	32.44	1170.43	5683.16
150	34.55	1343.53	6513.50
160	36.74	1533.9	7406.69

Appendix B
Equipment and instrumentation

(1) GEC G350AZ SCIM

Motor connection	: star	R_s	= 0.042 Ω
Rated line voltage	= 520 V	R_r	= 0.032 Ω
Rated line current	= 210 A	L_s	= 579.3 μH
Rated frequency	= 50 Hz	L_r	= 700.3 μH
No. of pole pairs	= 2	L_m	= 12.61 mH
Rated shaft power	= 140kW		
Rated output torque	= 890 Nm		

(2) 3.0 kW SCIM

Motor connection	: delta	R_s	= 2.775 Ω
Rated line voltage	= 220 V	R_r	= 2.25 Ω
Rated line current	= 11.7 A	L_s	= 11.75 mH
Rated frequency	= 50 Hz	L_r	= 11.75 mH
No. of pole pairs	= 2	L_m	= 0.21 H
Rated shaft power	= 3.0 kW		
Rated output torque	= 20.2 Nm		

(3) Separately exited DC generator

Rated speed	: 1500 rpm	R_a	= 3 Ω
Rated output voltage	= 200 V	R_f	= 110 Ω
Rated output current	= 17.5 A		
No. of pole pairs	= 2		
Rated output power	= 3.5 kW		

(4) Filter parameters

a. Practical system:

R_f = 0.047 Ω, L_f = 6.5 mH, C_f = 7.5 mF

b. Laboratory system:

R_f = 0.01 Ω, L_f = 9 mH, C_f = 1.8 mF

c. Three-phase AC-DC converter for lab. drive:

R_0 = 1.0 Ω, L_0 = 20 mH, C_0 = 4.2 mF

(5) Instruments

a. Torque transducer: British Hovercraft Corporation Ltd

Type -- TT2/4/AS

sensitivity -- 2.348 mV/V

Range -- 0 -- 25 lb.ft

b. Tacho generator: Evershed and Vignoler Ltd.

Type -- FDH 202T/7/T

Sensitivity -- 7.0 V/1000 rpm

Range -- 0 -- 4500 rpm

c. Current transducer: LEM SA

Type -- LT 80 - P

Sensitivity -- 20 A/V

Range -- 0 -- 80 A

d. Pulse counter: Racal Instruments

Type 9903 Universal Counter Timer

e. Oscilloscope: LeCroy

Type -- 9400 dual 125 MHz digital oscilloscope

Appendix C
Coefficients used in stability analysis

The coefficients used in section 4.4 for system stability analysis are derived from the equivalent impedance of the induction motor. The machine model is assumed to be represented by a synchronous rotating reference frame model. The matrix form of the model is given by

$$\begin{bmatrix} V_{qs} \\ V_{ds} \\ V_{qr} \\ V_{dr} \end{bmatrix} = \begin{bmatrix} R_s+pL_s & \omega_s L_s & pL_m & \omega_s L_m \\ -\omega_s L_s & R_s+pL_s & -\omega_s L_m & pL_m \\ pL_m & \omega_{sl} L_m & R_r+pL_r & \omega_{sl} L_r \\ -\omega_{sl} L_m & pL_m & -\omega_{sl} L_r & R_r+pL_r \end{bmatrix} * \begin{bmatrix} I_{qs} \\ I_{ds} \\ I_{qr} \\ I_{dr} \end{bmatrix}$$

or $$[V] = [Z][I] \qquad \text{(A-C.1)}$$

where ω_s and ω_{sl} are the synchronous and slip speeds. It can be shown that in the synchronous rotating reference frame model, $V_{ds} = 0$. Hence the only driving point is V_{qs}. The transfer impedance at this point may be written in the following form [102]:

$$Z_m = \det[Z]/\Delta \qquad \text{(A-C.2)}$$

where Δ is the cofactor of the (1,1) element in the impedance matrix [Z]. It is given by

$$\Delta = \det \begin{bmatrix} R_s+pL_s & \omega_s L_m & pL_m \\ \omega_{sl} L_m & R_r+pL_r & \omega_{sl} L_r \\ pL_m & -\omega_{sl} L_r & R_r+pL_r \end{bmatrix} \qquad \text{(A-C.3)}$$

Eqn. (A-C.2) can be expressed in the form of eqn. 4.36 with the coefficients given by

$$\Delta_1 = L_s L_r - L_m^2$$

$$a_4 = \Delta_1^2$$

$$a_3 = 2\Delta_1 (R_s L_r + R_r L_s)$$

$$a_2 = (R_s L_r + R_r L_s)^2 + 2R_s R_r \Delta_1 + \Delta_1^2 (\omega_s^2 + \omega_{sl}^2)$$

$$a_1 = 2 (R_s R_r^2 L_s + R_s^2 R_r L_r + \omega_s^2 R_s L_r \Delta_1 + \omega_s^2 R_r L_s \Delta_1)$$

$$a_0 = R_s^2 R_r^2 + \omega_s^2 R_r^2 L_s^2 + \omega_{sl}^2 R_s^2 L_r^2 + \Delta_1^2 \omega_s^2 \omega_{sl}^2 + 2\omega_s \omega_{sl} R_s R_r L_m$$

$$b_3 = L_r \Delta_1$$

$$b_2 = L_r (R_s L_r + R_r L_s) + R_r \Delta_1$$

$$b_1 = R_r (2R_s L_r + R_r L_s) + \omega_{sl}^2 L_r \Delta_1$$

$$b_0 = R_s R_r^2 + \omega_{sl}^2 R_s L_r^2 + \omega_s \omega_{sl} L_m R_r$$

The coefficients in eqn. 4.37 are given by

$$c_6 = kL_f C_f a_4$$

$$c_5 = kC_f (R_f a_4 + L_f a_3)$$

$$c_4 = k (a_4 + R_f C_f a_3 + L_f C_f a_2 + kL_f b_3)$$

$$c_3 = k (a_3 + R_f C_f a_2 + L_f C_f a_1 + kR_f b_3 + kL_f b_2)$$

$$c_2 = k (a_2 + R_f C_f a_1 + L_f C_f a_0 + kR_f b_2 + kL_f b_1)$$

$$c_1 = k (a_1 + R_f C_f a_0 + kR_f b_1 + kL_f b_0)$$

$$c_0 = k (a_0 + kR_f b_0)$$

$$d_5 = C_f a_4$$

$$d_4 = C_f a_3$$

$$d_3 = C_f a_2 + kb_3$$

$$d_2 = C_f a_1 + kb_2$$

$$d_1 = C_f a_0 + kb_1$$

$$d_0 = kb_0$$

where $k = 18/\pi^2$. In the case of the laboratory based drive, the auto-transformer can be described by an equivalent resistance R_0 and inductance L_0 which has the measured values of 1.0 ohm and 0.02 H. The total system input impedance is given by

$$Z_{in}' = R_0 + pL_0 + (1/pC_0)//Z_{in} \qquad \text{(A-C.4)}$$

where C_0 (0.0042 mF) is the value of the capacitor used to stabilise the output of the rectifier, and Z_{in} is given in eqn. 4.37. To analyse the stability of this system, eqn. (A-C.4) must be expressed in the form

$$Z_{in}' = \frac{e_8p^8 + e_7p^7 + \cdots + e_1p^1 + e_0}{f_7p^7 + f_6p^6 + \cdots + f_1p^1 + f_0} \qquad \text{(A-C.5)}$$

The coefficients (e_8 - e_0) used to analyse the system stability are given as follows

$$e_8 = kL_0C_0c_6$$
$$e_7 = kC_0(R_0c_6 + L_0c_5)$$
$$e_6 = k(c_6 + R_0C_0c_5 + L_0C_0c_4 + kL_0d_5)$$
$$e_5 = k(c_5 + R_0C_0c_4 + L_0C_0c_3 + kR_0d_5 + kL_0d_4)$$
$$e_4 = k(c_4 + R_0C_0c_3 + L_0C_0c_2 + kR_0d_4 + kL_0d_3)$$
$$e_3 = k(c_3 + R_0C_0c_2 + L_0C_0c_1 + kR_0d_3 + kL_0d_2)$$
$$e_2 = k(c_2 + R_0C_0c_1 + L_0C_0c_0 + kR_0d_2 + kL_0d_1)$$
$$e_1 = k(c_1 + R_0C_0c_0 + kR_0d_1 + kL_0d_0)$$
$$e_0 = k(c_0 + kR_0d_0)$$

Appendix D : FFT program

```
SECTION "FFT"

GET "libhdr"
GET "fphdr"
GET "storehdr"
GET "mylibhdr"

AND FFT(DATA,NN) BE     // DATA contains 2*NN data
$( LET YR,   YI   = getvec(NN), getvec(NN)
   LET FFT1, FFT2 = getvec(NN), getvec(NN)
   LET THETA      = PI#/FLOAT(NN)
   LET CC,   SS   = ?, ?
   LET RR1,  RR2  = ?, ?
   LET II1,  II2  = ?, ?

   COOLEY(DATA,NN,-1)
   FOR i = 1 TO NN DO
   $( YR!(i-1) := DATA!(2*i-1)
      YI!(i-1) := DATA!(2*i)
   $)
   FOR i = 1 TO NN-1 DO
   $( THETA := FLOAT(i)#/FLOAT(NN)
      CC := COSINE(PI#*THETA)
      SS := SIN(PI#*THETA)
      RR1 := 0.5#*(YR!i #+ YR!(NN-i))
      RR2 := 0.5#*(YR!i #- YR!(NN-i))
      II1 := 0.5#*(YI!i #+ YI!(NN-i))
      II2 := 0.5#*(YI!i #- YI!(NN-i))
      FFT1!i := RR1 #+ CC#*II1 #- SS#*RR2
      FFT2!i := II2 #- SS#*II1 #- CC#*RR2
   $)
   DATA!0 := YR!0#/float(NN)

   FOR i = 1 TO NN-1 DO
   $( FFT1!i := FFT1!i#/float(NN)
      FFT2!i := FFT2!i#/float(NN)
      DATA!i := sqrt(FFT1!i#*FFT1!i #+ FFT2!i#*FFT2!i)
   $)
   freevec(YR)
   freevec(YI)
   freevec(FFT1)
   freevec(FFT2)
$)
AND COOLEY(DATA,NN,ISIGN) BE  // ISIGN inverting sign
$( LET TEMPR, TEMPI = ?, ?
   LET UNIT,  STEP  = ?, ?
   LET J, K,  M, MM = ?, ?, ?, ?
   LET L, N    = ?, 2*NN
   LET THETA   = 2.0#*PI#/FLOAT(NN)
   LET WR      = GETVEC(NN/2)
   LET WI      = GETVEC(NN/2)
```

```
    WR!1 := 1.0
    WI!1 := 0.0
    WR!(NN/4+1) := 0.0
    WI!(NN/4+1) := #-1.0
    FOR i = 2 TO NN/4 DO
    $( J := FLOAT(i-1)
       WR!i := COSINE(J#*THETA)
       WI!i := FLOAT(ISIGN)#*SIN(J#*THETA)
       WR!(NN/2+2-i) := #-WR!i
       WI!(NN/2+2-i) := WI!i
    $)
    J := 1
    FOR i = 1 TO N BY 2 DO
    $( IF ( J>i ) THEN
       $( TEMPR := DATA!J
          TEMPI := DATA!(J+1)
          DATA!J     := DATA!i
          DATA!(J+1) := DATA!(i+1)
          DATA!i     := TEMPR
          DATA!(i+1) := TEMPI
       $)
       M := N/2
       WHILE ( ( M>=2 & J>M )) DO
       $( J := J-M
          M := M/2
       $)
       J := J + M
    $)
    MM := 2
    WHILE ( N>MM ) DO
    $( STEP := 2*MM
       L := 1
       UNIT := NN/MM
       FOR i = 1 TO MM BY 2 DO
       $( J := i
          $( K := J + MM
             TEMPR := WR!L#*DATA!K #- WI!L#*DATA!(K+1)
             TEMPI := WR!L#*DATA!(K+1) #+ WI!L#*DATA!K
             DATA!K     := DATA!J   #- TEMPR
             DATA!(K+1) := DATA!(J+1) #- TEMPI
             DATA!J     := DATA!J   #+ TEMPR
             DATA!(J+1) := DATA!(J+1) #+ TEMPI
             J := J + STEP
          $) REPEATWHILE ( J < N )
          L := L + UNIT
       $)
       MM := STEP
    $)
    FREEVEC(WR)
    FREEVEC(WI)
$)
```

Appendix E

Input and output of PWM generating programs

The following gives a brief description of the input and output for each of the programs used in generating three-phase PWM waveforms.

V-F PROGRAMS:

SUB.TS(train speed): Inputs: the maximum train speed and the number of speed-time points to be stored. Output: a speed-time table. The principle of the calculation is described in section 2.7.

SUB.RSF(rotor slip frequency): Inputs: speed-time table, motor rated values -- frequency, voltage, and torque; supply frequency at starting point and switching over points (from one drive region to another); and the number of rotor slip frequency-time points to be stored. Output: a rotor slip frequency-time table. The details are shown in sub-section 5.3.2.

SUB.SF(supply frequency): Inputs: speed-time table, rotor slip frequency-time table, and the initial time interval for updating the supply frequency. Output:

frequency-time table together with the repeat times for each frequency.

SUB.SV(supply voltage): Input: supply frequency-time table and motor rated values. Output: supply voltage-time table. Under constant torque operation, the V/*f* ratio is kept constant at a rated value. After this, the voltage is kept at its rated value. At low frequency, the voltage is boosted so as to keep the flux constant and hence the torque constant.

SUB.MD(modulation depth): Input: voltage-time table. Output: modulation depth-time table. The conversion is made by two linear relationships separated at $M_d = 1$.

Note that the system parameters are always available when they required by the above programs.

PWM PROGRAMS:

ASYN.PWM(asynchronous): Input: carrier frequency, frequency-time table and modulation depth-time table. Output: three sets of firing angles for three phases.

SSNS.PWM(single-side natural sampled):

DSNS.PWM(double-side natural sampled):

SRS.PWM(symmetrical regular sampled):

ARS.PWM(asymmetrical regular sampled):

Input: first and last frequencies, modulation ratio steps, frequency-time table and modulation depth-time table. Output: three sets of firing angles for three phases.

MARS.PWM(modified asymmetrical regular sampled):
Input: first and last frequencies, modulation ratio steps, frequency-time table and modulation depth-time table. Output: three sets of firing angles for three phases.

HE.PWM(harmonic elimination):

HM.PWM(harmonic minimisation):
Input: first and last frequencies, ranges of each of frequency steps, number of angles per quarter cycle at each step, frequency-time table and supply voltage-time table. Output: three sets of firing angles for three phases.

M-P PROGRAM:

S.PROG(sorting program): Input: the output of PWM programs and frequency-time table. Output: mode-period look-up table. To produce a whole look-up table in motoring mode, the PWM operation must be extended to the square wave operation. Using the frequency-time table again, the value of each frequency and the number of repetition are appended to the mode-period table.

Appendix F
Program structures
for master and console tasks

MASTER TASK PROGRAM:

```
LET start() BE
$( initialising working environment
   getdata from pre-calculated look-up table
   getdata from single.task simulation results
   load console task obj.code
   load calculator task obj.code
   load FFT task obj.code
   load display task obj.code
   send packets to all tasks
        and activate them
   $( waiting for a packet from console task
      if the packet contains simulating instruction
      then
         return an answer packet to console task
         fetch the look-up-table and initial values
           and send them to the calculator task
      if the packet contains QUIT
      then break the loop
   $) REPEAT
   send packets to all tasks
        and terminate them
   tidyup working environment
$)
```

CONSOLE TASK PROGRAM:

```
LET start(pkt) BE
$( initialising local environment
   take over the control of the console
   $( go subroutine CONSOLE, fetch an instruction
         and return a packet
      waiting for a packet from master task
      if the packet contains terminating instruction
      then break the loop
      if the packet contains interacting instruction
      then loop
   $) REPEAT
   hand over the control of the console
   tidyup working environment
   return an answer packet
   terminate itself
$)
AND console(pkt) BE
$( option 1: continue the simulation? (yes/no)
             yes, goto option 2
             no,  goto end.prog
   option 2: select simulation starting point (1--120)
   option 3: select one of the system variables
   option 4: select the length of window and the number
             of sampling points
end.prog:
$)
```

Appendix G
Main part of μP control program

A microprocessor control program written in assembly language was used to generate three-phase PWM waveform. The following presents the main part of the program. After the system initialisation, the program start as

```
          MOVE.W (A4)+,D7      ; get No. of steps
REPEAT:   MOVE.W (A4)+,D0      ; get No. of modes      (8)
          MOVE.W (A4)+,D2      ; get No. repeat        (8)
CYCLE:    MOVE.W D0,D1         ; restore No. of modes  (4)
          MOVE.L A5,A6         ; restore pointer2      (4)
MODE:     MOVE.W (A6)+,D4      ; get period of mode    (8)
          MOVE.W (A6)+,D3      ; get mode              (8)
          MOVEP.W D3,$0(A3)    ; output mode           (8)
PERIOD:   DBF D4,PERIOD      ; count down period (10/14)
          DBF D1,MODE        ; check No. of mode (10/14)
          DBF D2,CYCLE       ; check No. of cycle (10/14)
          MOVE.L A6,A5       ; save new pointer2     (4)
          DBF D7,REPEAT      ; check No. of step (10/14)
```

Note that the numbers in bracket at the end of each line indicate the numbers of machine cycles for that command to be executed. Since the microprocessor runs at 10 MHz, each cycle is equivalent to 0.1 us.

Appendix H
Simulation of ripple current

In chapter 7, it was observed that the ripple on the system input current from the experiment is larger than that from the simulation. This is because of the introduction of inductance from the auto-transformer and the rectifier output capacitor. The following presents the simulation results with an extra inductor and capacitor added to the model described by eqns. 4.22 and 4.30.

The total impedance matrix for the modified model is given by

$$\begin{pmatrix} R_0+pL_0 & 1 & 0 & 0 & 0 & 0 & 0 & 0 \\ 1/C_0 & -p & -1/C_0 & 0 & 0 & 0 & 0 & 0 \\ 0 & -1 & R_f+pL_f & 1 & 0 & 0 & 0 & 0 \\ 0 & 0 & 1/C_f & & & & & \\ 0 & 0 & 0 & & & & & \\ 0 & 0 & 0 & & & \mathbf{Z} & & \\ 0 & 0 & 0 & & & & & \\ 0 & 0 & 0 & & & & & \end{pmatrix} \qquad \text{(A-H.1)}$$

where $\mathbf{Z} = \begin{pmatrix} -p & K_1 & K_2 & 0 & 0 \\ K_1 & R_s+pL_s & 0 & pL_m & 0 \\ K_2 & 0 & R_s+pL_s & 0 & pL_m \\ 0 & pL_m & -\omega_r L_m & R_r+pL_r & -\omega_r L_r \\ 0 & \omega_r L_m & pL_m & \omega_r L_r & R_r+pL_r \end{pmatrix}$ (A-H.2)

The state vector is

$$[x] = [V_0, I_0, I_{in}, V_{dc}, I_{qs}, I_{ds}, I_{qr}, I_{dr}]^t$$

and the input vector is

$$[V] = [V_{in}, 0, 0, 0, 0, 0, 0, 0]^t$$

Using the above model, the equivalent system input current I_{in} was simulated. The simulation input was the same as that used for the experiment. Figure A-H.1 shows I_{in} at the first and last step changes of the supply frequency. It can be seen that the current ripple from the simulation is in agreement with that from experiment.

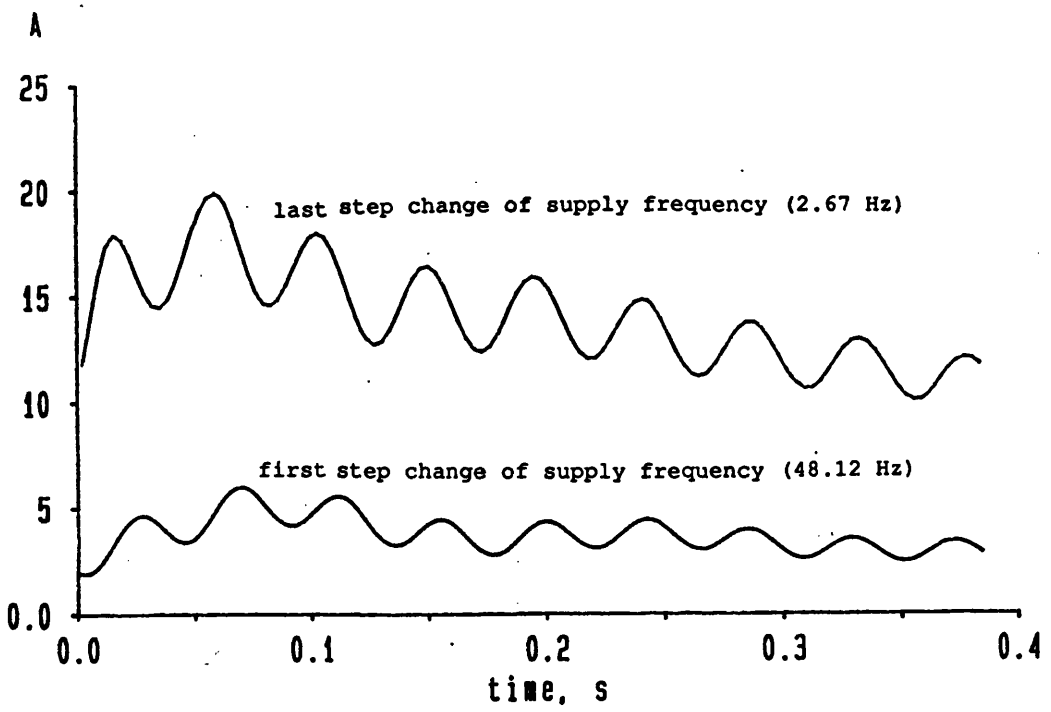

Figure A-H.1 System input current

Appendix I : Publications

1.

"Performance prediction of of inverter - induction motor drives for DC-fed railways", Conf. Rec. 4th International Conference on Power Electronics and Variable-Speed Drives, London, 1990

2.

"On-line simulator for transient behaviour of inverter-fed induction motor traction drives", Conf. Rec. 3th International Symposium on Modelling and Simulation of Electrical Machines and Static Converters, Nancy, 1990

3.

"An on-line FFT implementation for a parallel computer simulation of a VSI-IM rail traction drive", Conf. Rec. 13th IMACS World Congress, Dubin, 1991

4.

"Verification of an on-line simulator for VSI-IM rail traction drives", Conf. Rec. 4th European Conference on Power Electronics and Applications, Florence, 1991

Fourth International Conference on

Power Electronics and Variable-Speed Drives

17-19 July 1990

Organised by the
Power Division of the Institution of Electrical Engineers

in association with the
Institute of Electrical Engineers of Japan
Institute of Electrical and Electronics Engineers Inc
(Industry Applications Society & Industrial Electronics Society)
Institution of Engineers of Australia
Institution of Engineers of Ireland
Société des Electriciens et des Electroniciens
South African Institute of Electrical Engineers

Venue
The Institution of Electrical Engineers, Savoy Place, London WC2, UK

PERFORMANCE PREDICTION OF INVERTER-INDUCTION MOTOR DRIVES FOR DC-FED RAILWAYS

R. J. Hill, F. Huang

University of Bath, UK

INTRODUCTION

The use of computer-aided design (CAD) tools is necessary for the effective design of traction drives. The first stage of traction simulation involves the creation of a steady state model, to enable the system concept to be tested under the full range of anticipated load conditions and duty cycles. A comprehensive simulator should allow the designer to monitor all the system variables and optimise the fundamental system parameters. Subsequently, a transient model can provide information about the interference and disturbance responses, predicting the effect of wheelslip, supply voltage variation or converter modulation change.

Simulation of converter-fed AC traction drives as reported in the literature has been usually performed on mainframe computers in an off-line mode with software created in a high-level language such as FORTRAN, and with tabular or graphical output. Determination of the steady-state performance is relatively straightforward, the operation of multi-machine drives having received close attention [1]. Most published research literature has concentrated on dynamic performance, for example the optimisation of pulse-width modulation (PWM) switching strategies in constant torque operation [2]. A example of the successful use of CAD is the development of systems for on-line optimisation of pulse patterns [3].

New generation simulators exploiting novel computer hardware and software systems such as parallelism and multitasking, and providing interactive, user-friendly interfaces in addition to enhanced computer power, are now becoming available. Early applications of parallel computers for engineering system simulation were task specific [4], but recent research has concentrated on wider applications such as real-time simulation of power electronic circuits [5]. Many of the applications are dependent on efficient software structures, and parallel processing algorithm development has proceeded with, for example, techniques for solving linear equations [6] and for executing fast transient analyses [7]. For the simulation of continuous time systems, a time-stepping procedure is adopted using numerical methods which utilise historical variable values retained from previous iterations. Software structures in parallel computers are ideally suited to this type of simulation, through minimisation of the use of historical data during multitasking.

A further advantage of parallel computers is the ease of implementing interactive simulations. The requirement for processing to be carried out in real time or faster than real time means the computer must generate data at a faster rate than the system being modelled. In a time-stepping simulation, the solution time for the system equations must be less than one time step for the numerical integration method chosen. If this condition is satisfied, the plant being modelled may be directly replaced by the simulator, and the effectiveness of various control algorithms can be evaluated on line, with the simulator eventually replacing the controller.

In this paper, simulation of the steady state aspects of a converter-fed AC traction drive is demonstrated using a parallel computer. The solution of the system equations is carried out by exploiting concurrency, through multitasking software. The computer has an efficient hardware structure consisting of parallel processors with shared memory, the intelligence of each being exploited to retain operational independence from the others. Software then identifies data dependency and prioritises the tasks for execution on the separate processors. The results presented show the main system variables of an inverter-fed AC traction drive as the train accelerates through a given duty cycle and with predictable load characteristics.

SYSTEM AND SIMULATOR DESCRIPTION

Traction system

The traction system modelled is a single inverter and motor forming part of the power equipment of a three-car train in a DC-fed urban railway. The complete unit has two power cars, each with four motored axles driven by a single voltage-source inverter (VSI), and one trailer car. The DC supply has a nominal voltage of 750 V which is subject to a +20%, -33% variation. The system is shown in Figure 1.

The nominal train duty cycle (assuming straight track and level gradient) is shown in Figure 2. After an initial linear acceleration period, the train then accelerates at a decreasing rate until the designed speed is reached. It then runs at the constant route speed or balancing speed, finally braking at a constant rate to a stop. After a predetermined station dwell, the cycle is repeated. The amount of time spent in each operating region is determined by the station spacing, line speed limit, the presence of grades and curves, and the train resistance.

Simulator computer hardware and software

Hardware. The parallel computer used in the present simulator is based on the MC68000 series of 16-bit microprocessors. Figure 3 shows the hardware configuration. For the simulations described in this paper, a minimum system, comprising a control card and two additional CPU cards, was used. In the control card, the DRAM provided extra shared memory, the EPROM contained monitor/bootstrapping firmware, and the peripheral input/output (I/O) devices were standard RS232 asynchronous serial ports. There were also available real-time counter timers, bus status display-reset functions, and arithmetic hardware. The system is expandable up to a maximum of 64 CPU boards. The CPU clock frequency is 12.5 MHz, giving 1.5 MIPS (millions of instructions/second executed) of computer power.

The computer was designed in house [8]. Having a loosely-coupled system architecture, high-speed data transfer between processors was achieved using a completely-shared memory, allowing rapid transfer of complex data structures between tasks. A novel memory management scheme maximised the processor throughput by implementing cycle steal refresh using a synchronous state machine. Local bus arbitration was introduced with the following priorities: CPU, memory refresh, DMAC, and external cycle access state machine.

System and application software. Software and hardware must be complimentary to maximise computational efficiency. The critical features are the multitasking capability (task dispatcher and intertask communication) and the memory management. The soft- ware developed for the parallel computer is divided into system software (determining the run-time environment), application software (for simulation and monitoring) and support software (for debugging, loading and editing programs).

The system software consists of two operating environments: extended Macsbug™, for execution and basic debug facilities, and TRIPOS, for software creation (providing a high-level program development environment), execution and additional debugging facilities. Standard mechanisms are provided for accessing peripherals, allocating memory, passing messages and scheduling tasks.

Macsbug™ has been extended with an interrupt-driven I/O system, which routes I/O packets to the first available processor and provides efficient, interrupt-driven support of serial ports, timers and the high-resolution graphics board. The TRIPOS portable operating system has been adapted to a multiprocessor environment, with much of the system software written in assembler, and supporting a block-structured high-level systems language, BCPL. The system provides a hardware-independent task environment and the programmable command shell in the operating system allows more processors to be added without the need to alter programs.

The application software provides a library of mathematical subroutines for evaluation of the algebraic equations and integration of the dynamic equations. It also monitors the simulation, collects data for storage or display, and applies external disturbances or inputs to the model. The first task, written in assembly language and executed in Macsbug™, is subject to rescheduling between processors by the system software. Asynchronous tasks such as presentation of data to output devices are run in background mode to use up processor idle time.

Support software is executed under TRIPOS. Higher-level functions are built from various assembly language routines, callable from BCPL. Examples are: Startup, Restore, Reset, Plot, Show, Keep, Save, Quit and Graph.

SYSTEM MODELLING

The induction motor equivalent circuit for steady state conditions is based on the standard model described, for example, by Dewan et al [9], and shown in Figure 4. For traction applications, the motor is operated at constant flux and slip up to the base speed, by keeping the input voltage/frequency ratio constant, after which the inverter frequency alone is increased for operation at constant power and increasing slip. When the slip reaches the pull-out value, a reduced power operational mode is entered. The different regimes are shown in Figure 5. Because the train tractive resistance variation is small, the constant acceleration part of the duty cycle mainly corresponds to constant torque and flux operation in the motor and the power-limited acceleration part of the duty cycle corresponds mainly to the other regions in the motor characteristic. The detailed motor modelling follows the scheme described by Mouniemne and Mellitt [10].

The VSI - induction motor model has been created by considering the relationship between the input and output variables of the VSI and motor. The simulation model is divided into input, driving and load sections.

Input section model

The input section model requires the target duty cycle and actual DC supply voltage. From knowledge of the existing train kinematic variables, the required inverter output condition (output voltage and modulation ratio) at the next time step is calculated. Starting from rest, the first mode is the constant torque region, where the inverter uses PWM since the required output voltage is below the rated motor voltage. The voltage/frequency ratio

$$K = V_{ph}/f_e \qquad (1)$$

where V_{ph} is the inverter output phase voltage and f_e is the inverter frequency, is kept constant. The constant torque mode starts at 0.5 Hz and following the prescribed duty cycle, the input frequency is gradually increased. The exact modulation ratio is calculated from knowledge of the value of the DC supply voltage. This also determines the exact transition speed to constant power operation.

In the constant power region, quasi-square wave operation holds, with the DC rail voltage (V_{dc}) proportional to the inverter per phase output voltage according to

$$V_{ph} = 0.45\ V_{dc}. \qquad (2)$$

Driving section model

The simulation objective in the driving section model is to predict the motor variables (current, voltage and slip) from knowledge of its equivalent circuit and the input voltage and frequency. In the constant torque region, the motor line current (I_1) is kept constant. At any given input frequency, the motor phase voltage is calculated from

$$V_{ph} = I_1 Z_{in} \qquad (3)$$

where Z_{in} is the motor input impedance per phase. The motor line current is, for rated conditions,

$$I_1 = V_e/Z_{in.e} \qquad (4)$$

where V_e, $Z_{in.e}$ are the rated phase voltage and motor input impedance per phase. During constant torque operation, the rotor slip frequency is also constant.

At speeds greater than that at which the inverter output voltage has reached its maximum value, the voltage is maintained constant, and the motor enters the constant power region. To satisfy the constant power condition, and assuming constant DC supply voltage, the motor line current is kept constant by raising the rotor slip frequency according to

$$I_1 = V_e/Z_{in} \qquad (5)$$

where

$$Z_{in} = Z_s + Z_m Z_r/(Z_m+Z_r) \qquad (6)$$

from Figure 4, with

$$Z_s = R_s + j\omega L_{ls} \qquad (7)$$

$$Z_r = R_r/s + j\omega L_{lr} \qquad (8)$$

and

$$Z_m = j\omega_s L_{ms} R_c/(j\omega_s L_{ms} + R_c). \qquad (9)$$

When the slip reaches its maximum value at high speed, the constant power region gives way to reduced power operation with the power-speed product almost constant. Since both phase voltage and slip are now constant, the motor line current must decrease with further increase of motor input frequency.

Three other variables are also calculated in the driving section model: motor pull-out slip, DC rail current and motor power factor. The motor output power (P_0) is the product of developed torque T_e and speed ω_m:

$$P_0 = T_e\omega_m = 3\ I_r^2 R_r(1-s)/s. \qquad (10)$$

After making suitable assumptions regarding the relative magnitudes of the equivalent circuit parameters, it may be shown [9] that the motor pull-out slip is approximately

$$s_m = \pm R_r/\sqrt{(R_s^2 + \omega_s^2 L_l^2)}. \qquad (11)$$

The DC supply current is found from a power balance involving the motor input impedance (Equation 6), and the motor power factor from the angle of the input impedance.

Load section model

The simulation objective in the load section is to calculate the motor torque, train tractive effort and hence the train kinematic behaviour. The motor torque is calculated from the power and speed in Equation (10) and converted to tractive effort (TE) from knowledge of the driving wheel diameter and wheel/rail friction coefficient. The tractive resistance in the form

$$R_r = A + Bv + Cv^2 \quad (12)$$

(with A, B, C constants and v the train velocity) is extracted from a look-up table and the net propulsion force used to determine the train acceleration according to

$$TE - R_r = J d\omega_m/dt \quad (13)$$

where J is the total equivalent load inertia. Using the present and previous kinematic values, integration gives velocity and distance.

IMPLEMENTATION

The system hardware consists of one master processor and two slaves. Normally one slave processor carries out the working task, the other being for graphical management. The software is arranged to execute 20 tasks, and also if necessary to run simultaneously in a time-sharing mode. For the system simulation as described above, five tasks are necessary: master, watchdog, worker, local slave and remote slave tasks. The master task is used to create, enable and control all other tasks. The watchdog task is a means through which the operators and processors can interact. The operator can choose one of five display pages, and freeze, modify system parameters, restart and stop. The worker task executes the commands specified by the watchdog task, controls the slave tasks, and update the graphical displays. The local slave and remote slave tasks carry out the algebraic calculations.

Additionally, there are 15 library routines, called freely by both slave tasks. These calculate the variables on the five page displays shown in Figure 6. The first page shows a random DC input voltage, varying between -33% to +20% of the nominal value of 750V, the variation of modulation depth under the nominal DC input voltage, and the variable DC input voltage. Six routines are used for pages 2 and 3 to calculate the motor line current, phase voltage, DC rail current, motor pull-out slip, operating slip and motor power factor. The motor torque and train resistance are shown on page 4, and page 5 shows the train acceleration, speed and distance.

The simulation is initiated through the console by the *run* command. This enables the master task and initialises all other tasks. Control of the console is then passed from the master to the watchdog. After this happens, any page may be selected, or the simulation stopped or frozen. A default results in the first page being displayed after a short interval. When one of the pages is selected, the worker task sends a data request to the local or remote slave (or both slaves), depending on the complexity of the task in hand. The number of screen update calculation points can also be preset. When the worker task sends a data request to the slave, a search for any packet sent by the watchdog task is first made. If, for example, the stop command is received, the worker task will tidy up the working conditions and return a packet to the master. After the watchdog task sends out the stop packet, console control is then returned to the master task.

CONCLUSIONS

Computer simulation of the operation of inverter - induction motor traction drives can provide information about steady-state performance with variable loading and duty cycle. An interactive type of simulation is desirable to achieve good accessibility to the model during run time. Such a simulation has been implemented using parallel computer hardware and multitasking software.

In the simulator, all important system variables can be displayed graphically. With no operator intervention, the simulation will follow a prescribed duty cycle with random DC supply voltage. Otherwise, the system parameters may be modified on-line by the user. For example, the inverter frequency, and hence motor slip, can be changed by altering the load characteristics from the console, after having frozen the simulation. The capabilities of this simulator have been demonstrated using data representative of a practical rail traction drive.

ACKNOWLEDGEMENTS

The authors are grateful to the Electrical Engineering Control Systems group at the University of Bath, England, for the provision of the parallel computer. In particular, Mr Richard Daniels and Dr Tom Berry are acknowledged for technical assistance. Dr Barry Cardwell of Brush Electrical Machines Ltd, Loughborough, England is also acknowledged for the provision of data relating to a prototype inverter-fed AC traction drive.

REFERENCES

1. Dewan, S. B., Joshi, A. and Slemon, G. R., 1979, "A multiaxle AC induction motor drive with current source inverter", IEEE Trans. Magnetics, 15, 1785-1787.

2. Holtz, J. and Stadtfeld, S., 1983, "A predictive controller for the stator current vector of AC machines fed from a switched voltage source", Int. Power Electronics Conference (IPEC), Tokyo, 1665-1675.

3. Taufiq, J. A., Chance, R. J. and Goodman, C. J., 1987, "On-line implementation of optimised PWM schemes for traction inverter drives", Int. Conf. on Electric Railway Systems for a new Century, London, 63-67.

4. Pritchard, R. and Pottle, C., 1982, "High speed power flows using attached scientific ('array') processors", IEEE Trans. Power App. Syst., 101, 249-253.

5. Hozhabri, A. and Ehsani, M., 1987, "Real time simulation of power electronic systems on single and parallel processors", Int. Symp. on Applied Simulation and Modelling, Santa Barbara CA, 86-89.

6. Wallach, Y. and Konrad, V., 1980, "On block-parallel methods for solving linear equations", IEEE Trans. Computers, 29, 3454-3459.

7. Viegas de Vasconcelos, A. and Hosemann, G., 1984, "Transient studies on a multiprocessor", IEEE Trans. Power App. Syst., 103, 3260-3265.

8. Dale, L. A., "Real-time modelling of multi-machine power systems", Ph.D. Thesis, University of Bath, UK, 1986.

9. Dewan, S. B., Slemon, G. R. and Straughen, A., 1984, "Power Semiconductor Drives", Wiley, New York.

10. Mouniemne, Z. S. and Mellitt, B., 1988, "Modelling of inverter-controlled asynchronous drives for system simulation in DC railways", Proc. IEE, 135B, 210-217.

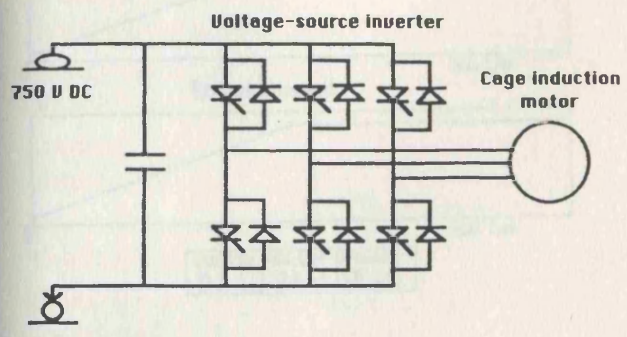

Figure 1: Inverter-fed induction motor traction drive

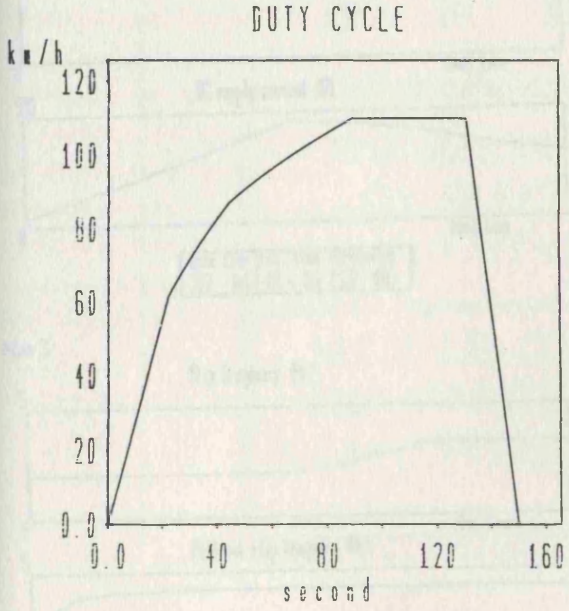

Figure 2: Traction duty cycle for mass transit railway

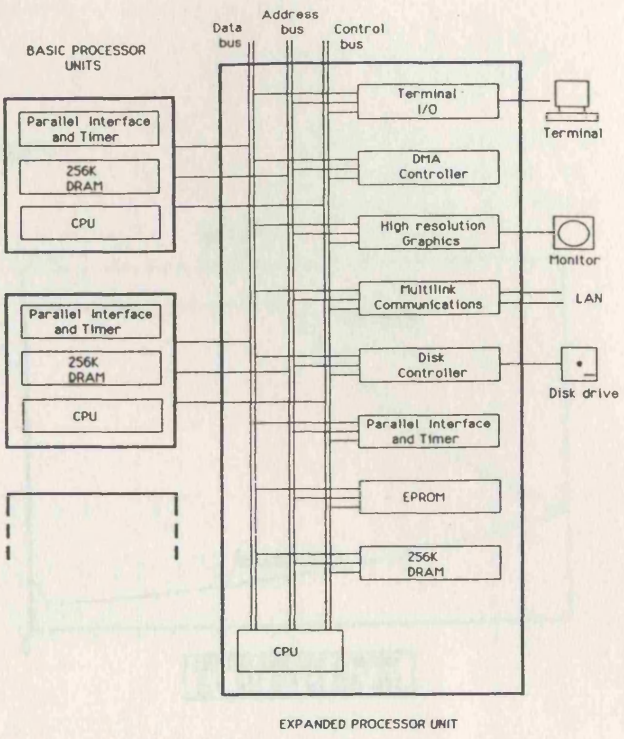

Figure 3: Parallel computer hardware

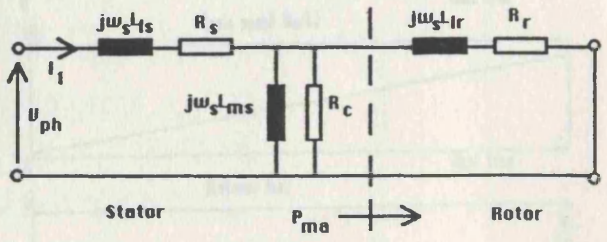

Figure 4: Induction motor steady-state equivalent circuit

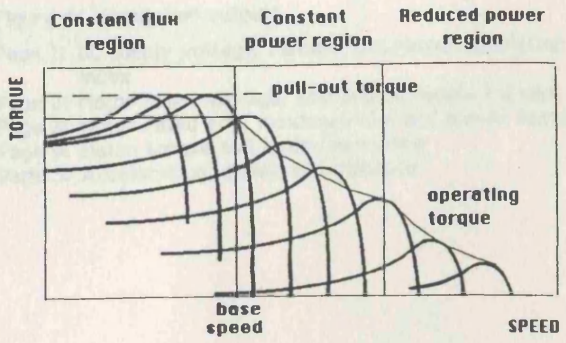

Figure 5: Induction motor torque-speed characteristics for traction

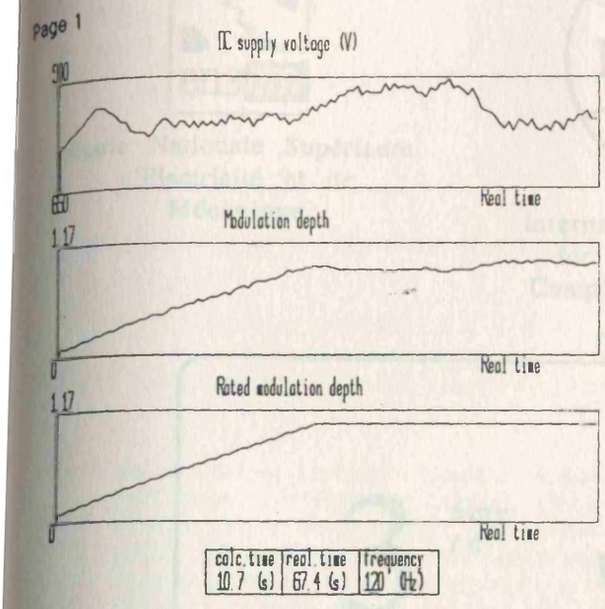

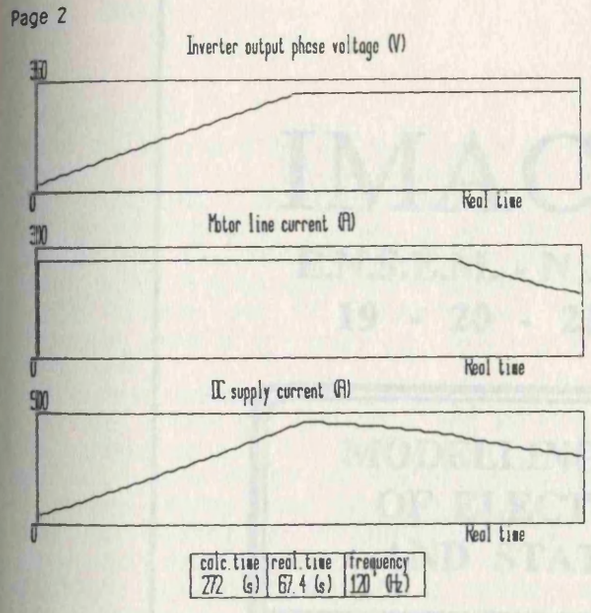

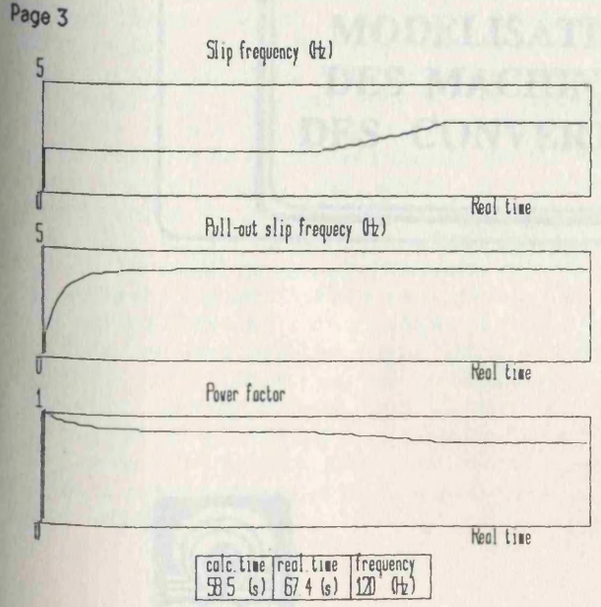

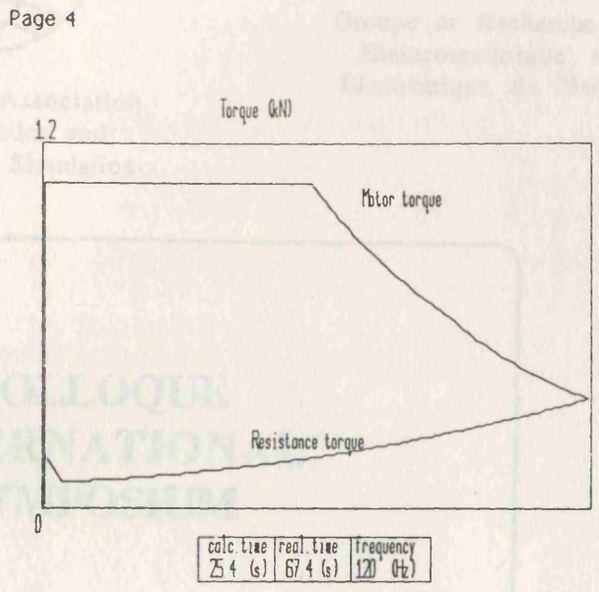

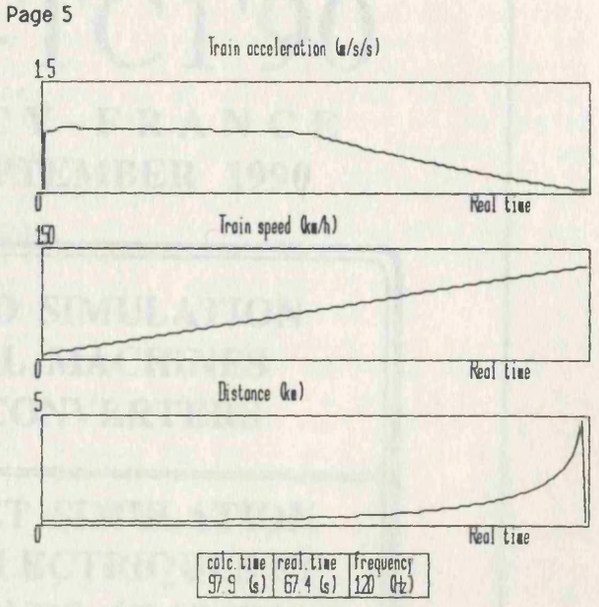

Figure 6: Simulation output:

Page 1: DC supply voltage, random and rated modulation index
Page 2: Motor phase voltage, line and DC supply current
Page 3: Motor rated slip, maximum slip and power factor
Page 4: Motor torque and train resistance
Page 5: Acceleration, speed and distance

Ecole Nationale Supérieure d'Electricité et de Mécanique

International Association for Mathematics and Computers in Simulation

Groupe de Recherche en Electrotechnique et Electronique de Nancy

3éme rd COLLOQUE INTERNATIONAL SYMPOSIUM

IMACS-TC1'90

E.N.S.E.M. - N A N C Y - F R A N C E
19 - 20 - 21 SEPTEMBER 1990

MODELLING AND SIMULATION OF ELECTRICAL MACHINES AND STATIC CONVERTERS

MODELISATION ET SIMULATION DES MACHINES ELECTRIQUES ET DES CONVERTISSEURS STATIQUES

PROCEEDINGS
VOL II

see
IEEE
IEE

IMACS-TC1'90
NANCY
19-20-21 SEPTEMBRE 1990

ON-LINE SIMULATOR FOR TRANSIENT BEHAVIOUR OF INVERTER-FED INDUCTION MOTOR TRACTION DRIVES

R. John HILL and Fengtai HUANG

School of Electrical Engineering, University of Bath, Claverton Down, Bath BA2 7AY, UK

An interactive simulator based on a parallel computer and intended for the evaluation of modulation strategies in DC-fed, voltage-source-inverter driven, induction motor rail traction drives is described. The modelling process to derive the switching device firing angles for asynchronous pulse-width modulation is given. The firing angles are used as input to a standard D-Q axis induction motor model to obtain the system transient response. The model continuously calculates the values of all important system variables, together with their harmonic spectra.

1. INTRODUCTION

The use of simulation in the design of power electronic traction drives enables system development time to be shortened by minimisation of prototype construction and testing. An effective traction drive simulator should be accurate and user-friendly. Precise mathematical models of the physical system must be combined with fast, convergent, solution processes for these aims to be achieved.

Voltage-source inverter (VSI) fed cage induction motor (IM) drives are economical and versatile arrangements suitable for rail traction. Large numbers of these drives are now in service for applications ranging from light rail vehicles to heavy duty locomotives. In operation, the drive follows a prescribed traction duty cycle by closed-loop control. Motor slip is usually the controlled variable, with both speed and current feedback loops present. During steady-state operation the inverter frequency is regulated to maintain a constant motor slip (for torque control) or variable slip (for speed control). In dynamic operation, variations in load and supply voltage may be regarded as disturbance inputs, the control system outputs being the stator and rotor currents, motor torque and supply current.

A major control objective in traction is to optimise the switching device modulation strategy. The various possible modulation schemes each have specific harmonic performances in terms of the converter input impedance and source current harmonics (1). Simulation can optimise these modulation strategies with the objectives of minimisation of electromagnetic interference (2), optimisation of transient step response (3) and studies of system behaviour with parallel inverters and/or motors (4).

Steady state and transient modelling techniques for VSI-fed IMs are well established, but most computer implementations reported in the literature have been carried out on mainframe computers in an off-line mode, with possible disadvantages of inaccessibility of the model during run time and poor user interface. This paper describes the construction of a user-interactive, on-line simulator to model the acceleration period of the traction drive according to a precalculated duty cycle. The modelling is in two sections: calculation of the VSI switching device firing angles according to a specific modulation scheme, and, using that information, the solution of the VSI-IM operational equations to obtain the continuous time variation of the system variables, together with their harmonic spectra. The simulator has the following advantages: the simulation can be frozen and the parameters changed during run-time; all variables are accessible in the time domain; and straightforward change in system parameters and switching device modulation strategy are available during run time. The variables that can be displayed at any time during the simulation are inverter input current, DC link current and voltage, stator and rotor current and motor torque.

2. FIRING ANGLE CALCULATION

The DC-fed traction drive illustrated in Figure 1 consists of a filter, VSI and 3-phase cage IM. The inverter supplies current at variable voltage and frequency to the motor. The output torque-speed characteristics over the complete operational speed range are shown in Figure 2. The steady state characteristics of the drive have been modelled in the frequency domain and are fully described in reference (5).

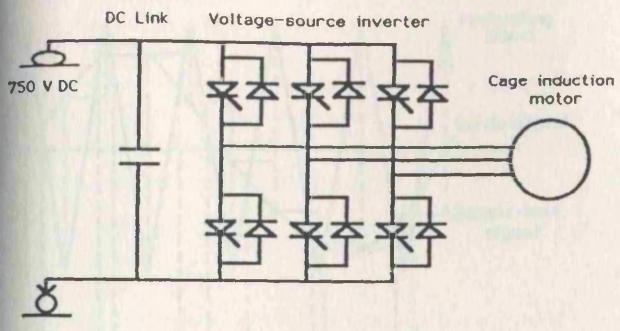

FIGURE 1. DC-fed VSI-IM drive

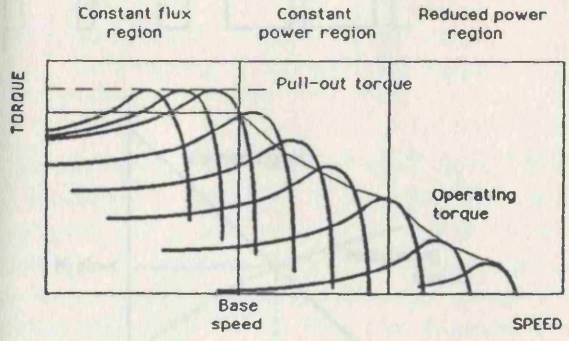

FIGURE 2. IM traction drive characteristics

The present simulation is concerned with operation up to the motor base speed. Calculation of the device firing angles to achieve a particular inverter voltage/frequency ratio during this region takes place assuming one of a number of possible modulation schemes. In this paper, asynchronous regular-sampled asymmetric double-edge pulse-width modulation (ARSADE PWM) is exemplified, with a constant carrier frequency of 500 Hz. The scheme is described in detail in reference (6).

The acceleration period corresponds to inverter frequencies between 0.5 and 60 Hz and during normal operation takes 20 s. The starting frequency of 0.5 Hz ensures rated torque is available from standstill. There is a frequency update every carrier cycle, where both amplitude and phase must be matched. This is illustrated in Figure 3.

The inverter output modulation frequency, f_m, and modulation depth M_i (the amplitude ratio of the modulating waveform to that of the carrier) are updated using the equations:

$$f_m = \alpha T + f_0 \qquad (1)$$

and

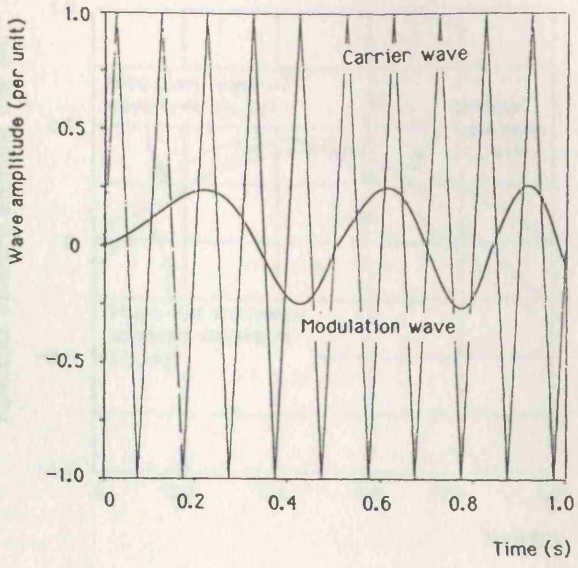

FIGURE 3. Inverter output waveform from 0.5 Hz to 3.475 Hz

$$M_i = \beta f_m + M_{io} \qquad (2)$$

where α is a constant determined by the required acceleration (= 2.975 Hz/s), T is the elapsed time in seconds, f_0 is the starting inverter frequency (0.5 Hz), β is a further constant determined by the slope of the motor flux characteristic (expressed in V/Hz) and M_{io} compensates for the initial offset of that curve at standstill. In ARSADE PWM, the sine wave modulation signal is sampled at every maximum carrier point and the sample value is transferred to the carrier crossing (Figure 4a). From Figure 4b, the modulation signal during the first quarter carrier cycle is given by

$$M_i \sin\alpha = X_0/T \qquad (3)$$

so the firing time is

$$X = T - X_0 = T(1 - M_i \sin\alpha). \qquad (4)$$

These equations give the upstroke and downstroke firing times

$$t_u = T[(3 + 4n) - M_i \sin\{(2 + 4n)2\pi f_m T + \phi_1\}] \qquad (5)$$

and

$$t_d = T[(1 + 4n) - M_i \sin(4n\, 2\pi f_m T + \phi_1)] \qquad (6)$$

where n is the carrier cycle number starting from zero, and ϕ_1 is the initial phase. When the frequency is updated, it is necessary to achieve a smooth transition by ensuring both amplitude and phase continuity. If at the transition between frequencies f_1 and f_2 the amplitudes are A_1 and A_2,

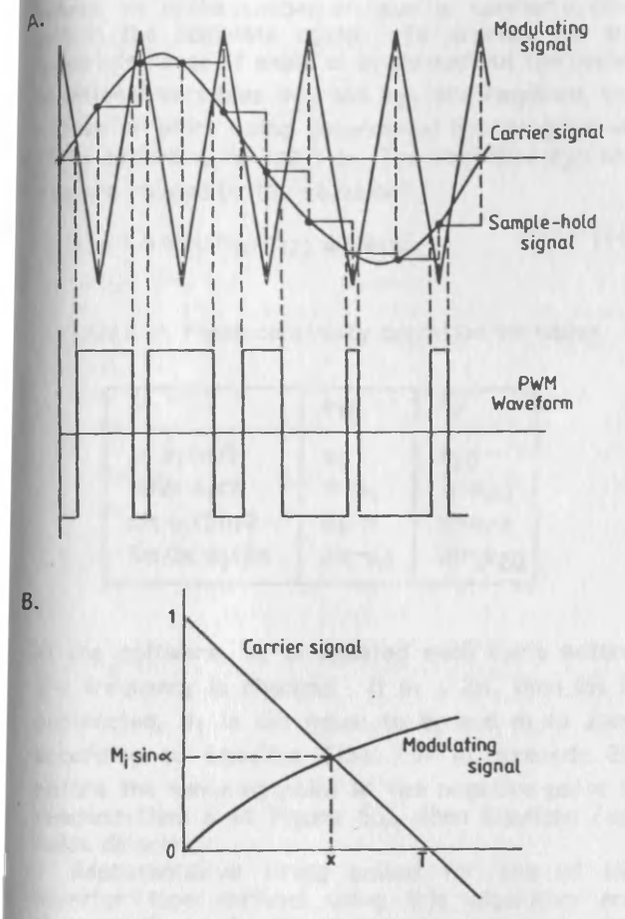

FIGURE 4. Asynchronous regular-sampled asymmetric double-edge PWM:
A, General principle
B, Firing angle calculation

and the initial phases are ϕ_1 and ϕ_2, then

$$A_1 = M_{11}\sin[\omega_1 t + \phi_1] = A_2 = M_{12}\sin[\omega_2 t + \phi_2]. \quad (7)$$

Since the parameters in the previous cycle (M_{11}, ω_1, ϕ_1) are known from Equations (1) and (2), M_{12} and ω_2 can be calculated for the following cycle. The other requirement is to obtain the new phase value (ϕ_2). Although by equating A_1 and A_2, the amplitude condition is met, in practice for any given amplitude A_1, there will be two possible values A_{21} and A_{22}. The phase condition is used to determine which one is appropriate. The situation is illustrated in Figure 5a. Setting

$$t_1 = \theta_1/2\pi f_1 \quad (8)$$

and

$$t_2 = \theta_2/2\pi f_2 \quad (9)$$

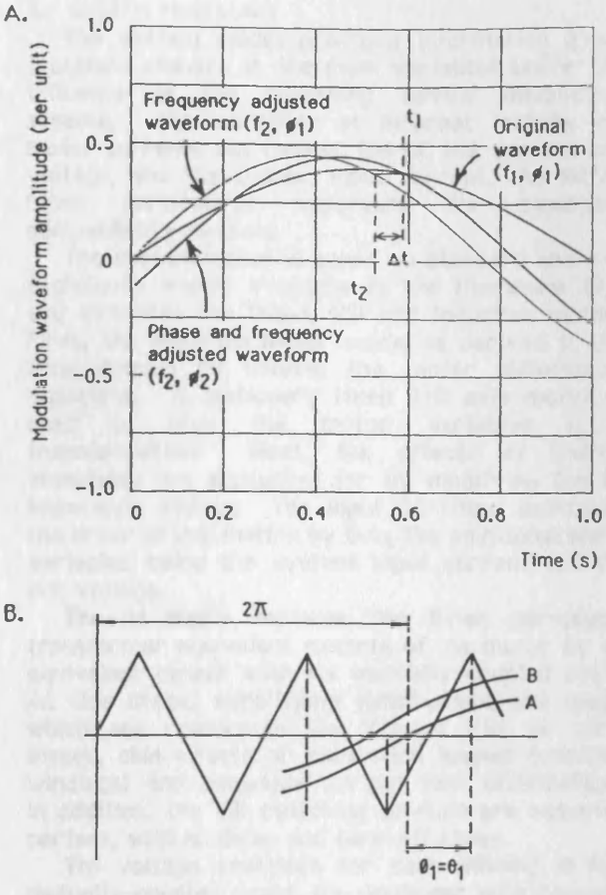

FIGURE 5. Phase and frequency update calculation:
A, Inverter modulation waveforms
B, Phase continuity condition

with

$$\Delta t = t_1 - t_2 \quad (10)$$

the phase becomes

$$\phi_2 = 2\pi f_2 \Delta t = (f_2/f_1)\theta_1 - \theta_2 \quad (11)$$

using equations (8) - (11). In Figure 5a, if $\Delta t > 0$, curve A should be shifted to the right (i.e. $\phi_2 < 0$), and if $\Delta t < 0$, it should shift to the left (i.e. $\phi_2 > 0$). Since the sinewave is sampled once during every half carrier cycle, at any instant the total time may be calculated from

$$t_T = 2nT_1 \qquad n = 0, 1, 2 \ldots \quad (12)$$

where T_1 denotes the period of a quarter carrier cycle. For any given frequency f_1, the angle θ_1 at the end of the duration is

$$\theta_1 = 4m\,2\pi\, f_{m1}\, T_1 + \phi_1 \quad (13)$$

where m is the number of quarter carrier cycles within the complete cycle. To account for the complete range of angle of θ_1 throughout the cycle, additional variables θ_{10} and θ_{20} are required, the values of which being determined by the quadrant of θ_1 according to Table 1. The variables θ_{20} and θ_{10} are related by the equation

$$\theta_{20} = a \sin[(M_{i1}/M_{i2}) \sin \theta_{10}]. \quad (14)$$

TABLE 1: Phase continuity condition variables

θ_1	θ_{10}	θ_2
$0< \theta_1<\pi/2$	θ_1	θ_{20}
$\pi/2< \theta_1<\pi$	$\pi-\theta_1$	$\pi-\theta_{20}$
$\pi< \theta_1<3\pi/2$	$\theta_1-\pi$	$\pi+\theta_{20}$
$3\pi/2< \theta_1<2\pi$	$2\pi-\theta_1$	$2\pi-\theta_{20}$

In the software, θ_1 is updated each cycle before the frequency is changed. If $\theta_1 \geq 2\pi$, then 2π is subtracted, ϕ_1 is set equal to θ_1 and m to zero according to Equation (13). If θ_1 exceeds 2π before the sampling point at the negative pulse is reached (line B of Figure 5b), then Equation (13) holds directly.

Representative firing pulses for one of the inverter legs derived using this algorithm are shown in Figure 6. The harmonic spectrum is also given.

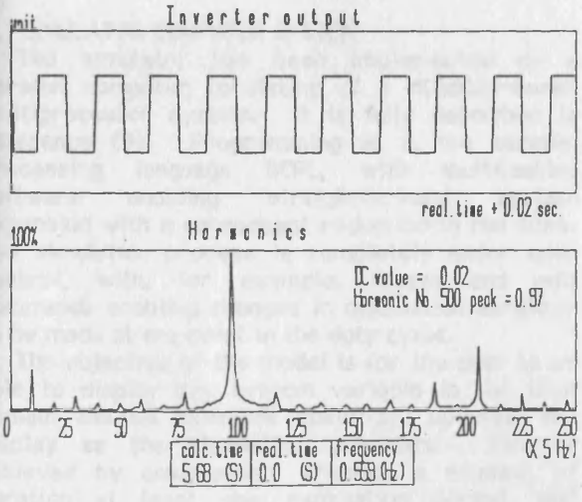

FIGURE 6. Inverter output waveform (one phase) and harmonic spectrum

3. SYSTEM MODELLING

The system model provides information about transient changes in the main variables under the influence of the switching device modulation scheme. The variables of interest include the motor currents and torque, the DC link current and voltage, and the system input current, the latter being particularly important for signalling compatibility reasons.

The system model is based on standard analytic techniques widely available in the literature (7), and simulates the filter, VSI and induction motor. First, the induction motor model is derived in the time domain by solving the motor differential equations. A stationary fixed D-Q axis model is used to give the motor variables after transformation. Next, the effects of source impedance are accounted for by modifying the IM impedance matrix. The input DC filter increases the order of this matrix by two, the additional state variables being the system input current and DC link voltage.

The IM model replaces the three per-phase transformer equivalent circuits of the motor by an equivalent circuit with six mutually-coupled coils. At this stage, simplifying assumptions are made which are reasonable for VSI-fed IMs: no core losses, skin effects or saturation losses; balanced windings; and sinusoidal airgap flux distribution. In addition, the VSI switching devices are assumed perfect, with no delay and turn-off times.

The voltage equations for each winding in the mutually-coupled model are nonlinear with respect to rotor angle and are of the form:

$$[V_{i0}] = [Z_{jk}][I_{i0}] \quad (15)$$

where the elements of $[V_{i0}]$ and $[I_{i0}]$ are the six stator and rotor voltages and currents, and the elements of $[Z_{jk}]$ are the parameters in the motor equivalent circuit, including mutual inductances, and the rotor displacement angle.

At constant rotational speed, by using a transformation matrix, Equation (15) can be transformed into a linear set of equations with constant coefficients. The matrix equation is that of a two-phase rotating axis model, and a further transformation is then made to obtain the two-axis stationary representation. This relates the pairs of direct and quadrature voltages to the corresponding currents. The resulting equation system is linear for constant speed operation (at variable speed, the mechanical system equation must be considered). The model equation is finally expressed in state variable form as

$$[V] = \{[R] + \theta'[G] + [L]p\}[I] \quad (16)$$

where [V] and [I] are the direct and quadrature voltage matrices, [R], [L] and [G] are composed of the rotor and stator equivalent circuit parameters,

θ' is the rotor speed, and p is the Laplace operator. The state variables are the motor currents.

Solution of equation (16) by computer is most conveniently carried out using the method of eigenvalues, with new state variables obtained by the further transformation

$$[X] = [E][Y] \qquad (17)$$

where [X] and [Y] are the original and new state variables and [E] is the eigenvector matrix. The result is four decoupled differential equations which are solvable by standard computer subroutines.

Source impedance effects are accounted for in the model by modifying the motor equation impedance matrix. Two extra state variables are necessary to represent the DC input current and voltage.

The VSI-IM circuit shown in Figure 1 operates with three of the six device switches closed at any instant of time, giving six normal modes of conduction. A seventh mode covers simultaneous closure of the three upper or lower switches, whereupon all the motor line-line voltages are zero. The modelling procedure is to write mesh equations for each of the seven modes, substitute the values for $[V_{i0}]$ from equation (15) and apply appropriate axis transformations to obtain the two-axis fixed model equations. The resulting matrix equation is then reduced to first order by treating the DC link voltage as a state variable. Finally, the seven sets of matrix equations are solved by the eigenvalue method, with the constraint that the final values of the state variables in each mode are equal to the initial values in the next.

4. SIMULATOR COMPUTER SYSTEM

The simulator has been implemented on a parallel computer consisting of a MC68020-based multiprocessor system. It is fully described in reference (5). Programming is in the parallel processing language BCPL, with multitasking software enabling straightforward system expansion with a consequent reduction in run time. The simulation process is completely under user control, with, for example, freeze and edit commands enabling changes in modulation strategy to be made at any point in the duty cycle.

The objective of the model is for the user to be able to display any system variable in the time domain and its harmonic spectrum, updating the display as the simulation proceeds. This is achieved by continuously creating a window, of duration at least one modulation period, and storing sufficient real-time variable values for the time display and calculation of the frequency spectrum by fast Fourier transform (FFT). The latter requirement has led to the development of a new software FFT implementation, written in BCPL and incorporating an economical sine look-up table.

5. RESULTS

The ouputs of the model are the inverter input current, DC link current and voltage, stator and rotor current and motor torque. All of these system variables are available in the time domain, at any time during the acceleration period. Figures 7 and 8 show typical results for the DC link capacitor voltage and the system input current.

6. CONCLUSIONS

A simulator has been constructed which models transient behaviour during the acceleration period

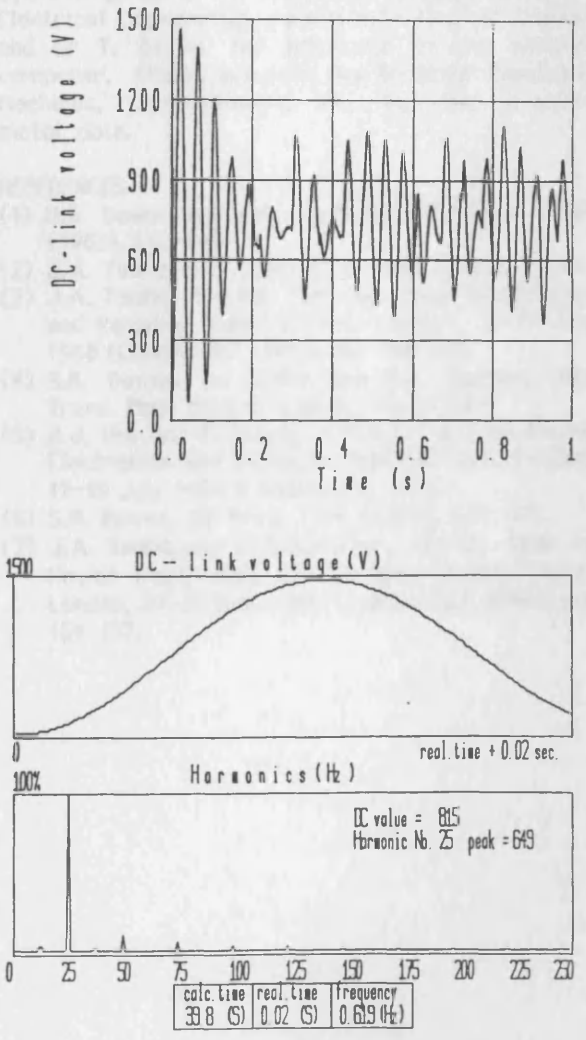

FIGURE 7. DC link voltage over long and short time scales and window frequency spectrum

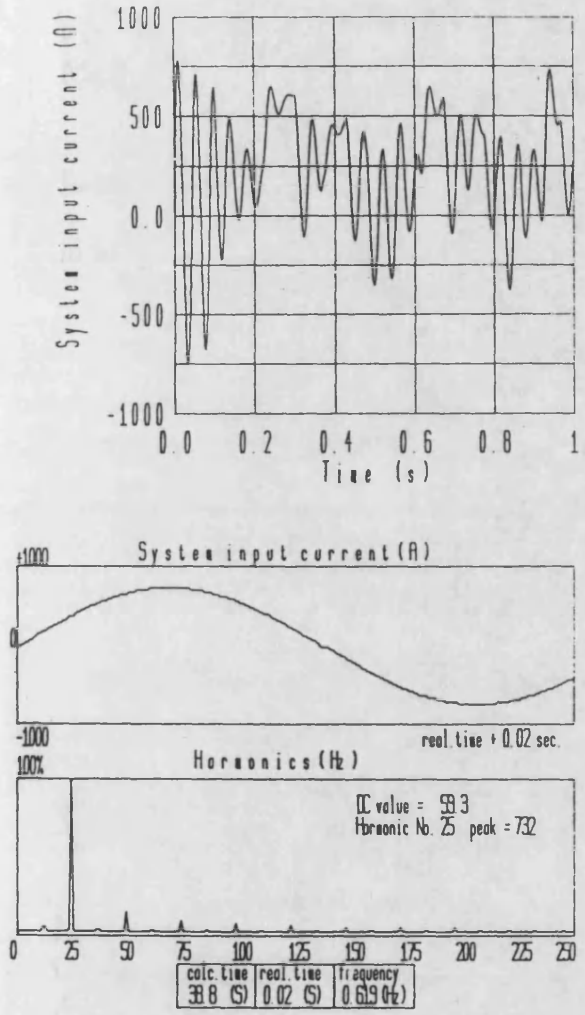

FIGURE 8. System input current over long and short time scales and window frequency spectrum

in a DC-fed VSI-IM traction drive. The simulation takes place in an interactive user environment, with the ability to freeze the display and change the system parameters during run time.

The IM model uses a standard D-Q axis transformation, and account is taken of DC-link source impedance. The model leads to a state variable formulation with solution by the method of eigenvalues.

The simulator may be used to study the effects of different modulation strategies on DC-link voltage and current, motor stator and rotor current and motor torque. The algorithm described has been tested in a non-optimal implementation of ARSADE PWM.

ACKNOWLEDGEMENTS

The authors would like to thank the Control Systems group at the University of Bath, School of Electrical Engineering, particularly Mr A.R. Daniels and Dr T. Berry, for provision of the parallel computer. Thanks are also due to Brush Electrical Machines, Loughborough, UK, for the traction motor data.

REFERENCES

(1) S.R. Bowes and R.R. Clements, IEE Proc. 130B (1983), 149-160.
(2) J.A. Taufiq et al., IEE Proc. 133B (1986), 71-84.
(3) J.A. Taufiq, 3rd Int. Conf. on Power Electronics and Variable-Speed Drives, London, 13-15 July 1988 (London: IEE 1988), pp. 340-342.
(4) S.B. Dewan, A. Joshi and G.R. Slemon, IEEE Trans. Mag. MAG-15 (1979), 1785-1787.
(5) R.J. Hill and F. Huang, 4th Int. Conf. on Power Electronics and Variable-Speed Drives, London, 17-19 July 1990 (London: IEE 1990).
(6) S.R. Bowes, IEE Proc. 132B (1985), 133-148.
(7) J.A. Taufiq and C.J. Goodman, 2nd Int. Conf. on Power Electronics and Variable-Speed Drives, London, 22-26 Nov. 1986 (London: IEE 1986), pp. 154-157.

IMACS '91

Proceedings of the 13th IMACS World Congress on Computation and Applied Mathematics

July 22-26, 1991,Trinity College, Dublin, Ireland

in four volumes

VOLUME 4

Modelling and Simulation for Electrical, Electronic and Semiconductor Devices
Computation for Management Systems
Applications of Modelling and Simulation
Environmental Systems Simulation
Software Forum
Poster Sessions
Author Index

EDITED BY: R Vichnevetsky
Rutgers University
New Brunswick, USA

J J H Miller
Trinity College
Dublin, Ireland

AN ON-LINE FFT IMPLEMENTATION FOR A PARALLEL COMPUTER SIMULATION OF A VSI-IM RAIL TRACTION DRIVE

R. JOHN HILL and FENGTAI HUANG

School of Electrical Engineering, University of Bath,
Claverton Down, Bath BA2 7AY, England

Abstract - An on-line interactive FFT calculation of the harmonic spectra of the voltage and current variables in a VSI-IM rail traction drive simulation is presented. The implementation is on a parallel computer and is user-driven by a 'freeze and display' command. Simulation results are give for the spectra of the line and motor current waveforms during synchronous PWM operation of the drive.

I. INTRODUCTION

A major simulation task in a VSI-IM rail traction drive is to determine the harmonic performance as the VSI modulation strategy is changed. Consequently, most industrial simulators based on PCs or workstations incorporate a harmonic analysis facility to continuously display the spectra of the main electrical and mechanical variables throughout the traction duty cycle. The problem addressed in this paper is to provide a flexible selection facility, under interactive user control, for the extraction of harmonic information during the simulation of a such a traction drive.

In the paper, a parallel-computer based VSI-IM rail traction drive simulator is outlined. The software structure to enable on-line window definition and extraction of FFT-derived spectra in real time is then described. The procedure is carried out under user-interactive control via a freeze and display facility. Sample results for the harmonic spectra of input and motor currents during synchronous PWM operation in the acceleration period of the drive are then presented.

II. CONVERTER-MOTOR SYSTEM MODELLING

The VSI-IM rail traction drive modelled is illustrated in Figure 1. It is operated under practical conditions with a three-part duty cycle. From standstill to motor base speed, the IM is driven at constant flux; this is followed by constant power motion, with a final region of reduced power up to maximum speed. To achieve this duty cycle, the inverter is operated by PWM to the base speed (asynchroncus PWM at startup, followed by synchronous PWM), and thence by quasi-square-wave modulation. In the PWM region, various modulation schemes are available which have the effect of reducing or minimising harmonic distortion of the supply current and motor voltage waveforms. However, these involve sudden change of the modulation ratio and/or index at certain speeds, which leads to poor harmonic performance at the changeover point.

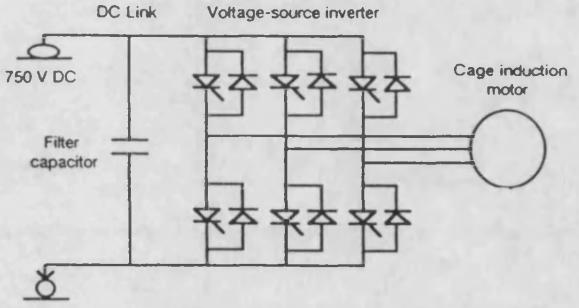

Fig. 1. VSI-IM rail traction drive.

The converter-motor system model, fully described in reference [1], simulates the filter, VSI and IM. The IM is modelled in the time domain by setting up and solving the motor differential equations. Transformation to a fixed D-Q axis model is then achieved giving the model equation in terms of the Laplace operator p as

$$[V] = \{[R] + \theta'[G] + [L]p\}[I] \qquad (1)$$

where [V], [I] are the direct and quadrature variable matrices, [R], [L], [G] are the elements of the IM rotor and stator equivalent circuits, and θ' is the rotor speed. The input DC filter is modelled as part of the IM impedance matrix, thus including the system input current and DC link voltage as additional state variables. The solution of Equation (1) is obtained by the method of eigenvalues. The model is then solved for each of the six VSI device conduction modes using nodal equations and matching boundary conditions.

Typical results for startup from rest are shown in Figure 2. The transition from asynchronous to synchronous PWM at

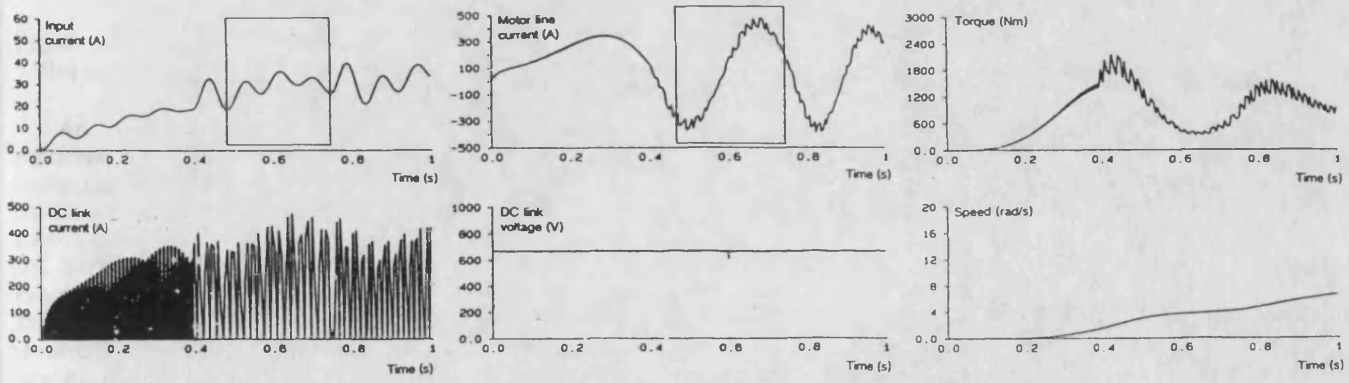

Fig. 2. Simulator outputs for one-second traction drive acceleration period.

about 0.4 s is clearly shown, as also are variations in input current and torque as the drive accelerates.

III. ON-LINE FFT GENERATION

The simulator has been implemented on a 68020-based parallel computer [2]. The task structure is shown in Figure 3. The procedure to initiate a FFT calculation is to initialise the system by keyboard command, and to define the time window of interest by selecting the starting instant , the sampling interval and the number of points. The master program then informs the calculator task that the FFT calculation is underway. The parallel structure of the simulator ensures the FFT and model calculations proceed simultaneously, although the FFT itself is calculated serially.

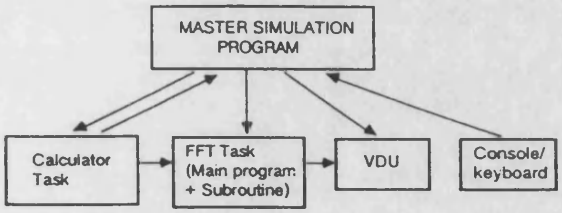

Fig. 3. Simulator task organisation.

Computation of the FFT is based on the Cooley-Tukey algorithm [3] developed by Brigham [4]. The algorithm implementation is acheved by a main program, which is a routine of the simulation model, with a subroutine to perform the Fourier analysis. The main program passes the data set (signal amplitude, total window angle) and the number of points (in binary) to the subroutine, where the sine/cosine value table is set up, and the calculations and sums performed, the results being returned to the main routine.

The procedure requires the input function to be represented in 2N points (Figure 4). An N-point transform is used to compute the real and imaginary parts, $X_r(n)$ and $X_i(n)$, of the discrete Fourier transform.

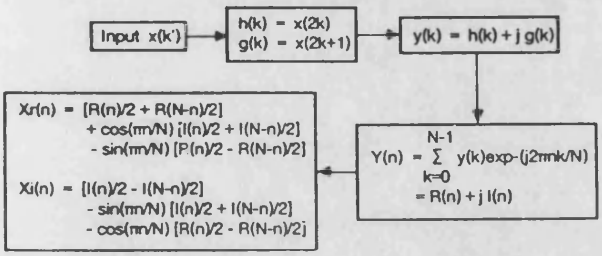

Fig. 4. FFT algorithm. x(k), h(k), g(k), R(n), I(n) are real; y(k), Y(n) are complex; k' = 0,1, . . . 2N-1, and k, n = 0,1, . . . N-1.

An advantage of the Cooley-Tukey algorithm is a reduction in the number of multiplications and additions in the computation. However this is at the expense of the need to de-scramble the output data. Thus after the values have been returned by the subroutine, the main routine separates the frequencies to return the completed harmonic analysis result to the simulation program for console display. The algorithm used to drive the results in natural order uses the decimation in time technique [4], where powers of exp-(j2π/N) are provided in the correct order needed for computation, thus eliminating the need for extensive storage tables.

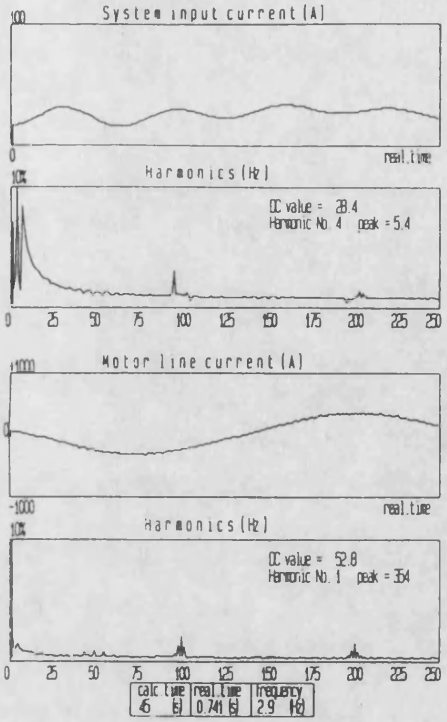

Fig. 5. System input and motor line currents and FFT spectra.

The system input and motor line currents in Figure 2 have been windowed as shown and subjected to FFT analysis. The results, Figure 5, show the motor line current as almost sinusoidal, with more harmonics in the input current. Shown are the amplitude of the most significant harmonic, and the modulation frequency (2.9 Hz), real time (0.871 s), and calculation time (45 s).

IV. DISCUSSION AND CONCLUSIONS

Measurement of periodic signal parameters is generally subject to errors from spectral leakage and harmonic interference. Normally, interpolation algorithms are used to minimise these errors. Careful choice of sampling frequency and truncation envelope is thus required. The use of flat-top windows, as described by Salvatore and Trotta [5], is currently being investigated to reduce errors.

The simulator has proved to be a convenient, flexible tool which has enabled harmonic production at switching transitions between various forms of PWM to be investigated.

V. REFERENCES

[1] Hill R.J. and Huang F.: On-line simulator for transient behaviour of inverter-fed induction motor traction drives. Proc. IMACS-TCI '90, Nancy, 19-21 Sept. 1990, pp. 417-22.

[2] Hill R.J. and Huang F.: Performance prediction of inverter-induction motor drives for DC-fed railways. 4th Int. Conf. PEVSD, London, 17-19 July 1990, pp. 529-33.

[3] Cooley J.W. and Tukey J.W.: An algorithm for machine calculation of complex Fourier series. Math. Computation, Apr. 1985, v. 19, pp. 297-301.

[4] Brigham E.O.: The Fast Fourier Transform. Englewood Cliffs NJ: Prentice-Hall 1974.

[5] Salvatore L. and Trotta A.: Flat-top windows for PWM waveform processing via DFT. Proc. IEE, Nov. 1988, v 135B, n 6, pp. 346-61.

EPE '91

First Day of Conference
Volume 1

4th European Conference on

Power Electronics and Applications

Centro Congressi di
FIRENZE
Piazza Adua 1 - 50123 FLORENCE (Italy)

Firenze September 3 - 6 , 1991

Editor:
P. Ferraris

Published by:
Litografia GEDA
Via Villa Glori, 6
10133 Torino - Italy

EPE FIRENZE 1991

VERIFICATION OF AN ON-LINE SIMULATOR FOR VSI-IM RAIL TRACTION DRIVES

R.J. Hill, F.Huang
School of Electronic and Electrical Engineering, University of Bath, Claverton Down, Bath BA2 7AY, England

Abstract. An on-line simulator for DC-fed, VSI-IM rail traction drives has been created using a parallel computer. The simulator implements a D-Q axis transient model and produces time domain outputs of the system voltages & currents, torque and speed as the drive accelerates through a typical traction duty cycle. FFT spectra are available of all the time waveforms at user-defined windows. This paper describes the verification of the simulator. This is achieved by comparing simulated results of the harmonic spectra of the system variables with those obtained by measurements on a small-scale laboratory model. The simulated and experimental results reported in the paper occur near a modulation step change and are in agreement within the bounds of experimental error.

Keywords. Rail traction, simulators, voltage-source inverters.

INTRODUCTION

The use of converter-fed induction motor drives on DC-supplied light rail and urban metro railways has been aided by computer simulation in the design process. The desired features of a simulator are that it should be convenient and quick to use, versatile in its range of applications and accurate in the modelling and calculation process. The objective of this paper is to demonstrate the verification of a simulator that has been constructed for on-line optimisation of the modulation strategy in voltage-source inverter, induction motor (VSI-IM) rail traction drives, by comparing experimental test results from a small-scale laboratory model drive with the simulated results.

The advantages of VSI-IM drives for rail traction applications derive from the use of the cage induction motor (with its high power-to-weight ratio, simple construction, ease of maintenance and low cost), in conjunction with solid state power conditioning (with the elimination of mechanical switches, improved energy management and reduced maintenance). However, careful design is necessary in VSI-IM traction drives to reduce motor current harmonics which give rise to torque pulsations, and to minimise supply current harmonics which can cause interference currents in the railway signalling and telecommunications system. The main control objective during the acceleration and deceleration of a drive is thus to optimise the inverter switching device modulation scheme, and for this, simulation is a vital tool. Knowledge of the harmonic performance at modulation step changes is particularly important in this respect since the subsequent transient currents can produce bursts of interference at critical frequencies which could excite system resonances.

Various types of pulse-width modulation (PWM) have been implemented for different VSI-IM drive applications. Many existing rail traction drives use a PWM strategy that minimises a weighted function of all harmonics, or eliminates all harmonics below a certain value at the expense of increasing the amplitude of higher-order harmonics (Bowes and Clements 1983). Generally, these schemes have been designed with the aid of off-line simulation (Taufiq and Goodman 1986). The novelty of the present simulator lies in its on-line mode of operation, achieved using a parallel computer. The software structure gives the time waveforms of six variables: filter input current, DC link current, motor line current, DC link voltage, motor torque and speed. It incorporates a facility to define a window and calculate the FFT of the captured waveform. This enables the user to identify key features of the waveform such as changes in modulation ratio, and to quickly calculate the associated transient response. In this paper, the simulation model is described, together with a verification process by comparing the simulation results with experimental measurements on a 3 kW laboratory traction drive.

SIMULATION MODEL

Traction duty cycle

The conventional rail traction duty cycle used in a VSI-IM drive in the accelerating mode can be divided into several regions (Fig. 1). In region 1, the torque quickly increases from zero to the rated value with the establishment of the motor flux. During region 2, the drive produces a constant motor torque by maintaining the inverter voltage/frequency ratio constant, most conveniently by PWM; the motor slip is hence maintained constant, and the power increases with speed. In region 3, operation is at constant power, so the acceleration of the drive reduces as the speed increases; the increasing traction frictional load causes a further reduction in acceleration; the inverter is operated using quasi-square wave modulation, with the motor speed range typically rising to about twice base speed; the torque therefore reduces and

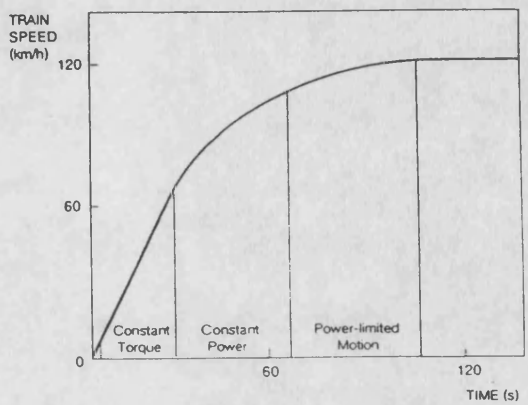

Fig. 1: Traction duty cycle for metro or light rail system.

the slip increases to the pullout value. Region 4 is the power-limited operational region, where the slip is maintained at pullout and the maximum speed of operation is determined by the value of the traction load.

Asynchronous PWM in region 1 of the traction duty cycle is followed by synchronous PWM in region 2. Various types of synchronous PWM are available. For the conventional VSI-IM drive of Fig. 2, , the main possibilities are natural sampled PWM, regular sampled PWM, or optimised PWM with reference to harmonic minimisation or elimination. Both natural and regular sampled PWM can be single or double sided, and all types are available as two or three level implementations (Bowes and Clements 1983). The choice of which to adopt for a specific application depends on the maximum allowed inverter switching frequency, the desirable input current harmonic spectrum, the design temperature rise of the motor from harmonic losses and the permitted torque pulsations. Practical rail traction drives can have from 4-10 different modulation ratios to satisfy these constraints, as illustrated by Halonen and Karha (1980).

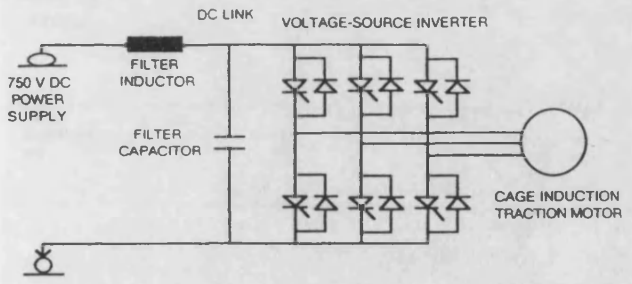

Fig. 2: VSI-IM traction drive.

For the purposes of verification of the present simulator, natural sampled PWM is used except above 0.75 of the base speed where modified natural sampled PWM is introduced according to Tsuboi and Nakamura (1986). The carrier frequency has been increased in discrete steps with modulation index changes at 51, 27, 15 and 9. Including the modified PWM, there are five step modulation changes, with a total of 21 carrier frequencies at which the transient performance of the simulator may be verified.

VSI-IM transient model

The simulation comprises a mathematical model with an inverter device firing angle look-up table. The contents of the table represent the input to the system model, and the model output is available as functions of time and frequency through on-line FFT analyses (Hill and Huang 1991).

The modelled system of Fig. 2 consists of a DC input filter, VSI and IM. All power switches are assumed to be ideal devices. The VSI operates in the π conduction mode, with three devices conducting simultaneously. There are seven switching modes, including that where the top three or bottom three devices are on simultaneously. The modelling task to create the inverter device firing angle look-up table is to determine the sequence of the seven switching modes, and the length of time for each mode.

The two-axis stationary reference frame model was used for the IM. The matrix form of the model in terms of voltage and current is (Taufiq and Goodman 1986):

$$\begin{bmatrix} V_{qs} \\ V_{ds} \\ V_{qr} \\ V_{dr} \end{bmatrix} = \begin{bmatrix} (R_s + sL_s) & 0 & sL_m & 0 \\ 0 & (R_s + sL_s) & 0 & sL_m \\ sL_m & -\omega_r L_m & (R_r + sL_r) & -\omega_r L_m \\ \omega_r L_m & sL_m & \omega_r L_r & (R_r + sL_r) \end{bmatrix} \begin{bmatrix} i_{qs} \\ i_{ds} \\ i_{qr} \\ i_{dr} \end{bmatrix} \quad (1)$$

This equation is applied to each mode to form seven system equations:

$$\begin{bmatrix} V_{in} \\ 0 \\ 0 \\ 0 \\ 0 \\ 0 \end{bmatrix} = \begin{bmatrix} (R_f + sL_f) & 1 & 0 & 0 & 0 & 0 \\ 1/C_f & -s & K_{1i}/C_f & K_{2i}/C_f & 0 & 0 \\ 0 & K_{1i}/C_f & (R_s + sL_s) & 0 & sL_m & 0 \\ 0 & K_{2i} & 0 & (R_s + sL_s) & 0 & sL_m \\ 0 & 0 & sL_m & -\omega_r L_m & (R_r + sL_r) & -\omega_r L_m \\ 0 & 0 & \omega_r L_m & sL_m & \omega_r L_r & (R_r + sL_r) \end{bmatrix} \begin{bmatrix} i_{in} \\ V_{dc} \\ i_{qs} \\ i_{ds} \\ i_{qr} \\ i_{dr} \end{bmatrix} \quad (2)$$

In equations (1) and (2), the component values refer to the standard IM equivalent circuit, K_{1i} & K_{2i} are constants determined by the individual modes and ω_r is the rotor angular frequency. The speed-torque relationship is:

$$T_e - T_1(\omega_m) = J\, d\omega_m/dt = 2J\, d\omega_r/dt \quad (3)$$

where T_e is the developed torque, $T_1(\omega_m)$ is the traction load torque, J is the system inertia, p is the number of motor poles and ω_m is the motor speed. The motor developed torque is related to the D-Q variables by

$$T_e = 1.5\,(p/2)\,L_m\,(i_{qs}\,i_{dr} - i_{ds}\,i_{qr}) \quad (4)$$

Equations (2) - (4) give the complete model of the VSI-IM traction drive in terms of a 7th order nonlinear system.

Implementation

The simulation model was implemented on an interactive parallel computer based on MC68000 microprocessors as described by Hill and Huang (1990a). Programming was in the BCPL language which allowed the Runge-Kutta integration method to be used with the advantage of high accuracy and small integration step lengths. The laboratory test drive and a full-scale traction drive were both modelled, the following details referring to the laboratory drive, where the base speed was 50 Hz and the constant power operation limit was 85 Hz.

The inverter device firing angle sequence was constructed from knowledge of the traction drive duty cycle (Fig. 1). The steady state performance requirement in the constant torque region required the motor speed variation as a function of time. Knowing the required slip frequency ω_1 then gave the system supply variation ω_s as a function of time through

$$\omega_s = \omega_1 + \omega_r \quad (5)$$

with

$$\omega_r = (p/2)\,\omega_m. \quad (6)$$

For each supply frequency, the model determines the modulation depth (M_d) from the V/f figure for the motor, and the modulation frequency (M_f). The model accelerates the drive in the constant power region by keeping the stator current constant, and in the reduced power region by keeping the motor slip at the pullout value. The details of the procedure for calculation and generation of the VSI device firing angles is described in Hill and Huang (1990b).

Simulation results

For the purpose of simulator verification, the modulation strategy given in Table 1 was implemented. This provided for 23 discrete operational steps with the possibility of 5 changes of modulation strategy (the modulation ratio of 9+ refers to the modified scheme with pulse dropping). The simulator output

Table 1: Accelerating duty cycle for laboratory drive

Modulation frequency (Hz)	Modulation ratio	Repeat cycles	Real time (s)	Modulation frequency (Hz)	Modulation ratio	Repeat cycles	Real time (s)
2.667	51	12	4.500	27.08	15	123	54.72
4.911	51	21	8.776	29.22	15	132	59.24
7.033	51	33	13.47	31.35	9	144	63.83
9.35	51	42	17.96	33.49	9	153	68.40
11.56	27	54	22.63	35.62	9	162	72.94
13.56	27	63	27.18	37.72	9+	171	77.48
16.06	27	75	31.86	39.81	9+	183	82.077
18.32	27	84	36.45	41.91	9+	192	86.66
20.53	15	93	40.98	44.0	9+	201	91.23
22.7	15	105	45.60	46.06	9+	210	95.79
24.91	15	114	50.18	48.12	9+	219	100.34

waveforms during the first 4 seconds of motion are shown in Fig. 3, where the input, DC link & motor line currents and torque all show the variations which arise from the modulation frequency changes of Table 1. In addition, the DC link voltage is almost constant and the speed increases linearly.

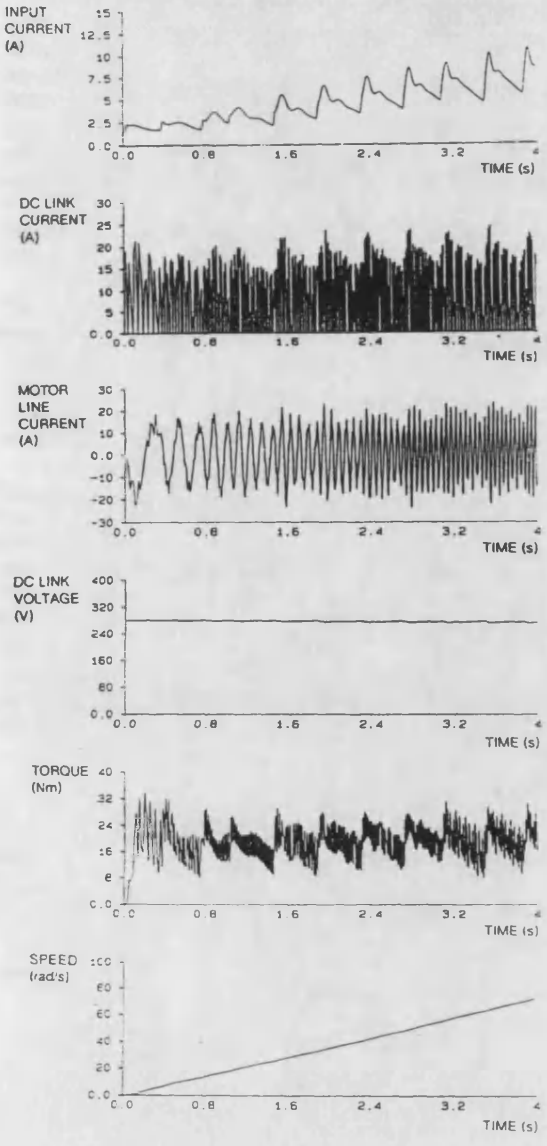

Fig. 3: Simulation model output for period 0-4 seconds.

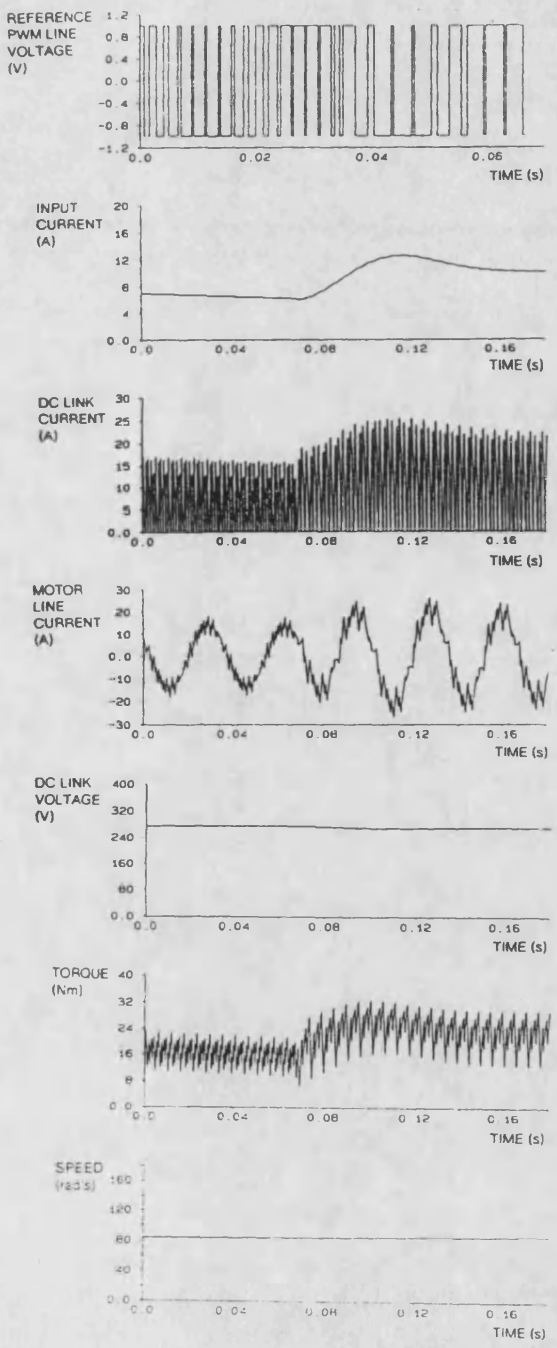

Fig. 4: Simulation model output after supply frequency and modulation change (reference time = 4.634 s).

The verification objective is to compare the transient performance with laboratory practical tests, and for this purpose Fig. 4 shows the variable changes when the supply frequency and hence also the modulation conditions change. Again, there is minimal effect on the DC link voltage and speed but all the other parameters show variations.

The model is able to compare the harmonic spectra just before, and just after, the transient. To illustrate this, Fig. 5 shows sample motor line current waveforms and their FFT analyses obtained by constructing windows at the appropriate times. The variation in harmonic spectra with increasing current is evident from these results.

LABORATORY TEST DRIVE AND VERIFICATION PROCEDURE

Test drive

The laboratory based experimental drive consists of a transformer, rectifier, filter, VSI with GTO thyristors and IM with a combined inertia and friction load, the latter simulated using a DC generator (Fig. 6). The drive is a scaled model of a rail traction drive with the parameters given in the appendix. The control of the VSI is via a 68000 single-board computer (SBC) with a logic control unit, linked by a 68230 parallel interface timer.

The usual precautions were taken to protect the VSI from simultaneous conduction of the GTOs in a single leg, and to account for the 1.25 µs switch-on time and 0.75 µs switch-off time of the GTOs. The simulation firing angle generator was used for the laboratory drive device firing angle look-up table with only slight modification. First, the triangular and sine waveforms are compared to obtain the phase A angle. Phases B and C are then calculated by symmetry. At each time instant, the status of the pulse sequences is stored using logic levels and pulse length information.

The operational software allows the user to select each supply frequency in turn and the number of repeat times for each frequency. During this operation, the circuit is interlocked to avoid spurious operation, and this is followed by initialisation. Time waveforms of the circuit during operation were recorded on a digital storage oscilloscope.

Experimental results

Fig. 7 gives typical experimental measured waveforms from startup for a period of 50 s. The input, DC link & motor line currents, DC link voltage and torque clearly show the step increases which occur each time the modulation frequency frequency is changed. The expanded timescale trace of motor line current shows the correct sinusoidal form. The speed increase is relatively smooth and exhibits constant acceleration in accordance with the traction duty cycle requirements.

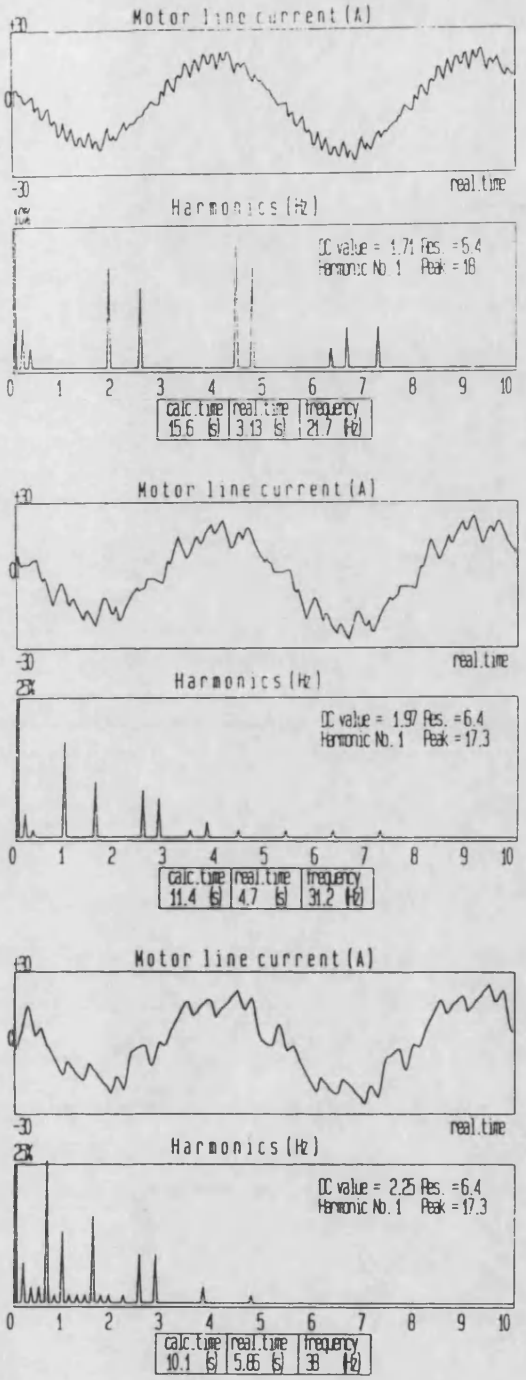

Fig. 5: Simulation model motor line current waveform and FFT analysis at 21.7, 31.2 and 38 Hz carrier frequency.

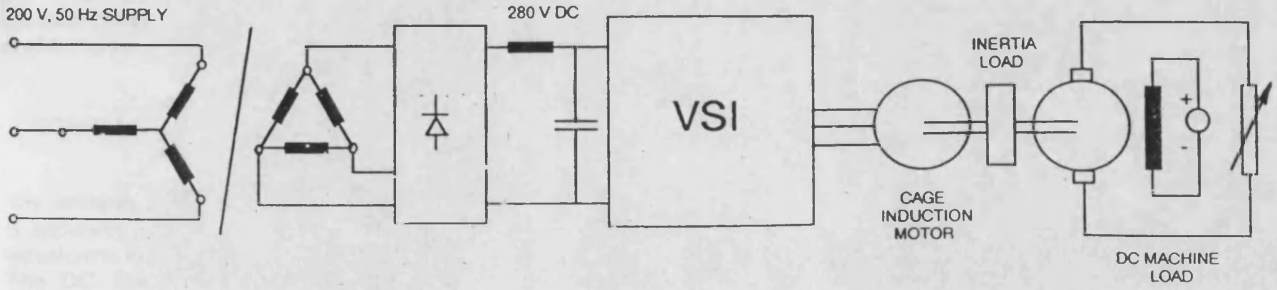

Fig. 6: Laboratory test drive.

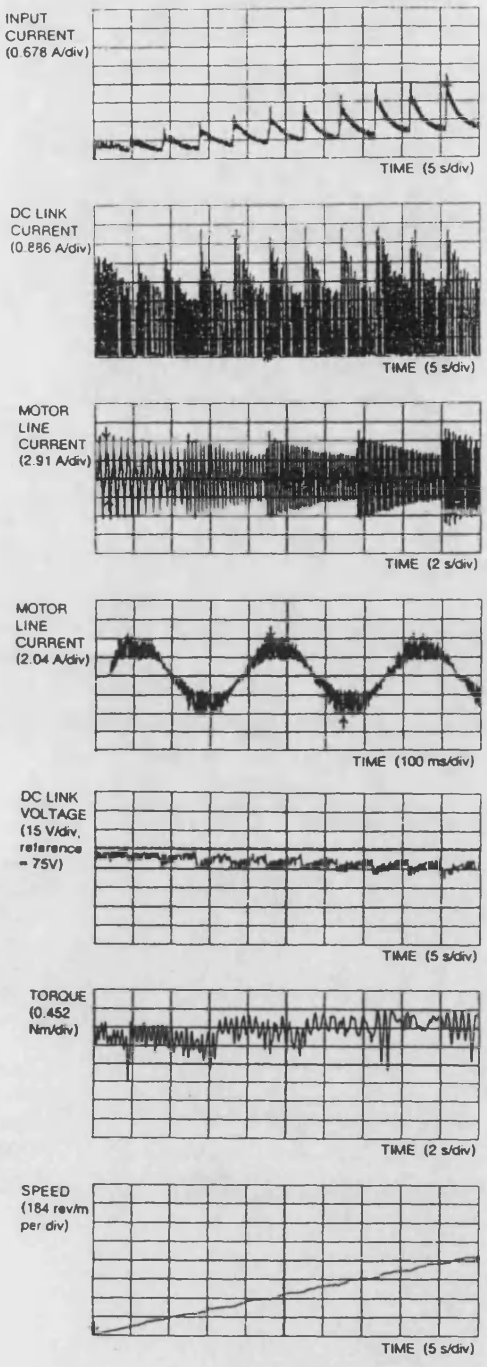

Fig. 7: Experimental test waveforms from startup.

Fig. 8 shows the experimental motor line current waveform at the modulation change which occurs at a time of 59.08 s after startup. FFT analyses of all such transients have been performed immediately before, and after the step change, samples being shown in Fig. 9, which includes the FFT of the post-transient motor current waveform of Fig. 8.

COMPARISON OF EXPERIMENTAL AND SIMULATION RESULTS

The similarity in simulated and experimental laboratory results is apparent from comparing the general system operational waveforms in Figs. 3 and 7, noting the different timescales. The DC link voltages cannot be compared since the simulation assumed a perfectly smooth supply whereas the laboratory drive was supplied from a 3-phase rectifier and filter.

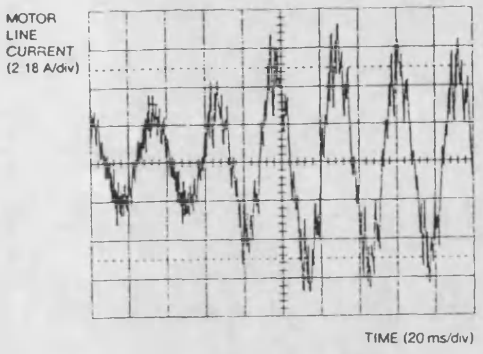

Fig. 8: Experimental motor line current waveform showing modulation change at 59.08 s after startup.

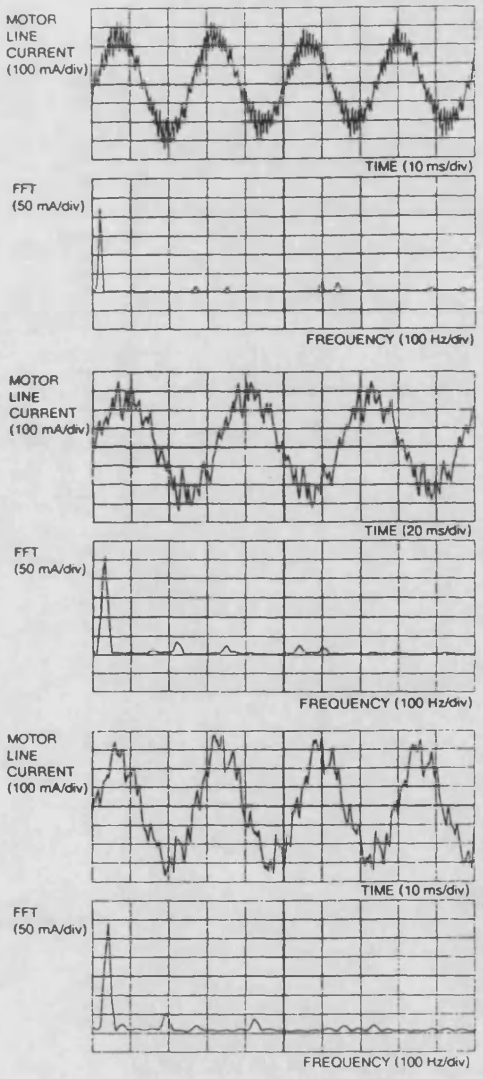

Fig. 9: Experimental motor line current waveforms and FFT analysis at 36.39, 59.10 and 72.742 s.

The motor line current has been selected for further analysis. By comparing the laboratory drive waveform (Fig. 8) with the motor line waveform in Fig. 4 during a step change, it was possible to compare the waveforms. The similarity is also borne out by comparing Figs. 5 and 7.

Harmonic spectra of motor line current were compared at the frequency points corresponding to the modulation changes given in Table 1. Table 2 shows the simulated and

Table 2: Comparison of simulated and laboratory measured motor line current harmonic spectra

Harmonic	SIMULATION			LABORATORY DRIVE		
Number	Freq	Amp	%	Freq	Amp	%
1	11.9	15.12	100	11.6	3.80	100
5	59.3	0.1598	1.057	57.8	0.045	1.20
7	83.0	0.1827	1.209	80.9	0.034	0.90
25	296.5	0.5079	3.359	289.0	0.114	3.01
29	343.9	0.5296	3.503	335.2	0.103	2.71
53	628.5	1.429	9.456	612.7	0.42	11.05
55	652.2	1.398	9.245	635.8	1.448	11.78
79	936.8	0.3986	2.637	913.2	0.086	2.25
83	984.3	0.3267	2.161	959.5	0.076	2.02

experimental results for a modulation frequency of 11.6 Hz. It should be noted that due to variation in the mains frequency of 50 Hz, the exact frequencies in the simulation and experimental test are not identical. Nevertheless, the table shows the trend of the results which indicates broad agreement between theory and experiment. This is especially true in the case of the 53rd and 55th harmonics which show a marked increase in magnitude over the adjacent table entries.

CONCLUSIONS

The simulator has proved to be a useful tool for the on-line inspection and analysis of modulation strategies for rail traction drives. The simulation model is implemented on a parallel computer and gives time domain waveforms of input, DC link & motor line current, DC link voltage, torque and speed. Windows can be defined in any of these variables from which on-line FFTs can be carried out.

Verification of the simulator has been demonstrated using a scale model of a traction drive constructed in the laboratory. The motor line current has been analysed in detail and agreement between experiment and simulated harmonic spectra at modulation changes has been obtained.

APPENDIX

Laboratory drive parameters

Motor - Delta connection, poles: 4, V: 380 V, I: 6.8 A, f: 50 Hz, P: 3 kW, T_e: 20.2 Nm, R_s: 3.08 Ω, R_r: 1.748 Ω, L_s: 11.75 mH, L_r: 11.75 mH, L_m: 0.21 H. Filter - C_f: 1.8 mF, L_f: 6 mH. Load - J: 2.0 kg.m, max. DC generator torque: 2 Nm, load inertia to motor torque ratio: 0.1.

REFERENCES

1) Bowes, S.R. and Clements, R.R. (1983). "Digital computer simulation of variable-speed PWM inverter - machine drives". IEE Proceedings, 130B, 149-160.

2) Halonen, A. and Karha, K. (1980). "AC induction motor drives in Helsinki metro cars". Conf. Rec. Advanced Propulsion Systems for Urban Rail Vehicles, Washington DC, 99-118.

3) Hill, R.J. and Huang, F. (1990a). "Performance prediction of inverter - induction motor drives for DC-fed railways". Conf. Rec. 4th International Conference on Power Electronics and Variable-Speed Drives, London, 529-533.

4) Hill, R.J. and Huang, F. (1990b). "On-line simulator for transient behaviour of inverter-fed induction motor traction drives". Conf. Rec. 3rd International Symposium on Modelling and Simulation of Electrical Machines and Static Converters, Nancy, 417-422.

5) Hill, R.J. and Huang, F. (1991). "An on-line FFT implementation for a parallel computer simulation of a VSI-IM rail traction drive". Conf. Rec. 13th IMACS World Congress, Dublin, 2 pp.

6) Taufiq, J.A. and Goodman, C.J. (1986). "Fast time domain modelling of inverter fed induction motor drive systems". Conf. Rec. 2nd International Conference on Power Electronics and Variable-Speed Drives, London, 154-157.

7) Tsuboi, T. and Nakamura, K. (1986). "Control system for traction drives". Hitachi Review, 35, 311-316.